Preparation of Piezo-, Pyro-electric and Ferroelectret Composites towards Multidimensional Applications

Thesis submitted for the degree of

Doctor of Philosophy (Science)

of

Jadavpur University

By

Krittish Roy

Department of Chemistry

Jadavpur University

Kolkata 700032

India

2022

CERTIFICATE FROM SUPERVISORS

This is to certify that the thesis entitled **"Preparation of Piezo-, Pyro-electric and Ferroelectret Composites towards Multidimensional Applications"** submitted by **Krittish Roy**, who got his name registered on 26/04/2017 for the award of Ph.D. (Science) degree of Jadavpur University, is absolutely based upon his own work under the joint supervision of **Dr. Subrata Sarkar and Dr. Dipankar Mandal** and that neither this thesis nor any part of it has been submitted for either any degree/diploma or any other academic award anywhere before.

Subrata Sarkar
11/02/202

Dr. Subrata Sarkar

(Signature of the supervisor, date with official seal)

Dr. Subrata Sarkar
Assistant Professor
Department of Physics
Jadavpur University
Kolkata-700 032

CERTIFICATE FROM SUPERVISORS

This is to certify that the thesis entitled **"Preparation of Piezo-, Pyro-electric and Ferroelectret Composites towards Multidimensional Applications"** submitted by **Krittish Roy,** who got his name registered on 26/04/2017 for the award of Ph.D. (Science) degree of Jadavpur University, is absolutely based upon his own work under the joint supervision of **Dr. Subrata Sarkar and Dr. Dipankar Mandal** and that neither this thesis nor any part of it has been submitted for either any degree/diploma or any other academic award anywhere before.

07.02.2022

Dr. Dipankar Mandal

(Signature of the supervisor, date with official seal)

Dr. DIPANKAR MANDAL
Scientist 'E'
Institute of Nano Science & Technology

Dedicated to My Inspiration,

My Mother "Saswati Roy"

Table of Contents

Preface

Preparation of Piezo-, Pyro-electric and Ferroelectret Composites towards Multidimensional Applications

In the present scenario of limited amount of fossil fuels and rapidly changing electronics dependent life style, development of new energy technology for harnessing renewable energy is the most desirable to achieve the increased energy requirement. In this regard, fabrication of nanogenerators (NGs) will be an alternative energy technology for harvesting mechanical and thermal energy from ambient environment to generate electricity. Moreover, advancement in various fabrication techniques of NGs extends its wide range of application ranging from self-powered portable electronics, wireless sensors, security to personal health care even in remote areas. As a matter of fact, the main motivation behind this thesis is to adapt effective strategies for design and preparation of polymer based highly efficient piezo- and pyroelectric NGs.

In this context, we have proposed a new strategy to develop self-polarized polymer ferroelectret based mechanical energy harvester (MEH), where addition of a 3D metal organic framework (MOF) enables successful preparation of ferroelectret film with enhanced piezoelectric co-efficient and sensing properties. Owing to its high sensitivity, it was further employed to detect human wrist pulse wirelessly. In addition, we have adapted electrospinning technique for composite poly(vinylidene fluoride) (PVDF) nanofiber preparation. The addition of external fillers such as a 2D MOF, graphene oxide (GO), CdS-rGO nanocomposite improves the piezo- and pyroelectric performances of the NGs. Furthermore, these devices were used in diversified applications, for example charging consumer electronics like LEDs, LCD and calculator; human physiological signal monitoring and pyroelectric breathing sensor. The aforementioned skin-interactive self-powered

approaches are scalable and cost-effective with multidimensional applications, stepping

forward to human-machine interface, electronic skin (e-skin) and artificial intelligence (AI).

11/02/2022   **Krittish Roy**

Department of Chemistry

Jadavpur University

Kolkata- 700032

Acknowledgement

Firstly, I would like to express my utmost gratitude to my principle supervisor, Dr. Dipankar Mandal, Former Assistant Professor, Department of Physics, Jadavpur University, Kolkata and Associate Professor (Scientist E), Institute of Nano Science & Technology (INST), Mohali, for giving me the opportunity to start and carry forward my doctoral research under his sincere supervision. I deeply appreciate his guidance, unconditional encouragement and attention. It would not be possible to complete my Ph.D. work during this pandemic (covid) without his continuous support and motivation. Additionally, whenever I needed time for health issues or regarding my family, He always showed his supportive nature. Moreover, I would miss his words "Do it faster Krittish, otherwise someone will publish this work before you".

I would like to thank Dr. Subrata Sarkar, who is my co-supervisor during my doctoral study. He has always guided me with his positive approach and contributed his valuable time for healthy conversations despite of his busy schedule.

I can barely express my deepest gratitude to Prof. Chittaranjan Sinha, Department of Chemistry, Jadavpur University for his support and guidance from the periods of bachelor degree to till date. His valuable ideas, scientific approach have enabled me to accomplish my thesis.

I thank profusely all the lab mates: Dr. Ayesha Sultana, Dr. Md. Mehebub Alam, Dr. Kuntal Maity, Dr. Prakriti Adhikary, Dr. Biswajit Mahanty, Dr. Santanu Jana, Dr. Wahida Rahman and most importantly Dr. Sujoy Kumar Ghosh for creating a homely environment in lab. Dr. Ghosh has always been a key person for me in inculcating the learning attitude towards research problems from the very first day of doctoral study. I will be forever obliged to him for giving me enough time for scientific discussions, his love and care.

It is my privilege to thank my uncle Nilanjan Sanyal and my teacher Asit Biswas for believing me and their constant support.

No words of thanks can sum up the gratitude that I owe to my family. My mother, Saswati Roy is the pillar of my academic life. She always encouraged me since my school life and she is the reason behind my all achievements. My father, Bhaskar Roy provided me all the comforts in all peaks and valleys of my life. I am privileged to have a father like him. My elder brother, Kaustav Roy always gave me valuable suggestions and encouraged me to do rigorous research for better output. Last but not the least, I would like to acknowledge my wife, Sayani Roy for being the constant support during my tough time and overcome the situation. Her optimism helped me a lot to focus in my research work.

List of Publications

Associated with this thesis

1. <u>K. Roy</u>, S. Jana, Z. Mallick, S. K. Ghosh, B. Dutta, S. Sarkar, C. Sinha*, D. Mandal*, "Two-Dimensional MOF Modulated Fiber Nanogenerator for Effective Acoustoelectric Conversion and Human Motion Detection", Langmuir 2021, 37, 7107-7117.

2. <u>K. Roy</u>, S. Jana, S. K. Ghosh, B. Mahanty, Z. Mallick, S. Sarkar, C. Sinha*, D. Mandal*, "Three-Dimnsional MOF-Assisted Self-Polarized Ferroelectret: An Effective Autopowered Remote Healthcare Monitoring Approach", Langmuir 2020, 36, 39, 11477–11489.

3. <u>K. Roy</u>, S. K. Ghosh, A. Sultana, S. Garain, M. Xie, C. Bowen, K. Henkel, D. Schemeisser, D. Mandal*, "A Self-powered Wearable Pressure Sensor and Pyroelectric Breathing Sensor Based on GO Interfaced PVDF Nanofibers", ACS Applied Nano Materials, 2019, 2, 2013-2025.

4. <u>K. Roy</u>, S. K. Ghosh, S. Jana, S. Sarkar, C. Sinha*, D. Mandal*, "CdS-rGO Nanocomposite Facilitated All Organic-Inorganic Pyroelectric Energy Harvester and Self-Powered Breathing Sensor" (under processing).

Additional work, not included this thesis

1. C. Ghosal, S. K. Ghosh, <u>K. Roy,</u> B. Chattopadhyay*, D. Mandal*, "Environmental Bacteria Engineered Piezoelectric Bio-organic Energy harvester towards Clinical Applications", Nano Energy, 2022, 93, 106843.

2. B. Mahanty, S. K. Ghosh, K. Maity, <u>K. Roy</u>, S. Sarkar, D. Mandal*, "All-Fiber Pyro- and Piezo-electric Nanogenerator for IoT Based Self-Powered Health-care Monitoring", Mater. Adv., 2021, 2, 4370-4379.

3. B. Mahanty, S. K. Ghosh, S. Jana, <u>K. Roy</u>, S. Sarkar, D. Mandal*, "All-fiber Acousto-electric Energy Harvester from Magnesium Salt-Modulated PVDF Nanofiber", Sustainable Energy Fuels, 2021, 5, 1003-1013.

4. S. K. Ghosh, T. K. Sinha, M. Xie, C. Bowen, S, Garain, B. Mahanty, <u>K. Roy</u>, K. Henkel, D. Schemeiβer, J. K. Kim and D. Mandal*, "Temperature–Pressure Hybrid Sensing All-Organic Stretchable Energy Harvester", 2020, ACS Applied Electronic Materials 2021, 3, 248-259.

5. S. Banerjee, B. Ghatak, Sk. B. Ali, <u>K. Roy</u>, K. Maity, N. Das*, R. Bandyopadhyay*, D. Mandal*, B. Tudu*, "Towards the Development of Triboelectricity-Based Virus Killer Face Mask for COVID-19: Role of Different Inputs", Healthcare Informatics for Fighting COVID-19 and Future Epidemics, 2021, 269-283.

6. S. K. Ghosh, <u>K. Roy</u>, H. K. Mishra, M. R. Sahoo, B. Mahanty, P. N. Vishwakarma, D. Mandal*, "Rollable Magnetoelectric Energy Harvester as a Wireless IoT Sensor", ACS Sustainable Chem. Eng. 2020, 8, 2, 864–873.

7. U. N. Guria, K. Maiti, S. S. Ali, A. Gangopadhyay, S. K. Samanta, <u>K. Roy</u>, D. Mandal, A. K. Mahapatra*, "An Organic Nanofibrous Polymeric Composite for Ratiometric Detection of Diethyl Chlorophosphate (DCP) in Solution and Vapor", ChemistrySelect, 2020, 5, 3770-3777.

8. A. Sultana, S. K. Ghosh, Md. M. Alam, P. Sadhukhan, <u>K. Roy</u>, M. Xie, C. R. Bowen, S. Sarkar, S. Das, T. R. Middya, D. Mandal*, "Methylammonium Lead Iodide

Incorporated Poly(vinylidene fluoride) Nanofibers for Flexible Piezoelectric-Pyroelectric Nanogenerator", ACS Appl. Mater. Interfaces 2019, 11, 27279-27287.

9. A. Sultana, Md. M. Alam, K. Roy, P. Sadhukhan, S. Sarkar, S. Das, T. R. Middya, D. Mandal*, "Perovskite Methylammonium Lead Bromide Incorporated Poly(vinylidene fluoride) Composite for Flexible Cantilever Based Self-Powered Vibration Sensor", Mater. Res. Express 2019, 6, 115709.

10. K. Roy, D. Mandal*, "CdS Decorated rGO Containing PVDF Electrospun Fiber Based Piezoelectric Nanogenerator for Mechanical Energy Harvesting Application", AIP Conf. Proc. 2018, 1942, 050125.

11. K. Roy, D. Mandal*, "PVDF/rGO Hybrid Film Based Efficient Piezoelectric Energy Harvester", AIP Conf. Proc. 2019, 2115, 030591.

List of Conference Presentations

Name of conference	Date & Year	Venue	Mode of presentation	Title	Authors
Fourth International Symposium on Semiconductor Materials and Devices (ISSMD-4)	March 8-10, 2017	Jadavpur University, India	Poster presentation	Cadmium Sulfide (CdS) Nanoparticle Assisted Electroactive β-phase Nucleation in Flexible Poly(vinylidene fluoride) Film	**Krittish Roy** and Dipankar Mandal
International Conference on Energy Option for Tomorrow: Technology to Sustainability (ICEOT 2017)	April 17-19, 2017	Kolkata, India	Poster presentation	The effect of Graphene Oxide and Reduced Graphene Oxide incorporation in PVDF Film and Nanofibers: A Comparative Study	**Krittish Roy** and Dipankar Mandal
62nd DAE Solid State Physics Symposium (DAE SSPS-2017)	Dec. 26-30, 2017	Mumbai	Poster Present-ation	CdS decorated rGO containing PVDF Electrospun Fiber Based Piezoelectric Nanogenerator for Mechanical Energy Harvesting Application	**Krittish Roy** and Dipankar Mandal
63rd DAE Solid State Physics Symposium (DAE SSPS-2017)	Dec. 18-22, 2018	Guru Jambheshar University of Science and Technology Hisar, Hariana	Poster Present-ation	PVDF/rGO hybrid Film Based Efficient Piezoelectric Energy Harvester	**Krittish Roy** and Dipankar Mandal
National Conference on Recent Developments in Nanoscience and Nanotechnology	Jan. 29-31, 2019	Jadavpur University	Poster Presentation	All-Fiber Wearable Pressure Sensor for Human Physiological Signal Acquisition	**Krittish Roy,** Sujoy Kumar Ghosh and Dipankar Mandal

List of Figures

List of Tables

List of Abbreviations

Full Name	Abbreviation
Particulate Matter	PM
Photovoltaic	PV
Internet of Things	IoT
Nanogenerator	NG
microwatt	μW
milliwatt	mW
Electromagnetic Generator	EMG
Piezoelectric Nanogenerator	PNG
Electronic Skin	e-skin
Poly(vinylidene fluoride)	PVDF
Poly(vinylidenefluoride-co-trifluoroethylene)	P(VDF-TrFE)
Poly(vinylidenefluoride-co-hexafluoropropylene)	P(VDF-HFP)
Scanning Tunnelling Microscopy	STM
Atomic Force Microscopy	AFM
Pyroelectric Nanogenerator	PyNG
Liquid Crystal Display	LCD
Electrocardiography	ECG
Electroencephalography	EEG
Electromyography	EMG
Field Effect Transistor	FET
Triboelectric Nanogenerator	TENG
Co-ordination Polymer	CP
Metal Organic Framework	MOF
N,N-dimethylformamide	DMF
Powder X-ray Diffraction	P-XRD
Fourier Transform Infrared Spectroscopy	FT-IR
Selected Area Electron Diffraction	SAED
Electroactive Phase Content	F_{EA}
Open-Circuit Voltage	*Voc*
Piezoelectric Co-efficient	d_{33}

Short-Circuit Current	I_{sc}
Figure of Merit	FoM_p
Piezoelectric Voltage Conversion Co-efficient	g_{33}
Dielectric Constant	ε_r
Power Density	P
Load Resistance	R_L
Poisson"s Ratio	v
Indium Tin Oxide	ITO
Polyethylene Terephthalate	PET
Finite Element Method	FEM
Short Time Fourier Transform	STFT
Sudden Infant Death Syndrome	SIDS
Transition Metal Dichalcogenide	TMDC
Polydimethylsiloxane	PDMS

Chapter 1

Introduction

1.1 Major Energy Sources and Need for Harvesting Renewable/Sustainable Energy

From the onset of the 21st century, the developing countries saw a boom in industrialization, a stark increase in population and need for more comfortable standard of living. Consequently, consumption of fossil fuel increases. Although fossil fuel-based industries for example, automobile exhaust, burning of coal, burn farming have raised serious threats to public health due to its tremendous emission of hazardous air/water pollutants [1]. In particular, inefficient burning of fossil fuels is one of the largest source of greenhouse gas (such as CO_2, CH_4, N_2O) and particulate matter (PM) (for example sulphate, nitrate, organic and elemental carbon) emission, which have resulted in the depletion of ozone layer, climate change and global warming [2]. Therefore, it causes serious health issues such as increasing certain type of skin cancers, eye cataracts and immune deficiency disorders. In addition, PMs can penetrate human respiratory system resulting in cardiovascular diseases even lung disorder [3]. However, current rate of fossil fuel consumption and growth in population lead many people to ask how long it will be until they run out. In contrast, renewable energy resources are naturally replenished on a human timescale. In this scenario, various clean and renewable energy sources such as wind, rain, waves, tides, solar, geo-thermal and bio-energy have been extensively exploited to their sustainability and environmental eco-friendliness [4-6].

An emerging advancement trajectory in technology and electronics contributes to smarter city and makes us more dependent on electronic gadgets. In general, conventional batteries are frequently used to run the electronic devices due to relatively high power consumption. On the other hand, batteries need to be replaced because of its limited lifetime. Moreover, disposal of batteries creates environmental pollution due to discharge of hazardous metals and chemicals. However, recent development in portable and flexible devices, integrated circuits, wireless communication, and miniaturization of electronic devices reduce the requirement of high power consumption day by day. Therefore, energy scavenging

approaches from ambient environment is a promising way to power electronic devices. It would be a sustainable approach especially for applications in sensor networks and low-powered personal consumer electronics, which can extend their capability by getting rid of batteries, power cables and providing a prolonged lifespan of power supply.
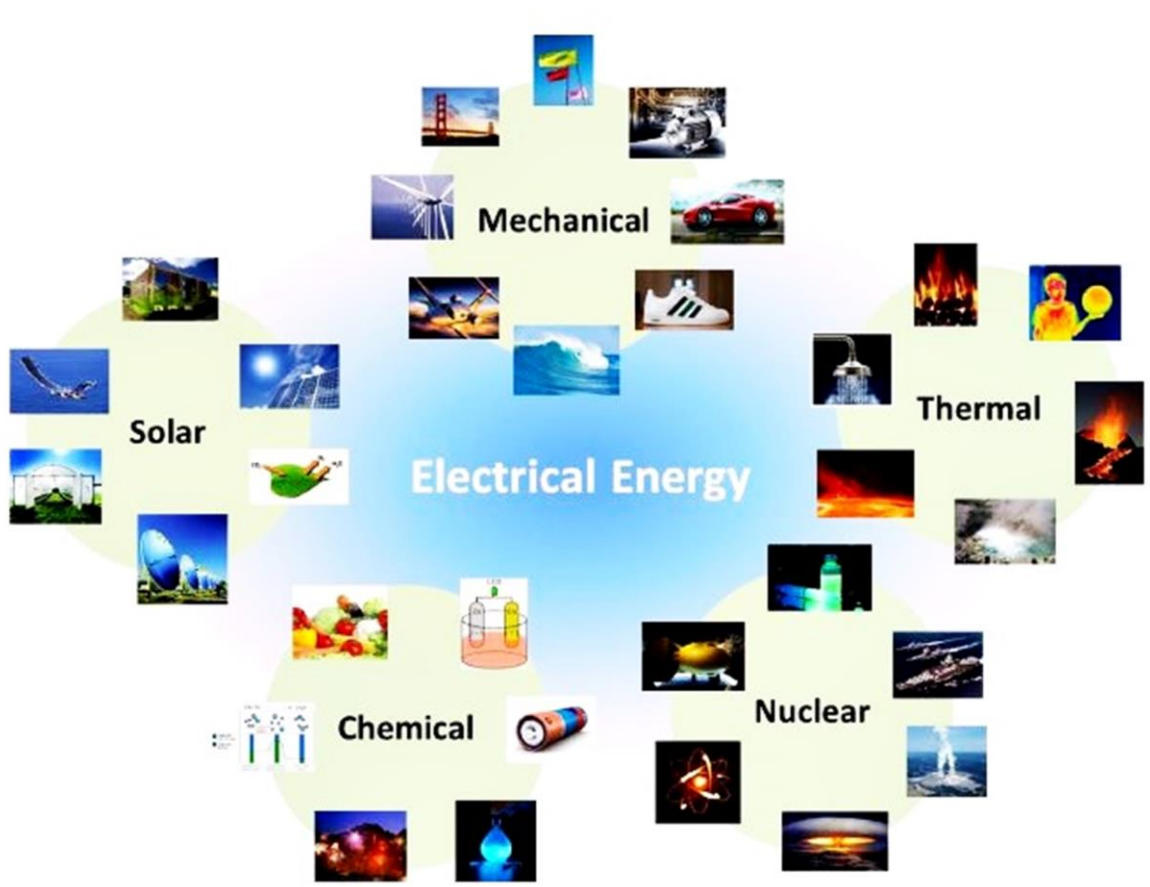
Figure 1.1 Various available energy sources in the environment and their respective forms. Reproduced with permission [7] Copyright 2015, Elsevier.

Various forms of renewable energy sources available in the working environment for energy harvesting have received varying degrees of attention such as mechanical, thermal, chemical, solar, nuclear energy etc., as shown in Figure 1.1 [7]. Till date, several technologies have been successfully developed to capture and convert the waste energy to electricity based on different energy conversion mechanism. Among these, piezoelectric and triboelectric effect

for harvesting mechanical vibrations, thermoelectric and pyroelectric effect to scavenge thermal energy and photovoltaic (PV) effect for harvesting solar energy, have been widely exploited for different sensory applications [8-12]. In addition, integration of all types of energy harvesters under micro/nanoscale systems would be a promising way to capture numerous forms of waste energy for efficient conversion into electricity. It is especially feasible for personalized health monitoring application and to power up mobile electronics by fully utilizing multiple forms of waste energy in anywhere including in complex situations.

1.2   Fundamental/Potential Sources of Energy Harvesting

1.2.1   Mechanical Energy

Among the various kinds of energy sources in the environment, mechanical energy in the form of vibrations, acoustic noise, gentle airflow, random displacements, structural vibrations like vehicles and industrial machinery, human body activities etc., is ubiquitous and one of the most available in our ambient environment at any time. Actually, the frequency and amplitude of the mechanical energy sources in the environment are typically random. Therefore, researchers are focusing on the design of a proper mechanical energy harvester which can easily function in complicated environmental conditions. Apart from the traditional cantilever based resonators and electromagnetic induction based electrical generator, devices utilize random mechanical energy to provide electricity precisely using four major transduction mechanisms, i.e., piezoelectric, triboelectric, electrostatic and magnetostrictive [13-15]. Furthermore, each of the aforementioned harvesting technologies can produce usable amount of power density depending on the frequency and acceleration of the vibrating sources.

1.2.2 Thermal Energy

Harvesting thermal energy provides us a great opportunity to reach the ever-growing demand of small scale power supply. Essentially, heat energy can be primarily classified in two forms. One is waste heat and other is nature heat. It has been reported that more than 50% of energy evolved from multiple sources like human body, industry, machines, friction, is forbidden in the form of waste heat. Moreover, natural sources rich in heat energy such as solar heat, geo-thermal heat, and volcanic heat remain unexplored. In this regard, a scalable strategy to convert the waste natural heat into electricity for different applications would be unarguably a promising approach. Thermal energy is mainly harvested in two forms: temperature gradient and temperature fluctuation. A conventional thermoelectric energy harvester primarily utilizes a spatial temperature gradient between the two ends of the device to drive the flow of charge-carriers (Figure 1.2(a)) [16]. In contrast, pyroelectric effect converts the time dependent temperature fluctuations into electricity (Figure 1.2(b)) [17].
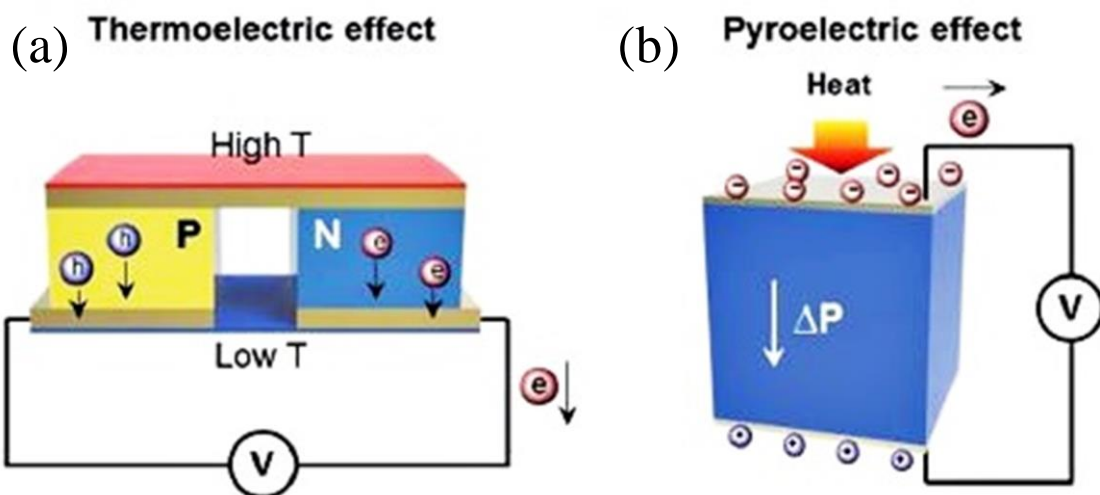
Figure 1.2 Schematic illustration of energy harvesters based on (a) the thermoelectric effect (b) the pyroelectric effect. Reproduced with permission [18] Copyright 2016, Royal Society of Chemistry.

Nevertheless, thermoelectric effect is particularly based on Seebeck effect, which is hardly effective to harvest thermal energy from ambient environment due to the temperature uniformity and time dependent temperature fluctuations. As an outcome, pyroelectric effect appears to be a very competitive method for low power consumption electronics.

1.2.3 Solar Energy

Converting solar energy into electricity has received immense attention due to its wide availability in many parts of the world, eco-friendliness and especially since the commercialization. Among the numerous solar energy harvesting techniques such as solar thermal collectors, concentrating solar power, PVs etc, the PV effect can directly convert the incident sunlight into usable electricity. In particular, when the sun light hits the solar cell, a potential difference is created through excitation and hole/electron separation as a result of light absorption by the active layer (usually semiconductor). Finally, it allows the charge carriers to flow through the material to the electrodes. Schematic of the mechanism is illustrated in Figure 1.3 [18].
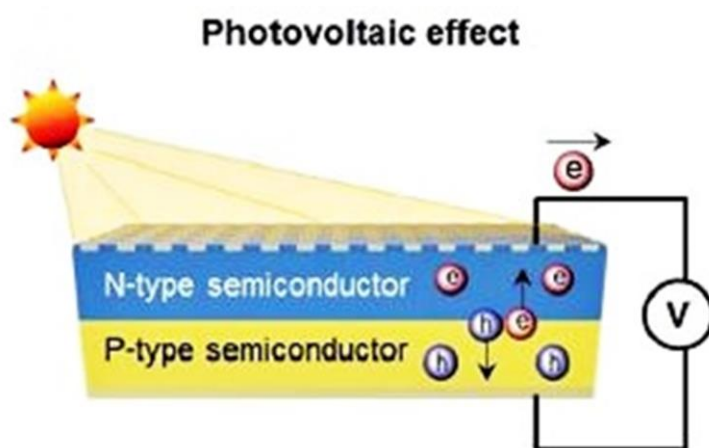
Figure 1.3 Schematic illustration of the PV effect. Reproduced with permission [18] Copyright 2016, Royal Society of Chemistry.

Furthermore, performance of a solar cell is determined in terms of conversion efficiency (η). To calculate the efficiency, it is necessary to know how much power the solar cell receives and how much it produces. The work efficiency (η) of a solar cell is determined using following equation [19]:

$$\eta = \frac{P_{out}}{P_{in}} \times 100\% = \frac{P_{out}}{E \times A_c} \times 100\%$$

Where, P_{out}= maximum power output (W), P_{in}= power of incident beam (W), E= incident radiation flux (W/m^2) and A_c= area of collector. The efficiency depends on the intensity of incident light, the temperature of the solar cell as well as material of the active layer. Depending on the semiconducting materials used for the active layer, various solar cells have been categorized, such as perovskite solar cell, organic solar cell, silicone solar cell, dye sensitized solar cell etc [19-22].

Figure 1.4 Solar energy application diagram.

In addition, the incident light absorption efficiency and conversion efficiency of the active material largely affect the performance of the solar cell. Furthermore, many challenges restrict the practical use of solar cell, for example high upfront cost, location sensitivity, installation requirements, needs access to sun etc. In spite of having such drawbacks, there are so many extensive applications of solar electricity even in remote areas as elaborated in Figure 1.4. Unarguably, solar energy would be one of the most significant renewable energy sources in near future for its diversified implementations.

1.2.4 Hybridized Energy Sources
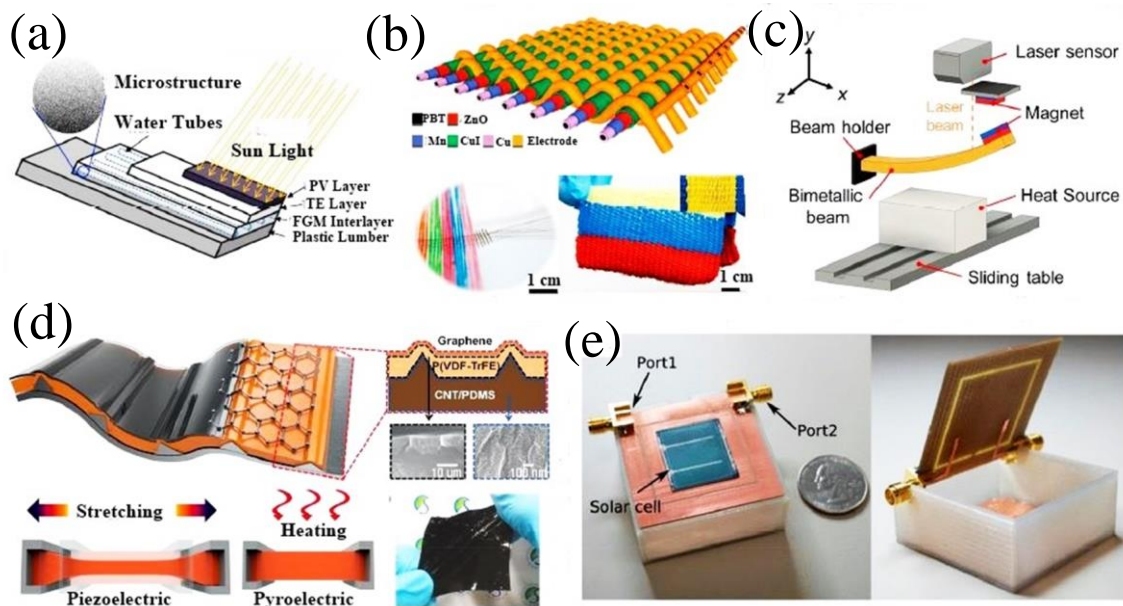
Figure 1.5 Hybrid energy harvesting systems. (a) Hybrid energy harvester from photovoltaic, thermoelectric and hot water energy [23], (b) hybrid solar and mechanical harvester [24], (c) hybrid piezoelectric and pyroelectric harvester [25], (d) stretchable piezoelectric and pyroelectric harvester [26] and (e) hybrid solar and EM harvester [24]. Reproduced with permission [23-26] Copyright 2020, Elsevier.

Until recently, energy harvesters have been designed to harvest energy from only one source and it can hardly fulfil the power requirement of the electronic devices. In this scenario, hybrid energy harvesting technology would be an emerging one to overcome the energy insufficiency at any time. A hybrid energy harvester integrates two or more energy harvesting technologies under one roof not only to scavenge energy from different sources but also to convert them into usable electricity using multiple transduction mechanisms. Moreover, hybrid materials with different architecture, device design and mechanisms are combined to improve the out power density and energy conversion efficiency. In the past few years, so many innovative strategies have been presented regarding hybridized energy harvesting technology (Figure 1.5) [23-26]. Furthermore, a variety of futuristic applications including healthcare monitoring, mobile micro-electronics, Internet of Things (IoT) can be performed using hybridized energy harvesters as a power source and self-powered sensors, discussed in Figure 1.6.
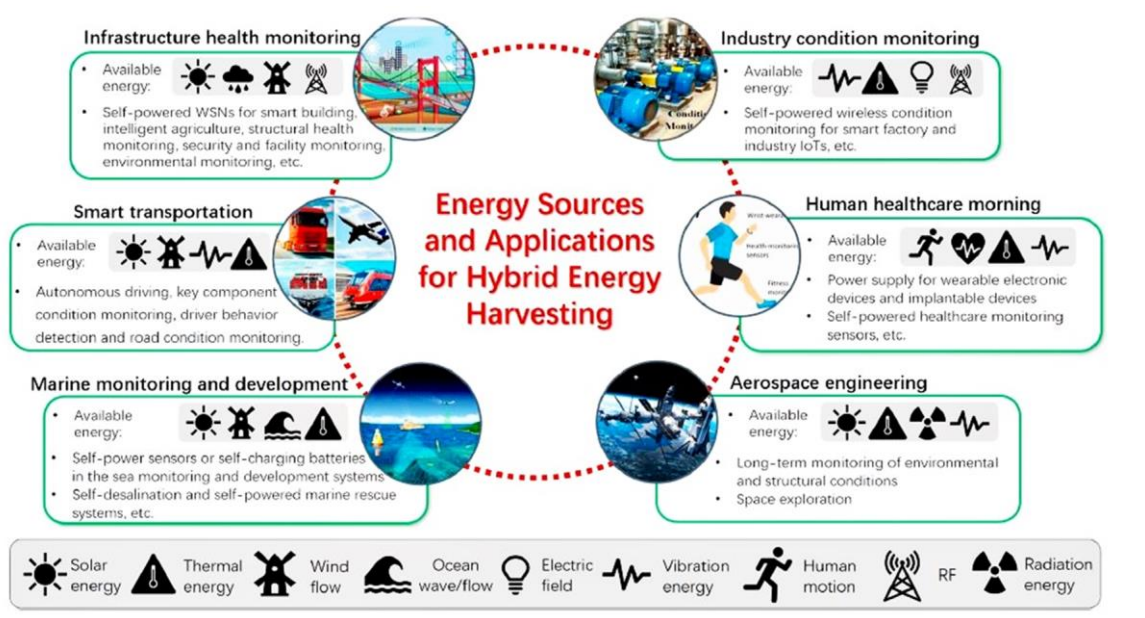
Figure 1.6 Energy sources and application prospect for hybrid energy harvesting systems. Reproduced with permission [27] Copyright 2020, Elsevier.

1.3   Self-Powered Systems/Electronics and Nanogenerator (NG)

A notable revolution in science and technology involves integration of multifunctional nano-systems, mobile and portable microelectronics with Internet of Things (IoT), wireless communication module for applications in personalized health monitoring, ultrasensitive chemical and biomolecule sensors, environmental protection and security. Moreover, miniaturization of these electronic devices is shrinking the power requirement day by day, for example microwatt (μW) to milliwatt (mW) level. As a matter of fact, it is consequently reducing the size of the batteries. However, the small size largely limits the lifetime of the battery. Moreover, chemical hazards that mix to soil due to the disposal of batteries become another threat to environment.   In this scenario, maintenance free, sustainable and clean renewable energy source is desperately needed, which will serve the purpose of self-powering the microelectronics, wireless devices and in-vivo medical sensors without any need of external power supply/battery. Therefore, construction of small-sized self-powered systems with extraordinary sensitivity, low power consumption ability and multi-functionality will resolve the concern. It is the key to sustainable economic growth as well as enhancing the quality of life. In a nut shell, self-powered technology is a system that can function without the need of an external power supply but by harvesting sufficient energy from the surrounding environment.

Among the multiple energy sources that can be harnessed in the ambient environment, mechanical energy is the most abundant as different forms such as human body movements, wind, water flow, waves. Conventional electromagnetic generators (EMGs) can harvest only high frequency mechanical energy using Faraday's law of electromagnetic induction and it was first invented in early 1800 [28]. However, most of the low frequency mechanical energy sources are wasted and unexplored. Scientists have developed an attractive approach that can

convert low frequency mechanical energy into electricity using piezoelectric effect and named it nanogenerator (NG). After the first invention of piezoelectric nanogenerator (PNG) based on ZnO nanowires, significant advancements have been carried out to develop NGs with different structures and high energy conversion efficiency [29].
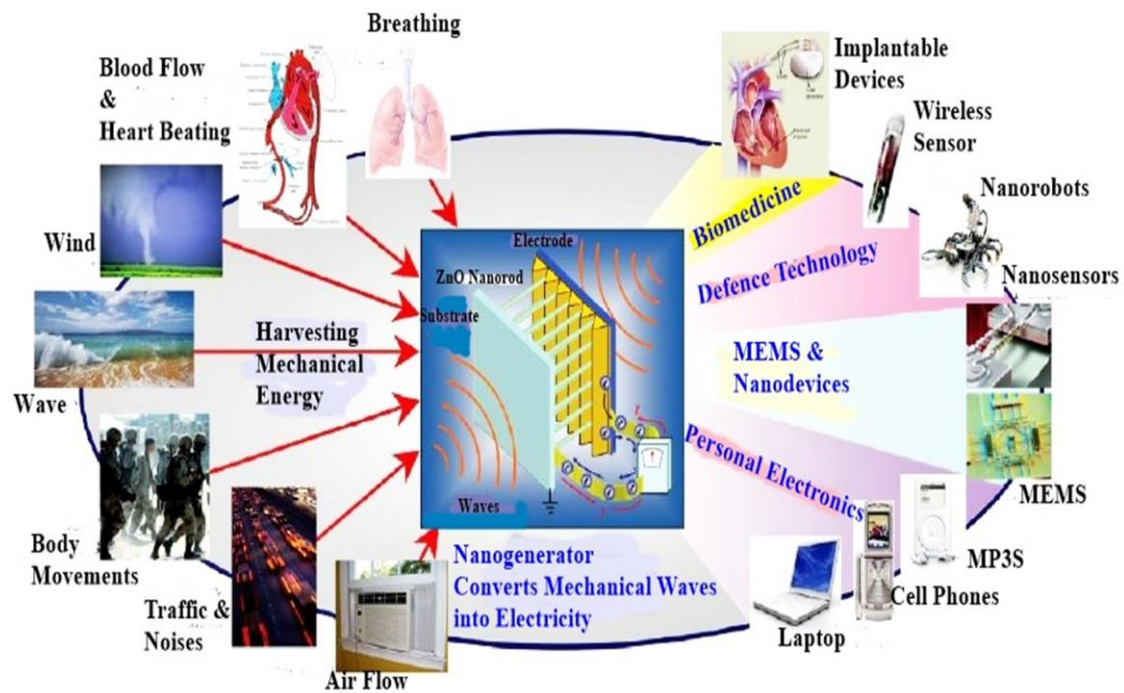
Figure 1.7 Perspectives of nanogenerators for harvesting mechanical energy and potential future applications. Reproduced with permission [30] Copyright 2020, Wiley.

NG is an emerging technology that can harvest weak mechanical/thermal energy to generate electricity. Primarily, NG can operate in three different mechanisms: Piezoelectric, triboelectric and pyroelectric. Among them, Piezoelectric and triboelectric are for mechanical energy harvesting whereas pyroelectric converts thermal energy to electrical energy. In addition, research in NG has gained remarkable popularity because of its importance not only as a power source but also in stretchable and flexible electronics such as electronic skin (e-skin) and self-powered wearable electronics. This is due to the fact that NGs can be

11

fabricated with diversified device design. Furthermore, NGs have a broad spectrum of applications as presented in Figure 1.7.

1.3.1 Piezoelectric Nanogenerator (PNG)

1.3.1.1 Piezoelectric Effect and Working Mechanism

Piezoelectric effect was first invented by Curie brothers in 1880. It can be fundamentally classified into direct piezoelectric effect and converse piezoelectric effect due to the electromechanical coupling of piezoelectric materials. Direct piezoelectric effect leads to induction of electric potential across the material under an applied mechanical stress, whereas generation of mechanical strain under the exposure to an electrical field is termed as converse piezoelectric effect. Both of these effects can be established using following piezoelectric constitutive equations [31].

$$\begin{bmatrix} \delta \\ D \end{bmatrix} = \begin{bmatrix} s^E & d^t \\ d & \varepsilon^T \end{bmatrix} \begin{bmatrix} \sigma \\ E \end{bmatrix}$$

Here σ and δ represent the stress and strain components, E and D are labelled as electric field and electric displacement respectively. s, ε and d refer to elastic compliance, dielectric constant and piezoelectric co-efficient respectively. Additionally, subscripts E and T stand for respective constants calculated under constant electric field and constant stress. Subscript t denotes the transpose. Typically, d is the most important parameter to quantify the efficiency of a piezoelectric material. It basically represents polarization generated per unit of applied mechanical stress or a mechanical strain experienced during application of electric field per unit area. The following equations describe the elctromechanical coupling and conversion of piezoelectric materials [32]:

$$S_i = s_{ij}^E T_j + d_{ki} E_k$$

$$D_i = d_{ij}T_j + \varepsilon_{ik}^T E_k$$

Where S and T define mechanical strain and stress, D, E and ε are electric displacement and electric field and dielectric permittivity under zero stress respectively.
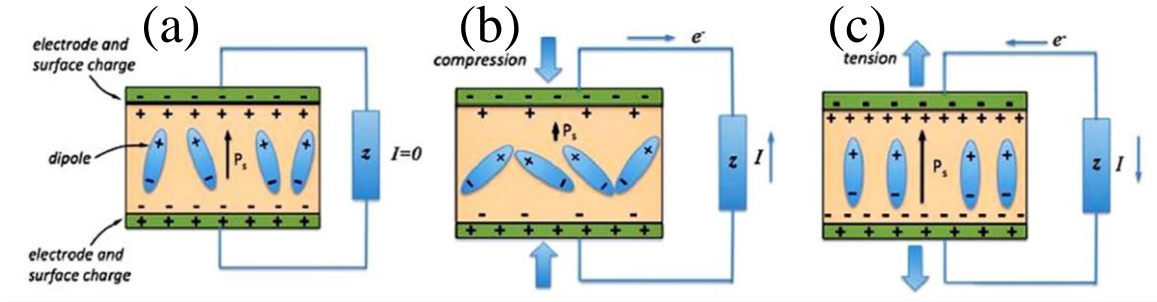
Figure 1.8 Piezoelectric effect for harvesting across electrical load. (a) No mechanical load (b) compressive load leading to a decrease in polarization relative to the no load condition (c) tensile load leading to an increase in polarization relative to the no load condition. Reproduced with permission [33] Copyright 2017, Royal Society of Chemistry.

Direct piezoelectric effect is mostly used for piezoelectric energy harvesting and sensing purpose. The direct piezoelectric effect is initiated when the material is subjected to a compressive stress. As a result, polarisation across the material decreases and potential difference is created between the two electrodes. As a consequence, external free electrons are forced the device and generates a current. Similarly, when the external load is withdrawn, polarisation level increases and leads to an opposite direction current to balance the surface charges. The whole phenomena are described through a schematic in Figure 1.8. The charge produced across the material during this procedure is evaluated as follows:

$$Q = d_{33} \times A \times \Delta\sigma$$

Where d_{33} is the piezoelectric co-efficient (C N^{-1}), A is the effective area and Δσ stands for applied mechanical stress.

In particular, d_{33} mode indicates that applied stress is in parallel to the polarisation direction i.e., 3 direction. Actually, most of the piezoelectric materials possess a well-defined polar axis, which is referred the "3" direction and the direction of applied stress is either in "3" direction (along the polar axis) or in "1" direction (right angle to the polar axis) [34]. Therefore, it leads to two main configurations for piezoelectric energy harvesting depending on the applied stress direction, "31 mode" and "33 mode" as elaborated in Figure 1.9. Usually, d_{33} co-efficient is higher compared to d_{31} mode and these are quantified to evaluate the piezoelectric performance efficiency.
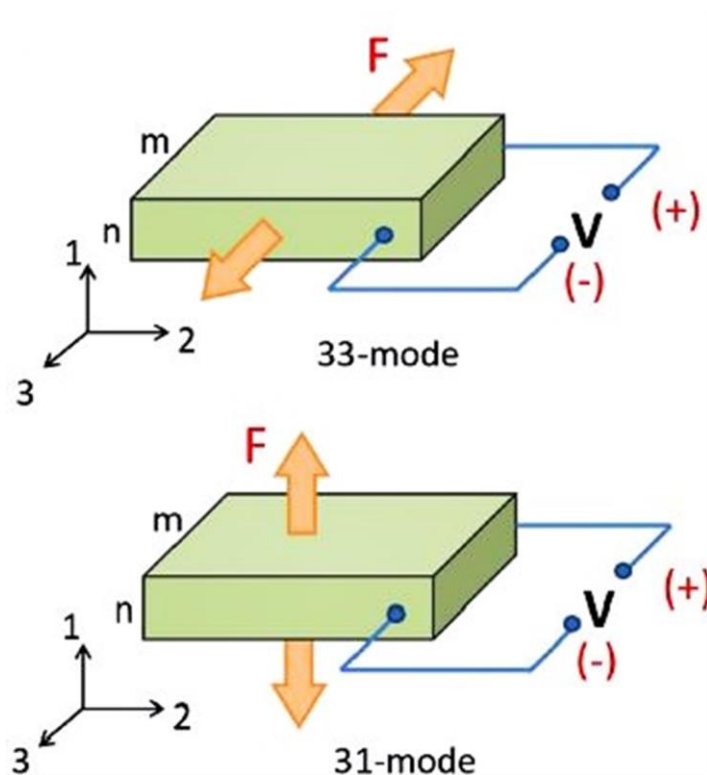
Figure 1.9 Piezoelectric material used in the 33-mode and the 31-mode. Reproduced with permission [34] Copyright 2018, AIP publishing.

1.3.1.2   Piezoelectric Materials

After the first discovery of piezoelectricity in quartz crystal by Jacques and Pierre Curie in 1880, many piezoelectric materials have been discovered as well as created by scientists including natural and artificial piezoelectric materials for different applications ranging from energy harvesting to sensors. Typically, piezoelectric materials are classified into three distinct sections such as inorganic piezoelectric materials, piezoelectric polymers and bio-piezoelectric materials.

Inorganic Piezoelectric Materials: Precisely, inorganic piezoelectric materials are categorized in two sections, one is piezoelectric crystals and another is piezoelectric ceramics. Piezoelectric crystals are typically exhibit a single-crystalline structure for example, quartz, ZnO NWs. In contrast, piezoelectric ceramics are polycrystalline, consisting of randomly oriented small crystals such as barium titanate ($BaTiO_3$), lead zirconate titanate ($Pb[Zr_xTi_{1-x}]O_3$, $0<x<1$), aluminium nitride (AlN), $(K,Na)NbO_3$, $BiFeO_3$, monolayer MoS_2[33, 35]. Moreover, it shows piezoelectricity only if the domains are aligned in a particular direction by applying a high electric field, termed as poling. Piezoelectric ceramic materials are widely applied in mechanical energy harvesting and transduction as they exhibit high piezoelectric constants and dielectric permittivity. However, low mechanical durability, costly processing route limits the practical application of inorganic piezoelectric materials.

Piezoelectric Polymers: piezoelectric polymers like PVDF and its co-polymers poly(vinylidenefluoride-co-trifluoroethylene) [P(VDF-TrFE)], poly(vinylidee fluoride-co-hexafluoropropylene) [P(VDF-HFP)] are highly acceptable wearable, flexible electronics and energy harvesting for their easy and cost-effective processing route, biocompatibility, light weight, flexibility, chemical inertness and low density [33]. Nevertheless, organic

piezoelectric materials suffer from low d_{33} value. Thus, several techniques are adapted to improve the performance of polymer based piezoelectric energy harvesters.

Bio-piezoelectric Materials: Interestingly, naturally obtained biological materials such as wood, silk, bone, specific viruses, fish scale exhibit piezoelectricity. A notable growth in biotechnology facilitates easy biodegradation as well as large-scale production of cellulose, collagen, chitin nanofibers, which further enables the potential application of bio-piezoelectric materials in eco-friendly energy harvesting and e-skin. Nevertheless, the short life time of bio-materials restricts their usage for multiple times.

1.3.1.3 Poly(vinylidene fluoride) (PVDF)

Among the variety of materials exhibiting piezoelectricity, polymer based piezoelectrics have found diverse applications which include transducers, sensors, actuators, energy harvesting and energy storage devices. Polymers that possess a net molecular dipole moment perpendicular to the backbone are of particular interest for energy harvesting and storage application. This property is typically evident in electroactive fluorinated polymers such as PVDF and its co-polymers. The electroactive property highly depends on the macromolecular chain structure including the crystalline structure, dipolar orientation and chain conformation. PVDF and its co-polymers are the most widely employed polymeric materials for smart flexible electronics.

1.3.1.3.1 Molecular and Crystalline Structure of PVDF

PVDF is a thermoplastic semi-crystalline polymeric material with a unique molecular structure. It typically exhibits five distinct crystalline polymorphs related to different chain conformations: α (phase II), β (phase I), γ (phase III), δ (phase IV) and ε [36]. Among the crystalline phases, α-phase is the most common polymorph of PVDF consisting of trans-

gauche-trans-gauche (TGTG′) conformations with aligned polymer chains antiparallel to each other (Figure 1.10). Hence it is non-polar exhibiting zero dipole moment. α-phase crystallizes in hexagonal packing with unit cell dimensions approximately a = 0.964 nm, b = 0.496 nm and c = 0.462 nm [37]. β-phase has an all-trans (TTTT) planar zigzag conformation. It means that majority of fluorine atoms are separated from the hydrogen atoms with the dipole parallel to the b-axis. Therefore, the polar crystalline form contributes to the highest dipole moment (8×10^{-30} C m) per unit cell, perpendicular to the polymer chain. β-crystal is orthorhombic and experimentally derived unit cell parameters are given as a = 0.847 nm, b = 0.49 nm, c = 0.256 nm [38].
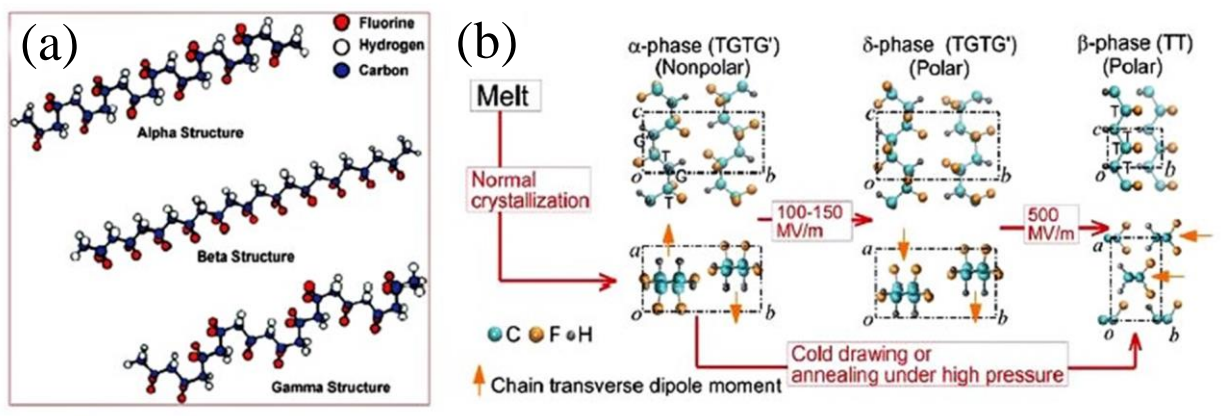
Figure 1.10 Diagrams of (a) the three α, β and γ primary polymorphic crystalline phases of PVDF [39]. (b) Electric field-induced phase transitions of PVDF. The transverse dipole moment of each polymer chain is shown using an orange arrow that points from the negatively charged fluorine atoms to the positively charged hydrogen atoms. T-trans; G-gauche [40]. Reproduced with permission [39, 40] Copyright 2017, Royal Society of Chemistry.

In contrast, γ-phase is semi-polar and the chain orientation is a transitional structure between α and β phase (TTTGTTTG′) (Figure 1.10). δ-phase is also polar but very difficult to isolate

from α-phase through conventional techniques as it is a parallel version of α- phase. γ and δ phase are responsible for piezo- and pyroelectric properties in PVDF along with β-crystal. However, achieving β-phase is the most desirable for energy harvesting and several conventional strategies have been adapted to achieve β-phase in PVDF as elaborated in Figure 1.11.
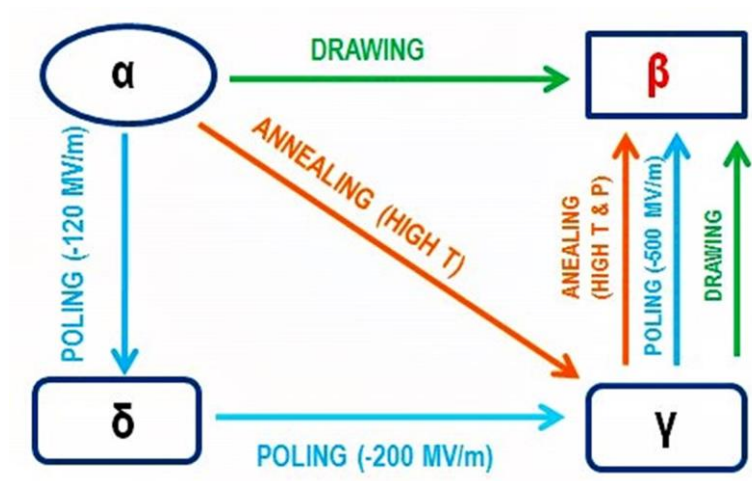
Figure 1.11 Techniques used for effective phase transformation.

1.3.1.3.2 Properties of PVDF

PVDF is a homopolymer, containing 59.4 wt% of fluorine and 3 wt% of hydrogen. The presence of fluorine atoms with large van der walls radius (1.35 A˚ and hydrogen 1.2 A˚) and electronegativity in the polymer chain induces a dipole moment perpendicular to the chain in each monomer unit. In addition, the electroactive phase melting (T_m) of PVDF is approximately at around 170 ˚C. However, minor differences have been noted depending on the phase content. The Curie transition temperature (Tc) of PVDF is highly debatable and referred to as the phase transition from the ferroelectric β-phase to the paraelectric α-phase. Moreover, it largely varies with polymer chain structure, processing condition and post treatment. The glass transition temperature (T_g) of PVDF varies between -60 ˚C to -20 ˚C. As

a result, it shows rubbery nature above 0 ˚C irrespective of the phase content. In addition, β polymorph of PVDF shows an increased density (ρ = 1.97 g mL^{-1}) compared to amorphous PVDF (ρ = 1.78 g mL^{-1}) because of having higher crystallinity (above 50%), hence higher packing [32, 41].

1.3.1.4 Application of Piezoelectric Materials and PNGs

In recent years, piezoelectric materials have been employed in a variety of applications ranging from tiny pacemakers to spacecraft according to the operational mode of the piezoelectric materials. Piezoelectric material was first used as sonar transducers or megacycle quartz resonators. In this section, a wide range of applications of piezoelectric materials have been summarized briefly.

Energy Harvesting: Piezoelectric materials can harvest electrical energy from waste mechanical energy from various sources including human activities such as running, walking, jumping, body parts movement and keyboard typing etc., in the form of nanogenerators to power portable electronic devices. The harvested energy is usually used either to extend the life time of batteries or self-powering the devices. Moreover, it combines the possibility of strain sensing as well as energy harvesting in a single piezoelectric device. The first flexible polymeric piezoelectric nanogenerator was inserted in part of the shoe, allowing the wearer to generate electricity from walking [42]. Moreover, a variety of publications have been reported, which shows considerable amount of electricity production, enabling self-powered wireless sensors and systems [43-49].

Implanted Biomedical Applications: Another promising application of PNGs is to harvest biomechanical energy to power implantable medical devices such as pacemakers, cardioverter-defibrillators, cardiac resynchronization therapy devices, and so on. However, there remain some underlying challenges regarding the integration of fully bio-compatible

self-powered energy harvesting systems for in vivo biomedical devices. Self-powered technology will reduce the use of traditional battery system as implanted batteries have limited life time and replacement of batteries requires frequent costly surgeries. Therefore, piezoelectric energy would be more advantageous for powering these devices. Deterre et al. have developed a micro spiral-shaped piezoelectric energy harvester and its associated micro-fabricated packaging for collecting energy from ordinary blood pressure variations in the cardiac environment [50]. Hwang et al. designed a self-powered deep brain stimulation via a PIMNT energy harvester for neural prosthetics and brain-computer interfacing [51]. Hasuler et al. demonstrate the in vivo operation of a piezoelectric nanogenerator attached to a rib of a dog in order to harvest energy from respiration [52]. In addition, Cheng et al. designed a PVDF based self-powered blood pressure sensor [53].

Sensors: Piezoelectric materials are used to detect and monitor pressure variations in longitudinal, transversal and shear modes. The commonest use of piezoelectric material as sensor is in accelerometers [54]. In addition, piezoelectric sensors are broadly applied to detect waves of lower frequencies, sounds in microphones and acoustic/electric guitar pickups. Moreover, piezoelectric energy harvesters are also used as self-powered sensors such as, a PVDF based device was used as strain sensor, reported by Elvin et al. [55].

Actuators: the reverse piezoelectric effect has enabled piezoelectric materials to be used as precision actuators. Since a carefully controlled electric signal can create precisely deformations in piezoelectric materials, they have been used in applications that require extremely precise positioning [56]. In addition, piezoelectric actuators have been employed in atomic microscopy instruments, including scanning tunnelling microscopy (STM) and atomic force microscopy (AFM) equipment. It is also used in every day consumer devices for example digital camera, cellular phone terminals etc.

1.3.2   Pyroelectric Nanogenerator (PyNG)

Pyroelectric nanogenerator (PyNG) has the ability to directly convert thermal energy into electricity. It is more useful for harvesting wasted heat energy compared to thermoelectric effect because a temperature gradient is needed for the latter case. However, in our environment where temperature is spatially uniform, Seebeck effect cannot be used to harvest thermal energy. In contrast, time dependent fluctuation of temperature exists almost everywhere due to sunlight, wind, numerous heating and cooling sources. In this scenario, PyNGs must be choice. Pyroelectric effect depends on the spontaneous polarization in certain anisotropic solids as a consequence of thermal fluctuations. Among the 32 point groups, 21classes do not possess a centre of symmetry, therefore non-centrosymmetric and 20 of these are piezoelectric effect. Out of these, 10 exhibit pyroelectricity because of their spontaneous polarization associated with the unit cell (Figure 1.12). Thus, all pyroelectrics are basically piezoelectric.
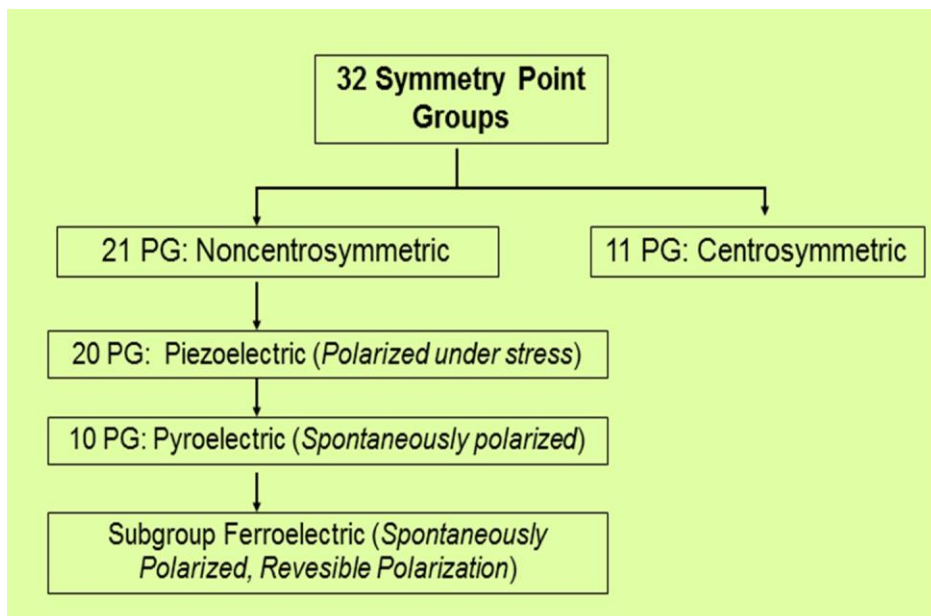
Figure 1.12 Crystallographic point groups and piezoelectricity.

1.3.2.1 Pyroelectric Effect and Working Principle of PyNGs

Pyroelectricity originates from the change in polarization level (dPs_{ij}) (C/m^2) governed by externally induced temperature change (dT) (K) in a pyroelectric material. Moreover, thermal to electrical conversion activity is determined by pyroelectric co-efficient (P^*) (C/(m^{2}K)) [57]:

$$P^* = \frac{dPs_{ij}}{dT}$$
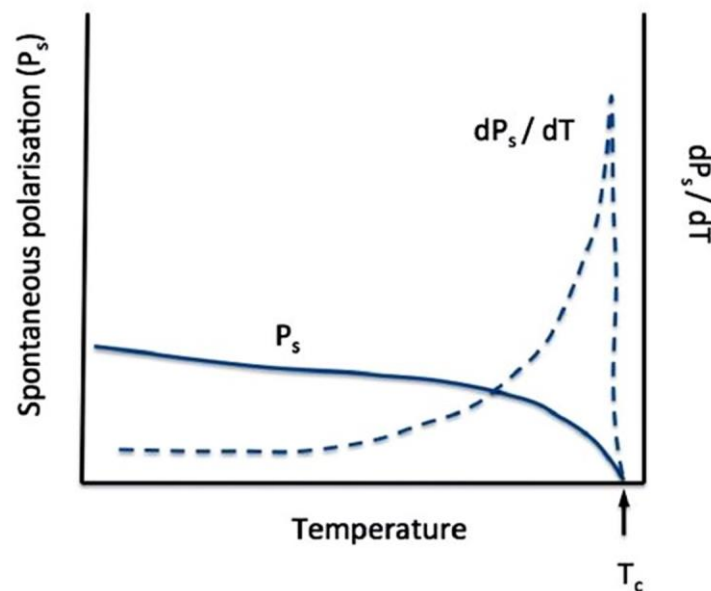
Figure 1.13 Temperature dependence of spontaneous polarization P$_s$ and pyroelectric coefficient dPs/dT of a ferroelectric material [58]. Reproduced with permission [58] Copyright 2014, Royal Society of Chemistry.

When the temperature increases (dT/dt > 0), polarization level (Ps_{ij}) decreases due to the break in dipolar orientation. As a result, an electric current is generated. On the other hand, if the temperature decreases (dT/dt > 0), the dipole reorients. Consequently, polarization level increases and a current flow in reverse direction can be observed (Figure 1.13). The change in

polarization as a result of temperature change can be directly measured as the pyroelectric short circuit current (i_p) as follows:

$$i_p = \frac{dQ}{dt} = P^* A \frac{dT}{dt}$$

Where A = effective surface area of the material, dT/dt = temperature gradient.

Thus, the net charge (Q) produced due to a temperature change (ΔT) can be quantified using the following equation, $Q = P^* A \Delta T$

Assuming a parallel plate capacitor geometry for the pyroelectric device architecture, the stored energy ($E = 1/2CV^2$) due to temperature variation can be calculated as [27],

$$E = \frac{1}{2} \frac{P^{*2}}{\varepsilon} Ah(\Delta T)^2$$

Where, ε is the dielectric permittivity of the material with thickness h in polarization direction.

1.3.2.2 Primary, Secondary and Tertiary Pyroelectric Effect

Primary pyroelectric effect originates from the alteration of degree of polarisation induced by temperature variation under constant strain with a homogeneous heat distribution without an external field bias. As we know, pyroelectrics are a subclass of piezoelectrics, thus, change in polarization can be affected by a secondary contribution originated from thermal strain that alters the electric displacement via the piezoelectric effect. Secondary pyroelectric effect can be presented using the following equation [57],

$$\frac{dPs_{ij}}{dT} = \left(P^* + d_{ij} c_{ijk} \alpha_i \right)$$

$$\frac{dPs_{ij}}{dT} = P^* - d_{ij}c_{ijk}(\alpha_i - \frac{dS_{ij}}{dT})$$

Here, d_{ij} denotes the piezoelectric co-efficient with a mechanical stiffness c_{ijk}. α_i indicates thermal expansion along with thermally induced strain dS_{ij}/dT. Secondary pyroelectric effect is likely observed in wurtzite crystals (for example CdS, ZnO).

In addition, tertiary pyroelectric effect arises due to generation of shear stress due to non-uniform heating [58]. It leads to polarization through piezoelectric effect. In that case, generated current relies on the magnitude of the temperature gradient.

1.3.2.3   Application of PyNGs

Recently, PyNGs have achieved outstanding consideration owing to their effective thermal energy conversion ability as well as widespread applications. Some of the applications of PyNGs will be discussed in this section. Guo et al. have developed a PyNG composed of a composite photoactuator comprising a LCE/graphene-doped PDMS bilayer structure and an Al-coated PVDF. It works as a photoelectric energy converter as well as a self-powered NIR light sensor for intensity monitoring and environmental temperature detector [59]. Xue et al. designed and fabricated a wearable PyNG using PVDF thin film integrated in a N95 respirator for scavenging heat energy of human respiration. Therefore, the PyNG can act as a self-powered human breathing and temperature sensor (Figure 1.14) [60]. Wang et al. have prepared near infrared induced photothermal triggered pyroelectric nanogenerator based on pn-junctions comprising p-Si/n-ZnO NWs hetero-structure for self-powered NIR photo sensing (Figure 1.15) [61]. Additionally, they have prepared a PZT film based pyroelectric nanogenerator for driving a liquid crystal display (LCD). Furthermore, a Li-ion battery was charged by this NG to drive a green light emitting diode. Therefore, it has a potential use in wireless sensors [62].
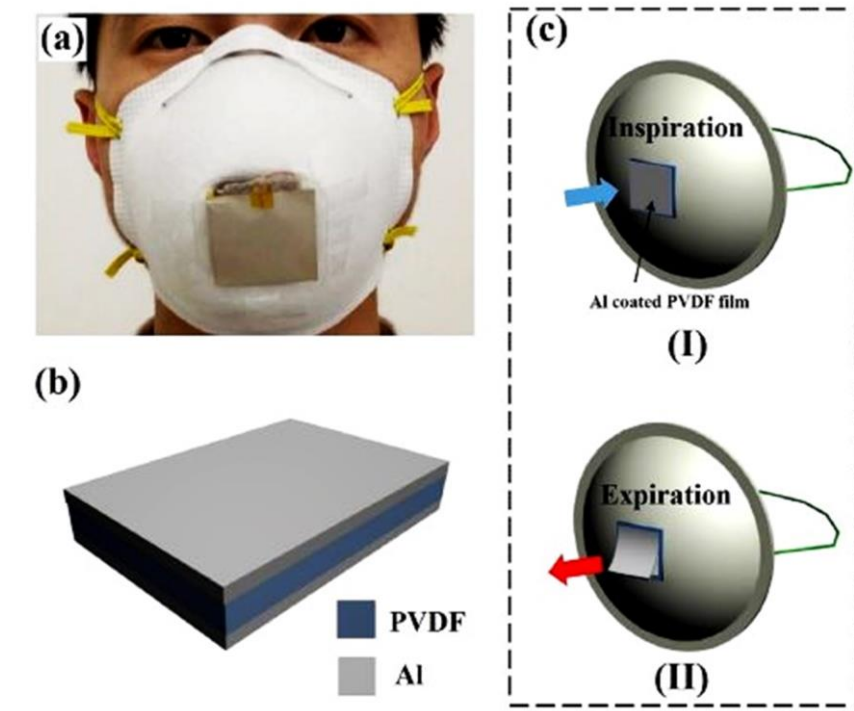
Figure 1.14 (a) The physical photo of the wearable PyNG. (b) The schematic of the pyroelectric PVDF film. (c) Schematic of a wearable PyNG driven by human respiration (I) Inspiration; (II) Expiration [60]. Reproduced with permission [60] Copyright 2014, Elsevier.

Bowen et al. have proposed a strategy of wind driven pyroelectric energy harvester, which can charge a 100 nF capacitor through a signal conditioning circuit [63]. Jiang et al. have fabricated a pyroelectric nanogenerator composed of transparent PEDOT:PSS, which can serve the purpose of stimulating the sciatic nerve of from when applied in frog muscle. As an outcome, it shows the potential of being a self-powered candidate for implantable medical electronics [64].

1.4 Wearable Health Monitoring and Physiological Sensors

Skin is the largest organ of human body and it offers an ideal surface for evaluating vital physiological signals associated with inner organs, blood vessels, muscles and dermis/epidermis. Moreover, skin can both generate and transmit biological signals revealing
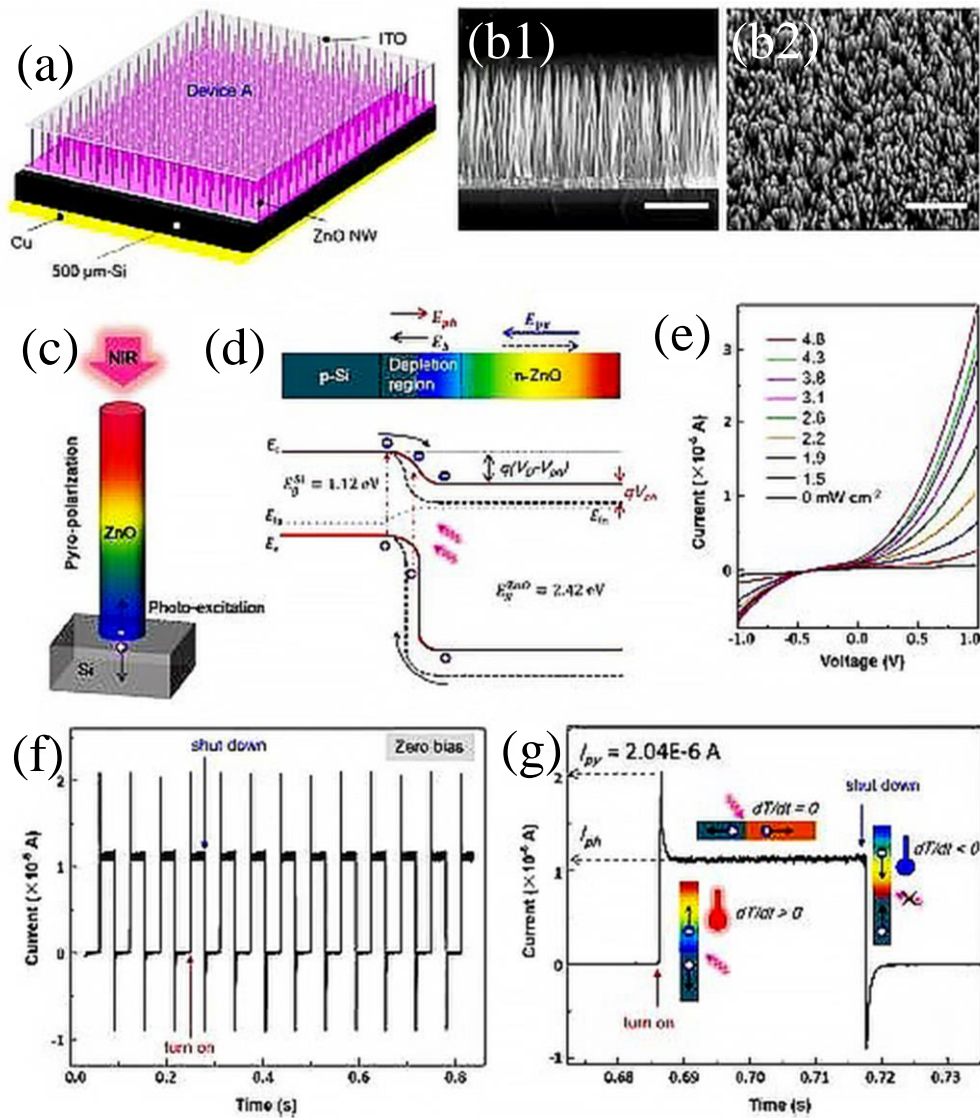
Figure 1.15 Structural and photoresponse characteristics of the NIR PDs based on the 500 μm p-Si/n-ZnO NW heterostructure. (a) Schematic image of the 500 μm p-Si/n-ZnO NW heterostructure devices. Cross-section-view (b1) and tilt-top-view (b2) scanning electron microscopy (SEM) images of the as-grown ZnO NWs, both with scale bars of 500 nm. (c) Upon the illumination of 1064 nm light, two optical processes are induced in the pn-junction device: the instantaneous pyro-polarization inside the ZnO NW and the photoexcitation at the local junction. (d) Photogenerated holes and electrons are separated, leading to the generation of Eb. (e) I−V characteristics of the p-Si/n-ZnO NIR PDs under nine different power densities of NIR illumination. (f) Under bias-free conditions, the output-current response of

the pn-junction PDs to 4.8 mW cm^{-2} NIR illumination under periodical NIR illumination. (g) One typical cycle of the short-circuit I−t curve. Reproduced with permission [61] Copyright 2014, American Chemical Society.

important health parameters of an individual as described through the Figure 1.16. Therefore, skin is indeed a signal source and an enormous effort has been paid on skin-integrated wearable medical devices for the last few decades to improve continuous health monitoring, disease diagnosis and therapy.
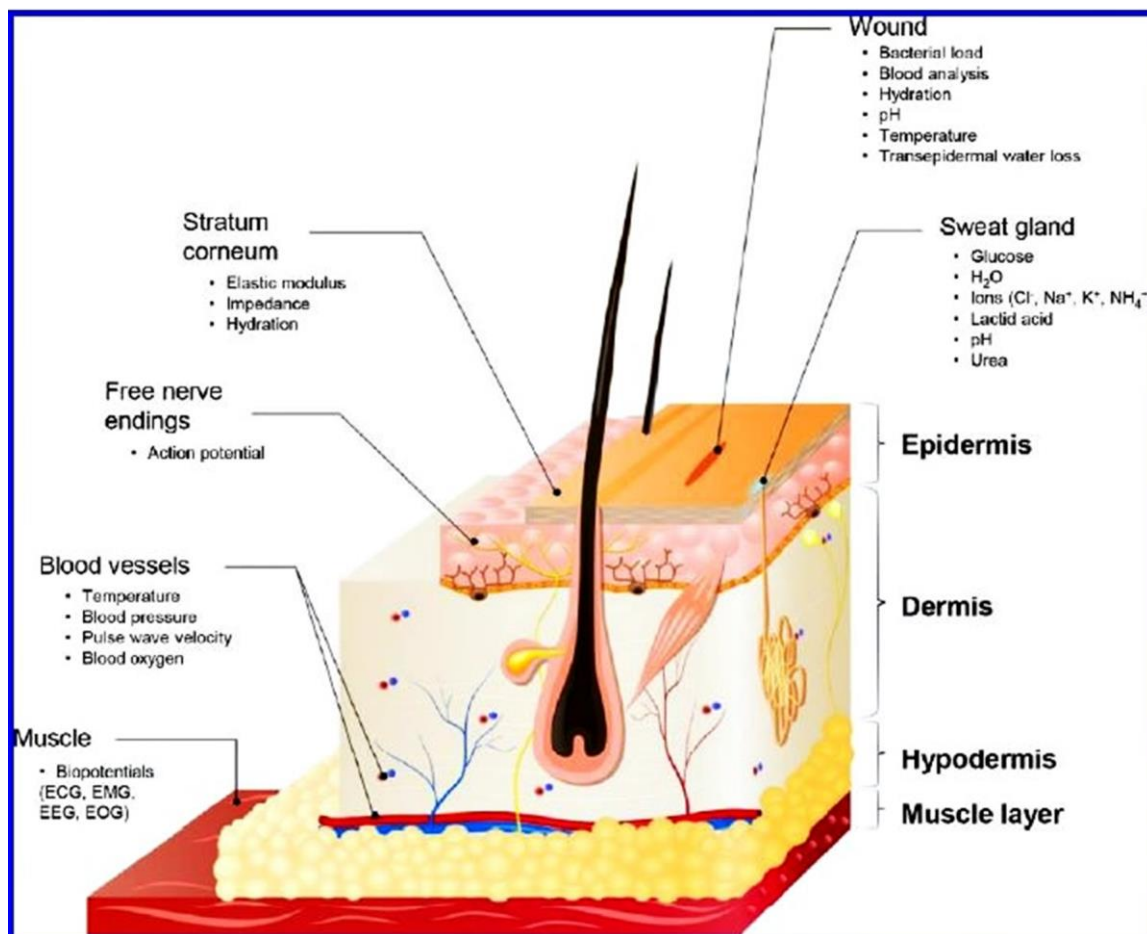
Figure 1.16 Skin as a diagnostic platform. Diagnostic signals from muscles, blood vessels, free nerve endings, stratum corneum, wounds, and sweat glands. Reproduced with permission [65] Copyright 2017, American Chemical Society.

In this regard, commercially available medical electronics give accurate and reliable outcomes for clinical assessment. However, brittle components, rigid and bulky device structure along with cumbersome wiring reduce the device integration with skin. These disadvantages prohibit mobile, comfortable and continuous long-term precision monitoring. Therefore, miniaturization of the device structure and integrated circuits, enhancing skin mounting ability would be the key for next generation wearable medical electronics to non-invasively measure the health issues.

Figure 1.17 shows some of the soft electronics which can be easily mounted on the skin at various locations on the human body for monitoring and diagnostic purpose. These devices provide important biometrics related to current physiological status, for example temperature hydration, blood pressure, blood oxygen level, skin mechanics, wound-healing, electrophysiology, and various biomarkers in sweat [65]. Such devices could expand the applications from neurology, dermatology, cardiology and hematology to urgent care. For example electrograms including electrocardiography (ECG), electroencephalography (EEG) and electromyography (EMG) provide detailed information about cardiac diseases; electrical activity of the brain related to sleep apnea, epilepsy and other neurological disorders; muscle health respectively. However, the traditional devices for electrograms are based on conventional design where electrodes of the devices are attached to the organs using adhesive tapes, gels, mechanical clamps or straps or by penetrating needles. Thus, flexible and stretchable devices are the emerging options which enable robust and soft contact on the skin with continuous, long-term and accurate sensing. These are difficult to obtain with conventional wet electrodes due to their propensity for drying out. Moreover, multifunctional wearable sensors can comprise various types of small physical sensors (temperature, pressure, strain sensors) with self-powered systems, which might facilitate low-cost solution

for recording electrophysiological activity continuously generated from the human body and personal health care.
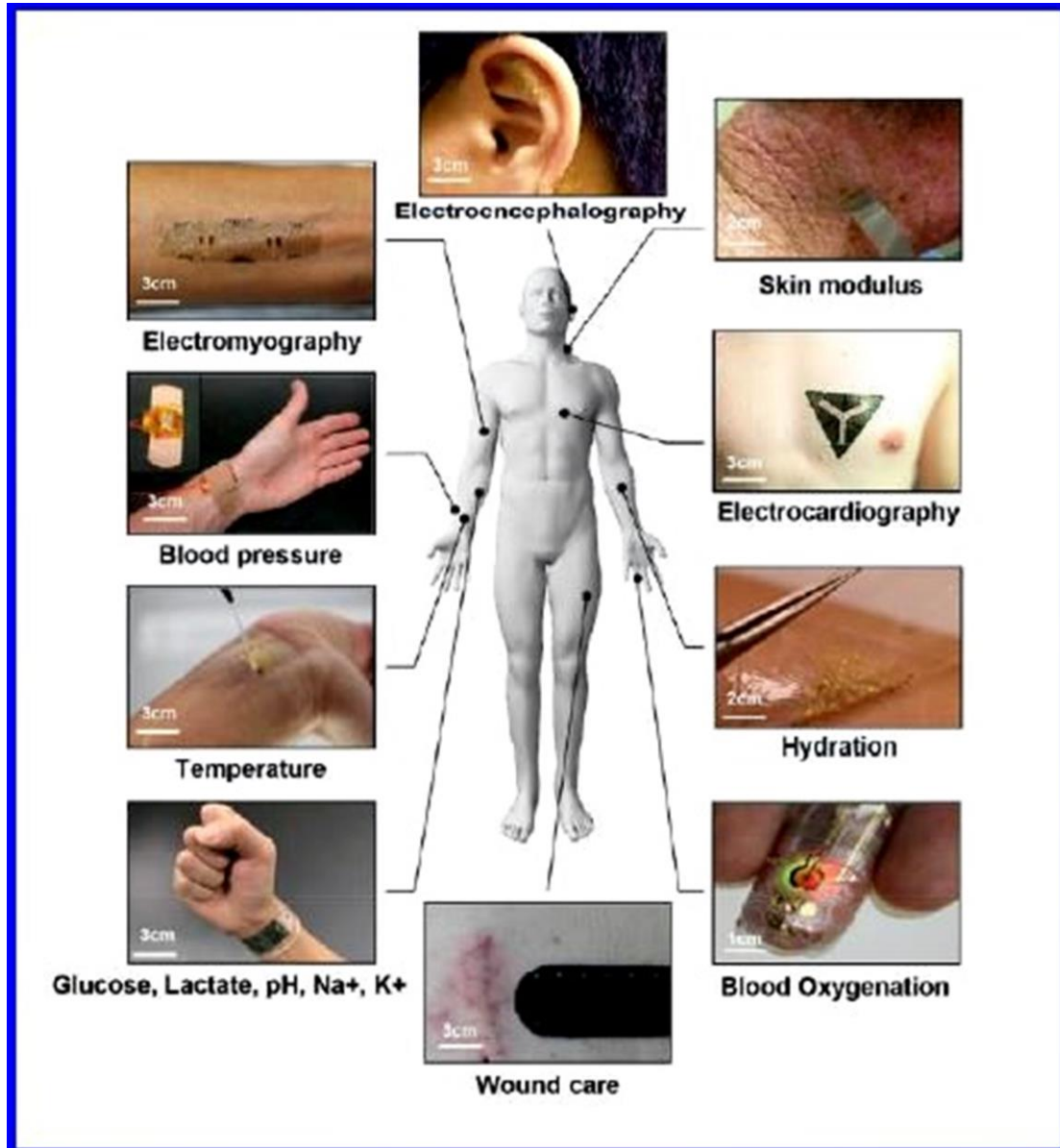
Figure 1.17 A lab-on-skin. Stretchable and flexible electronic devices as biosensors for measuring (clockwise from top right) skin modulus, electrocardiology, hydration, blood oxygen, wound-healing rate, sweat content, skin surface temperature, blood pressure, electromyography, and electroencephalography. (Reprinted with permission from (clockwise from top right) ref [66], Copyright 2013, Nature Materials; ref [67], Copyright 2014,

Scientific Reports; ref [68], Copyright 2013, IEEE; ref [69], Copyright 2016, Science Advances; ref [70], Copyright 2015, Advanced Healthcare Materials; ref [71], Copyright 2016, Nature; ref [72], Copyright 2013, Nature Materials; ref [73], Copyright 2013, Nature Communications; ref [74], Copyright 2013, Advanced Materials; ref [75], Copyright 2015, PNAS.)

1.5 Research Objectives

The works demonstrated in this thesis are to investigate the feasibility and applicability of PVDF based NGs in versatile fields ranging from self-powered portable electronics to wearable health monitoring. The works have been performed by keeping the following objectives in mind.

a) Development of high throughput piezoelectric and pyroelectric nanogenerator for harvesting mechanical and thermal energy respectively.

b) Adapting new techniques and synthesis of new type of filler material to improve the piezoelectric co-efficient, energy harvesting efficiency as well as mechano-sensitivity.

c) To construct a multifunctional system for non-invasive detecting and monitoring different physiological matrices for the real time.

d) To design a hybrid energy harvesting system to harvest both mechanical and thermal energy simultaneously.

1.6 Outline of the Thesis

This thesis covers total *five* chapters and subsequently arranged in following manner.

Chapter 1 deals with a general introduction on fundamental sources of renewable energy and different energy harvesting technologies. Moreover, this chapter tells the evolution of self-powered electronics, wearable health monitoring and NGs. It also introduces the theoretical

background, mechanism of piezo- and pyroelectric effect along with the feasible applications associated with piezoelectric and pyroelectric NGs.

In **chapter 2**, preparation of a composite PVDF nanofiber (C-PVDF) using 2D metal organic framework (MOF) is presented. The 2D MOF was synthesized using solvent layering method. Furthermore, a composite fiber based piezoelectric nanogenerator (C-PNG) was fabricated for diversified applications. It was used to monitor different human physiological motions. Additionally, C-PNG was demonstrated to be a very effective acoustoelectric energy harvester.

In **chapter 3**, fabrication of a self-poled ferroelectret film based mechanical energy harvester (MEH) is reported. The porous ferroelectret film was developed by comprising a 3D MOF with PVDF using solvent casting method. The MEH was further employed as a promising pressure sensor to detect and monitor several physiological signals such as coughing, pronunciation, gulping behaviour and wrist pulse.

In **chapter 4**, an all organic-inorganic pyroelectric nanogenerator (A-PyNG) was prepared, which include CdS-rGO nanocomposite assisted PVDF nanofiber as active material and PEDOT:PSS as organic electrode. It was finally applied as a breathing sensor.

Chapter 5 summarizes the fabrication strategy of a PVDF/GO nanofiber based piezo- and pyroelectric nanogenerator (GPPNG), which was actively demonstrated as a self-powered multifunctional pressure sensor and pyroelectric breathing sensor.

1.7   References

1. Laden, F.; Neas, L. M.; Dockery, D. W.; Schwartz, J. Association of Fine Particulate Matter from Different Sources with Daily Mortality in Six U.S. Cities. *Environ. Health Perspect.* **2000**, *108*, 941-947.

2. Seinfeld, J. H. Urban Air Pollution: State of the Science. *Science* **1989**, *243*, 745-752.

3. Brunekreef, B.; Holgate S. T. Air Pollution and Health. *Lancet* **2002**, *360*, 1233-1242.

4. Ellabban, O.; Abu-Rub. H.; Blaabjerg, F. Renewable Energy Resources: Current Status, Future Prospects and Their Enabling Technology. *Renew. Sust. Energ. Rev.* **2014**, *39*, 748-764.

5. Jacobson, M. Z.; Delucchi, M. A.; Bauer, Z. A. F.; Goodman, S. C.; Chapman, W. E.; Cameron, M. A. 100% Clean and Renewable Wind, Water, and Sunlight All-Sector Energy Roadmaps for 139 Countries of the World. *Joule* **2017**, *1*, 108-121.

6. Brown, T. W.; Bischof-Niemz, T.; Blok, K.; Breyer, C.; Lund, H.; Mathiesen, B. V. Response to 'Burden of Proof: A Comprehensive Review of the Feasibility of 100% Renewable-Electricity Systems'. *Renew. Sust. Energ. Rev.* **2018**, *92*, 834-847.

7. Hu, Y.; Wang, Z. L. Recent Progress in Piezoelectric Nanogenerators as a Sustainable Power Source in Self-Powered Systems and Active Sensors. *Nano Energy* **2015**, *14*, 3-14.

8. Wu, W.; Wang, L; Li, Y.; Zhang, F.; Lin, L.; Niu, S.; Chenet, D.; Zhang, X.; Hao, Y.; Heinz, T. F.; Hone, J.; Wang, Z. L. Piezoelectricity of Single-atomic-layer MoS2 for Energy Conversion and Piezotronics. *Nature* **2014**, *514*, 470-474.

9. Zhu, G.; Chen, J.; Zhang. T.; Jing, Q.; Wang, Z. L. Radial-arrayed Rotary Electrification for High Performance Triboelectric Generator. *Nat. Commun.* **2014**, *5*, 3426.

10. Yang, Y.; Guo, W.; Pradel, K. C.; Zhu, G.; Zhou, Y.; Zhang, Y.; Hu, Y.; Lin, L.; Wang, Z. L. Pyroelectric Nanogenerators for Harvesting Thermoelectric Energy. *Nano Lett.* **2012**, *12*, 2833-2838.

11. Kim, S. I.; Lee, K. H.; Mun, H. A.; Kim, H. S.; Hwang, S. W.; Roh, J. W.; Yang, D. J.; Shin, W. H.; Li, X. S.; Lee, Y. H.; Snyder, G. J.; Kim, S. W. Thermoelectrics

Dense Dislocation Arrays Embedded in Grain Boundaries for High-Performance Bulk Thermoelectrics. *Science* **2015**, *348*, 109-114.

12. You, J.; Dou, L.; Youshimura, K.; Kato, T.; Ohya, K.; Moriarty, T.; Emery, K.; Chen C.-C.; Gao, J.; Li, G.; Yang, Y. A Polymer Tandem Solar Cell with 10.6% Power Conversion Efficiency. *Nat. Commun.* **2013**, *4*, 1446.

13. Glynne-Jones, P.; Beeby, S.P.; White, N.M. Towards a Piezoelectric Vibration-Powered Microgenerator. *IEE Proc.-Sci. Meas. Technol.* **2001**, *148*, 68–72.

14. Amirtharajah, R.; Chandrakasan, A.P. Self-Powered Signal Processing Using Vibration-Based Power Generation. *IEEE J. Solid-State Circuits* **1998**, *33*, 687–695.

15. Sample, A.; Smith, J. R. Experimental Results with Two Wireless Power Transfer Systems, *IEEE radio and wireless Symp.* San Diego, CA, USA, **2009**, 16-18.

16. Bell, L. E. Cooling, Heating, Generating Power, and Recovering Waste Heat with Thermoelectric Systems. *Science* 2008, 321, 1457–1461.

17. Lingam, D.; Parikh A. R.; Huang, J.; Jain, A.; Minary-Jolandan, M. Nano/Microscale Pyroelectric Energy Harvesting: Challenges and Opportunities. *Int J Soc Netw Min* **2013**, *4*, 229–245.

18. Lee, J-H.; Kim, J.; Kim, T. Y.; Al Hossain, M. S.; Kim, S. W.; Kim, J. H. All-in-one energy harvesting and storage devices. *J. Mater. Chem. A* **2016**, *4*, 7983–7999.

19. Clarke, T. M.; Durrant, J. R. Charge Photogeneration in Organic Cells. *Chem. Rev.* **2010**, *110*, 6736-6767.

20. Saga, T. Advances in Crystalline Silicon Solar Cell Technology for Industrial Mass Production. *NPG Asia Mater.* **2010**, *2*, 96-102.

21. Lin, J.; Heo, Y.-U.; Nattestad, A.; Shahabuddin, M.; Yamauchi, Y.; Kim, J. H. N719- and D149-sensitized 3D Hierarchical Rutile TiO_2 Solar Cells- a Comparative Study. *Phys. Chem. Chem. Phys.* **2015**, *17*, 7208-7213.

22. Liu, Y.; Ji, S.; Li, S.; He, W.; Wang, K.; Hu, H.; Ye, C. Study on Hole-Transport-Material-Free Planar TiO$_2$/CH$_3$NH$_3$PbI$_3$ Heterojunction Solar Cells: the Simplest Configuration of a Working Perovskite Solar Cell. *J. Mater. Chem. A* **2015**, *3*, 14902-14909.

23. Yang, D.; Yin H. Energy Conversion Efficiency of a Novel Hybrid Solar System for Photovoltaic, Thermoelectric, and Heat Utilization. *IEEE Trans Energy Convers* **2011**, *26*, 662–70.

24. Bito, J.; Bahr, R.; Hester, J. G.; Nauroze, S. A.; Georgiadis, A.; Tentzeris M. M. A Novel Solar and Electromagnetic Energy Harvesting System with a 3-D Printed Package for Energy Efficient Internet-of-Things Wireless Sensors. *IEEE Trans Microw Theor Tech* **2017**, *65*, 1831–1842.

25. Kang, M.; Yeatman E. M. Coupling of Piezo- and Pyro-electric Effects in Miniature Thermal Energy Harvesters. *Appl. Energy* **2020**, *262*, 114496.

26. Lee, J-H.; Lee, K. Y.; Gupta, M. K.; Kim, T. Y.; Lee, D-Y.; Oh, J. Highly Stretchable Piezoelectric-Pyroelectric Hybrid Nanogenerator. *Adv. Mater.* **2014**, *26*, 765–769.

27. Liu, H.; Fu, H.; Sun, L.; Lee, C.; Yeatman E. M. Hybrid Energy Harvesting Technology: From Materials, Structural Design System Integration to Applications. . *Renew. Sust. Energ. Rev.* **2021**, *137*, 110473.

28. Zi, Y.; Guo, H., Wen, Z., Yeh, M. H.; Hu, C., Wang, Z. L. Harvesting Low-Frequency (<5 Hz) Irregular Mechanical Energy: A Possible Killer Application of Triboelectric Nanogenerator. *ACS Nano* **2016**, *10*, 4797-4805.

29. Wang Z. L.; Song, J. Piezoelectric Nanogenerators Based on Zinc Oxide Nanowire Arrays. *Science* **2006**, *312*, 242-246.

30. Wang, Z. L. Towards Self-Powered Nanosystems: Nanogenerators to Nanopiezotronics. *Adv. Funct. Mater.* **2008**, *18*, 3553-3567.

31. Erturk, A.; Inman, D. J. Piezoelectric Energy Harvesting. *John Wiley & Sons* New York, **2011.**

32. Shepelin, N. A.; Glushenkov, A. M.; Lussini, V. C.; Fox, P. J.;Dicinoski, G. W.; Shapter, J. G.; Ellis, A. V. New Developments in Composites, Copolymer Technologies and Processing Techniques for Flexible Fluoropolymer Piezoelectric Generators for Efficient Energy Harvesting. *Energy Environ. Sci.* **2019**, *12*, 1143-1176.

33. Wan, C.; Bowen, C. R. Multiscale-Structuring of Polyvinylidene Fluoride for Energy Harvesting: the Impact of Molecular-, Micro- and Macro-Structure. *J. Mater. Chem. A* **2017**, *5*, 3091–3128.

34. Liu, H.; Zhong, J.; Lee, C., Lee, S-W., Lin, L. A Comprehensive Review on Piezoelectric Energy Harvesting Technology: Materials, Mechanisms, and Applications. *Appl. Phys. Rev.* **2018**, *5*, 041306.

35. Kim, H.; Kim, J.; Kim, J. A Review of Piezoelectric Energy Harvesting Based on Vibration. *Int. J. Precis. Eng. Manuf.* **2011**, *12*, 1129-1141.

36. Martin, J.; Zhao, D.; Lenz, T.; Katsouras I., Leeuw , D. M. de.; Stingelin, N. Solid-State-Processing of δ-PVDF. *Mater. Horizons* **2017**, *4*, 408-414.

37. Bachmann, M. A.; lando, J. B. A Re-examination of the Crystal Structure of Phase II of Poly(vinylidene fluoride). *Macromolecules* **1981**, *14*, 40.

38. Ruan, L.; Yao, X.; Chang, Y.; Zhou, L.; Qin, G.; Zhang, X. Properties and Applications of the β Phase Poly(vinylidene fluoride). *Polymers* **2018**, *10*, 228.

39. B. Ameduri, From Vinylidene Fluoride (VDF) to the Applications of VDF-Containing Polymers and Copolymers: Recent Developments and Future Trends†. *Chem. Rev.* **2009**, *109*, 6632–6686.

40. Yu, Y.-J.; McGaughey, A. J. H. Energy Barriers for Dipole Moment Flipping in PVDF-Related Ferroelectric Polymers. *J. Chem. Phys.* **2016**, *144*, 014901.

41. B. Ameduri, From Vinylidene Fluoride (VDF) to the Applications of VDF-Containing Polymers and Copolymers: Recent Developments and Future Trends†. *Chem. Rev.* **2009**, *109*, 6632–6686.

42. Kymissis, J.; Kendall, C.; Paradiso J.; Gershenfeld, N. Parasitic power harvesting in shoes, USA, **1998**.

43. Zhao, J.; You, Z. A Shoe-Embedded Piezoelectric Energy Harvester for Wearable Sensors. *Sensors* **2014**, *14*, 12497–12510.

44. Han, Y.; Cao, Y.; Zhao, J.; Yin, Y.; Ye, L.; Wang, X.; You, Z. A Self-Powered Insole for Human Motion Recognition. *Sensors* **2016**, 16, 1502.

45. Fan, K.; Liu, Z.; Liu, H.; Wang, L.; Zhu, Y.; Yu, B. Scavenging Energy from Human Walking through a Shoe-Mounted Piezoelectric Harvester. *Appl. Phys. Lett.* **2017**, *110*, 143902.

46. Jung, W. S.; Lee, M. J.; Kang, M. G.; Moon, H. G.; Yoon, S. K.; Baek, S. H.; Kang, C. Y. Powerful Curved Piezoelectric Generator for Wearable Applications. *Nano Energy* **2015**, *13*, 174–181.

47. Shukla, R.; Bell, A. J. A Novel Energy Harvesting Concept for Low Frequency Human Waistline. *Sens. Actuators, A* **2015**, *222*, 39–47.

48. Kuang, Y.; Ruan, T.; Zheng, J. C.; Zhu, M. Energy Harvesting During Human Walking to Power a Wireless Sensor Node. *Sens. Actuators, A* **2017**, *254*, 69–77.

49. Izadgoshasb, I.; Lim, Y. Y.; Lake, N.; Tang, L.; Padilla, R. V.; Kashiwao, T. Optimizing Orientation of Piezoelectric Cantilever Beam for Harvesting Energy from Human Walking. *Energy Convers. Manage.* **2018**, *161*, 66–73.

50. Deterre, M.; Lefeuvre, E.; Zhu, Y.; Woytasik, M.; Boutaud, B. Molin, R. D. Micro Blood Pressure Energy Harvester for Intracardiac Pacemaker. *J. Microelectromech. Syst.* **2014**, *23*, 651–660.

51. Hwang, G. T.; Kim, Y.; Lee, J. H.; Oh, S.; Jeong, C. K.; Park, D. Y., Ryu, J.; Kwon, H. S.; Lee, S. G.; Joung, B.; Kim, D.; Lee, K. J. Self-powered Deep Brain Stimulation *via* a Flexible PIMNT Energy Harvester†. *Energy Environ.Sci.* **2015**, *8*, 2677–2684.

52. Hausler, E.; Stein L.; Harbauer, G. Implantable Physiological Power Supply with PVDF Film Ferroelectrics. **1984**, *60*, 277-282.

53. Cheng, X. L.; Xue, X.; Ma, Y.; Han, M. D.; Zhang, W.; Xu, Z. Y.; Zhang, H.; Zhang, H. X. Implantable and Self-Powered Blood Pressure Monitoring Based on a Piezoelectric Thin Film: Simulated, in vitro and in vivo studies. *Nano Energy* **2016**, *22*, 453-460.

54. Tadigadapa, S.; Mateti, K. Piezoelectric MEMS Sensors: State of the Art and Perspectives. *Meas Sci Technol.* **2009**, *20*, 092001.

55. Elvin, N.; Elvin, A.; Choi, D. H. A Self-Powered Damage Detection Sensor. *J. Strain Anal. Eng. Des.* **2003**, *38*, 115–124.

56. Gao, J.; Xue, D.; Liu, W.; Zhou, C.; Ren, X. Recent Progress on $BatiO_3$-Based Piezoelectric Ceramics for Actuator Applications. *Actuators* **2017**, *6*, 24.

57. Zabek, D.; Seunarine, K.; Spacie, C.; Bowen, C. R. Graphene Ink Laminate Structures on Poly(vinylidene difluoride) (PVDF) for Pyroelectric Thermal Energy Harvesting and Waste Heat Recovery. *ACS Appl. Mater. Interfaces* **2017**, *9*, 9161−9167.

58. Bowen, C. R.; Taylor, J.; LeBoulbar, E.; Zabek, D.; Chauhanc A.; Vaish, R. Pyroelectric Materials and Devices for Energy Harvesting Applications. *Energy Environ. Sci.* **2014**, *7*, 3836-3856.

59. Wei, W.; Gao, J.; Yang, J., Wei, J.; Guo J. A NIR Light-Triggered Pyroelectric-Dominated Generator Based on a Liquid Crystal Elastomer Composite Actuator for Photoelectric Conversion and Self-Powered Sensing†. *RSC Adv.* **2018**, *8*, 40856.

60. Xue, H.; Yang, Q.; Wang, D.; Luo, W.; Wang, W.; Lin, M.; Liang, D.; Luo Q. A Wearable Pyroelectric Nanogenerator and Self-Powered Breathing Sensor. *Nano Energy* **2017**, *38*, 147-154.

61. Wang, X.; Dai, Y.; Liu, R.; He, X.; Li, S.; Wang Z. L. Light-Triggered Pyroelectric Nanogenerator Based on a pn-Junction for Self-Powered Near-Infrared Photosensing. *ACS Nano* **2017**, *11*, 8339−8345.

62. Yang, Y.; Wang, Zhang, S.; Wang Z. L. Pyroelectric Nanogenerators for Driving Wireless Sensors. *Nano Lett.* **2012**, *12*, 6408−6413.

63. Xie, M.; Zabek, D.; Bowen, C.; Abdelmageed, M.; Arafa. M. Wind-Driven Pyroelectric Energy Harvesting Device. *Smart Mater. Struct.* **2016**, *25*, 125023.

64. Jiang, W.; Zhao, T.; Liu, H.; Jia, R.; Niu, D.; Chen, B.; Shi, Y.; Yina L.; Lu, B. Laminated Pyroelectric Generator with Spin Coated Transparent Poly(3,4-ethylenedioxythiophene) Polystyrene Sulfonate (PEDOT:PSS) Electrodes for a Flexible Self-Powered Stimulator†. *RSC Adv.* **2018**, *8*, 15134.

65. Liu, Y.; Pharr, M.; Salvatore, G. A. Lab-on-Skin: A Review of Flexible and Stretchable Electronics for Wearable Health Monitoring. *ACS Nano* **2017**, *11*, 9614-9635.

66. Dagdeviren, C.; Shi, Y.; Joe, P.; Ghaffari, R.; Balooch, G.; Usgaonkar, K.; Gur, O.; Tran, P. L.; Crosby, J. R.; Meyer, M.; Su, Y.; Webb, R. C.; Tedesco, A. S.; Slepian, M. J.; Huang, Y.; Rogers, J. A. Conformal Piezoelectric Systems for Clinical and Experimental Characterization of Soft Tissue Biomechanics. *Nat. Mater.* **2015**, *14*, 728−736.

67. Lee, S. M.; Byeon, H. J.; Lee, J. H.; Baek, D. H.; Lee, K. H.; Hong, J. S.; Lee, S.-H. Self-Adhesive Epidermal Carbon Nanotube Electronics for Tether-Free Long-Term Continuous Recording of Biosignals. *Sci. Rep.* **2015**, *4*, 6074.

68. Huang, X.; Cheng, H.; Chen, K.; Zhang, Y.; Zhang, Y.; Liu, Y.; Zhu, C.; Ouyang, S.-C.; Kong, G.-W.; Yu, C.; Huang, Y.; Rogers, J. A. Epidermal Impedance Sensing Sheets for Precision Hydration Assessment and Spatial Mapping. *IEEE Trans. Biomed. Eng.* **2013**, *60*, 2848− 2857.

69. Yokota, T.; Zalar, P.; Kaltenbrunner, M.; Jinno, H.; Matsuhisa, N.; Kitanosako, H.; Tachibana, Y.; Yukita, W.; Koizumi, M.; Someya, T. Ultraflexible Organic Photonic Skin. *Sci. Adv.* **2016**, *2*, 1501856.

70. Hattori, Y.; Falgout, L.; Lee, W.; Jung, S. Y.; Poon, E.; Lee, J. W.; Na, I.; Geisler, A.; Sadhwani, D.; Zhang, Y.; Su, Y.; Wang, X.; Liu, Z.; Xia, J.; Cheng, H.; Webb, R. C.; Bonifas, A. P.; Won, P.; Jeong, J.-W.; Jang, K.-I. Multifunctional Skin-Like Electronics for Quantitative, Clinical Monitoring of Cutaneous Wound Healing. *Adv. Healthcare Mater.* **2014**, *3*, 1597−1607.

71. Gao, W.; Emaminejad, S.; Nyein, H. Y. Y.; Challa, S.; Chen, K.; Peck, A.; Fahad, H. M.; Ota, H.; Shiraki, H.; Kiriya, D.; Lien, D.-H.; Brooks, G. A.; Davis, R. W.; Javey, A. Fully Integrated Wearable Sensor Arrays for Multiplexed in Situ Perspiration Analysis. *Nature* **2016**, *529*, 509−514.

72. Webb, R. C.; Bonifas, A. P.; Behnaz, A.; Zhang, Y.; Yu, K. J.; Cheng, H.; Shi, M.; Bian, Z.; Liu, Z.; Kim, Y.-S.; Yeo, W.-H.; Park, J. S.; Song, J.; Li, Y.; Huang, Y.; Gorbach, A. M.; Rogers, J. A. Ultrathin Conformal Devices for Precise and Continuous Thermal Characterization of Human Skin. *Nat. Mater.* **2013**, *12*, 938−944.

73. Schwartz, G.; Tee, B. C.-K.; Mei, J.; Appleton, A. L.; Kim, D. H.; Wang, H.; Bao, Z. Flexible Polymer Transistors with High Pressure Sensitivity for Application in Electronic Skin and Health Monitoring. *Nat. Commun.* **2013**, *4*, 1859.

74. Yeo, W. H.; Kim, Y. S.; Lee, J.; Ameen, A.; Shi, L.; Li, M.; Wang, S.; Ma, R.; Jin, S. H.; Kang, Z.; Huang, Y.; Rogers, J. A. Multifunctional Epidermal Electronics Printed Directly onto the Skin. *Adv. Mater.* **2013**, *25*, 2773−2778.

75. Norton, J. J.; Lee, D. S.; Lee, J. W.; Lee, W.; Kwon, O.; Won, P.; Jung, S.-Y.; Cheng, H.; Jeong, J.-W.; Akce, A.; Umunna, S.; Na, I.; Knwon, Y. H.; Wang, X.-Q.; Liu, Z.; Paik, U.; Huang, Y.; Bretl, T.; Yeo, W.-H.; Rogers, J. A. Soft, Curved Electrode Systems Capable of Integration on the Auricle as a Persistent Brain−Computer Interface. *Proc. Natl. Acad. Sci. U. S. A.* **2015**, *112*, 3920−3925.

Chapter 2

2D MOF Modulated Nanofiber Based Piezoelectric Nanogenerator

2.1 Introduction

In the past few years, flexible and wearable electronics including solar cell, nanogenerator, field effect transistor (FET), and electronic skin (e-skin) have been extensively investigated due to their potential application in human-machine interface, internet of things (IoT), robot automation and biomedical field [1-8]. Of particular interest, nanogenerators and e-skins have attracted widespread attention around the world because of their ability of mimicking comprehensive properties of human skin and detecting different mechanical stimuli such as pressure, strain and flexion in self-power mode [9-15]. Additionally, miniaturization, portability and easy integration with apparels for scavenging mechanical energy from human body motion established the human and machine integration that may have potential utility in healthcare sector such as rehabilitation assistance after orthopaedic surgery, voice recognition and circulatory system monitoring the overall health status [11]. Moreover, wearable pressure sensors must satisfy the following necessary pre-requisites, such as high sensitivity, wide pressure sensing range and quick response/recovery time. In this regard, various materials such as conductive polymers, carbon nanotube, graphene, zinc oxide nanowires and electrostrictive materials have been widely explored to fabricate flexible pressure/strain sensors [13, 16-20]. The working mechanisms of the sensors are classified as piezoresistive, piezocapacitive, piezoelectric and triboelectric mechanisms [10, 21-25]. Among them, piezoelectric and triboelectric nanogenerators become an active research field for harvesting different body motions with the advantages of self-powered, high sensitivity, broad material aspect, light weight, easy fabrication, and most importantly external bias is not required which is prerequisite in the case of piezo-resistive and capacitive sensors. A recent hybridization trend has been noticed where piezoelectric and triboelectric generators are coupled in order to enhance the overall output performances of the resulting devices [26, 27]. However, some triboelectric nanogenerators (TENGs) are facing some disadvantages due to

the complex stereo structure and lower working stability that restrict its use in harvesting mechanical energy from body movements [28]. In addition, textile based TENGs offer limited possibility to increase the sensing capabilities of the sensing material in a limited contact area [28, 29]. Additionally, detection and utilization of acoustic wave gathered significant attention in the past few years as human are continuously exposed to noise pollution in our modern society and harvesting acoustic energy by utilizing noise can be suitable power source for low power consuming electronic devices [30-32]. Besides this, detection of acoustic signals, such as speech from human with high degree of accuracy, is also proposed to have enormous potential to diagnoses the primary health status [11].

Thus, a universal energy harvester is highly desirable with simple device structure and excellent flexibility so that it can be easily attached on musculoskeletal system as well as simultaneously achieving superior acoustoelectric conversion efficiency. On this aspect, polymer based piezoelectric materials have good application prospect owing to their inherent superiority in terms of flexibility, easy fabrication route and skin mountable device structure [33-35]. However, piezoelectric polymers typically possess lower piezoelectric performance compared to piezoceramics because of having lower piezoelectric co-efficients. Although polymer piezoelectrics are extensively used in acoustoelectric conversion due to their wider frequency response range, flexibility, impedance matching abilities with biological tissues, sensitivity and tuneable device structure [31, 36]. Recently, electrospinning technique to produce continuous nanoscale one dimensional (1D) fibers has attracted considerable attention due to the multiplication and diversified exertion of stress by the nanofibers assembly, which leads to an increased piezoelectric potential. In this process, primarily polymer solution jets are ejected and stretched to form high aspect ratio nanofibers, collected in the form of a non-woven network under a high electric field [33, 34].

In this regard, PVDF and its co-polymers demonstrated various fiber based applications in several branches of flexible electronics including acoustoelectric conversion technology [33]. Previous studies reveal that numerous inorganic micro, nano-sized materials have been adapted in PVDF matrix to increase the overall piezoelectric performance and sensing property [33-35, 37]. Among the novel materials developed for piezoelectric nanogenerator mimicking to speech recognition, PVDF is working to its infancy [11]. PVDF-composite nanocellulose, polyamides, polyurethans, ferroelectric ceramic powder have shown great potential for energy harvesting applications [38, 39]. However, molecular level impregnation using coordination complexes, co-ordination polymers (CPs) or Metal-Organic Polymers are not well developed. Recently we have developed a MOF impregnated self-polarized ferroelectret as highly mechano-sensitive skin sensor [35]. In this context, MOF can be an effective class of material. Typically, MOF is a conjugation of metal centre and organic moieties. Till date, various applications such as gas storage and sensing, catalysis, optoelectronics, chemo-sensor and thermo-sensor for organic pollutants have been conducted by MOF and MOF-polymer composite [40-45]. Although there is rare example regarding the direct use of MOF in wearable and flexible electronics such as motion sensing, acoustoelectric conversion and acoustic vibration sensing.

In this concern, we propose a simple, cost-effective manufacturing strategy of a 2D MOF comprising CdI_2 and 1,5-diaminonaphthalene (NAP) organic linker using mixed solvent layering method. The synthesized MOF was further integrated into PVDF through electrospun nanofiber fabrication which was further utilized to build composite fiber based PNG (C-PNG). The device performance was evaluated by repetitive pressing, bending, twisting and under the acoustic vibration in lower frequency range (20-330 Hz). Moreover, its flexibility, high pressure sensitivity of 7.4 V/kPa, broad pressure sensing range, excellent cyclic stability, durability and fast response/recovery time of 5 ms trigger to respond to a

wide range of human motions when conveniently attached on body joints and soft surfaces. Therefore, the promising detection and feasibility of C-PNG make it suitable for detecting physiological signs of health. In addition, high precision of C-PNG towards detecting different acoustic vibration (various pressure and frequency range) with high sensitivity of 0.95 V/Pa, superior acoustic-to-electric conversion efficiency, capability of capacitor charging and blue LED enlightening independently by scavenging acoustic energy expand its application in portable electronics and low frequency noise detection.

2.2 Experimental Section

2.2.1 Synthesis of CdI_2-NAP, $[CdI_2(NAP)]_n$
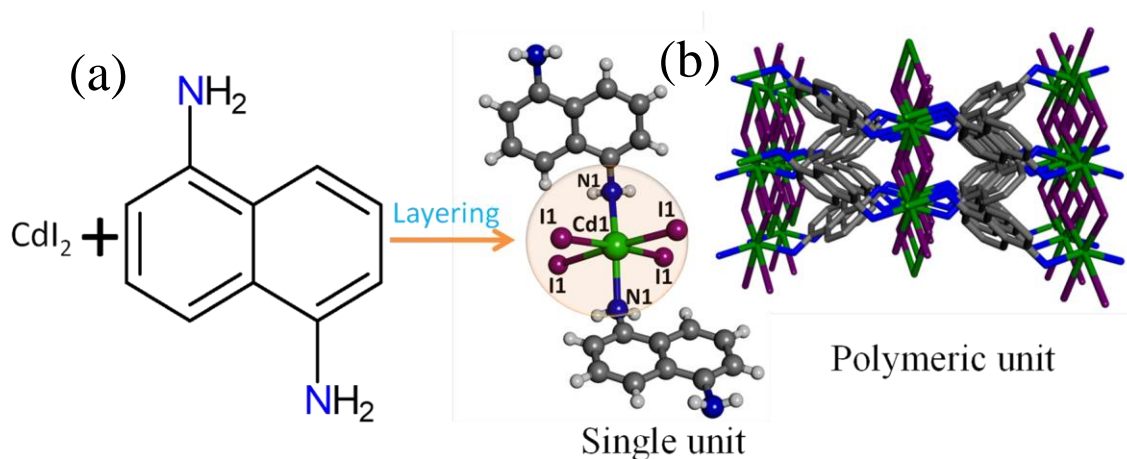
Figure 2.1 (a) Schematic illustration of the synthetic route of CdI_2-NAP 2D MOF with its single unit structure. (b) Schematic diagram of the as-synthesized MOF displaying the connectivity of the structure.

A methanolic solution (1 ml) of 1,5-Diaminonaphthalene (NAP) (0.1 mmol) was carefully layered by the help of water-methanol mixed solvent over the aqueous solution of (1 ml) of CdI_2 (0.1 mmol). It was then allowed to diffuse for a week. The violet coloured needle-shaped crystals were deposited on the glass wall. The crystals were separated mechanically under a microscope and washed with methanol and water (1:1) mixture, and dried. The scheme of the synthesis of $[CdI_2(NAP)]_n$ along with the polymeric structure is provided in

Figure 2.1(a,b). The yield of $[CdI_2(NAP)]_n$ was 87 % and estimated elemental analysis of C, H and N is found to be 18, 4 and 4% respectively.

2.2.2 Preparation of Nanofibers

The CdI_2-NAP MOF incorporated PVDF nanofiber (composite fiber) (as shown in Figure 2.2(b)) and neat PVDF fiber (NPV fiber) was prepared using electrospinning technique (depicted in Figure 2.2(a)) following the previous method [34]. Firstly, a spinning solution of pure PVDF was prepared by dissolving PVDF pellets in a mixed solvent of 6:4 volume ratio of N,N-dimethylformamide (DMF)/acetone at a polymer/solvent concentration of 12 % w/v under continuous stirring at 60 ˚C for 3 h until a clear homogeneous solution was obtained. Afterwards, as-synthesized MOF (1 wt% (w/v)) was added into the pure PVDF solution and kept for gentle stirring at 60 ˚C prior to complete dissolution. Finally, it was sonicated for some time before electrospinning. Additionally, pure PVDF solution was also taken for electrospinning as a reference. The electrospinnig process was conducted by filling the resulting solution in a 10 mL hypertonic syringe (Dispovan) tipped with a stainless steel needle (22G). The positive electric field/bias voltage between tip to Al foil wrapped grounded collector plate (at a distance of 12 cm) was maintained at 10 kV with a constant flow rate of 0.6 mL/h. Moreover, a relative humidity of 40-50 % was adjusted throughout the experiment. Same parameters were maintained during the electrospinning of pure PVDF solution for executing controlled experiments. In addition, collected NPV and composite fibers were further dried at 60 ˚C for 4 h to remove all the residual solvents to obtain stable nanofibers for characterization and device fabrication. The inset of Figure 2.2(b) presents its inherent flexibility.

2.2.3 Fabrication of PNGs

The nanofiber mat was cut into required dimension (5 cm × 2 cm) and highly flexible composite fiber made PNG (C-PNG) was fabricated (seen in Figure 2.2(c,d)) subsequently by

electroding both side (with an active area of 4 cm × 1.5 cm, using Cu-Ni plated polyester fabric) and encapsulating between two layers of PDMS respectively. In addition, a neat fiber made PNG (N-PNG) was also fabricated by the same method to compare the device performance.
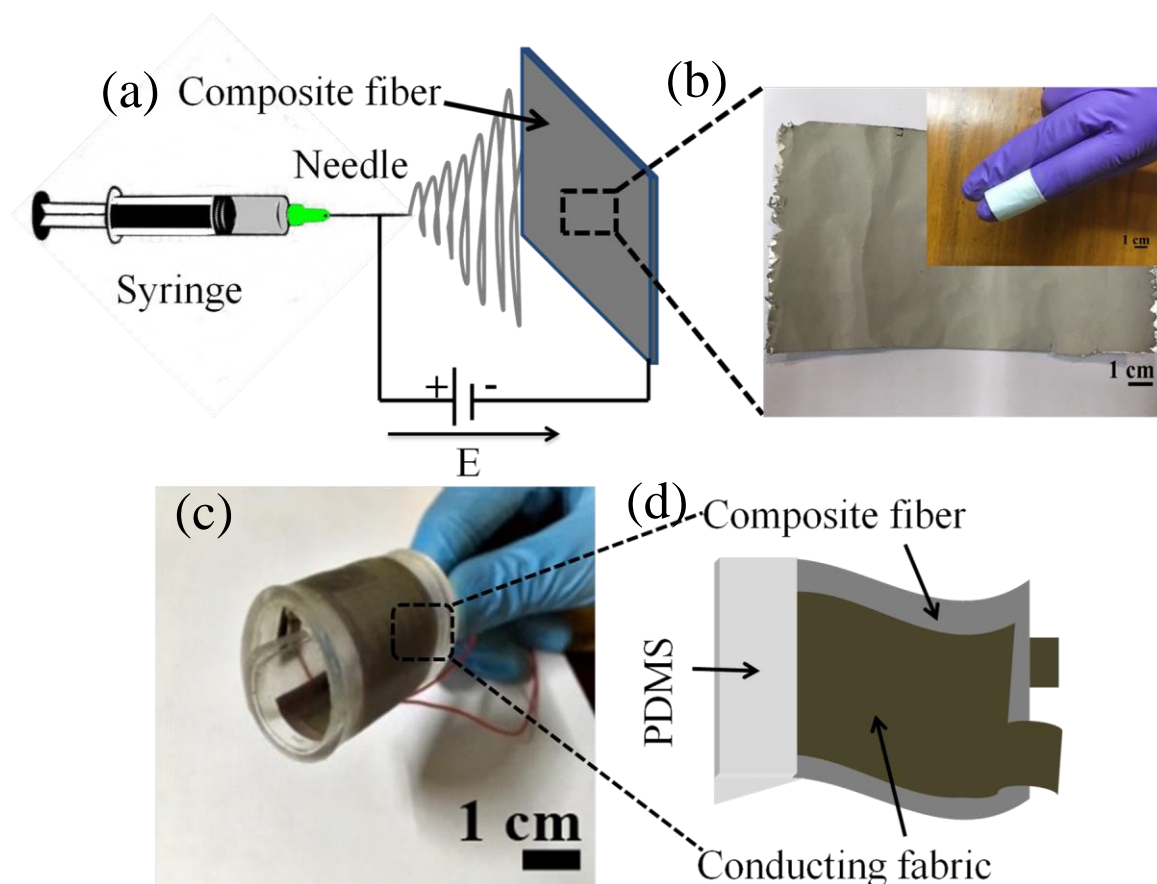
Figure 2.2 (a) Schematic of the electrospinning set up where needle is connected to positive terminal of high voltage supply and plate collector is grounded. (b) Digital photograph of the electrospun nanofiber mat. Another photograph showing the intrinsic flexibility of the composite nanofiber (in the upper inset). (c) Photograph of C-PNG demonstrating rollability and flexibility. (d) Schematic of C-PNG showing its fabrication process.

2.2.4 Characterization

Single crystal X-ray diffraction datas of synthesized MOF were collected using Bruker SMART APEX II diffractometer equipped with graphite-monochromated Mo-Kα radiation

(λ = 0.71073 Å) with the ω scan method and processed with the SAINT+ program. Crystal structures were refined using SHELXTL software package. It is noteworthy to mention that during the analysis, non-hydrogen atoms were refined with anisotropic thermal parameters and hydrogen atoms were placed in their geometrically idealized positions and constrained to ride on their parent atoms. Micro-analytical data (C, H, N) were measured by Perkin-Elmer 2400 CHNCS/O elemental analyser. Bruker D8 Advance X-ray diffractometer (using Cu Kα radiation (λ = 1.548 Å) generated at 40 kV and 40 mA) was used to obtain the crystalline phases and powder X-ray diffraction pattern (P-XRD) of the as-prepared MOF and composite fibers. Vibrational bands and crystalline phases of fibers (in the wavenumber range of 4000-400 cm^{-1} and 16 number of scans is employed) were collected using Fourier Transform Infrared Spectroscopy (FT-IR, TENSOR II, Bruker). Morphological analysis were conducted by FE-SEM (INSPECT F50, FEI) functioning at an acceleration voltage of 20 kV. The elemental mapping was obtained by EDX spectroscopy recorded in a Bruker Nano X-flash detector (410M) equipped with a FE-SEM chamber. TEM images were obtained using JEM 2100, JEOL under acceleration voltage of 200 kV. The piezoelectric output performance of PNGs in terms of open-circuit voltage (V_{oc}) and short-circuit current (I_{sc}) were measured using a digital storage oscilloscope (Tektronix TDS 2024C) and a picoammeter (Keithley 6485) respectively. The vertical impacts were obtained by a 3-axial force pressure sensor (FlexiForce A201).

2.3 Results and Discussion

2.3.1 Structural Analysis of CdI$_2$-NAP, [CdI$_2$(NAP)]$_n$

The crystallographic data, selected bond lengths and angles of the single-crystal are summarized in Table 2.1 and 2.2 respectively. CdI$_2$-NAP crystallized in the monoclinic *C2/c* space group with Z=4 and consists of 2D [CdI$_2$(NAP)]$_n$ neutral networks, as shown in Figure 2.1(b) and Figure 2.3(a). The divalent metal centres have a slightly distorted octahedral

coordination, with four μ_2-I and two bridging NAP at trans positions, yielding a CdI_4N_2 octahedron. The bond length of Cd1-N1 is 2.353(4) Å, which is in the normal range [40]. The bond length of Cd1-I1 is 2.8341(6) Å, which is comparable with those reported. The CdI_4N_2 octahedra interconnect to each other via two μ_2-I atoms,
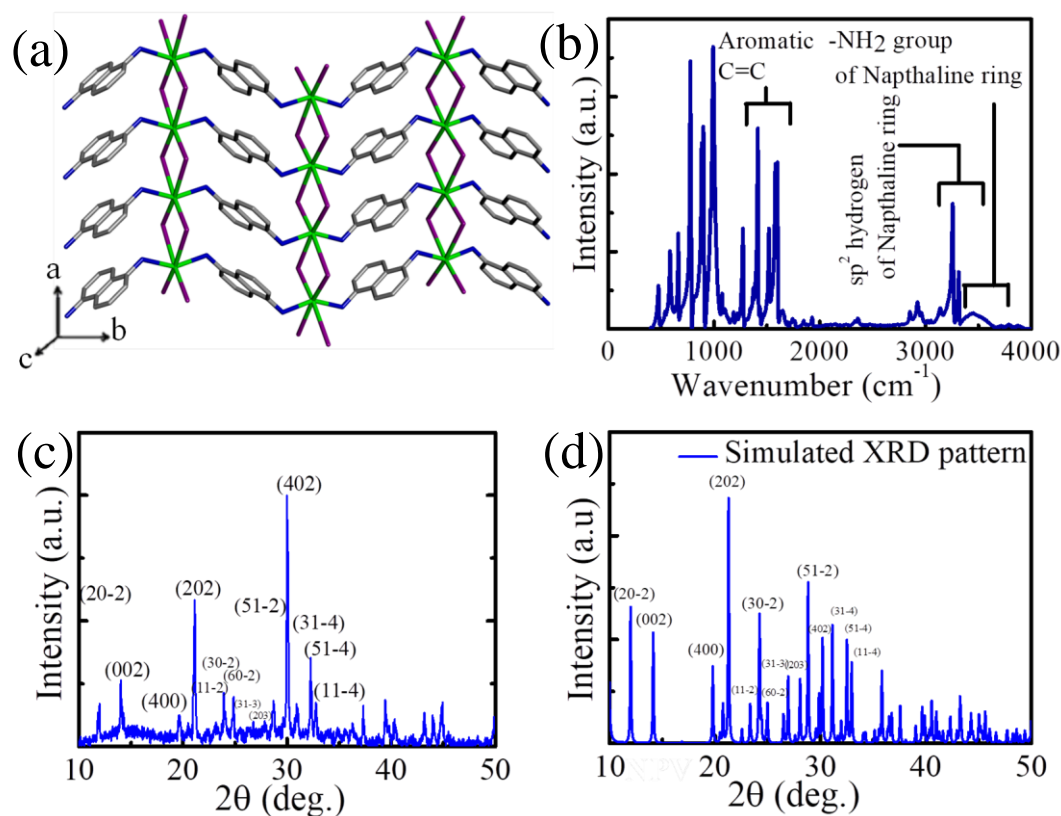
Figure 2.3 (a) 2D layered structure, (b) FT-IR spectra (in the wavenumber range of 4000-400 cm^{-1}) (c) X-ray diffraction pattern and (d) simulated XRD pattern (extracted from single crystal data) of the as-synthesized CdI_2-NAP.

forming a linear inorganic chain running along the *c* direction. These chains are bridged by μ_2-NAP ligands to form an inorganic organic hybrid 2D layer (Figure 2.3(a)) parallel to the *ac* plane. These layers stack in an ABAB mode along the *b* axis to yield a 3D structure. In this case, the $\pi\bullet\bullet\bullet\bullet\bullet\bullet\pi$ stacking interactions in the layer also give rise to perfect facial alignment. In each layer, the neighbouring μ_2-NAP ligands interact through weak $\pi\bullet\bullet\bullet\bullet\bullet\bullet\pi$

contacts (ca. 4.469 Å). Furthermore, FT-IR spectra of the as-synthesized MOF (seen in Figure 2.3(b)) revealed the presence of vibrational bands related to aromatic C=C, sp^2 hydrogen of naphthalene ring and $-NH_2$ group of naphthalene ring. Additionally, powder XRD (Figure 2.3(c)) of the MOF was acquired to verify the bulk purity of the as-synthesized sample, which is analogous to the simulated XRD (Figure 2.3(d)) obtained from single-crystal XRD data.

Table 2.1 Crystal data and refinement parameters of CdI_2-NAP (CCDC-1904947).

empirical formula	$C_{10} H_{10} Cd I_2 N_2$
formula weight (f_w)	524.41
crystal system, space group	Monoclinic, *C 2/c*
unit cell dimensions	a (Å) = 21.4576(12)
	b (Å) = 4.4693(3)
	c (Å) = 14.9836(9)
volume V (Å^3)	1201.00(13)
angles between three edges	α(deg) = 90
	β(deg) = 123.300(3)
	γ(deg) = 90
Z, calculated density (g/cm^3)	4, 2.900
μ (mm^{-1})	6.928
wavelength λ(Å)	0.71073
data[$I > 2\sigma(I)$]/parameters	1055/69
GOF on F^2	1.024
final R indices [$I > 2\sigma(I)$]^{a,b}	R1 = 0.0232
	wR2 = 0.0605

$^a R1 = \Sigma||F_o| - |F_c||/ \Sigma|F_o|$, $^b wR2 = [\Sigma w(F_o^2 - F_c^2)^2/\Sigma w(F_o^2)^2]^{1/2}$

Table 2.2 Selected bond lengths and bond angles in CdI_2-NAP (CCDC-1904947).

I(1) - Cd(1)	2.8341(6)	Cd(1) - I(1) - Cd(1)b	92.89(2)
I(1) - Cd(1)b	3.3160(6)	I(1) - Cd(1) - N(1)	98.50(10)
Cd(1) - N(1)	2.353(4)	I(1) - Cd(1) - I(1)a	92.89(1)
Cd(1) - N(1)d	2.353(4)	I(1) - Cd(1) - I(1)c	171.48(2)
N(1) - C(2)	1.438(6)	I(1) - Cd(1) - I(1)d	95.63(2)
C(1) - C(2)	1.415(7)	I(1) - Cd(1) - N(1)d	101.69(11)
C(1) - C(1)f	1.434(6)	N(1) - Cd(1) - I(1)a	76.98(11)
C(1) - C(5)f	1.418(6)	N(1) - Cd(1) - I(1)c	79.72(10)
C(2) - C(3)	1.365(7)	N(1) - Cd(1) - I(1)d	101.69(11)
C(3) - C(4)	1.409(7)	N(1) - Cd(1) - N(1)d	149.76(14)
C(4) - C(5)	1.359(8)	I(1)a - Cd(1) - I(1)c	78.59(2)
I(1)c - Cd(1) - N(1)d	76.98(11)	I(1)a - Cd(1) - I(1)d	171.48(2)
I(1)d - Cd(1) - N(1)d	98.50(10)	I(1)a - Cd(1) - N(1)d	79.72(10)
Cd(1) - N(1) - C(2)	122.3(3)	I(1)c - Cd(1) - I(1)d	92.89(1)
Cd(1) - N(1) - H(1A)	107	Cd(1) - N(1) - H(1B)	107

a = x,-1+y,z   b = x,1+y,z   c = 1-x,-1+y,3/2-z   d = 1-x,y,3/2-z   f = 1/2- x,3/2-y,1-z

2.3.2 Morphology of Nanofibers

Figure 2.4(a) reveals bead-free, arbitrarily oriented network structured morphology of the MOF assisted composite nanofibers with a thickness of 60 μm (illustrated in Figure 2.4(b)). Because of assimilation of the CdI_2-NAP MOF, surface of the composite nanofibers is comparatively rough in comparison to that of NPV electrospun fibers (Figure 2.4(c)). The prepared fibers are designed with a steady morphology without any bead defect due to uninterrupted Taylor cone formation. It is noteworthy to mention that the incorporation of CdI_2-NAP MOF significantly reduces the fiber diameter. For instances, the average fiber diameter of resulting composite and NPV nanofibers exhibiting ∼90 nm and ∼180 nm respectively as presented in Figure 2.4(a) and Figure 2.4(c) along with corresponding histogram profiles in the upper inset of each respective figure. The reduction in fiber diameter

upon assimilation of MOF particle is the result of increased charge density of the composite electrospinning solution. As an outcome, relatively stronger Coulombic force is exerted on the spinning jet of composite (PVDF/CdI$_2$-NAP) solution rather than NPV solution under the same applied positive electric field strength [34, 37]. This phenomenon further may accelerate the overall crystallinity, mechanical strength and piezoelectric performance.
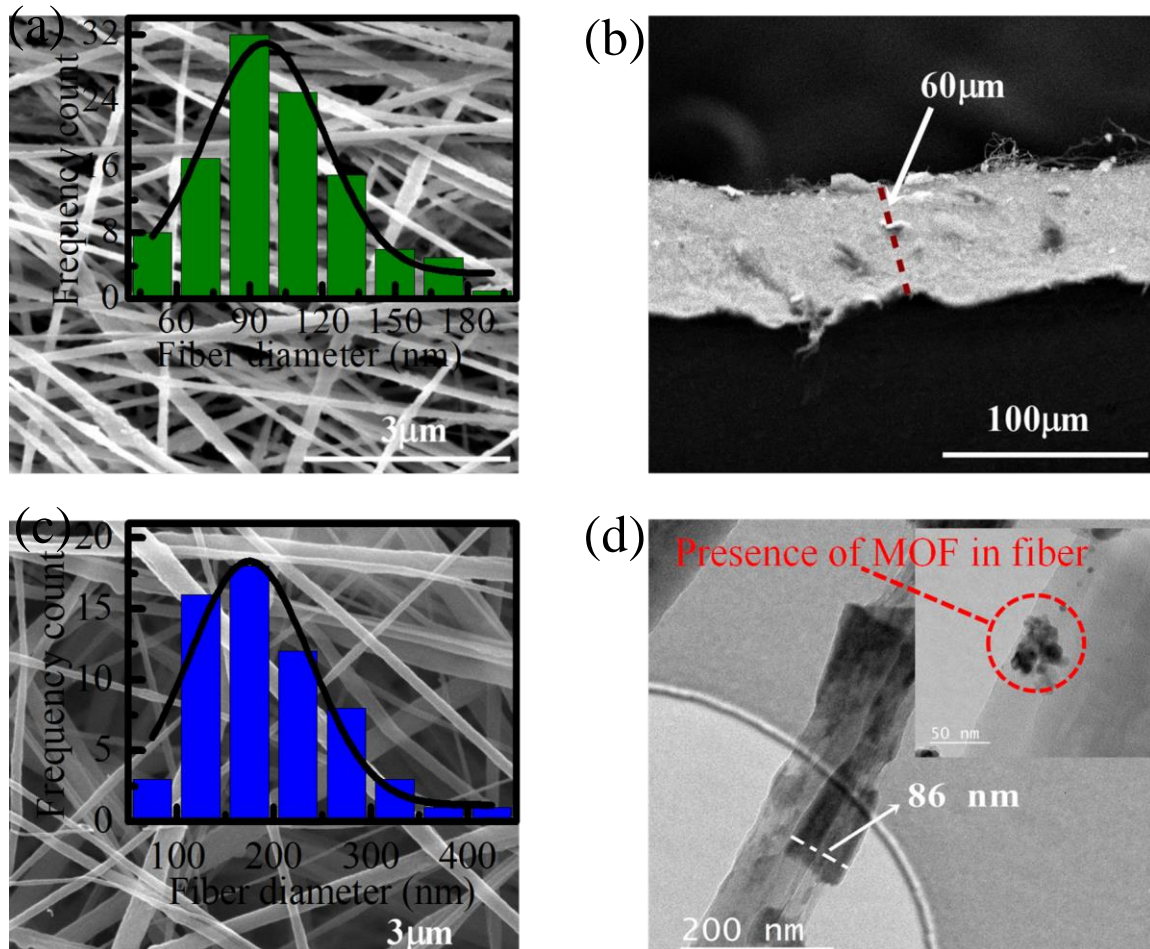
Figure 2.4 (a) FE-SEM image of the electrospun composite nanofiber along with the histogram profile of fiber diameter distribution in the upper inset. (b) Cross-sectional FE-SEM image of composite nanofiber exhibits the fiber thickness. (d) FE-SEM image of NPV fiber along with its fiber diameter distribution in the upper inset. (d) TEM image of composite nanofiber with an enlarged view revealing the encapsulation of MOF in PVDF fiber.

The MOF particles are well dispersed in the electrospinning solution and encapsulated within the PVDF nanofibers, which was examined by TEM analysis (marked in Figure 2.4(d) and its upper inset). The dipole moment of $-CF_2-$ dipoles are comparatively higher than that of $-CH_2-$ dipoles. There might be dipole-dipole interaction between PVDF dipoles and $CO^{\delta-}$, $^{\delta+}N(CH_3)_2$ of DMF solvent, which is solely responsible for dissolution of PVDF in DMF solvent to prepare an agglomeration free homogeneous solution. Additionally, it should be mentioned that the homogeneous dissolution of MOF is attributed to the presence of π-electronic cloud of naphthalene ring and presence of adequate amine functional groups in the MOF structure which construct a great interaction with PVDF-DMF solution. Notably, the MOF particles recrystallize to be confined in nano-dimension during electrospinning as PVDF might act as a capping agent which forced CdI_2-NAP to be restricted in a nano-dimension within the macromolecular chain of PVDF. The presence of MOF particle and its distribution throughout the fiber skeleton were investigated by elemental mapping images as shown in Figure 2.5(a-e) (different colours for different elements). In addition, the presence of carbon, fluorine, cadmium, iodine, and nitrogen in each fiber are further confirmed by electron dispersive X-ray spectroscopy (EDX) (Figure 2.5(f)), which indicates the presence of nitrogen functional groups (associated with the MOF) in the fiber matrix. It can also be concluded that residual solvents like acetone and DMF solvents evaporated completely from the as-prepared nanofibers mat as evident from the absence of oxygen element in EDX spectra (oxygen is the part of acetone and DMF solvent). Furthermore, a fixed relative humidity of 40-50% was maintained throughout the experiment as higher humidity leads to high content of $\beta-$phase [46]. The selected area electron diffraction (SAED) pattern confirms the presence of $\beta-$ and $\gamma-$phases corresponding to the planes of (110), (200) and (202), which are indicated above the blurry rings present in the Figure 2.5(g). Additionally, the embedded

CdI$_2$-NAP MOF enhances the electroactive phase content in the composite nanofibers, which is further elaborated through FT-IR and XRD spectrum.
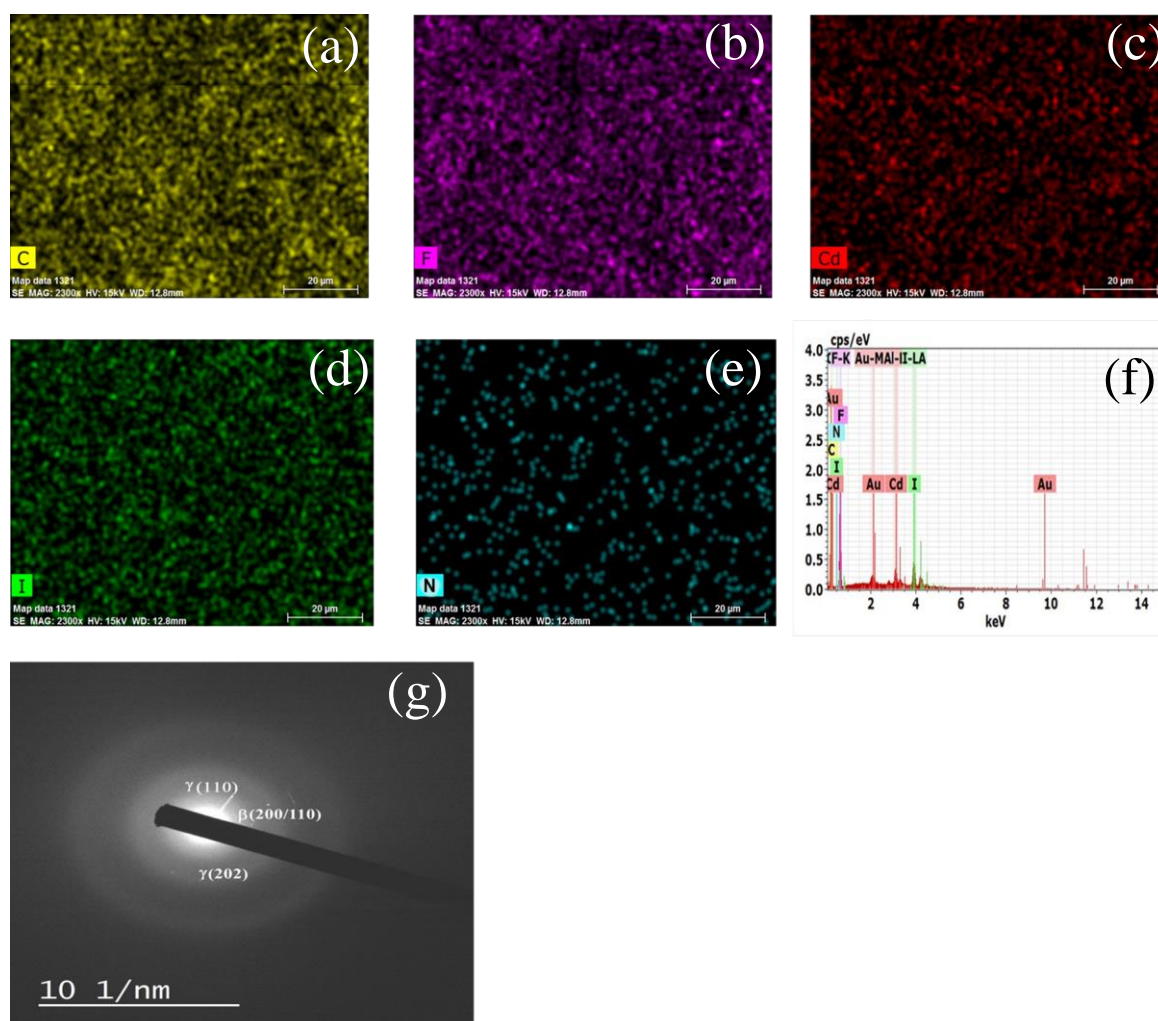
Figure 2.5 (a) Elemental mapping image of (a-e) carbon (C), fluorine (F), cadmium (Cd), iodine (I), nitrogen (N) in the composite fiber. (f) EDX spectra and (g) SAED pattern of composite fiber.

2.3.3 Crystallographic Phase Identification and Quantification

The predominance of polar β– and γ–phase in the as-spun composite nanofibers can be clearly observed from FT-IR spectra (Figure 2.6(a)). In contrast, NPV nanofibers consist of a combination of non-polar (α–phase) and polar phases (β– and γ–phase) with the characteristic vibrational bands at the wavenumbers (υ) of 613, 764, 796, and 975 cm^{-1} for α–
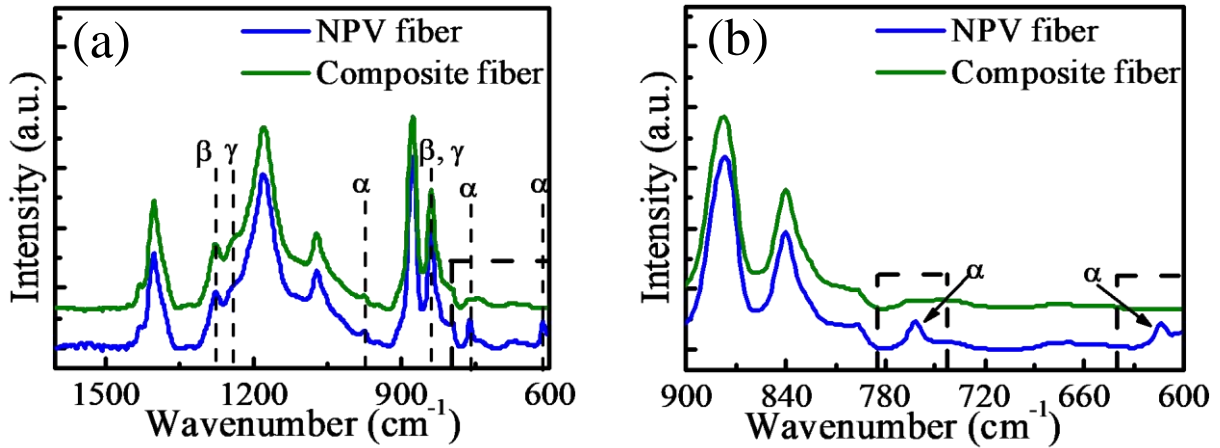
Figure 2.6 FT-IR spectra of NPV and composite fibers in the wavenumber region of (a) 1600-600 cm^{-1} (b) 900-600 cm^{-1}.

phase, $\upsilon = 1275$ and 1233 cm^{-1} are for polar β-phase (TTTT) and the semipolar γ-phase (TTTG), respectively [33-35]. It is interesting to note that 1 wt % MOF addition can completely supress the formation or growth of non-polar α- phases (marked in Figure 2.6(a) and illustrated in Figure 2.6(b)), and the intensities of electroactive β- and γ-phases are amplified compared to NPV fibers, which are further corroborated by XRD pattern of NPV and composite fibers. The curve deconvoluted XRD pattern of NPV fiber in Figure 2.7 clearly indicates the presence of characteristic peak of α crystalline phase at 2θ= 18.2˚ indicative of (202) reflection plane, whereas it was totally absent in composite fiber. In addition, the characteristic dual nature diffraction peak of β (110/200 reflection) and γ (110 reflection) phase at 20.8˚ was significantly intensified in composite fiber over the NPV fiber [37]. To provide quantitative analysis of the α, β, and γ–phases, the absorbance intensities are normalized to the 1072 cm^{-1} peak as it has linear dependency on fiber thickness regardless of crystalline polymorph. Total electroactive phase content (F_{EA}) considerably increased in composite fiber and reached upto ~97% due to the sufficient increase of band intensity at 841 cm^{-1}. The intensity of the band has been used (as shown in curve deconvoluted Figure 2.8) to

55
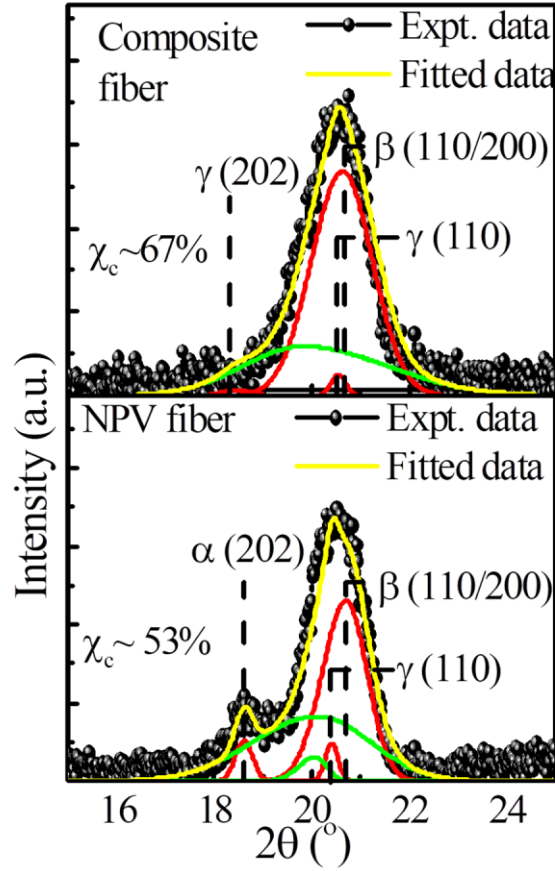
Figure 2.7 Deconvoluted XRD pattern of NPV and composite nanofibers in 2θ range of 15˚-25˚.

quantify the relative proportion of β and γ–phases because both appeared as identical vibrational band due to their alike chain orientation of TTT conformation [35]. The F_{EA} along with relative proportion of β and γ phase (i.e.; $F(\beta)$ and $F(\gamma)$) can be evaluated using the following equations.

$$F_{EA} = \frac{A_{841}}{\left(\frac{K_{841}}{K_{764}}\right)A_{764} + A_{EA}} \times 100\%$$

$$F(\beta) = F_{EA} \times \left(\frac{A_\beta}{A_\beta + A_\gamma}\right)$$

$$F(\gamma) = F_{EA} \times \left(\frac{A_\gamma}{A_\beta + A_\gamma}\right)$$
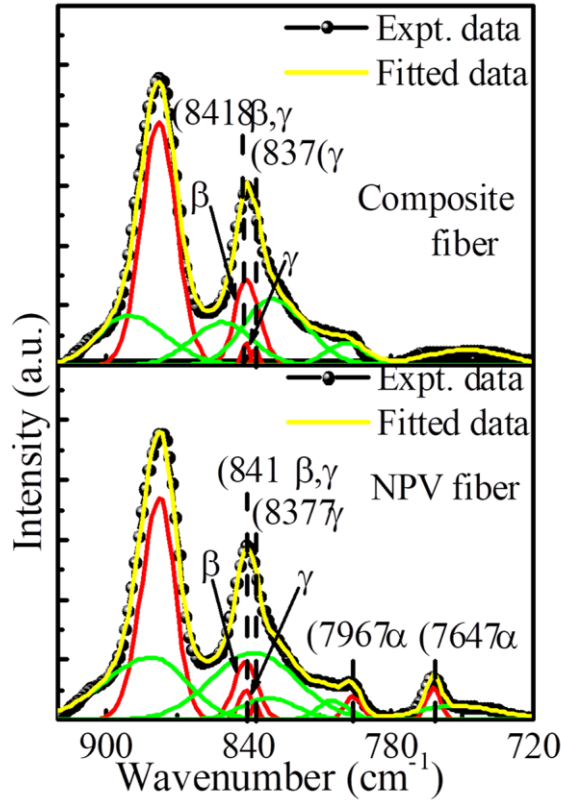
Figure 2.8 Deconvoluted FT-IR spectra of NPV and composite fibers in the range of 920-720 cm^{-1}.

where, A_{841} and A_{764} imply the absorbance intensities at 841 cm^{-1} and 764 cm^{-1}, respectively. K_{841} (7.7×10^4 cm^2 mol^{-1}) and K_{764} (6.1×10^4 cm^2 mol^{-1}) are the absorption coefficients concerning respective wavenumbers. A_β and A_γ indicate the intensities regarding the β and γ phases under the deconvoluted curves of the 841 cm^{-1} main peak. It can be clearly observed from Figure 2.9(a), β–phase growth is more significant relative to γ–phase. Eventually, the total degree of crystallinity (χ_C) is also increased due to MOF incorporation. Total degree of crystallinity (χ_C) of each sample is calculated using the following equation.

$$\chi_C = \frac{\sum A_{cr}}{\sum A_{cr} + \sum A_{amr}}$$

Where, ΣA_{cr} and ΣA_{amr} denote the collective whole integral areas related to the crystalline peaks and the amorphous halo, respectively. Decrease in fiber diameter might play a crucial role in enhanced degree of crystallinity of the composite fiber in association with MOF addition [47].
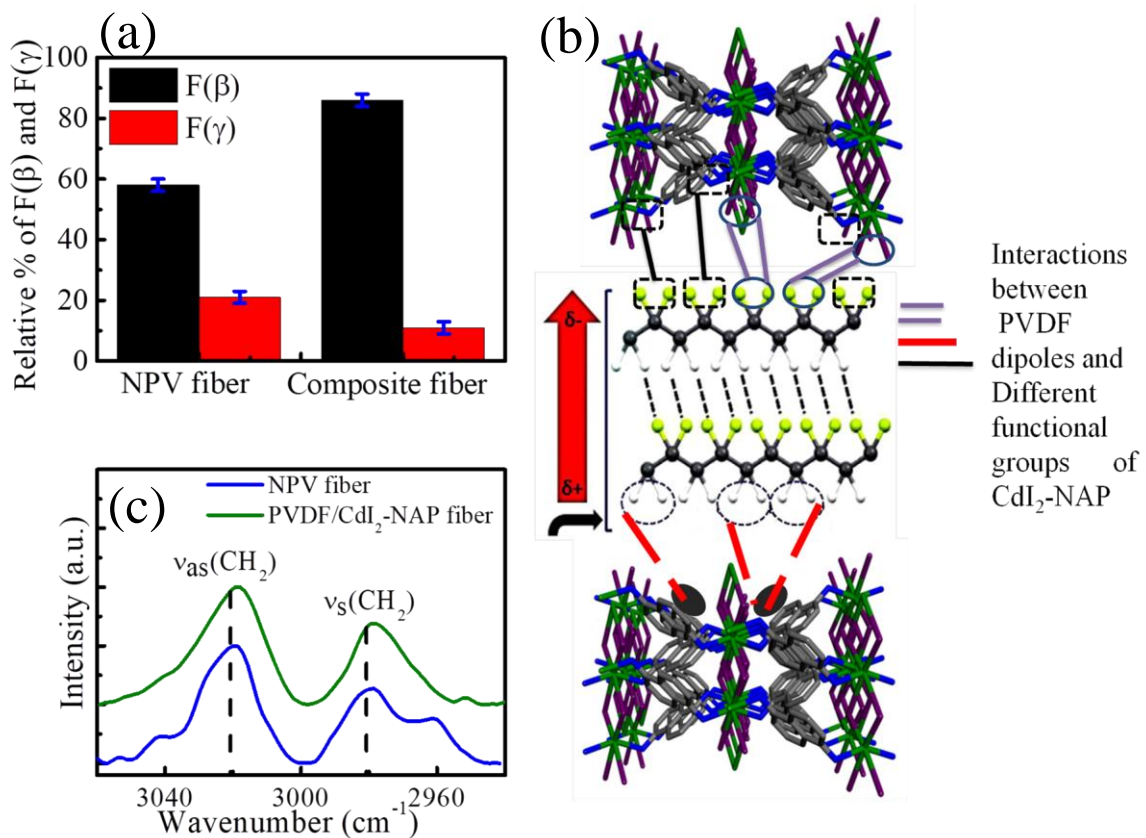
Figure 2.9 (a) Relative proportion of β and γ–phase, (b) schematic demonstration of MOF and PVDF interaction. (c) FT-IR spectra in the range of 3060-2940 cm^{-1} for composite and NPV fiber.

2.3.4 Mechanism of Phase Conversion:

In view of these observations, few questions are raised:

1. What is the role of added 2D MOF?

2. Why does electroactive phase content (β and γ phase) increase?

During electrospinning process, the viscous polymer solution is uniaxially stretched under the applied electric field, which induces the phase conversion from non-polar to polar. When a high DC voltage is applied on a typical electrospinning set up, Taylor cone is formed from the charged droplet due to electrostatic repulsion between surface charges and coulombic force exerted by the external field. At a critical applied voltage, repulsion between surface charges surpass the coulombic force of electric field and the jet is issued from the charged droplet and forced to be elongated several times of its original length. As a result, more elongated all-trans conformation (β–phase) are obtained.

Although more electroactive phases were obtained due to the extensional force (simultaneous stretching and poling) exerted during electrospinning technique, considerable amount of α–phase was present in NPV fibers as shown in Figure 2.6(a,b). So, it is clear that only electrospinning could not eliminate the α–phase totally. But it was entirely eradicated in composite fibers as well as β–phase enhancement was also observed for composite nanofibers. Therefore, the added MOF played a pivotal role in composite fiber, which can be explained in the following way:

> The PVDF might be absorbed on the 2D layer of MOF. In addition, presence of different functional groups on MOF skeleton induce a number of interactions with –CH_2–/–CF_2– dipoles of PVDF, such as intermolecular H-bonding between –NH_2 groups of MOF and CF_2 dipoles of PVDF (N–H···F–C), Halogen-Halogen interaction (Cd–I···F–C) and C–H···π interaction between π cloud of aromatic rings of MOF and Hs of CH_2 dipoles of PVDF. In this way, the MOF acted as a nucleating agent and facilitated in reduction of α–phase and leads to more stretched out all-trans orientation of PVDF chain. A schematic is provided in Figure 2.9(b) to explain the possible interactions between MOF and PVDF dipoles.

➢ In addition, the growth of electroactive phase upon addition of very small amount of MOF particle can be explained by expanded Flory mixing theory developed by Mackay et al [48]. According to this theory, owing to the addition of MOF, PVDF nanofiber swells which leads to increase in radius of gyration of the composite nanofiber. As a consequence, it promotes the extension of the chain leading to all-trans (TTTT) β–phase or γ–phase.

➢ Moreover, the probable interaction between MOF and PVDF can be supported by the frequency shift of CH_2 symmetric and CH_2 asymmetric vibrational modes for composite fiber in the lower frequency region in comparison with NPV fiber. Essentially, the interfacial interaction between the MOF and $–CH_2/–CF_2$ dipoles leads to damping of oscillations of the $–CH_2$ dipoles, which co-ordinates the shifting of vibrational band (seen in Figure 2.9(c)).

In particular, the cooperative effect of electrospinning and specific interfacial interactions between different functional groups of MOF and PVDF dipoles promoted the enhanced piezoelectric properties in composite fiber.

2.3.5 Investigation of Mechanical Property

According to the below mentioned piezoelectric strain-charge equation, it is evident that piezoelectric charge separations and thus piezoelectric output performance are significantly influenced by Young's modulus [47].

$$D_i = d_{ij}\sigma_j = d_{ij}Y_{kj}\varepsilon_k$$

where D_i, d_{ij}, σ_j, Y_{kj} and ε_k particularly represent electric charge separation, piezoelectric co-efficient, applied stress, Young's modulus and applied strain respectively. Therefore, Young's modulus (Y_{kj}) of material contributes equally accompanied by piezoelectric co-efficient (d_{ij}) to enhance the overall output performance. As shown in stress-strain curve Figure 2.10, composite fiber exhibits higher elongation/sretch-ability (48 %) compared to

NPV fiber (40 %). Moreover, Young's modulus increased from 7 MPa (for NPV fiber) to 30 MPa (for composite fiber). The improvement of mechanical properties of composite fiber might be attributed to the stress concentration due to MOF incorporation into PVDF matrix leading to an enhanced degree of crystallinity. Interestingly, reduction in fiber diameter might also improve the degree of crystallinity. As a result, the mobility of polymer chains get restricted with increased crystalline part. Therefore, it is difficult to elongate and hence providing improved mechanical strength. Thus, MOF incorporation preferentially prepared the composite fiber for real time application.
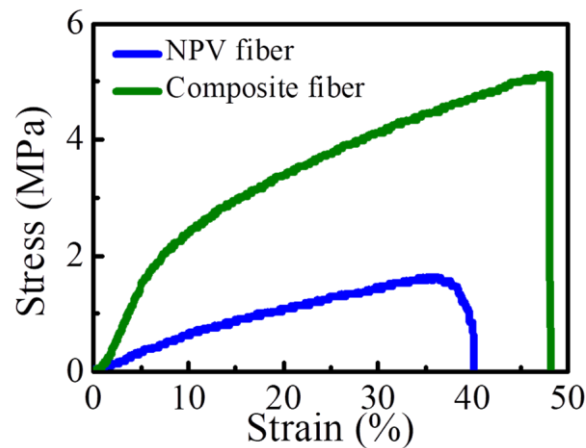
Figure 2.10 Stress-strain curve of NPV and composite nanofibers.

2.3.6 Mechanical Energy Harvesting Performance

In order to investigate the energy harvesting ability of the fiber based PNGs, they were subjected to vertical compressive pressure impacted by a hand-punch covered in a polyethylene glove at an average frequency of $f \sim 2$ Hz. As a result, C-PNG harvested an open-circuit voltage (V_{oc}) of 22 V under the periodical stress amplitude (σ_a) of 22 kPa exhibiting very quick response/recovery time (t_r) of 5 ms (as shown in Figure 2.11(a) and Figure 2.11(b)). It points that C-PNG does not require additional time to regain its original state. On the other hand, N-PNG can generate only 3 V under the same circumstance (Figure 2.11(c)). It clearly indicates that assimilation of MOF into fiber matrix highly
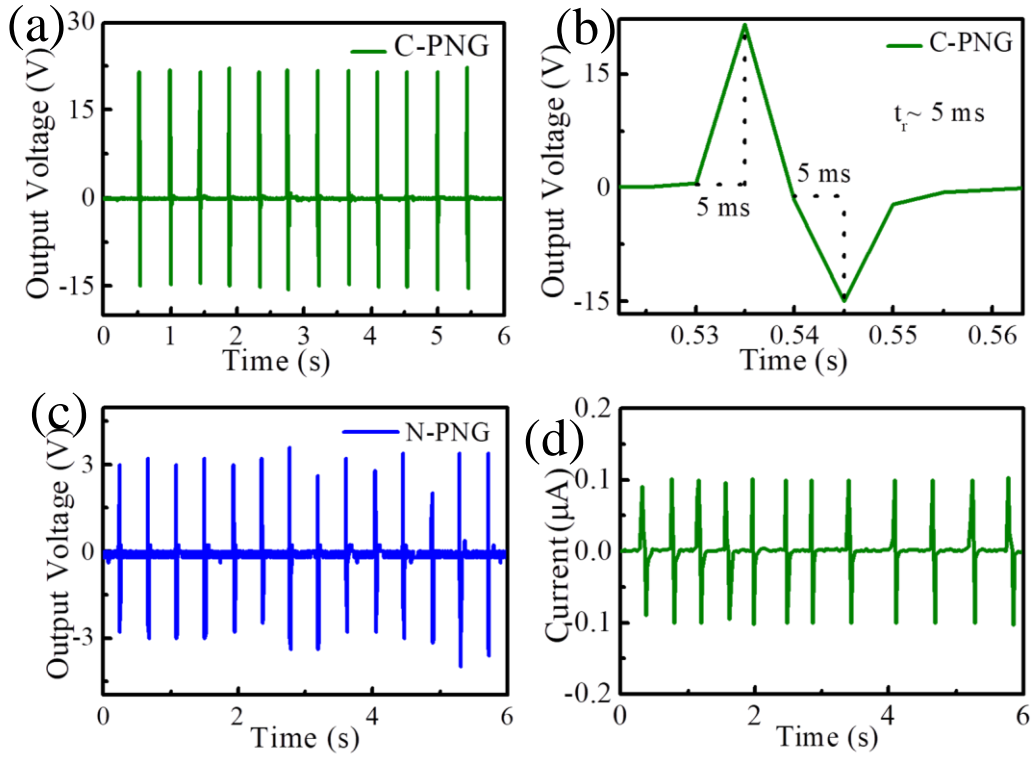
Figure 2.11 (a) Open-circuit output voltage of C-PNG under compressive pressure of 22 kPa. (b) Enlarged view of one single peak of open-circuit voltage generated from C-PNG. (c) Open-circuit output voltage (V_{oc}) from N-PNG during repetitive hand imparting (under compressive stress of 22 kPa). (d) Short-circuit current (I_{sc}) of C-PNG under same pressure amplitude.

stimulates the piezoelectric performance of the composite fiber. During this repetitive compress-release, the axial strain (ε) induced in the C-PNG is 7.3×10^{-4} with corresponding strain rate ($\dot{\varepsilon}$) of 0.584 % S^{-1} [following the work, 33]. Additionally, a short-circuit current (I_{sc}) of 0.1 μA was recorded for C-PNG under identical stress amplitude by human hand as shown in Figure 2.11(d). Thus, the charge (Q) generated during the same applied pressure` was calculated by integrating one current pulse applying the following equation, $Q = \int I_{sc}\, dt$. So, the estimated charge is 1390 pC. Furthermore, a quasi-static method (via direct piezoelectric effect) was applied to determine the piezoelectric co-efficient (d$_{33}$) of the

composite fiber. The magnitude of d$_{33}$ can be calculated from $/d_{33}/=/\frac{Q}{F}/= 41 \, pC/N$. Furthermore, the empirically derived d$_{33}$ value (/d$_{33}$/= 39 pC/N) of composite fibers from log-log relationship of fiber diameter dependent d$_{33}$ is in close agreement with the calculated one. Piezoelectric charge co-efficient (d$_{33}$) varies with fiber diameter by following the equation [47]:

$$log/d_{33}/= 1.96 + 0.19 log\frac{1}{d}$$

Where, d is the fiber diameter. C-PNG shows higher mechanical energy harvesting ability owing to the superior piezoelectric charge co-efficient of composite fibers over NPV fibers [33]. As a result, it leads to improved piezoelectric figure of merit ($FoM_P \approx d_{33}.g_{33} \approx 16 \times 10^{-12}Pa^{-1}$, and g$_{33}$ is piezoelectric voltage conversion co-efficient, represented by $g_{33} = \frac{d_{33}}{\varepsilon_r\varepsilon_0}$, where, ε_0 = permittivity of the free space, ε_r = dielectric constant which is 12 for composite fiber). The corresponding switching polarity test was further conducted by changing the electrode connections to verify whether the piezoelectric voltage is producing from C-PNG or not. Figure 2.12(a) shows that voltage of equivalent amplitude with opposite polarity was generated in reverse connection. It proves that the observed phenomenon is due to the polarization reversal of –CH$_2$–/–CF$_2$– dipoles and originated output voltage truly belongs to the piezoelectric properties of composite fiber. There is no underlined contribution of contact electrification or instrumental artefacts in the performance. Additionally, it can be noticed from Figure 2.12(b) that an instantaneous output power density ($P = \frac{1}{A} \times \frac{V_L^2}{R_L}$) of 24 µW/cm^2 was reached at a load resistance of 1 MΩ, when instantaneous voltage drop (V_L) was measured by connecting C-PNG across increasing load resistances (R_L) ranging from 100 KΩ to 40 MΩ. Interestingly, the observed output power density of C-PNG is superior/comparable to previously reported PVDF nanofiber based devices [33, 49].
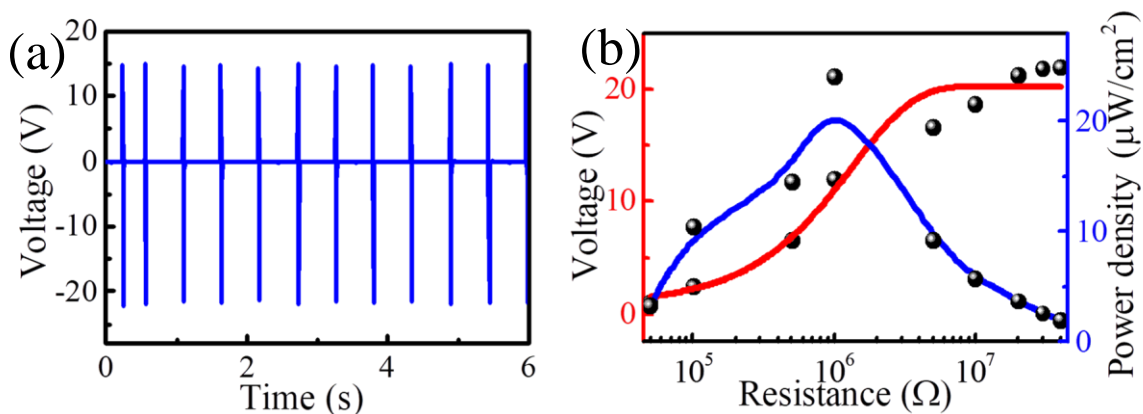
Figure 2.12 (a) Open-circuit output voltage of C-PNG with reverse electrode polarity. (b) Output voltage and corresponding instantaneous output power density across variable load resistance.

2.3.7 Mechanism of Improved Piezoelectric Performance

According to the crystal data and refinement parameters of the as-synthesized MOF, it can be concluded that the MOF belongs to monoclinic crystal system of centrosymmetric *C2/c* space group. Thus, MOF has no direct piezoelectric contribution in composite fiber. Moreover, the incorporated MOF enhanced the overall piezoelectric performance of composite fiber resulting higher piezoelectric co-efficient (d_{33}). Actually, different interactions between different polar surface of MOF moiety and $-CH_2/-CF_2$ dipoles of PVDF nanofibers provide superior electroactive phase content mostly β−phase through surface charge induced polarization. In addition to it, applied mechanical force builds a potential which in turn aligns the PVDF dipoles via stress induced polarization. Therefore, interaction of several polar groups of MOF additive with PVDF dipoles in association with other phenomena such as electrospinning process (simultaneous stretching and poling), surface charge and stress induced polarization and self-orientation of PVDF dipoles played a key role to induce improved piezoelectric crystalline β−phase compared to NPV fiber. In addition, MOF incorporation subsequently reduced the fiber diameter and thus enhanced the mechanical

property (Young's modulus). As a result, when vertical compressive force was applied on the C-PNG, it reflected better output performance with respect to N-PNG.

Actually, under the application of external mechanical impact, the overall crystal structure of the composite nanofibers was deformed resulting in a potential difference between the top and bottom electrodes due to stress induced piezoelectric bound charges. As an impact, the free external charges were forced to drive to the nanogenerator to neutralize the built-in-potential giving rise to an electrical signal. Then, when the imparted stress was removed, the potential difference diminished and the free charges accumulated on the two electrodes flow back through the external circuit leading to an electrical signal opposite to the previous one. It is noteworthy to mention that output positive voltage peak produced from the C-PNG (due to the direct application of stress) was much greater than its negative part, however as such no discrepancy was reflected in case of positive and negative current peaks. This scenario can be explained in terms of damping effect [50]. Actually, it is due to the fact that the distorted state does not return to its original state with the same rate as it gets compressed. Consequently, some charges will be stored on the surface of electrodes. That's why negative voltage peak is smaller compared to positive voltage peak during repetitive press release motion. Meanwhile, piezoelectric output current solely depends on piezoelectric potential strength not relying upon the damping effect considerably. Therefore, no observable difference was noted for positive and negative current peaks.

2.3.8 Mechanical Durability and Sensitivity Test

Eventually, mechanical durability test was carried out for a wide range of time (~ 2 hr, 37500 cycles) in order to understand the stability of output performance and robustness of the device using a stepping motor (impact frequency of 5 Hz, under the pressure of 0.3 MPa, shown in Figure 2.13(a)). The collected data indicates stable output pattern without any significant
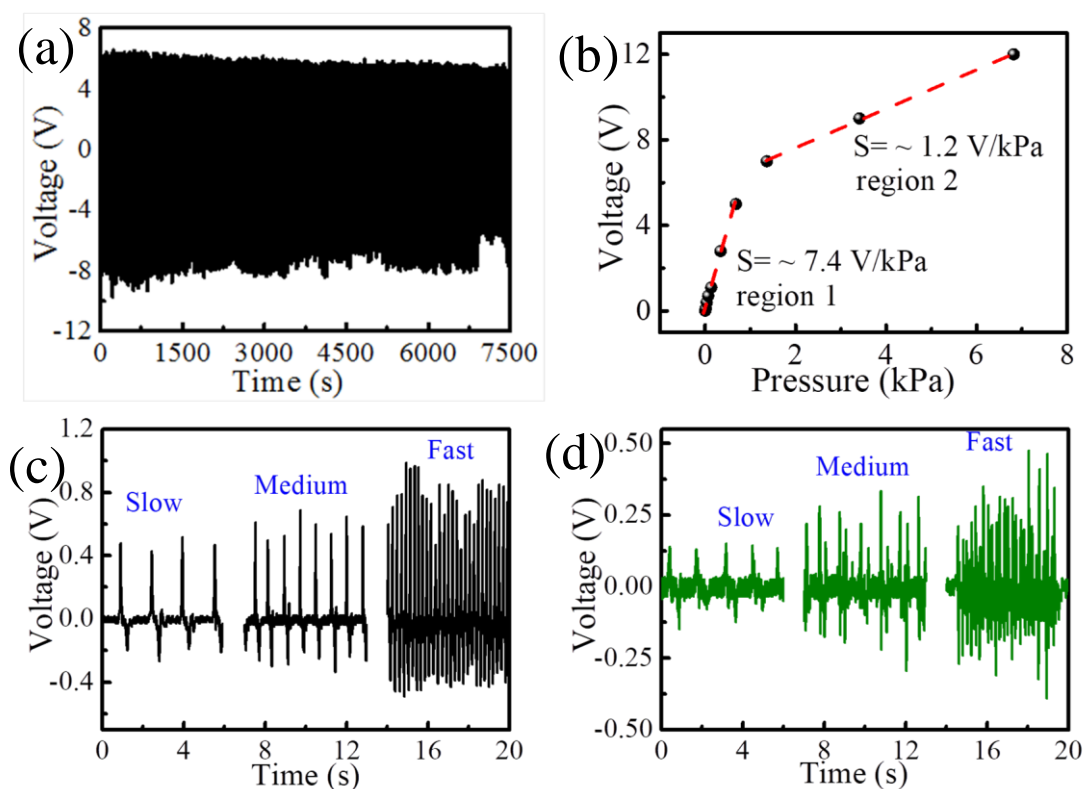
Figure 2.13 (a) Fatigue test of output voltage response at 5 Hz frequency over 37500 cycles under the vertical pressure of 0.3 MPa. (b) Output voltage of C-PNG as a function of applied compressive pressure in a wide pressure range during different weight fall from a fixed height (from an analytical weight box). Output voltage response of C-PNG during (c) bending and (d) twisting deformation by changing the rate from slow to fast.

degradation. Therefore, the cyclic fatigue test strongly confirmed the device durability under harsh environment.

Additionally, the mechano-sensitivity (S) of the C-PNG in a wide pressure range (subtle to moderate pressure change) has been evaluated by dropping different weights from an analytical weight box following our previous work [35]. As shown in Figure 2.13(b), the pressure-voltage response curve is composed of two distinct regions. The C-PNG exhibited very high sensitivity of ~7.4 V/kPa in the low pressure region (< 1 kPa, region 1), whereas relatively lower sensitivity of ~ 1.2 V/kPa was observed in high pressure region (> 1 kPa,

region 2). This is probably because of the theoretical limits of effective strain in piezomaterials at high pressure region [51, 52]. Actually, the voltage increases instantaneously upon subjected to very small pressure change as the nanofibers get deformed easily in the first case. As a result, a large deformation is obtained for a large number of nanofibers, which leads to rapid increase in output voltage. Moreover, for region 2 (> 1 kPa), higher pressure is required for further deformation, results in decreasing sensitivity. It is noteworthy to mention that C-PNG can sense very small input of pressure change as low as ~ 1 Pa, indicating its low pressure detection limit. Therefore, wide range of pressure sensing, high mechsno-sensitivity, fast response time, broad stress-strain of the composite fiber collectively make the C-PNG suitable for most of the human motion detection.

2.3.9 Bending-Unbending and Twisting Responses

The piezoelectric output voltage responses from C-PNG due to repeated bending-releasing and twisting by human fingers are presented in Figure 2.13(c and d). In other words, it proves the high flexibility of C-PNG, which in turn makes it suitable for different human motion sensing. It can be noticed from Figure 2.13(c) that slow to fast bending rate at constant given strain increased the output voltage gradually and maximum of ~1 V was obtained. The tensile strain originated in the thickness direction (ε_y, parallel to dipole orientation) during bending the device into an arc shape can be calculated as $\varepsilon_y = \frac{L}{2r} = 0.88\,\%$, where r= bending radius= 16 mm and L= thickness= 280 μm. Likewise, the strain developed in the length direction is ε_x~ 0.39 %, obtained using the relation of Poisson's ratio, $\nu = \left|\frac{\varepsilon_x}{\varepsilon_y}\right|$ [47]. However, bending leads to lower output voltage compared to vertical compressive stress because bending strain is antiparallel with the $-CH_2-/- CF_2-$ dipole orientations. The tensile strain produced in the length direction during squeezing results in lower change in dipole moment due to the preferential orientation of the dipoles along the thickness direction (perpendicular

to the fiber length). Thus, lower amount of piezoelectric charge generation occurred on the electrodes compared to axial stress, exhibiting lower output voltage. In addition, twisting of C-PNG (from slow to fast rate) shows a maximum voltage generation of 0.5 V (illustrated in Figure 2.13(d)) when the rate of twisting was increased from slow to fast. These abilities of C-PNG may be helpful in different human physiological motion sensing.

2.4 Applications

2.4.1 Motion Sensing Application
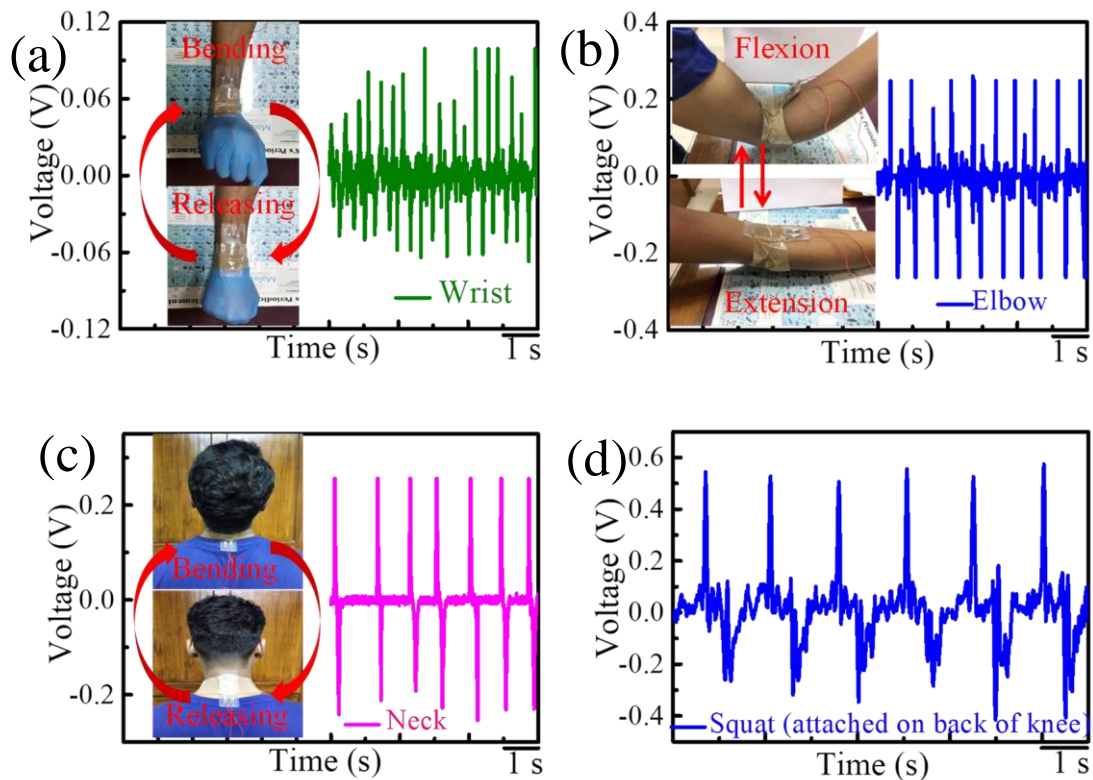
Figure 2.14 Real time voltage response of C-PNG attached on (a) wrist (b) elbow (c) neck induced by bending and releasing (with digital photographs). (d) Voltage response of C-PNG when attached on the back of knee due to extension and flexion movement during squat.

Therefore, considering its high sensitivity towards bending performance and the large deformation of the human body, firstly C-PNG was employed in order to evaluate multiple dynamic biomechanical motions related to different body joints such as wrist, elbow, finger,

neck and knee. The skin of the joints is not only the reason behind the bending effect, but also the joints itself induce pressure during the bending motion. As depicted in Figure 2.14(a, b, c and d) C-PNG was directly attached to the wrist, elbow, neck and back of the knee and corresponding device output was measured. It can easily detect and moreover provided distinguishable piezoelectric signals in each case. When the sensor was placed on the back of the knee joint and squatting movement was carried out, it was subjected to a pressure during the motion related to the extension and flexion of the knee. As the knee joint constantly rolls and glides during movement, consequently the deformation site of the skin is constantly changing, leading to the corresponding piezoelectric waveforms through the device (Figure 2.14(d)).
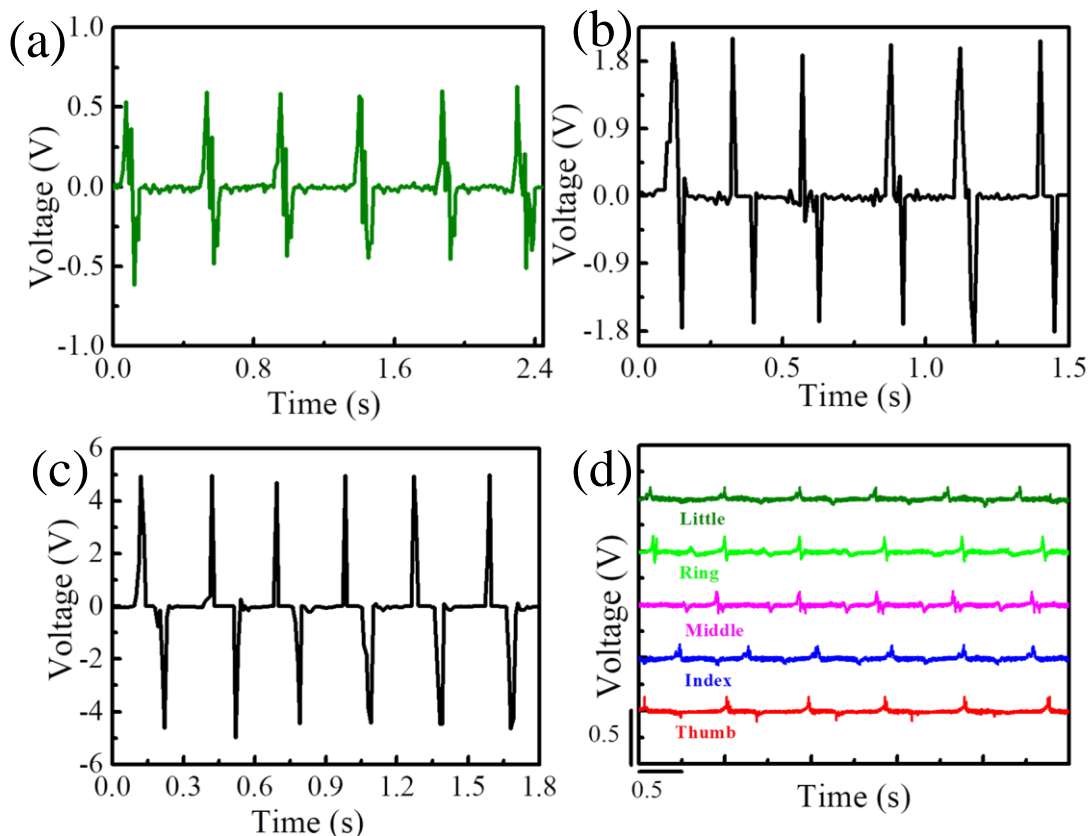
Figure 2.15 Output voltage signal generated from C-PNG attached under insole of shoe during (a) walking, (b) jogging and (c) jumping. (d) Finger motion monitoring when C-PNG attached to different hand fingers.

In addition, C-PNG was attached to a tester's shoe-sole (preferable under the toe) using adhesive tape to monitor the walking, jogging and jumping activities (Figure 2.15(a, b, c)) respectively. Figure 2.15(b and c) illustrate that C-PNG can harvest more kinetic energy compared to jogging and walking due to more impact. However, no substantial loss of performance was noticed even after multiple steps due to the violent deformation of C-PNG during jogging and jumping for prolonged period of time. Thus, it indicates that C-PNG might be appropriate to be implemented in smart shoes for recognizing gait and walking speed for exhibiting high stability during continuous extreme stress. On the basis of its multidimensional sensing ability, C-PNG was mounted on each finger joint with the aid of an adhesive tape to detect bending-stretching movement of fingers and corresponding voltage response was recorded in real time as shown in Figure 2.15(d).Additionally, piezoelectric output voltage signals were also recorded due to pressure impact on C-PNG during toe and heel pressing (as shown in Figure 2.16(a and b)). Finite element method based theoretical analysis supports the fact that heel pressing generates more voltage than that of toe as illustrated in Figure 2.16(c). It can be observed that each finger movement generated well recognizable distinct piezoelectric signal. Thus, five C-PNGs can be assembled on a single glove to prepare a smart data glove for detecting fine finger motions. In addition, C-PNG is also able to detect gentle body motion such as speech recognition. To investigate its capability of identifying speech signal, C-PNG was attached to one tester's throat. When the volunteer was asked to pronounce different words such as "Acoustic", "Motion", "Napthalene", and the sensor produced distinct piezoelectric signals (Figure 2.16(d)) associated with different words enabling its application in speech rehabilitation programme. The sensing property may be attributed to the complex muscle movements during pronunciation of different words. Above results demonstrate that C-PNG has great potential in parallel monitoring of multiple joint motion gesture by integrating multiple devices, which

facilitates its application in wearable medical devices, robotic arm, human-machine interactions and artificial e-skin.
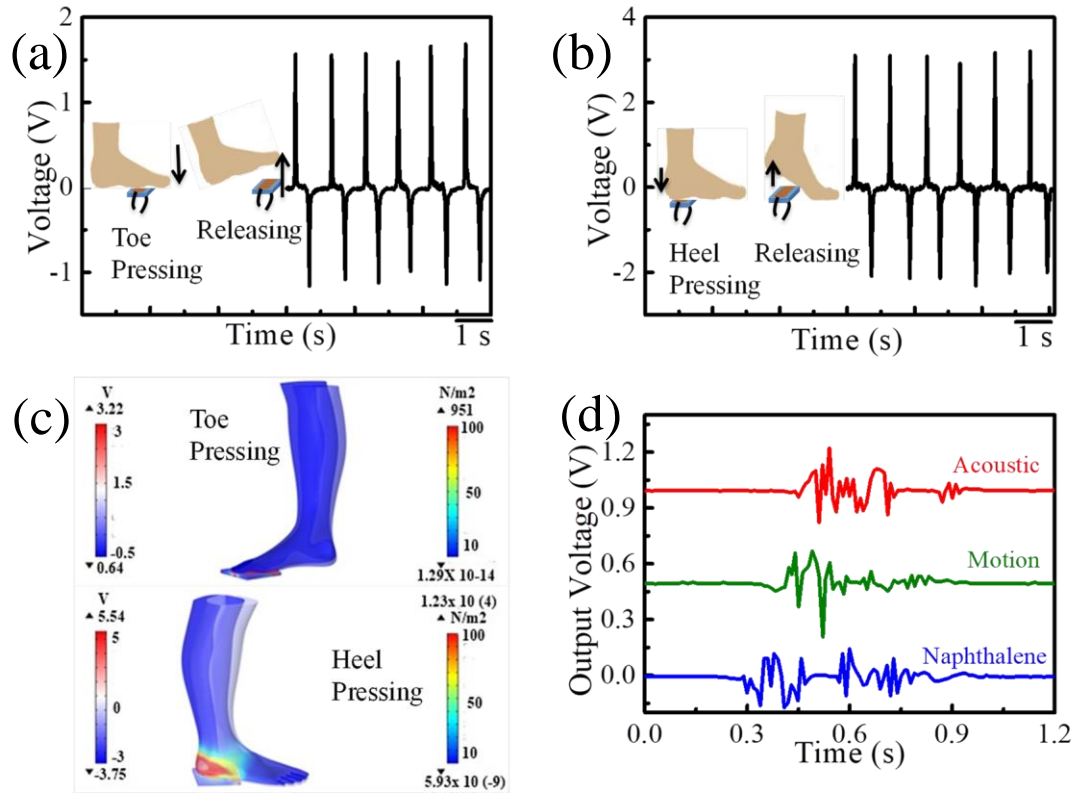
Figure 2.16 Voltage signal of C-PNG during (e) toe and (f) heel pressing in addition with corresponding (g) FEM based simulation. (h) Voltage response curve of C-PNG attached on throat during phonation of "Acoustic", "Motion", "Napthalene".

2.4.2 Acoustoelectric Conversion and Application

To evaluate the acoustoelectric energy conversion performance of the MOF/PVDF composite nanofiber, firstly an acoustic nanogenerator (A-NG) device was fabricated by sandwiching the nanofiber mat in between two indium tin oxide (ITO) coated on polyethylene terephthalate (PET) sheet with an effective device dimension of (4×4) cm^2 and nanofiber mat thickness of 60 μm. The nanofiber mat was pasted on the conducting side of the PET sheet. Additionally, one circular hole (diameter: 1 cm) was cut on each PET films so that nanofibers
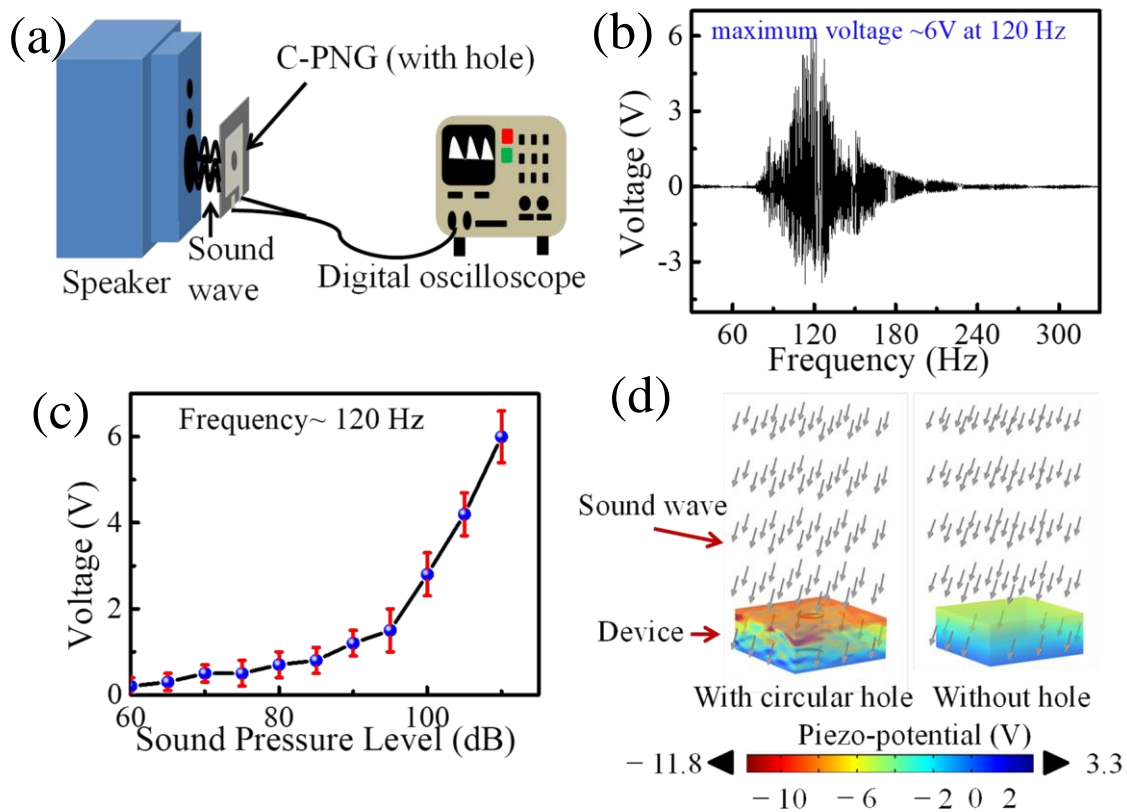
Figure 2.17 (a) Schematic illustration for the acoustoelectric conversion. Voltage output due to the (b) effect of acoustic wave frequency variation fixing the sound pressure level (SPL) at 110 dB (c) effect of SPL at fixed sound wave frequency 120 Hz. (d) FEM based theoretical analysis piezo-potential distribution and SPL dependency due to acoustoelectric conversion.

can directly experience the sound vibration originating from the speaker [30]. Finally, the A-NG was placed in front of a sound speaker (specification: iball tarang multimedia speaker 2.1) to collect the electrical output produced because of acoustoelectric conversion as presented through a schematic in Figure 2.17(a). As an outcome, an open-circuit voltage (V_{oc}) of 6 V was obtained at a sound wave frequency of 120 Hz and 110 dB SPL.

The variation of piezoelectric output induced by different frequency sound waves was extensively studied by changing the frequency from 20-330 Hz and maintaining the sound

pressure level at 110 dB. The 110 dB SPL was chosen because it is very nearer to the threshold of discomfort and considered as the edge of extreme noisy sound wave [30]. It is noteworthy to mention that piezoelectric output voltage increased with increasing frequency sweep and obtained the maximum voltage of 6 V at 120 Hz and then it gradually decreased as shown in Figure 2.17(b). Moreover, SPL dependency of the device was also examined retaining the frequency at 120 Hz (Figure 2.17(c)). A finite element method based theoretical calculation shows that composite fiber based device with circular hole in the central part of electrode generates higher output voltage than the device without any hole (Figure 2.17(d)). This result supports our experimental observation. The calculated piezoelectric output voltage at the SPL of 110 dB and at 120 Hz frequency was matched well with our experimental findings. Here, negative voltage was generated due to negative piezoelectric charge co-efficient of PVDF. Furthermore, considering one particular point at the device, we have observed that the increment of output voltage with the increasing SPL follows the same tendency as observed experimentally (Figure 2.18(a)) which further validated our precise acoustic experiments. It was observed that the output voltage increased slowly in the first place and attained a sharp linear growth from 95 dB and achieved the maximum voltage at 110 dB. Thus, A-NG might be beneficial in monitoring and detection of low frequency noise (20-200 Hz and above 90 dB) arising from road traffic, vehicle horns, public gatherings etc.

Accordingly, the acoustoelectric sensitivity (S) of our self-powered A-NG can be calculated using the following equation [31]:

$$S = \frac{V}{P} = \frac{V}{P_{ref} \cdot 10^{\frac{L_P}{20}}}$$

Where P is the sound pressure, P_{ref} is the reference sound pressure of 2×10^{-5} Pa, L_P is the sound pressure level in decibel and V is the obtained piezoelectric output voltage. The maximum achieved sensitivity of the device is 0.95 V/Pa which is higher than commercial

PVDF film and nanofibers based device [30]. Additionally, it was noticed in Figure 2.17(c), the acoustic sensitivity is higher above the SPL of 95 dB, which makes it a promising candidate for noise detection.
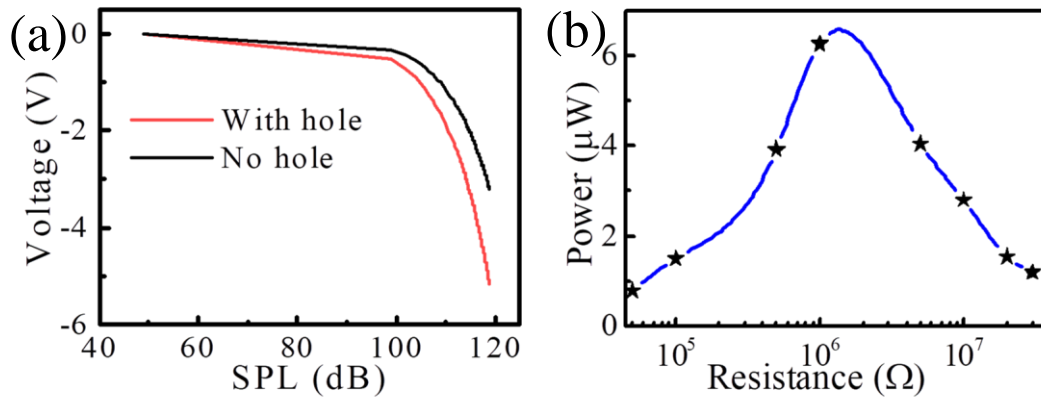
Figure 2.18 (a) FEM based theoretical analysis: SPL dependency of acoustoelectric output voltage. (b) Acoustoelectric output power of C-PNG.

Furthermore, the instantaneous output power of A-NG (Figure 2.18(b)) was quantified by measuring the piezoelectric output voltage as a function of external load resistances (R_L) as presented in Figure 2.19(a). The output voltage gradually increased with increasing load resistances and converged to the open-circuit voltage at an infinitely high resistance of 30 MΩ under acoustic input of 120 Hz and 110dB SPL. In contrast, theoretical output current showed opposite behaviour as the load resistance increased (Figure 2.19(a)). The A-NG generated maximum instantaneous output power of 6.25 μW (Figure 2.18(b)) at an external load resistance of 1 MΩ, which is higher/comparable to other PVDF based acoustic sensors [32, 53-55]. The MOF induced decreased fiber diameter of the bead free composite fiber and higher β–phase content might synergistically enhance the acoustic vibration to electrical energy conversion efficiency and sensitivity of the A-NG. According to linear circuit theory, highest output power is achieved only when the external resistance is equivalent to the

internal resistance due to the impedance matching. Thus, internal resistance of the A-NG is 1 MΩ.

In order to demonstrate the practical application of the device, the A-NG was connected to a 0.5, 1 and 2.2 μF capacitors through a full wave bridge rectifier circuit to provide the charging-discharging process at a very short time, as shown in Figure 2.19(b). The A-NG was able to sufficiently charge up the 2.2 μF capacitor under the acoustic response of 110 dB and 120 Hz frequency and attained the steady state of 4.4 V within a very short range of time (8s). Owing to its fast charging-discharging ability, A-NG might have the potential to power up the tiny portable electronic gadgets. On the basis of capacitor charging, the average power stored inside the capacitor or the overall output power (P_{out}= 2.66 μF) delivered by the A-NG was calculated from the following equation:

$$P_{out} = \frac{1}{2t}CV^2$$

Where, C is the capacitance of the capacitor, V is the saturated voltage and t is the time required to reach the steady state. These features collectively make the A-NG highly efficient for potential applications with overall energy conversion efficiency (η) of 37.6% which is superior to commercial and nanofiber based PVDF acoustic sensors reported in previous article [31]. The energy conversion efficiency factor can be calculated using the following equations:

$$P_{in} = \frac{Ap^2}{\rho C}cos\theta = 7.08\ \mu w$$

$$\eta = \frac{P_{out}}{P_{in}} \times 100\%$$

Where p is sound pressure, A is active/working area of the device, ρ is the mass density of air and θ is angle between the directions of the sound propagation and the normal of the active part. Furthermore, 5 blue LEDs connected in series were directly turned on when the A-NG
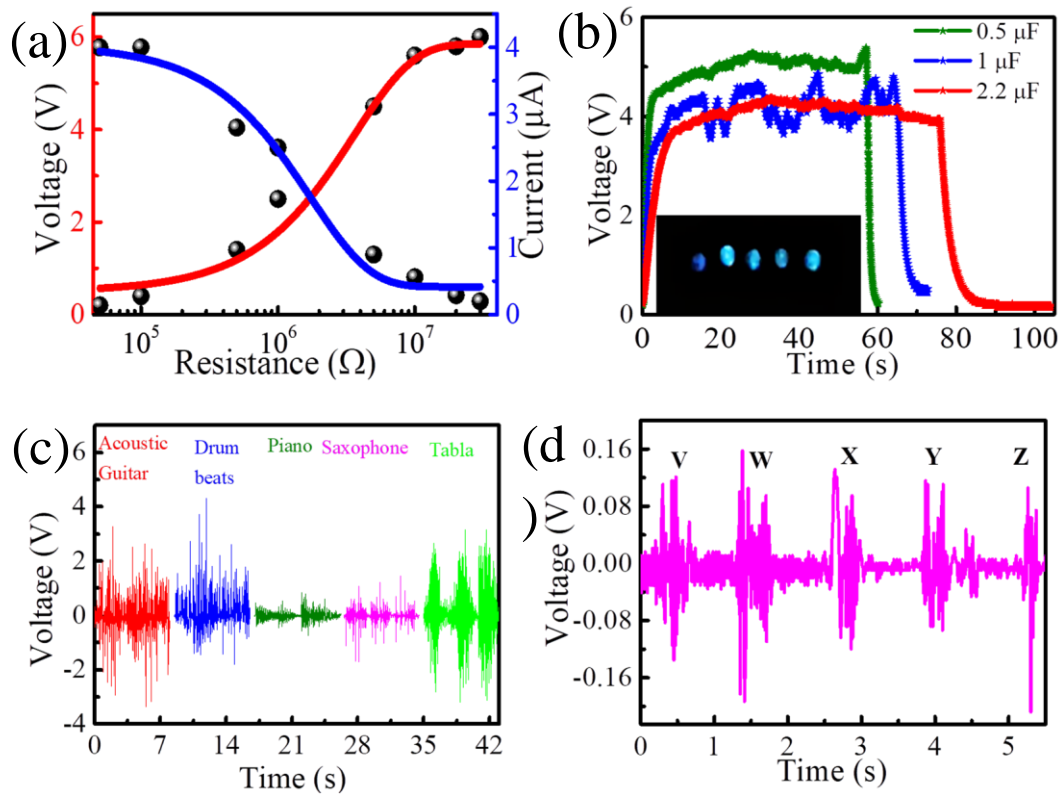
Figure 2.19 (a) Output voltage and current variation with the increasing external load resistance. (b) Capacitor charging performance of C-PNG by harvesting acoustic energy from a sound wave at 120 Hz, 110 dB and Lighting up 5 blue LEDs by same acoustic wave. Output voltage signal from C-PNG (c) conducted by different musical instruments under the SPL of 110 dB and (d) in response to recorded alphabetic characters under 80dB SPL from sound speaker.

was subjected to an instrumental chorus song from a speaker at 110 dB SPL without the help of any external storage system (presented in the lower inset of Figure 2.19(b)). Figure 2.19(c) shows different output voltage patterns associated with different musical instruments originated from the A-NG when placed in similar manner under the same SPL. It is clearly evidenced from Figure 2.19(c) that A-NG is very much sensitive to distinguish different waveforms generated from different musical instruments. Moreover, our device is also useful to produce distinct voltage patterns when exposed to recorded alphabetic characters under

sound pressure level of 80 dB as shown in Figure 2.19(d). Thus, our device might be suitable for possible applications such as voice recognition, speech therapy, low frequency noise detection and acoustic energy harvester for charging small scale electronics.

2.5 Conclusion

In summary, fabrication of a self-powered multifunctional pressure sensor has been proposed, which is able to detect and monitor human motions linked to different physical activity and simultaneously behaves as an efficient acoustoelectric sensor. The active layer of the C-PNG was prepared by a 2D single crystalline MOF doped PVDF nanofiber network. The coupling effect between the MOF and PVDF nanofibers resulted in the significantly high piezoelectric output performance of the C-PNG (open-circuit voltage ~ 22 V and maximum power density ~ 24 μW/cm^2) with enhanced piezoelectric co-efficient (d_{33}) of 41 pC/N. Considering its excellent response towards bending and twisting deformation, the capacity of C-PNG to harvest kinetic energy from different biomechanical motions was further explored. C-PNG produced distinct and distinguishable output patterns associated with a variety of dynamic motions when attached to the joints of human body. Meanwhile, it displayed superior acoustoelectric performance of 6 V under the exposure of 110 dB acoustic vibration. With an acoustoelectric sensitivity of 0.95 V/Pa, C-PNG widens its futuristic application in low frequency noise detection because of demonstrating excellent performance in the working frequency range of 20-330 Hz. Therefore, our approach demonstrates a cost-effective technique to fabricate a self-powered active sensor capable of sensing human motions as well as sensitive to different acoustic vibration enabling its wide range of application from wearable health monitoring to noise detection and reduction.

2.6 References

1. Zhang, N.; Chen, J.; Huang, Y.; Guo, W.; Yang, J.; Du, J.; Fan, X.; Tao, C.: A Wearable All-Solid Photovoltaic Textile. *Adv. Mater.* **2016**, *28*, 263-269.

2. Chai, Z.; Zhang, N.; Sun, P.; Huang, Y.; Zhao, C.; Fan, H. J.; Fan, X.; Mai, W.: Tailorable and Wearable Textile Devices for Solar Energy Harvesting and Simultaneous Storage. *ACS Nano* **2016**, *10*, 9201-9207.

3. Amjadi, M.; Kyung, K.-U.; Park, I.; Sitti, M.: Stretchable, Skin-Mountable, and Wearable Strain Sensors and Their Potential Applications: A Review. *Adv. Funct. Mater.* **2016**, *26*, 1678-1698.

4. Wang, H.; Ma, X.; Hao, Y.: Electronic Devices for Human-Machine Interfaces. *Adv. Mater. Interfaces* **2017**, *4*, 1600709.

5. Kim, M S.; Kim, K.; Kwon, D.; Kim, S.; Gu, J.; Oh, Y S.; Park, I.: Microdome-Induced Strain Localization for Biaxial Strain Decoupling Toward Stretchable and Wearable Human Motion Detection. *Langmuir* **2020**, 3*6*, 8939-8946.

6. Tee, B. C. K.; Tee, B. C. K.; Wang, C.; Allen, R.; Bao, Z.: An Electrically and Mechanically Self-Healing Composite with Pressure- and Flexion-Sensitive Properties for Electronic Skin Applications. *Nat. Nanotechnol.* **2012**, *7*, 825-832.

7. Ai, Y.; Lou, Z.; Chen, S.; Chen, D.; Wang, Z. M.; Jiang, K.; Shen, G.: All rGO-on-PVDF-Nanofibers Based Self-Powered Electronic Skins. *Nano Energy* **2017**, *35*, 121-127.

8. Lou, M.; Abdalla, I.; Zhu, M.; Wei, X.; Yu, J.; Li, Z.; Ding, B.: Highly Wearable, Breathable, and Washable Sensing Textile for Human Motion and Pulse Monitoring. *ACS Appl. Mater. Interfaces* **2020**, *12*, 19965-19973.

9. Bai, Z.; Xu, Y.; Li, J.; Zhu, J.; Gao, C.; Zhang, Y.; Wang, J.; Guo, J.: An Eco-friendly Porous Nanocomposite Fabric-Based Triboelectric Nanogenerator for Efficient Energy Harvesting and Motion Sensing. *ACS Appl. Mater. Interfaces* **2020**, *12*, 42880-42890.

10. Seung, W.; Gupta, M. K.; Lee, K. Y.; Shin, K.-S.; Lee, J.-H.; Kim, T. Y.; Kim, S.; Lin, J.; Kim, J. H.; Kim, S.-W.: Nanopatterned Textile-Based Wearable Triboelectric Nanogenerator. *ACS Nano* **2015**, *9*, 3501-3509.

11. Ghosh, S. K.; Mandal, D.: Envisioned Strategy for an Early Intervention in Virus-Suspected Patients through Non-Invasive Piezo- and Pyro-electric Based Wearable Sensors. *J. Mater. Chem. A* **2021**, *9*, 1887-1909.

12. Deng, Z.; Hu, T.; Lei, Q.; He, J.; Ma, P X.; Guo, B.: Stimuli-Responsive Conductive Nanocomposite Hydrogels with High Stretchability, Self-Healing, Adhesiveness, and 3D Printability for Human Motion Sensing. *ACS Appl. Mater. Interfaces* **2019**, *11*, 6796-6806.

13. Yamada, T.; Hayamizu, Y.; Yamamoto, Y.; Yomogida, Y.; Izadi-Najafabadi, A.; Futaba, D. N.; Hata, K.: A Stretchable Carbon Nanotube Strain Sensor for Human-Motion Detection. *Nat. Nanotechnol.* **2011**, *6*, 296-301.

14. Jiang, L.; Yang, P.; Fan, Y.; Zeng, S.; Wang, Z.; Pan, Z.; He, Y.; Xiong, J.; Zhang, X.; Hu, Y.; Gu, H.; Wang, X.; Wang, J. Ultrahigh Piezoelectric Coefficients of Li-Doped (K,Na)NbO3 Nanorod Arrays with Manipulated O-T Phase Boundary: Towards Energy Harvesting and Self-Powered Human Movement Monitoring. *Nano Energy* **2021**, *86*, 106072.

15. Wan, H.; Cao, Y.; Lo, L. W.; Zhao, J.; Sepúlveda, N.; Wang, C. Flexible Carbon Nanotube Synaptic Transistor for Neurological Electronic Skin Applications. *ACS Nano* **2020**, *14*, 10402–10412.

16. Pan, L.; Chortos, A.; Yu, G.; Wang, Y.; Isaacson, S.; Allen, R.; Shi, Y.; Dauskardt, R.; Bao, Z.: An Ultra-Sensitive Resistive Pressure Sensor Based on Hollow-Sphere Microstructure Induced Elasticity in Conducting Polymer Film. *Nat. Commun.* **2014**, *5*, 3002.

17. Sheng, L.; Liang, Y.; Jiang, L.; Wang, Q.; Wei, T.; Qu, L.; Fan, Z.: Bubble-Decorated Honeycomb-Like Graphene Film as Ultrahigh Sensitivity Pressure Sensors. *Adv. Funct. Mater.* **2015**, *25*, 6545-6551.

18. Xiao, X.; Yuan, L.; Zhong, J.; Ding, T.; Liu, Y.; Cai, Z.; Rong, Y.; Han, H.; Zhou, J.; Wang, Z. L.: High-Strain Sensors Based on ZnO Nanowire/Polystyrene Hybridized Flexible Films. *Adv. Mater.* **2011**, *23*, 5440-5444.

19. Luna, A.; Pruvost, M.; Yuan, J.; Zakri, C.; Neri, W.; Monteux, C.; Poulin, P.; Colin, A. Giant Electrostrictive Response and Piezoresistivity of Emulsion Templated Nanocomposites. *Langmuir* **2017**, *33*, 4528–4536.

20. Cheng, Z. Y.; Bharti, V.; Xu, T. B.; Xu, H.; Mai, T.; Zhang, Q. M. Electrostrictive Poly(Vinylidene Fluoride-Trifluoroethylene) Copolymers. *Sensors and Actuators, A: Physical* **2001**, *90*, 138–147.

21. Chen, X.; Li, X.; Shao, J.; An, N.; Tian, H.; Wang, C.; Han, T.; Wang, L.; Lu, B.: High-Performance Piezoelectric Nanogenerators with Imprinted P(VDF-TrFE)/BaTiO$_3$ Nanocomposite Micropillars for Self-Powered Flexible Sensors. *Small* **2017**, *13*, 1604245.

22. Gong, S.; Lai, D. T. H.; Su, B.; Si, K. J.; Ma, Z.; Yap, L. W.; Guo, P.; Cheng, W.: Highly Stretchy Black Gold E-Skin Nanopatches as Highly Sensitive Wearable Biomedical Sensors. *Adv. Electron. Mater.* **2015**, *1*, 1400063.

23. Takamatsu, S.; Kobayashi, T.; Shibayama, N.; Miyake, K.; Itoh, T.: Fabric Pressure Sensor Array Fabricated with Die-Coating and Weaving Techniques. *Sensor Actuat A-Phys* **2012**, *184*, 57-63.

24. Yang, J.; Chen, J.; Yang, Y.; Zhang, H.; Yang, W.; Bai, P.; Su, Y.; Wang, Z. L. Broadband Vibrational Energy Harvesting Based on a Triboelectric Nanogenerator. *Adv. Energy Mater.* **2014**, *4* (6), 1301322.

25. Wang, Z. L. Triboelectric Nanogenerators as New Energy Technology for Self-Powered Systems and as Active Mechanical and Chemical Sensors. *ACS Nano* **2013**, *26*, 9533–9557.

26. Lapčinskis, L.; Mā Lnieks, K.; Linarts, A.; Blū Ms, J.; Šmits, K. N.; Järvekülg, M.; Knite, M. R.; Šutka, A. Hybrid Tribo-Piezo-Electric Nanogenerator with Unprecedented Performance Based on Ferroelectric Composite Contacting Layers. *ACS Applied Energy Materials* **2019**, *2*, 4027–4032.

27. Wang, W.; Zhang, J.; Zhang, Y.; Chen, F.; Wang, H.; Wu, M.; Li, H.; Zhu, Q.; Zheng, H.; Zhang, R. Remarkably Enhanced Hybrid Piezo/Triboelectric Nanogenerator via Rational Modulation of Piezoelectric and Dielectric Properties for Self-Powered Electronics. *Appl. Phys. Lett.* **2020**, *116*, 023901.

28. Dong, K.; Peng, X.; Wang, Z. L.: Fiber/Fabric-Based Piezoelectric and Triboelectric Nanogenerators for Flexible Stretchable and Wearable Electronics and Artificial Intelligence. *Adv.Mater.* **2020**, *32*, 1902549.

29. Gu, P.; Fan, N.; Wang, Y.; Wang, J.; Müller-Buschbaum, P.; Zhong, Q.: Linear Control of Moisture Permeability and Anti-adhesion of Bacteria in a Broad Temperature Region Realized by Cross-Linking Thermoresponsive Microgels onto Cotton Fabrics. *ACS Appl. Mater. Inter.* **2019**, *11*, 30269-30277.

30. Lang, C.; Fang, J.; Shao, H.; Ding, X.; Lin, T.: High-Sensitivity Acoustic Sensors from Nanofibre Webs. *Nat. Commun.* **2016**, *7*, 11108.

31. Lang, C.; Fang, J.; Shao, H.; Wang, H.; Yan, G.; Ding, X.; Lin, T.: High-Output Acoustoelectric Power Generators from Poly(vinylidenefluoride-co-trifluoroethylene) Electrospun Nano-Nonwovens. *Nano Energy* **2017**, *35*, 146-153.

32. Hwang, Y. J.; Choi, S.; Kim, H. S.: Highly Flexible All-Nonwoven Piezoelectric Generators Based on Electrospun Poly(vinylidene fluoride). *Sensor Actuat A-Phys* **2019**, *300*, 111672.

33. Ghosh, S. K.; Mandal, D.: Synergistically Enhanced Piezoelectric Output in Highly Aligned 1D Polymer Nanofibers Integrated All-fiber Nanogenerator for Wearable Nano-Tactile Sensor. *Nano Energy* **2018**, *53*, 245-257.

34. Roy, K.; Ghosh, S. K.; Sultana, A.; Garain, S.; Xie, M.; Bowen, C. R.; Henkel, K.; Schmeiβer, D.; Mandal, D.: A Self-Powered Wearable Pressure Sensor and Pyroelectric Breathing Sensor Based on GO Interfaced PVDF Nanofibers. *ACS Appl. Nano Mater.* **2019**, *2*, 2013-2025.

35. Roy, K.; Jana, S.; Ghosh, S. K.; Mahanty, B.; Mallick, Z.; Sarkar, S.; Sinha, C.; Mandal, D.: Three-Dimensional MOF-Assisted Self-Polarized Ferroelectret: An Effective Autopowered Remote Healthcare Monitoring Approach. *Langmuir* **2020**, *36*, 11477-11489.

36. Yang, Y.; Zhang, H.; Wang, Z. L.: Direct-Current Triboelectric Generator. *Adv. Funct. Mater.* **2014**, *24*, 3745-3750.

37. Mandal, D.; Kim, K. J.; Lee, J. S. Simple Synthesis of Palladium Nanoparticles, β-Phase Formation, and the Control of Chain and Dipole Orientations in Palladium-Doped Poly(vinylidene fluoride) Thin Films. *Langmuir* **2012**, *28*, 10310−10317.

38. Mishra, S.; Unnikrishnan, L.; Nayak, S. K.; Mohanty, S.: Advances in Piezoelectric Polymer Composites for Energy Harvesting Applications: A Systematic Review. *Macromol. Mater. Eng.* **2019**, *10*, 1800463.

39. Shin, D-J.; Lim, D-H.; Koo, B-K.; Kim, M-S.; Kim, I-S.; Jeong, S-J.: Porous Sandwich Structures Based on BaZrTiO$_3$-BaCaTiO$_3$ Ceramics for Piezoelectric Energy Harvesting. *J. Alloys Compd.* **2020**, *831*, 154792.

40. Naskar, K.; Dey, A.; Maity, S.; Bhunia, Manas K.; Ray, P. P.; Sinha, C.:Novel Porous Polycatenated Iodo-Cadmium Coordination Polymer for Iodine Sorption and Electrical Conductivity Measurement. *Cryst. Growth Des.* **2019**, *19*, 2206–2218.

41. Jana, S.; Jana, R.; Sil, S.; Dutta, B.; Sato, H.; Ray, P. P.; Datta, A.; Akitsu, T.; Sinha, C.: Influence of Axial Linkers on Polymerization in Paddle-Wheel Cu(II) Coordination Polymers for the Application of Optoelectronics Devices. *Cryst. Growth Des.* **2019**, *19*, 6283-6290.

42. Botas, J. A.; Calleja, G.; Sánchez-Sánchez, M.; Orcajo, M. G.: Cobalt Doping of the MOF-5 Framework and Its Effect on Gas-Adsorption Properties. *Langmuir* **2010**, *26*, 5300-5303.

43. Guo, Q.; Ren, L.; Kumar, P.; Cybulskis, V. J.; Mkhoyan, K. A.; Davis, M. E.; Tsapatsis, M.: A Chromium Hydroxide/MIL-101(Cr) MOF Composite Catalyst and Its Use for the Selective Isomerization of Glucose to Fructose. *Angew. Chem. Int. Ed.* **2018**, *57*, 4926-4930.

44. Kim, J.-O.; Kim, J. Y.; Lee, J.-C.; Park, S.; Moon, H. R.; Kim, D.-P.: Versatile Processing of Metal–Organic Framework–Fluoropolymer Composite Inks with Chemical Resistance and Sensor Applications. *ACS Appl. Mater. Inter.* **2019**, *11*, 4385-4392.

45. Hu, L.; Zhang, Y.; Lu, W.; Lu, Y.; Hu, H.: Easily Recyclable Photocatalyst Bi_2WO_6/MOF/PVDF Composite Film for Efficient Degradation of Aqueous Refractory Organic Pollutants Under Visible-Light Irradiation. *J. Mater. Sci.* **2019**, *54*, 6238-6257.

46. Szewczyk, P. K.; Gradys, A.; Kim, S. K.; Persano, L.; Marzec, M.; Kryshtal, A.; Busolo, T.; Toncelli, A.; Pisignano, D.; Bernasik, A.; Kar-Narayan, S.; Sajkiewicz, P.; Stachewicz, U.: Enhanced Piezoelectricity of Electrospun Polyvinylidene Fluoride Fibers for Energy Harvesting. *ACS Appl. Mater. Inter.* **2020**, *12*, 13575-13583.

47. Ico, G.; Showalter, A.; Bosze, W.; Gott, S. C.; Kim, B. S.; Rao, M. P.; Myung, N. V.; Nam, J.: Size-Dependent Piezoelectric and Mechanical Properties of Electrospun P(VDF-TrFE) Nanofibers for Enhanced Energy Harvesting. *J. Mater. Chem. A* **2016**, *4*, 2293-2304.

48. Mackay, Michael E.; Tuteja, A.; Duxbury, Philip M.; Hawker, Craig J.; Horn, B. V.; Guan, Z.; Chen, G.; Krishnan, R. S.: General Strategies for Nanoprticle Dispersion. *Science* **2006**, *311*, 1740–1743.

49. Sultana, A.; Ghosh, S. K.; Alam, M. M.; Sadhukhan, P.; Roy, K.; Xie, M.; Bowen, C. R.; Sarkar, S.; Das, S.; Middya, T. R.; Mandal, D.: Methylammonium Lead Iodide Incorporated Poly(vinylidene fluoride) Nanofibers for Flexible Piezoelectric–Pyroelectric Nanogenerator. *ACS Appl. Mater. Inter.* **2019**, *11*, 27279-27287.

50. Maity, K.; Mandal, D.: All-Organic High-Performance Piezoelectric Nanogenerator with Multilayer Assembled Electrospun Nanofiber Mats for Self-Powered Multifunctional Sensors. *ACS Appl. Mater. Inter.* **2018**, *10*, 18257-18269.

51. Qi, Y.; Kim, J.; Nguyen, T. D.; Lisko. B.; Purohit, P. K.; McAlpine. M. C.: Enhanced Piezoelectricity and Stretchability in Energy Harvesting Devices Fabricated from Buckled PZT Ribbons. *Nano Lett.* **2011**, *11*, 1331-1336.

52. Palosaari, J.; Leinonen, M.; Hannu, J.; Juuti, J.; Jantunen, H.; : Energy Harvesting with a Cymbal Type Piezoelectric Transducer from Low Frequency Compression. *J. Electroceram.* **2012**, *28*, 214-219.

53. Lee, B.-S.; Park, B.; Yang, H.-S.; Han, J. W.; Choong, C.; Bae, J.; Lee, K.; Yu, W.-R.; Jeong, U.; Chung, U. I.; Park, J.-J.; Kim, O.: Effects of Substrate on Piezoelectricity of Electrospun Poly(vinylidene fluoride)-Nanofiber-Based Energy Generators. *ACS Appl. Mater. Inter.* **2014**, *6*, 3520-3527.

54. Noh, S.; Lee, H.; Choi, B.: A Study on The Acoustic Energy Harvesting with Helmholtz Resonator and Piezoelectric Cantilevers. *Int. J. Precis. Eng. Man.* **2013**, *14*, 1629-1635.

55. Li, B.; Laviage, A. J.; You, J. H.; Kim, Y.-J.: Harvesting Low-Frequency Acoustic Energy Using Quarter-Wavelength Straight-Tube Acoustic Resonator. *Appl. Acoust.* **2013**, *74*, 1271-1278.

Chapter 3

3D MOF Facilitated Self-Polarized Ferroelectret

Nanogenerator

3.1 Introduction

In current era, revolution on wearable tactile sensor networks and internet of things (IoT) not only changes the traditional understanding about fossil fuel based energy resources, it also focuses toward the realization of mobile bio-monitoring prostheses and advanced robotic systems [1-9]. In this regard, utilization of clean and renewable energy sources with wireless signal transfer is one of the prime criteria to develop remote heath care monitoring [10-12]. Moreover, miniaturization of commercial portable devices, wireless sensors and small electronic systems has reduced their power requirement to mW and even μW level. Thus, immense attention has been paid to fabricate wearable pressure sensors to detect subtle pressure changes of different human activities (e.g., movements of body parts, muscle movement associated with coughing, swallowing, speech pronunciation), which are essential for human physiological signal monitoring. Precisely, pressure sensors are driven by different mechanisms such as piezoelectric [5-6], piezocapacitive [13], piezoresistive [14] and triboelectric [15] effect. Among them, piezocapacitive and piezoresistive sensors depend on external power supply. However, triboelectric sensors primarily rely on air-gap capacitor and suffer from undesirable sensitivities to static electricity, stray capacitances and temperature changes. On the other hand, piezoelectric pressure sensor has gathered immense attention due to its promising response of change in-electrical polarization towards very small ambient vibrations (wind flow, raindrop, acoustic noises, transportation vehicles, etc.). As a result, wireless piezoelectric pressure sensors open up new insight towards continuous non-invasive health care monitoring without any trade-off between benefits of light weight, flexibility and excellent wearability. Till date, enormous efforts have been paid on different organic/inorganic piezoelectric materials and their device structures to obtain high sensitivity and output performance. In spite of higher piezoelectric activity, utilization of inorganic and lead based piezoelectric materials (e.g., barium titanate, lithium niobate, lithium tetraborate,

87

lead zirconate titanate, lead magnesium niobate, lead tantalite, triglycine sulfate, etc.) is restricted in the development of flexible pressure sensors for biomedical applications due to their brittleness and complex processing route [16-19]. In this regard, semi-crystalline poly(vinylidene fluoride) (PVDF, chemical formula: $(CH_2-CF_2)_n$) is a suitable choice of organic materials due to its flexibility, light weight, chemical inertness, biocompatibility and easy large area processability [6, 20-24]. Depending on the macromolecular chain conformation, among five crystalline polymorphs (α, β, γ, δ and ε phases) of PVDF [25-27], β–phase (orthorhombic unit cell with $Cm2m$ (C_{2v}^{14}) space group) is the mostly desired crystalline phase to obtain optimum piezoelectric response [21-24].

Typically, mechanical stretching followed by electrical poling is required to obtain effective piezoelectric functionality in β–phase. This technique is not suitable for tailoring electronic device design due to inhomogeneous neck formation in active stretching process that often leads to poor yield of electrical poling [28]. Alternatively, over the past few years, several techniques (e.g., spin coating, electrospinning, epitaxial film formation, Langmuir–Blodgett method, incorporation of fillers and nanoimprinting) have been adopted to induce β–phase in PVDF to avoid direct stretching techniques [6, 11, 22-24, 29-35]. Particularly, incorporation of micro/nano-fillers in PVDF matrix found to be most promising technique for successful conversion of non-polar α–phase to polar β– and γ–phases [24, 36, 37]. However, due to lower piezoelectric coefficients of PVDF in comparison to inorganic piezoelectrics, it is hard to develop auto-powered epidermal biomedical sensors. In this context, the straight forward strategy to enhance the piezoelectric property is to create porous ferroelectret structure [38-43]. The main reason for enormous increment of piezoelectricity in porous PVDF is the synchronized combination of nano-dipoles (arises from β-phase) and micro-dipoles (attributing from porous structure) along with stress confinement [44, 45]. It is noteworthy to mention that easy fabrication scheme and high electrical breakdown strength of ferroelectrets

are other added advantages [40]. We have established that hygroscopic salts can be readily used to create self-aligned porous ferroelectrets that exhibit significantly higher piezoelectric activity [36, 37, 40, 41]. In recent years, metal–organic frameworks (MOFs) are considered as an exciting material towards a new class of porous materials. In particular, MOFs are a class of crystalline materials constructed by metal ions or metal ion clusters (serving as node) and interlinked through organic ligands. The attractive features of MOFs arise from their highly regulated and well-defined framework structures possessing nanochannels with tunable size, shape, dimensionality, and surface environment. Due to their versatile properties, MOFs have been widely studied in several applications including gas storage, separation and sensing, catalysis, filtering device, electrical energy storage, optoelectronic component, non-volatile memory element and drug delivery [46-52]. Unfortunately, the powder form of MOF restricts its more diverse application. Particularly, MOF-polymer composites in the form of film, ink and nanofibers are extensively studied to expand its versatility in different sensing platforms such as chemical protection and decontamination of chemical warfare agents, H_2S sensing, metal recovery from acidic solution, chemosensor and thermosensor for aromatic pollutants, piezoresistive health monitoring and motion sensing [53-60]. Although, till date, the direct use of MOF in auto-powered pressure sensor, such as electronic skin is rarely studied.

In this thesis chapter, a 3D porous MOF (CdI_2-INH=CMe_2) was synthesized by optimizing acetone layering method. In addition, PVDF and 3D MOF composite (PVDF@MOF) films were prepared by solvent casting technique, where porous ferroelectret like structure can be observed. Finally, we fabricated a MOF derived PVDF (PVDF@MOF) composite ferroelectret film based mechanical energy harvester (MEH) that shows much more superior mechano-sensitivity of 8.52 V/kPa and fast response time of 8 ms due to its ferroelectret behaviour generating from porous structure. Here, noteworthy to mention that as synthesized
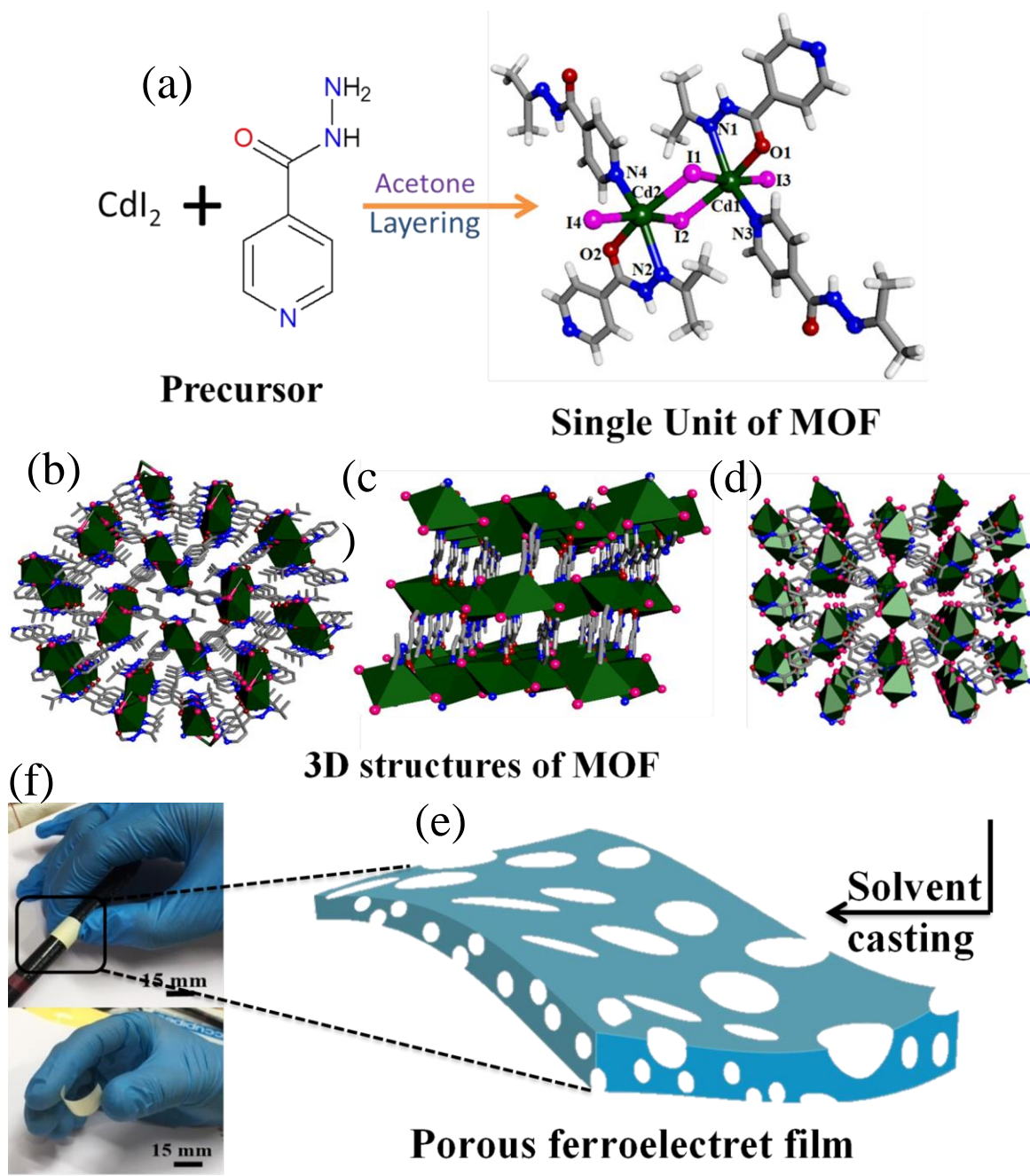
Figure 3.1 (a) Schematic route for the synthesis of 3D porous [CdI$_2$-INH=CMe$_2$] MOF. 3D porous structure of the as synthesized MOF along (b) a-axis and (c) b-axis and (d) c-axis along with (e) preparation of porous PVDF@MOF composite film. (f) Two digital photographs show the rollability (upper side) and flexibility (lower side) of the PVDF@MOF1.0 composite film.

MOF, i.e., [CdI$_2$-INH=CMe$_2$] played a significant role in the nucleation of stable piezoelectric β−phase as well as controllable porous structure in PVDF. In addition, it has a broad range of application towards sensing of subtle to moderate range of pressure change in association with different human physiological signals, such as vibration of speech articulators (throat), opening and closing motion of glottis, respiration air flow motion and most importantly heart rate (radial pulse). These physiological signals tracking system may give rise a suitable tool in predicting the influenza and pulmonary disease related symptoms that deviates from healthy behaviour. Furthermore, the potential of MEH in real time wrist pulse signal detection and wireless data-transmission indicates its potential utilization in wearable medical electronics and remote health monitoring.

3.2 Experimental Section

3.2.1 Synthesis of [CdI$_2$-INH=CMe$_2$]

The synthesis follows the previously reported procedure [47, 48]. A methanol solution of isoniazid (INH) (13.7 mg, 0.1 mmol) was carefully layered with the help of water-methanol mixed solvent over the aqueous solution of of CdI$_2$ (36.62 mg, 0.1 mmol) (1:1) followed by 3-4 drops of acetone. It was then allowed to diffuse over the week. The yellow coloured block-shaped crystals were deposited on the glass wall. The crystals placed under a microscope and separated mechanically, then washed with methanol and water (1:1) mixture, and dried. The yield of compound was 85 %. Microanalytical data (C, 19.8; H, 1.98; N, 7.68%) is in well accordance with the calculated primary elemental analysis (C, 19.88; H, 2.02; N, 7.73%) of [CdI$_2$-INH=CMe$_2$]. A schematic route of synthesis along with 3D porous structures (along a, b, c-axis) is provided in Figure 3.1(a-d).

3.2.2 Preparation of Composite Ferroelectret Film

PVDF@MOF composite film was prepared by solution casting technique. Firstly, 4 wt% PVDF was completely dissolved in DMF under 6 h of stirring. Then, two sets (0.25 and 1

wt%) of [CdI$_2$-INH=CMe$_2$] were mixed in the PVDF-DMF solution and left under stirring until the homogeneous solutions were attained. Afterwards, the resulting solutions including the Neat PVDF solution were casted on the clean glass slides and kept for drying at 60 $^{\circ}$C for 5 h. Finally, the films were peeled off from glass slides and proceed for further experimentation. The films were abbreviated as PVDF@MOF0.25 (where 0.25 wt% of [CdI$_2$-INH=CMe$_2$] is incorporated), PVDF@MOF1.0 (1.0 wt% of [CdI$_2$-INH=CMe$_2$] is incorporated) and Neat PVDF (in the case of without [CdI$_2$-INH=CMe$_2$]). A schematic illustration of the preparation of porous film is demonstrated in Figure 3.1(a-e). Specifically, in Figure 3.1(a), precursor of the as synthesized MOF ([CdI$_2$-INH=CMe$_2$]) and associated chemical reaction are mentioned, where a single unit of MOF is presented. The corresponding 3D structures are illustrated in Figure 3.1(b-d). The flexibility and rollability of the composite film (Figure 3.1(f)) respectively indicates that it is perfectly suitable in mechanical energy harvesting applications and flexible electronic devices.
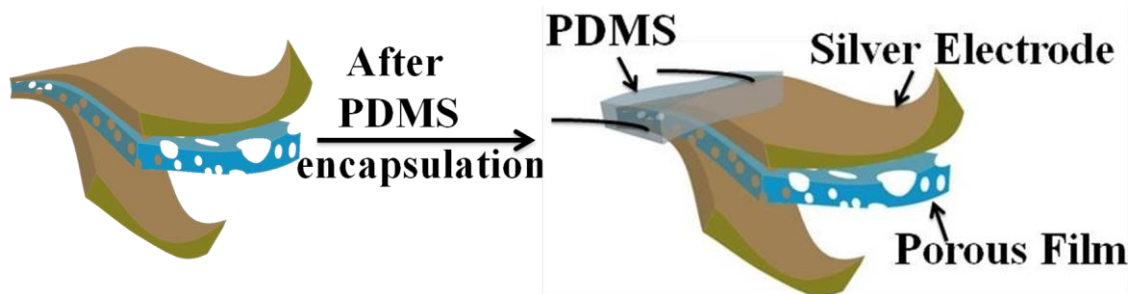
Figure 3.2 Schematic illustration of the MEH fabrication.

3.2.3 Fabrication of MEH

The MEH was fabricated using silver paste printing as top-bottom electrodes over the active layer of PVDF@MOF composite film. Firstly, a rectangular shaped film (area: 25 mm × 15 mm) was cut and then silver paste was used to construct the top and bottom electrode with an active area of (20 mm × 10 mm). Finally, the entire structure was encapsulated by polydimethylsiloxane (PDMS) to avoid direct contact with skin as described in earlier work

[29]. A fabrication scheme is illustrated in Figure 3.2. In addition, a reference MEH (Neat PVDF-EH) is also fabricated in similar way where Neat PVDF is used as an active layer.

3.2.4 Characterization

A Bruker SMART APEX II diffractometer equipped with graphite-monochromated MoKα radiation (λ = 0.71073 Å) was used for collecting single crystal diffraction data of the synthesised MOF. The detail crystal structure was evaluated using the SHELX-97 software package. It is noteworthy to mention that during the analysis, non-hydrogen atoms were refined with anisotropic thermal parameters and hydrogen atoms were placed in their geometrically idealized positions and constrained to ride on their parent atoms. Micro-analytical data (C, H, N) were measured by Perkin-Elmer 2400 CHNCS/O elemental analyser. The crystalline phases and powder X-ray diffraction pattern (P-XRD) of the as-prepared MOF and PVDF/Cd-INH composite films were collected by a Bruker D8 Advance X-ray diffractometer using Cu Kα radiation (λ = 1.548 Å) generated at 40 kV and 40 mA. Differential scanning calorimetry (DSC, STA 800, Parkin Elmer) was performed from 30 to 210 $^{\circ}$C at a heating rate of 5 $^{\circ}$C/min. Fourier Transform Infrared Spectroscopy (FT-IR, TENSOR II, Bruker) was used to characterise vibrational bands and crystalline phases of PVDF (in the wavenumber range of 4000-400 cm^{-1} and 16 number of scans is employed). Morphological analysis were carried out by FE-SEM (INSPECT F50, FEI) functioning at an acceleration voltage of 20 kV. The elemental mapping was obtained by EDX spectroscopy recorded in a Bruker Nano X-flash detector (410M) equipped with a FE-SEM chamber. Dielectric properties were studied using a precision impedance analyzer (Wayne Kerr, 6500B) at room temperature. The piezoelectric output performance of MEH in terms of open-circuit voltage (V_{oc}) and short-circuit current (I_{sc}) were measured using a digital storage oscilloscope (Tektronix TDS 2024C) and a picoammeter (Keithley 6485) respectively. The

vertical impact from hand imparting was recorded by a 3-axial force pressure sensor (FlexiForce A201).

3.3 Results and Discussion

3.3.1 Structural Analysis of [CdI$_2$-INH=CMe$_2$]

The crystallographic data of the single crystalline [CdI$_2$-INH=CMe$_2$] compound is summarized in Table 3.1 and selected bond lengths and bond angles are given in Table 3.2.

Table 3.1 Crystal data and refinement parameters of [CdI$_2$-INH=CMe$_2$] (CCDC 1938436).

empirical formula	C$_9$H$_{11}$Cd I$_2$N$_3$O
formula weight (f$_w$)	543.42
crystal system, space group	monoclinic, *P 21/n*
unit cell dimensions	*a* (Å) = 8.594(9)
	b (Å) = 14.579(14)
	c (Å) = 11.552(14)
volume *V* (Å^3)	1447(3)
angles between three edges	α (^{o}) = 90
	β (^{o}) = 90.36(4)
	γ (^{o}) = 90
Z, calculated density (g/cm^3)	4, 2.495
μ (mm^{-1})	5.761
wavelength λ (Å)	0.71073
data[$I > 2\sigma(I)$]/parameters	1589/147
GOF on F^2	1.585
final *R* indices[$I > 2\sigma(I)$]^{a,b}	R1 = 0.1167
	wR2 = 0.3312

^{a}R1 = $\Sigma||F_o| - |F_c||/ \Sigma|F_o|$, ^{b} wR2 = $[\Sigma w(F_o^2 - F_c^2)^2/\Sigma w(F_o^2)^2]^{1/2}$

From single crystal X-ray diffraction data, it is confirmed that Isoniazid (INH) undergoes condensation with acetone (Me$_2$C=O) in presence of CdI$_2$ in-situ mode to synthesize [CdI$_2$-INH=CMe$_2$]$_n$. The compound is crystallized in the monoclinic crystal system with

centrosymmetric space group P$2I/n$ and $Z = 4$. Each Cd (II) centre in the [CdI$_2$-INH=CMe$_2$] compound adopts a distorted octahedral geometry and bonded as N, O chelator and one peripheral pyridyl-N coordinates to adjacent Cd(II) from INH-Schiff base (INH=CMe$_2$). The I atoms are bridging and make the 2D polymeric structure. The connectivity of INH=CMe$_2$ via N donor centres with Cd(II) resulted in a 1D polymer chain. The N-H of chelated

Table 3.2. Selected bond lengths and bond angles in [CdI$_2$-INH=CMe$_2$] (CCDC 1938436).

I1 - Cd1	2.872(4)	O1 - Cd1 - N1	67.1(5)
I2 - Cd1	2.815(4)	O1 - Cd1 - I2_b	75.8(4)
I2 - Cd1_b	3.406(5)	O1 - Cd1 - N3_c	84.7(6)
Cd1 - O1	2.335(15)	N1 - Cd1 - I2_b	78.6(4)
Cd1 - N1	2.54(2)	N1 - Cd1 - N3_c	147.8(6)
Cd1 - N3_c	2.371(19)	I2_b - Cd1 - N3_c	79.7(4)
Cd1 - I2 - Cd1_b	94.00(7)	Cd1 - O1 - C9	119.7(12)
I1 - Cd1 - I2	106.48(8)	Cd1 - N1 - N2	109.7(13)
I1 - Cd1 - O1	91.7(4)	Cd1 - N1 - C10	131.0(15)
I1 - Cd1 - N1	97.2(5)	N2 - N1 - C10	119(2)
I1 - Cd1 - I2_b	167.51(9)	C4 - N3 - Cd1_d	125.2(15)
I1 - Cd1 - N3_c	98.9(4)	C8 - N3 - Cd1_d	118.7(14)
I2 - Cd1 - O1	161.8(4)	N1 - N2 - C9	120(2)
I2 - Cd1 - N1	108.3(4)	C4 - N3 - C8	115.9(19)
I2 - Cd1 - I2_b	86.00(7)	I2 - Cd1 - N3_c	93.5(5)

a = 3/2-x,-1/2+y,1/2-z   b = 1-x,1-y,-z   c = -1/2+x,1/2-y,-1/2+z   d = 1/2+x,1/2-y,1/2+z

hydrazine undergoes intermolecular hydrogen bonding with bridging I atoms to form supramolecular networks. In the solid state structure, the 1D chains undergo polymerisation to form 2D network and self-assembled through weak C–H⋯π and π…π interactions among the pyridine rings of INH ligands with edge-to-face manner which contributes to build 3D

supramolecular network as shown in Figure 3.1(b-d). In addition, P-XRD (Figure 3.3(a)) was conducted to check the bulk purity of the as-synthesized MOF, which is in accordance with the simulated XRD (Figure 3.3(b)) retraced from single crystal XRD data. Furthermore, FT-IR spectra of [CdI$_2$-INH=CMe$_2$] (Figure 3.3(c)) indicates the presence of both exocyclic and endocyclic C=N (1670-1630 cm^{-1}), ν(N-H) (3340-3320 cm^{-1}), conjugated ketone (C=O) (1670-1630 cm^{-1}) and aromatic C=C (1550-1500 cm^{-1}) regions in the MOF skeleton.
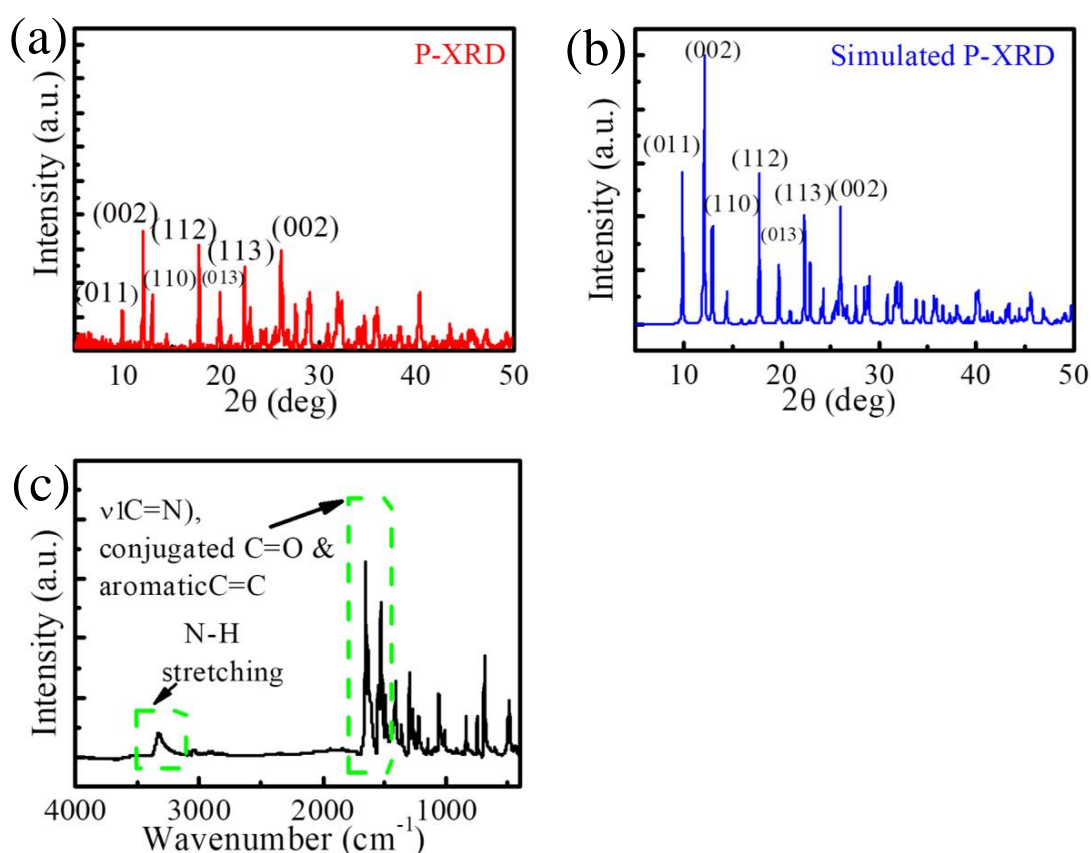
Figure 3.3 (a) XRD pattern (b) simulated XRD pattern (from single crystal XRD) and (c) FT-IR spectra (in the range of 4000-400 cm^{-1}) of the as synthesized [CdI$_2$-INH=CMe$_2$].

3.3.2 Surface Morphology

The as synthesized 3D MOF was used to fabricate porous PVDF based composite ferroelectret films (Figure 3.4(b-d)) in contrast to the smooth surface morphology of Neat
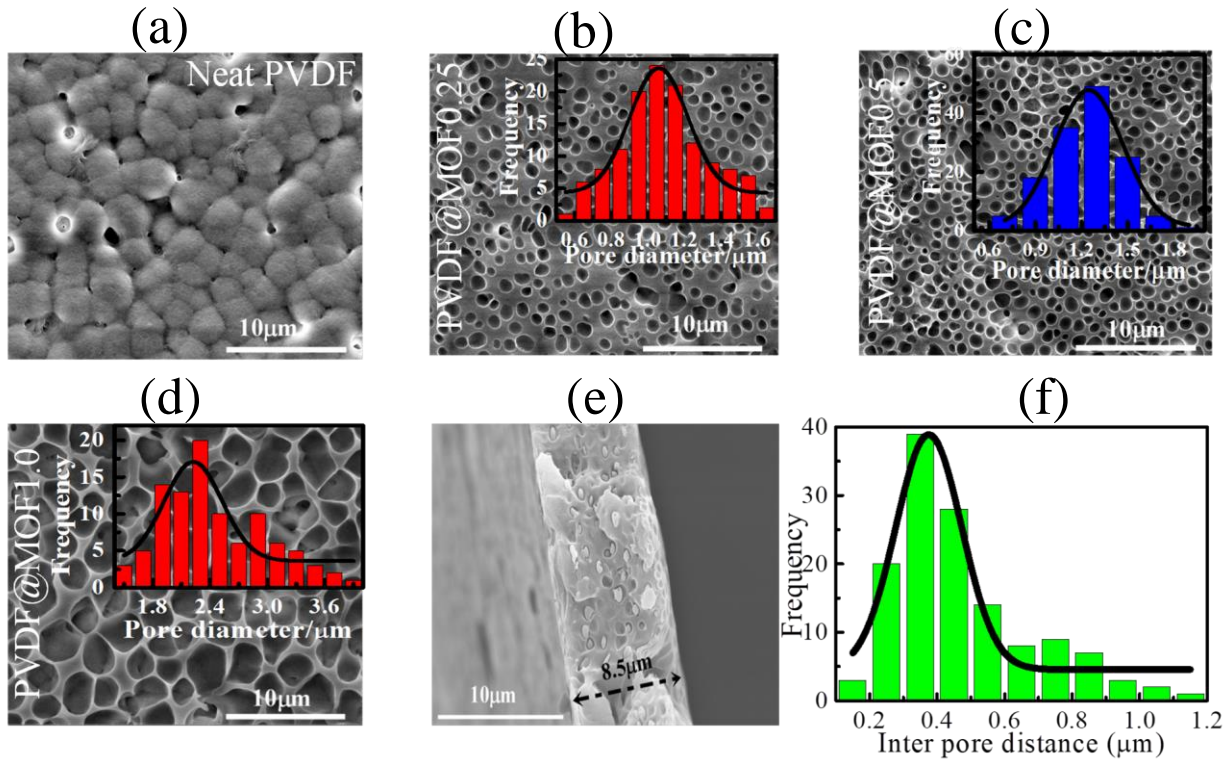
Figure 3.4 FE-SEM images of (a) Neat PVDF, (b) PVDF@MOF0.25 (pore diameter distribution in the inset) (c) PVDF@MOF0.5 (pore diameter distribution in the inset) and (d) PVDF@MOF1.0 (pore diameter distribution in the inset). (e) The cross-sectional FE-SEM image of PVDF@MOF1.0 film indicates the presence of void as well as the MOF particle. (f) Histogram profile of the inter-pore distance in PVDF@MOF1.0.

PVDF film (Figure 3.4(a)). The fibril growth (as observed in Neat PVDF film, evidenced in Figure 3.4(a)) was totally disappeared with the addition of very small amount (0.25 wt%) of [CdI$_2$-INH=CMe$_2$], as prepared 3D MOF (Figure 3.4(b)). As a prerequisite of ferroelectret material, the effect of 3D MOF towards porous structure formation in PVDF was systematically investigated, this is one of the novel approaches of ferroelectret film preparation. The average pore diameter of the cavities was found to increase with increasing concentration of external filler, for example, 1 µm of average pore diameter is found in PVDF@MOF0.25 film (evidenced from surface morphology, illustrated in Figure 3.4(b), and pore diameter distribution histogram in the inset), whereas it is increased to 2.4 µm in the

case of PVDF@MOF1.0 film (corresponding surface morphology and pore diameter distribution is shown in Figure 3.4(d) and its inset respectively). As a consequence, surface coverage by pores (thus porosity) also increases up to 90% in PVDF@MOF1.0 film. As a result, PVDF@MOF1.0 film showed excellent flexibility and rollability (Figure 3.1(f)). In addition, pores are uniformly distributed on the entire surface of the film (Figure 3.4(d)) as well as along the thickness (8.5 µm) of the film (Figure 3.4(e)) and well separated by dielectric layer of PVDF with an average thickness of 0.4 µm (Figure 3.4(f)). The presence of MOF particles are also evidenced from Figure 3.4(e).
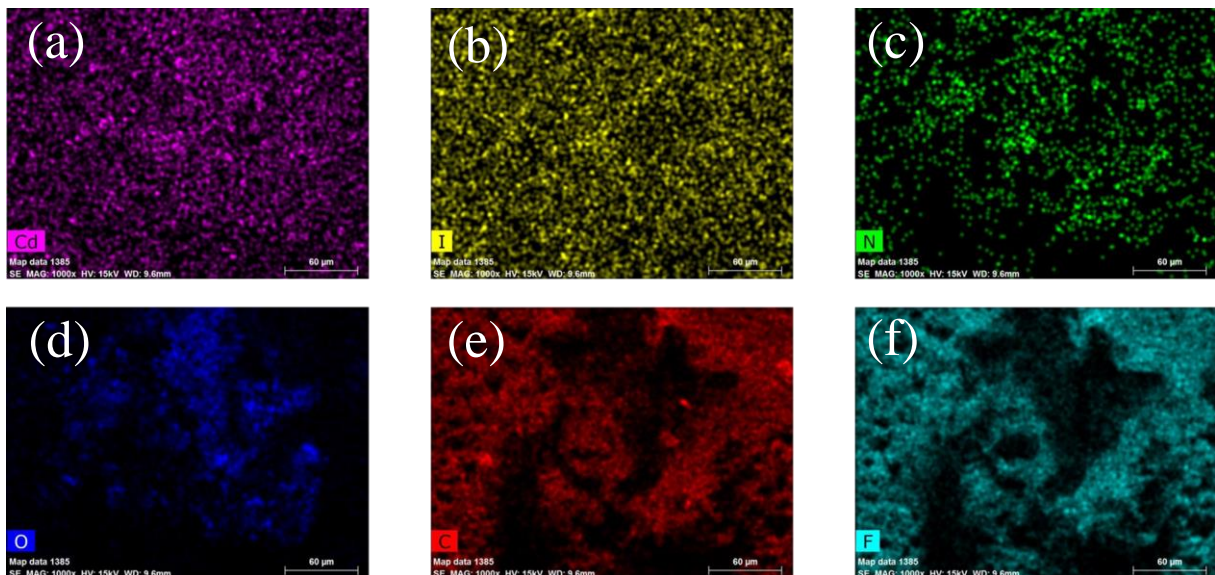
Figure 3.5 Elemental mapping (scale bar: 60 µm) of PVDF@MOF1.0 film: (a) Cd, (b) I, (c) N, (d) O, (e) C, (f) F.

Additionally, elemental mapping reveals the presence of Cd, I, N, O (from the MOF skeleton) throughout the entire surface of the film (including the inside and boundary of pores) along with C, F (from PVDF) as shown in Figure 3.5(a-f). It proves that well dispersed [CdI$_2$-INH=CMe$_2$] (3D MOF) within PVDF matrix played a crucial role in porous ferroelectret film

formation. In contrast, random and very few (rarely) pores are found in Neat PVDF film prepared under the identical conditions (as depicted in Figure 3.4(a)).

3.3.3 Mechanism of Pore Formation

Actually, the porous three-dimensional supramolecular network structure of the as-synthesized MOF [Figure 3.1(b-d)] is also retained in the casted film. Moreover, PVDF matrix might penetrate the permanent pores of [CdI_2-INH=CMe_2], which in turn facilitates the pore formation. During the film preparation, once the MOF was incorporated in PVDF-DMF solution, moisture from environment was absorbed in the solution due to its polar aprotic nature and morphology of MOF. Those water molecules evaporate gradually at a faster rate (because of its comparatively lower density and boiling point) during crystallization. It also triggers the pore generation.
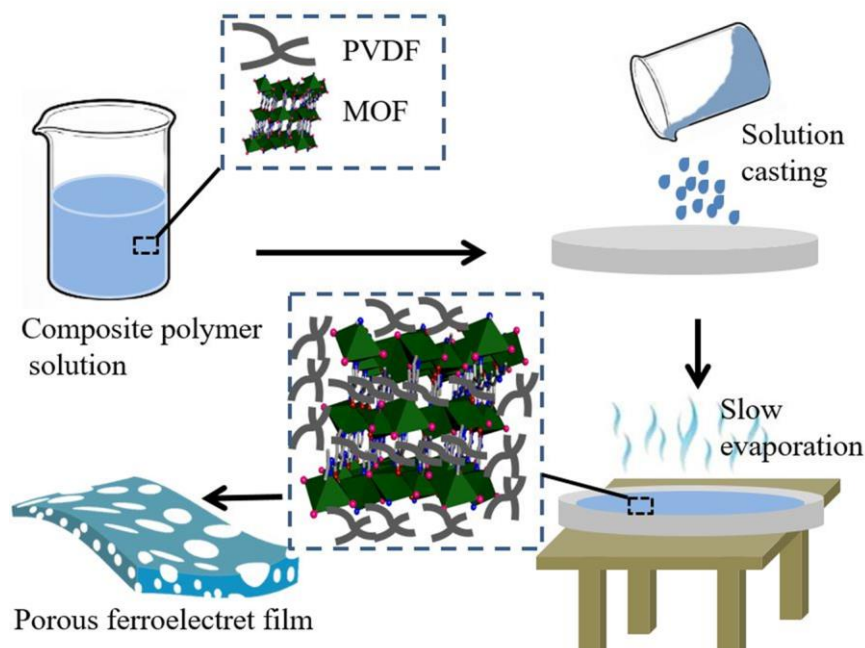
Figure 3.6 Pore formation mechanism of PVDF@MOF composite film.

If the porous morphology was only evaporation controlled, then same kind of even pore distribution can also be observed for Neat PVDF surface as well. Thus it is expected that

MOF incorporation in PVDF matrix is playing the significant role in pore formation. In addition, average pore diameter increment trend has been observed upon the increment of MOF incorporation in PVDF@MOF composite film. Eventually it can be concluded that the 3D porous structure of MOF and slow evaporation of solvent molecules during crystallization result in the formation of porous, spongy and flexible composite film in comparison to the rarely porous, smooth surface of the Neat PVDF film. A schematic (Figure 3.6) is illustrating the pore formation in MOF derived PVDF@MOF composite film.

3.3.4 Crystallographic Phase Identification and Quantification

In addition to the porous structure formation, 3D MOF also induces electroactive phases in PVDF. FT-IR spectra of Neat PVDF and PVDF@MOF films are depicted in Figure 3.7(a).
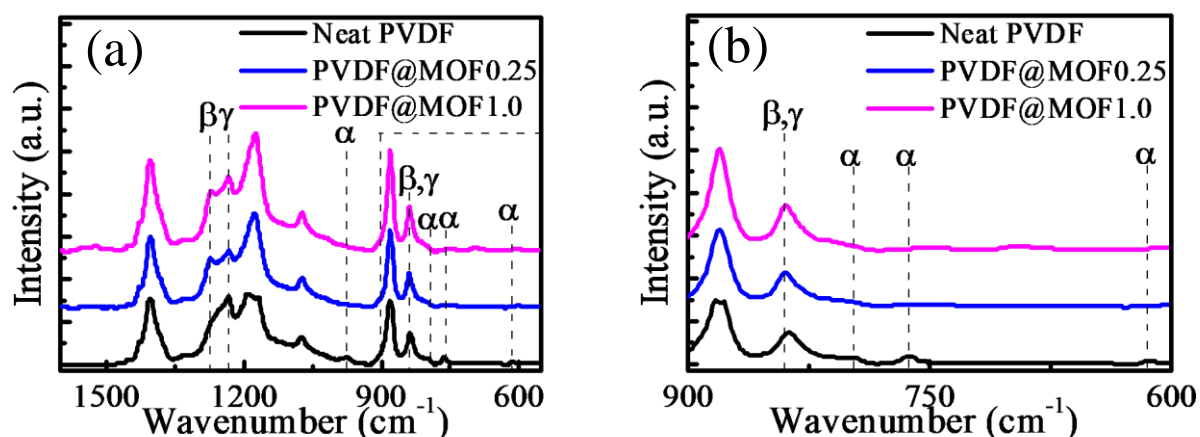
Figure 3.7 FT-IR spectra of Neat PVDF, PVDF@MOF0.25 and PVDF@MOF1.0 film in the region of (a) 1600-550 cm^{-1} (b) 900-600 cm^{-1}.

It clearly exhibits the presence of α-crystalline phase in Neat PVDF as evidenced from corresponding characteristic vibrational bands appeared at 613, 764, 796 and 976 cm^{-1} respectively [6, 20, 61, 62]. In addition, Neat PVDF film consists of a large amount of semi-polar γ- phase at solvent evaporation temperature less than 70 ^{o}C as strongest appearance of vibrational bands at 1233 cm^{-1} [63-66]. This is attributed to the interaction between PVDF

and solvent DMF. At lower drying temperature, the polar moieties of the DMF greatly influence the rotation of strong dipoles of C−F bond around C−C bonds of chain backbone [63, 65]. As a result, the interaction reduces the energy barrier/supplies the sufficient amount of activation energy to form polar conformation γ−phase. Therefore, T_3GT_3G' conformation is induced in Neat PVDF during crystallization. A schematic model is provided in Figure 3.8 to establish the above mentioned fact.
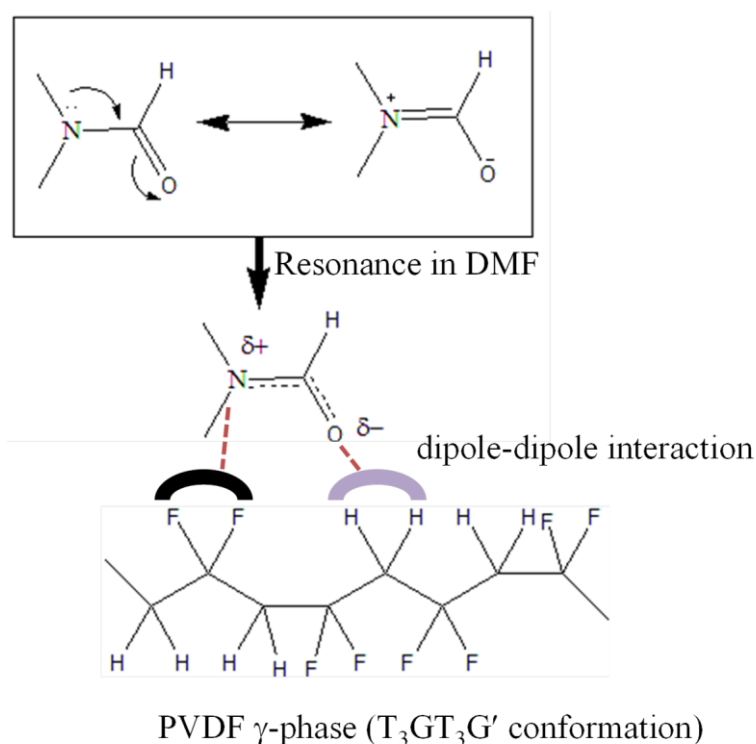
Figure 3.8 A hypothetical model of interaction between solvent DMF and PVDF dipoles.

This interaction is also present in PVDF@MOF composite film to induce more expanded all-trans conformation. In composite films, one additional band appears at 1275 cm^{-1} due to the nucleation of polar β-phase and all α-phase associated vibrational bands are diminished as observed in Figure 3.7(a and b) [21]. It is noteworthy to mention that the electroactive β- and γ-phase (F_{EA}) content gradually increases with the increasing concentration of [CdI$_2$-INH=CMe$_2$] in the PVDF matrix and reached to 98% when 1 wt% of [CdI$_2$-INH=CMe$_2$]
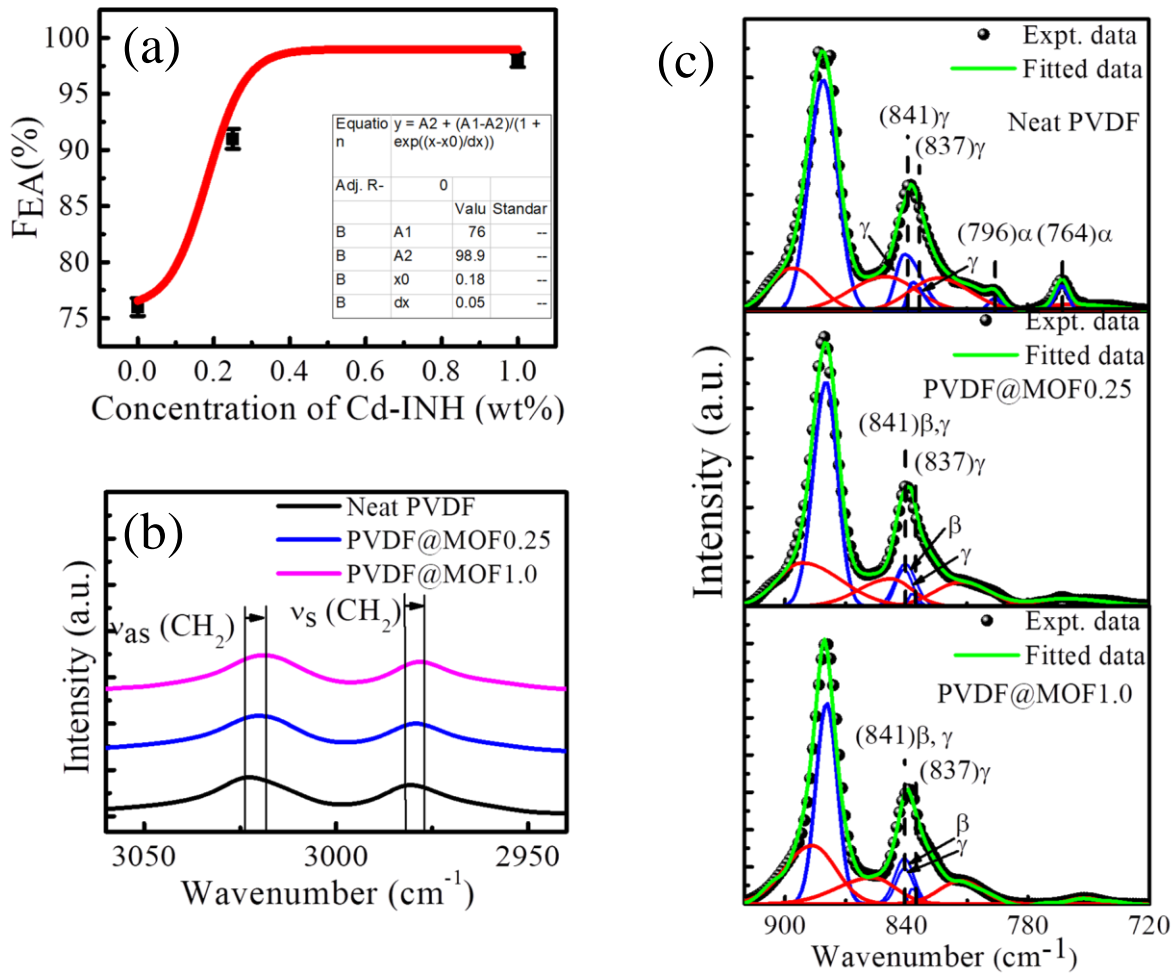
Figure 3.9 (a) %F_{EA} (calculated from FT-IR spectra) (b) FT-IR spectra in the range of 3060-2940 cm^{-1} and (c) deconvoluted FT-IR spectra in the range of 940-720 cm^{-1} for Neat PVDF and ferroelectret composite (*viz.*, PVDF@MOF0.25 and PVDF@MOF1.0) films.

loading is selected (Figure 3.9(a)). The electroactive phase (F_{EA}) content and the relative proportion of β- and γ-phases are quantified by assigning the band arising at 841 cm^{-1}, which is a common characteristic of both β- and γ-phases (Figure 3.9(b)) [24, 27]. The total electroactive phase content (F_{EA}) and relative proportion of electroactive phases (*β* and *γ*) i.e., *F(β)* and *F(γ)* can be calculated using these following equations.

$$F_{EA} = \frac{A_{841}}{\left(\frac{K_{841}}{K_{764}}\right)A_{764} + A_{EA}} \times 100\%$$

$$F(\beta) = F_{EA} \times \left(\frac{A_\beta}{A_\beta + A_\gamma}\right)$$

$$F(\gamma) = F_{EA} \times \left(\frac{A_\gamma}{A_\beta + A_\gamma}\right)$$

where, A_{841} and A_{764} signify the absorbance intensities at 841 cm^{-1} and 764 cm^{-1}, respectively, and K_{841} (7.7×10^4 cm^2 mol^{-1}) and K_{764} (6.1×10^4 cm^2 mol^{-1}) are the absorption coefficients regarding respective wavenumbers. A_β and A_γ are the intensities related to the β and γ phases under the deconvoluted curves of the 841 cm^{-1} main peak.

Nucleation of β-phase is more prominent than that of the γ-phase nucleation in the composite ferroelectret film. The proportional content of β- and γ-phases is provided in Table 3.3.

Table 3.3 The overall *%F$_{EA}$, %F$_\beta$, and %F$_\gamma$* of Neat PVDF and MOF assisted ferroelectret composite (*viz.*, PVDF@MOF0.25 and PVDF@MOF1.0) films (calculated from FT-IR spectra using deconvolution technique, referred to equation (1-3)).

Sample	%F$_{EA}$	%F$_\beta$	%F$_\gamma$
Neat PVDF	76	0	76
PVDF@MOF0.25	91	51	40
PVDF@MOF1.0	98	55	43

So, it is clear that, the addition of [CdI$_2$-INH=CMe$_2$] helps the crystallographic phase transformation (non-polar to electroactive phase) in PVDF. The interactions between the [CdI$_2$-INH=CMe$_2$] and the –CH$_2$–/–CF$_2$– of PVDF are involved in the polymer chain orientation. The sharp N–H stretching band (in the frequency region of 3340-3320 cm^{-1}) present in the [CdI$_2$-INH=CMe$_2$] is broadened and shifted to the lower frequency range in PVDF@MOF1.0 film (Figure 3.10(a)). This is because of the intermolecular hydrogen-
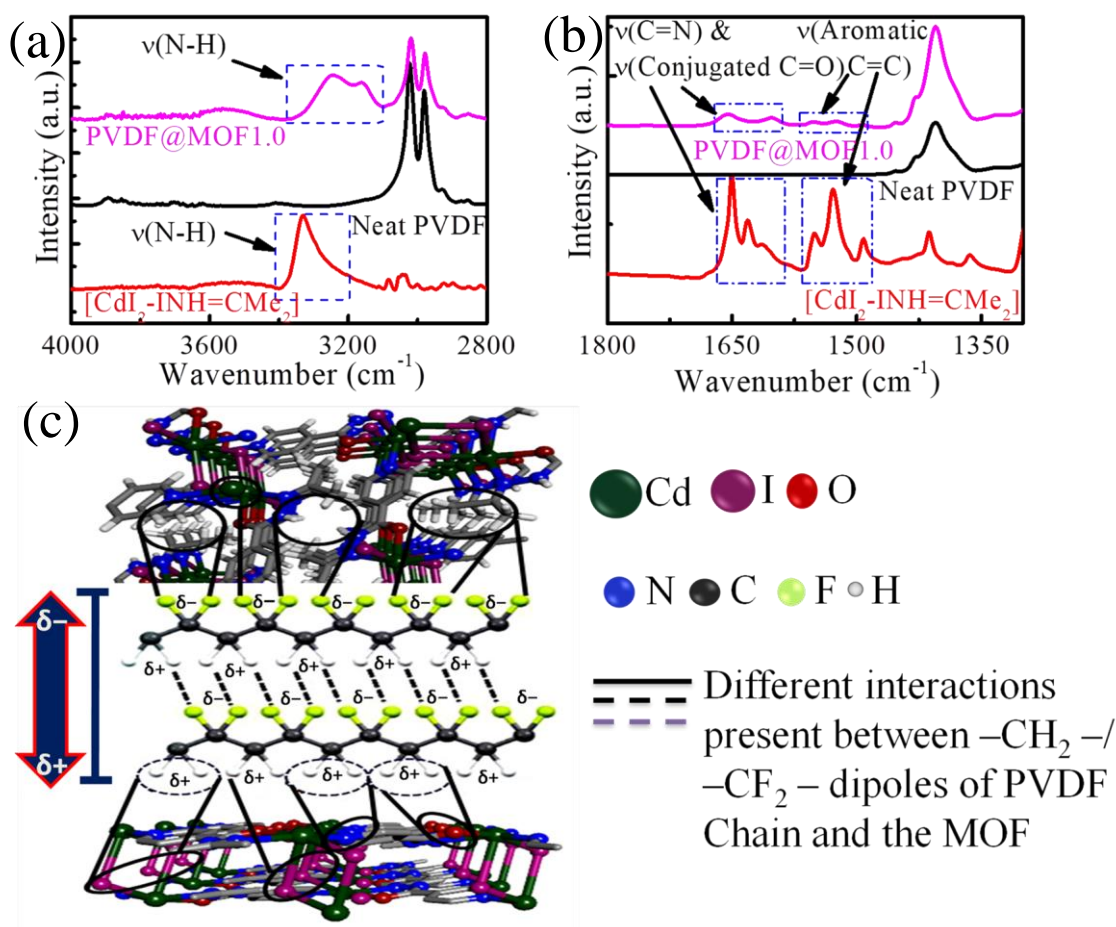
Figure 3.10 FT-IR spectra of [CdI$_2$-INH=CMe$_2$], Neat PVDF and PVDF@MOF1.0 film in the region of (a) 4000-2800 cm^{-1} (b) 1800-1300 cm^{-1}. (c) A schematic presentation describes different interactions between [CdI$_2$-INH=CMe$_2$] (MOF) and PVDF chain, indicating the self-poled structure in the PVDF chains.

bonding interaction present between the N–H bond of [CdI$_2$-INH=CMe$_2$] and the –CF$_2$– dipoles of PVDF (i.e., N–H···F–C hydrogen bonding). In addition, the sharp absorption bands appeared from conjugated ketone (C=O)/ exocyclic and endocyclic C=N and aromatic C=C at the stretching frequency level of 1670-1630 cm^{-1} and 1550-1500 cm^{-1} respectively in case of [CdI$_2$-INH=CMe$_2$]. In the PVDF@MOF1.0 film, the band broadening and shifting towards lower frequency region (Figure 3.10(b)) indicates the dipole-dipole interaction between C=O

from [CdI$_2$-INH=CMe$_2$] and –CH$_2$– of PVDF chain. Additionally, there must be some specific interaction (C–H$\cdots\pi$ and halogen/halogen interaction) present between the –CH$_2$–/–CF$_2$– dipoles and the π-electron cloud of the aromatic ring and/or iodine present in the [CdI$_2$-INH=CMe$_2$] structure. These two significant interactions trigger the proper chain orientation in the PVDF@MOF films which leads to enhanced electroactive phase (i.e., β and γ). The band broadening is associated with the change in microenvironment of the particular vibrational band. The hydrogen bonding interaction and dipole-dipole interaction also influence the stretching vibrations of –CH$_2$– dipoles of PVDF resulting in the frequency shifting towards lower regions of CH$_2$ symmetric and asymmetric vibrational modes in the frequency region of 3060−2940 cm^{-1} in PVDF@MOF films in comparison to the Neat PVDF film, as shown in the Figure 3.9(c). Furthermore, the dipole moment of –CF$_2$– dipoles are comparatively higher than that of –CH$_2$– dipoles due to the electronegativity difference between C, F and H atoms. So, there may be an interaction present between PVDF molecular chains, which results in self-oriented/self-poled PVDF chain in all-trans manner in association with PVDF-MOF interaction [67-68]. A schematic is provided in Figure 3.10(c) to illustrate these interfacial interactions between PVDF and MOF moiety. It is also noticed that degree of crystallinity (χ_c) of the PVDF@MOF composite films are improved in comparison to the Neat PVDF film. The curve deconvolution of XRD pattern (Figure 3.11) is clearly demonstrating the presence of polar β and γ and nonpolar α phases as well as the quantification of χ_c. The degree of crystallinity (χ_c) is calculated using the following equation,

$\chi_c = \frac{\sum A_{cr}}{\sum A_{cr} + \sum A_{amr}} \times 100\%$, where, ΣA_{cr} and ΣA_{amr} epitomise the summation of the whole integral areas corresponding to the crystalline peaks and amorphous halo, respectively [6]. Likewise, individual phase crystallinity is also possible to estimate using the following equations.

$$\chi_{C\beta} = \chi_C \times \frac{\sum A_\beta}{\sum A_\beta + \sum A_\gamma}$$

$$\chi_{C\gamma} = \chi_C \times \frac{\sum A_\gamma}{\sum A_\beta + \sum A_\gamma}$$

where, ΣA_β and ΣA_γ are the total integral intensities (area) under crystalline $\beta-$ and $\gamma-$ phases, respectively.
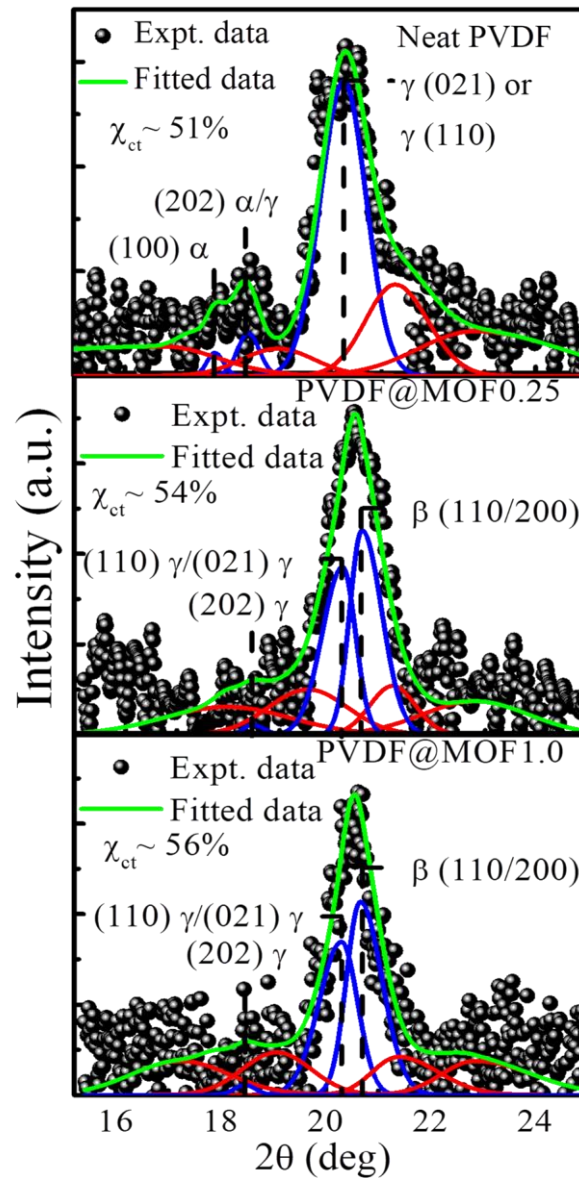
Figure 3.11 The curve deconvolution of the XRD pattern in the 2θ range of 15-25°. The scattered dotted points and solid line represent the experimental data and the best fit respectively. The total degree of crystallinity of each sample is also mentioned in the figures.

Figure 3.11 (upper part) clearly depicts that the Neat PVDF film consists of the diffraction peaks related to α–crystalline phases, which are located at 17.6^o (100), 18.2^o (202) and these nonpolar phases are totally contracted in the hybrid PVDF@MOF films (i.e.,0.25 and 1 wt% [CdI$_2$-INH=CMe$_2$] incorporated PVDF ferroelectret films) [6, 23]. Moreover, the Neat PVDF film predominantly consists of semi-polar γ–phase as evidenced from strong diffraction peak at 20.3^o (021) and overlapped diffraction peak at 18.2^o (202) [61-63, 65]. The addition of [CdI$_2$-INH=CMe$_2$] single crystalline MOF filler subsequently decreases the content of γ–crystalline phase (evidenced from the reduced peak area appeared at 20.3^o) and enhances the β–crystalline part (as manifested from the strong diffraction peak at 20.8^o) as depicted in Figure 3.11. In conjugation, these two phases give rise to a sharp peak at 20.5^o [6]. The XRD results evidently support the outcomes obtained from the FT-IR spectra (Figure 3.7(a)). Therefore, it can be concluded that, the dipole-dipole interaction and hydrogen bonding present between different functional groups and π–electron clouds of [CdI$_2$-INH=CMe$_2$] MOF with the –CH$_2$–/–CF$_2$– dipoles of PVDF chain tend to nucleate the polar β– and γ–phases by converting *TGTG′* conformation into *all-trans* (*TTTT*) conformation.

3.3.5 DSC Thermograms

Eventually, thermal properties of the PVDF@MOF composite films were also improved. It can be clearly concluded from the heating and cooling cycle of DSC thermograms (the melting and crystallization temperature) of Neat PVDF and PVDF@MOF composites provided in Figure 3.12(a and b) respectively. As the concentration of [CdI$_2$-INH=CMe$_2$] increases, the melting temperature gradually shifted to lower temperature side. The Neat PVDF film predominantly consists of α– and γ–phases, which is confirmed from FT-IR and XRD studies. The melting endothermic peak for Neat PVDF film arises at 171 ^{o}C, which is accredited to the superposition of the α and γ melting peaks.
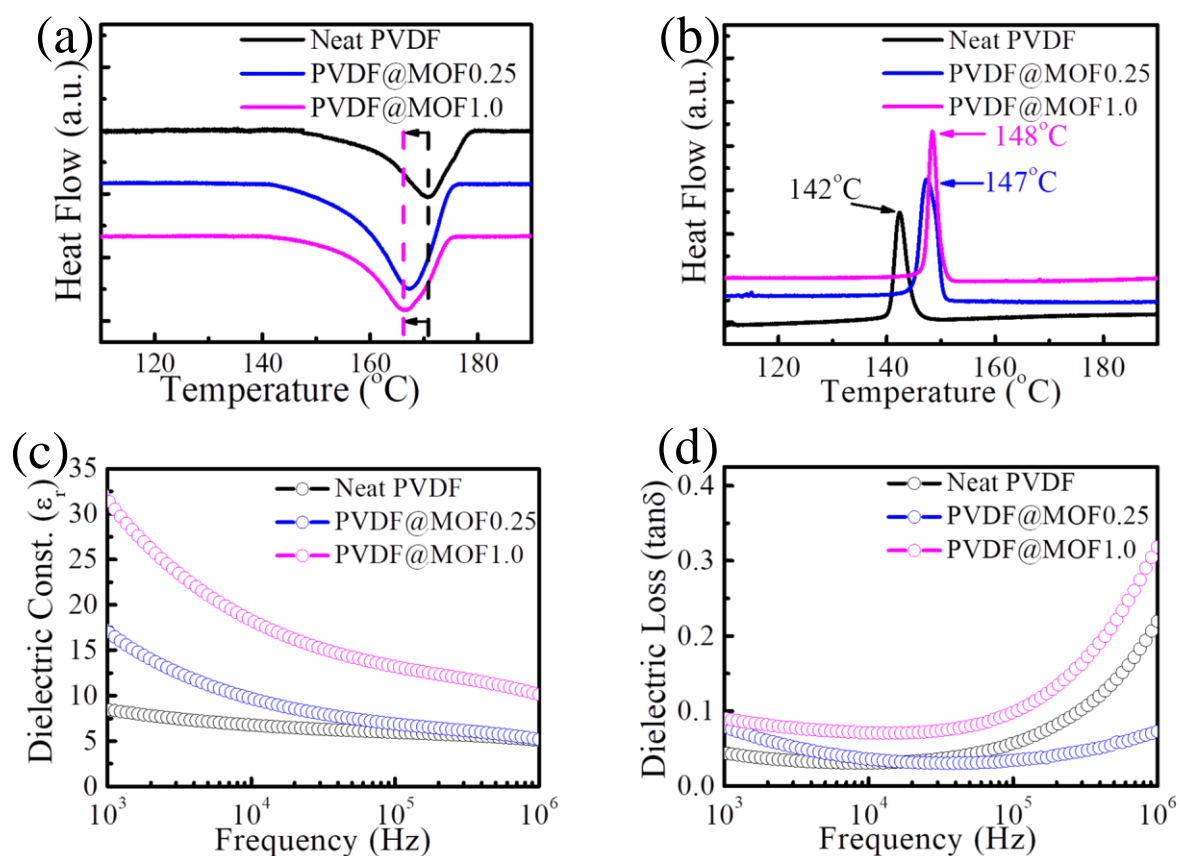
Figure 3.12 DSC thermograms of the (a) 1st heating (melting) and (b) cooling (crystallization) cycles, frequency dependent (c) dielectric constant (ε_r) and (d) dielectric loss (tanδ) of the Neat PVDF and PVDF@MOF composite films.

However, in case of PVDF@MOF0.25 and PVDF@MOF1.0 films, the melting peak arises at 168 °C and 166 °C respectively, which is well below than combined melting peaks of α and γ phases appeared in Neat PVDF. The input of [CdI$_2$-INH=CMe$_2$] particle in the PVDF matrix diminishes the α−phases, as a result, the preferential growth of electroactive β−phase takes place. The growth of β−phase is more prominent compared to γ−phase (refer to Table 3.3). It is noteworthy to mention, since β−phase has a comparatively lower melting temperature compared to α−phase, the melting endothermic peak appeared at lower temperature in PVDF@MOF composite films than that of Neat PVDF film, which ensures the presence of enriched β−phase in composite films [23].

Moreover, crystallization temperature shows notable variation towards higher temperature region upon [CdI$_2$-INH=CMe$_2$] MOF addition into PVDF matrix, that indicates the role of 3D-MOF as a heterogeneous nucleating agent during the non-isothermal cooling process [41].

3.3.6 Dielectric Properties

The combined improvement of electroactive phase content and degree of crystallinity coupled with porous morphology significantly increases the dielectric constant of the PVDF@MOF composite based ferroelectret films, which can be clearly observed from the frequency dependent dielectric study demonstrated in Figure 3.12(c and d). The dielectric constant (ε_r) of the composite films gradually increases with increasing concentration of [CdI$_2$-INH=CMe$_2$] into PVDF matrix (Figure 3.12(c)). It reached a maximum value, for example, $\varepsilon_r \sim$ 32 at 1 kHz is found in PVDF@MOF1.0 film, which is almost 4 times higher compared to the Neat PVDF film ($\varepsilon_r \sim$ 9 at 1 kHz). However, a very minor change in dielectric loss (tan$\delta \sim$ 0.09 in PVDF@MOF1.0 film and tan$\delta \sim$ 0.05 in Neat PVDF film) at 1 kHz is noticed from Figure 3.12(d). The improved dielectric constant of the PVDF@MOF composite films can be observed throughout the entire frequency range. But it decreases as the frequency shifts from 10^3 Hz to 10^6 Hz, which is because of the reduction of polarization contribution. The entire observation attributes to the frequency dependence of dielectric constant for the PVDF@MOF films. There are several parameters which might collectively increase the dielectric constant of composite films: i) effect of self-poled orientation of the PVDF chain (electroactive β−phase content); ii) the hydrogen bonding effect between the different functional moieties of [CdI$_2$-INH=CMe$_2$] MOF and PVDF dipoles iii) the micropores of the PVDF@MOF composite ferroelectret film (as evidenced in Figure 1e) behave as microcapacitors and iv) Maxwell-Wagner-Sillars polarization due to the large internal interface of the composite polymer electret dielectric [36, 41]. Moreover, the

improved dielectric property renders the charge leakage during mechano-electrical conversion process from piezoelectric based MEH. Thus, PVDF@MOF1.0 porous ferroelectret film has been chosen for the fabrication of MEH to explore the energy harvesting performance.

3.3.7 Piezoelectric Performance
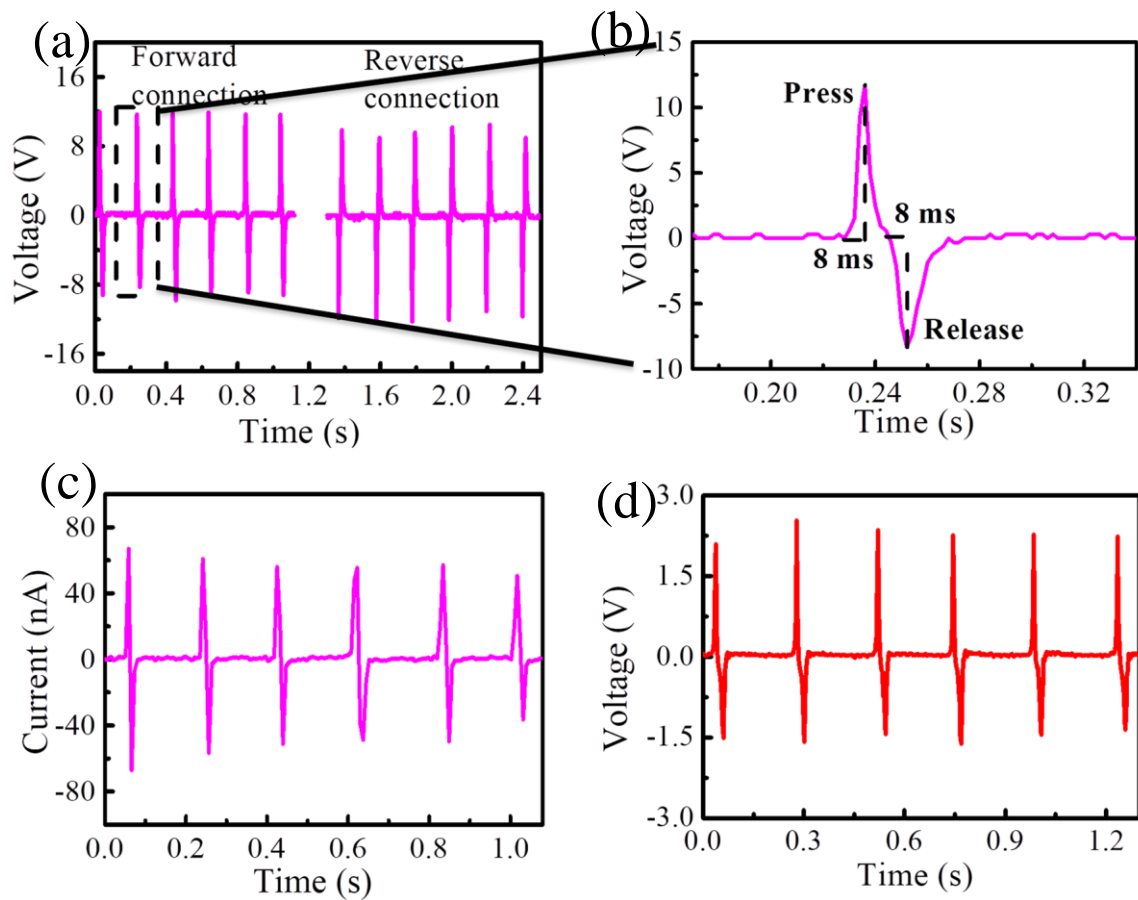
Figure 3.13 (a) Open-circuit voltage of the MEH in forward and reverse connection under continuous hand imparting. (b) Enlarged view of single peak in forward connection representing the response time. (c) Short-circuit current of the MEH during continuous pressing by hand. (d) Open-circuit voltage of the Neat PVDF-EH under repetitive hand imparting where 10 kPa of stress amplitude are employed.

In this context, an open-circuit voltage (V_{oc}) and short circuit current (I_{sc}) of 12 V and 60 nA (Figure 3.13(a and c) respectively) are measured when the MEH is subjected to a vertical

stress amplitude of 10 kPa during repetitive press-release condition by a bare hand wrapped with a polyethylene glove. Most importantly, a very fast response time (t_r) of 8 ms is recorded as shown in Figure 3.13(b), which is 12.5 times superior to nanohybrid PVDF in a previous report [69]. So, the rapid release of electrons led to lower value of t_r that induce the significant output voltage (V_L) and current (I) response and the fast response time t_r is beneficial to build high performance pressure sensors.

In addition to the fast response time, the magnitude of piezoelectric coefficient (d_{33}) of the ferroelectret film is evaluated using the following equations, $d_{33} = \frac{Q}{F}$ and $Q = \int_{t_1}^{t_2} I_{sc} dt$ where Q and I_{sc} are generated charge and short-circuit current amplitude under the applied force (F) of 4 N, t_1 and t_2 are the current limits to estimate Q [70-72]. Interestingly, the magnitude d_{33} of PVDF@MOF1.0 film is found to be 143 pC/N which is almost 5 times improved value than uniaxial stretched and poled PVDF film [73]. This increment is mainly due to the high content of piezoelectric β–phase as well as the electret micro-dipoles, both arise due to the presence of [CdI$_2$-INH=CMe$_2$] MOF in the PVDF matrix. In contrast, the recorded V_{oc} of Neat PVDF-EH is 2.5 V under the same condition (Figure 3.13(d)), which is attributed to the presence of semipolar electroactive γ–phase. To confirm that the output voltage truly arises from the PVDF@MOF1.0 film, a switching polarity test was carried out (corresponding forward and reverse connection related responses are shown in Figure 3.13(a)). Subsequently, it also proves that the generated signal is truly piezoelectric where the effect due to contact electrification is not participating. Furthermore, instantaneous voltage drop (V_L) of the MEH was measured as a function of externally connected load resistance (R_L) to investigate the effective output power. As seen in Figure 3.14(a), the output voltage (V_L) steadily increases with increasing load resistance (R_L) and finally reached the open-circuit voltage at infinitely high resistance of 40 MΩ. Thus, the maximum instantaneous output power density of 32 μW/cm^2 has been attained from the MEH at a R_L of 1 MΩ during
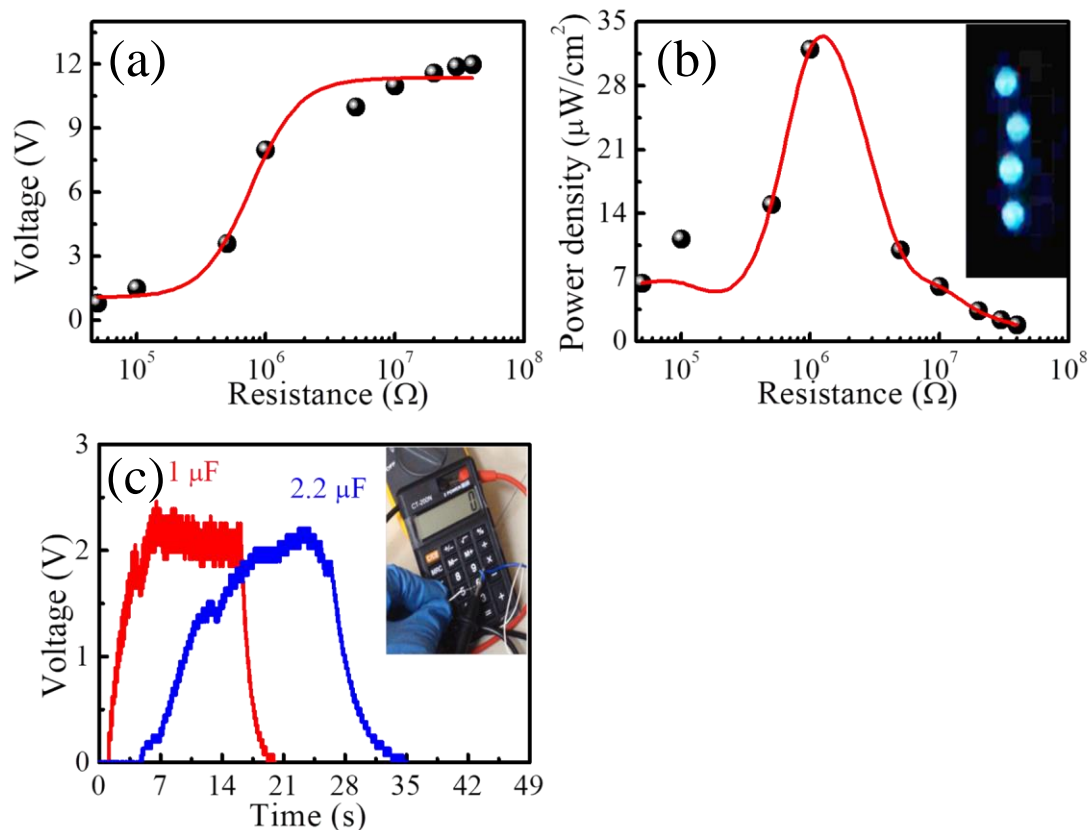
Figure 3.14 The variation of (a) output voltage and (b) instantaneous output power density of the MEH as a function of increasing load resistance ranging from 50 kΩ to 40 MΩ. The inset shows the charging up of 4 LEDs connected in series by the MEH. (c) Capacitor (1 and 2.2 µF) charging performance of the MEH with an added advantage of powering up calculator during discharging of 1 µF capacitor (in the upper inset).

repetitive hand imparting (Figure 3.14(b)). The effective output power density is quantified using the following equation, $P = \frac{1}{A}\frac{V_L^2}{R_L}$, where A is the effective electrode area and V_L signifies the voltage drop across R_L. The superior piezoelectric power density of the MEH is sufficient to turn on several blue LEDs without the need of any external storage system (inset of Figure 3.14(b)). In order to provide a potential application of fast charging and energy storage, the MEH was connected to two capacitors (1 µF and 2.2 µF) individually via a full wave bridge rectifying circuit. It was noticed that the 1 µF and 2.2 µF capacitors were easily

charged up and gained the steady state within a very short range of time of 20 and 35s respectively (Figure 3.14(c)) during the application of periodic vertical stress (10 kPa) on the MEH surface. The stored energy density inside the capacitors during this procedure can be calculated from the following equation: $E = \frac{CV^2}{2A}$. The stored energy density (1.44 μJ/cm^2) in 1 μF capacitor was further used to drive a commercial calculator, as shown in the inset of Figure 3.14(c). Therefore, it is evident from the short time capacitor charging performance that the power generator is a promising candidate to power up tiny portable electronic gadgets.

3.3.8 Mechanism of Energy Harvesting

Actually, the porous film originates giant micro-sized dipoles in association with the intrinsic self-polarized behaviour of the PVDF@MOF composite ferroelectret film. A schematic illustration is provided in Figure 3.15 to describe how the micro-dipoles affect the overall piezoelectric energy harvesting property of the composite ferroelectret film.
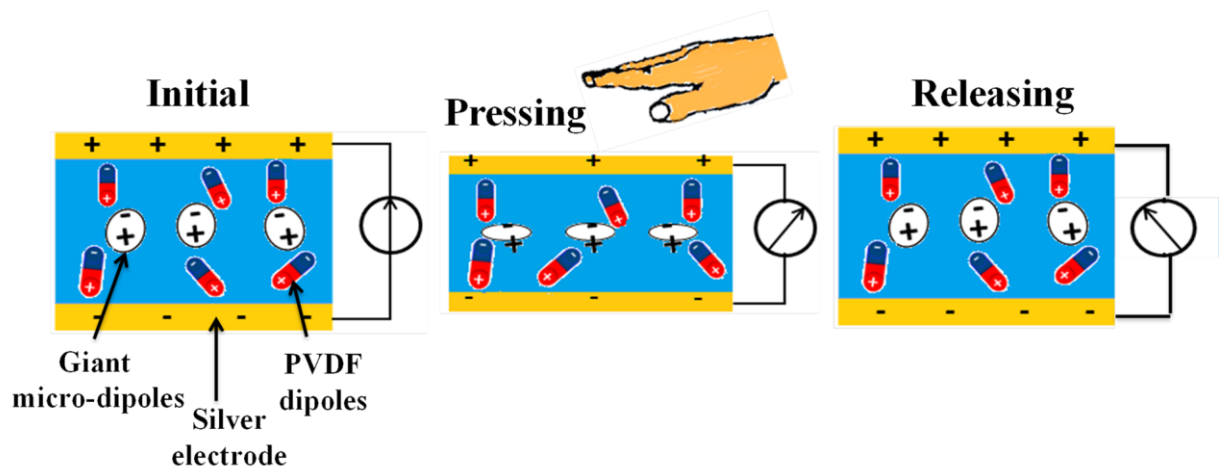
Figure 3.15 The schematic illustrates the working mechanism of the MEH under repetitive hand imparting.

The crystalline [CdI$_2$-INH=CMe$_2$] MOF is homogeneously dispersed within the PVDF matrix (as noticed in cross-sectional FE-SEM image, shown in Figure 3.4(e) and the

elemental mapping of components present in the MOF, such as Cd, I, N, O illustrated in Figure 3.5(a to f) respectively). Owing to different interactions present between PVDF and [CdI$_2$-INH=CMe$_2$], the dipoles within PVDF chains are self-oriented (as shown in Figure 3.10(c)). In addition, electrons are delocalized in the skeleton of [CdI$_2$-INH=CMe$_2$] MOF. So, the incorporated MOF acts as charge trapping as well as charge carriers. It also reduces the need for charge injection to prepare electret film [37, 41]. Moreover, charges can also be trapped at the adjoining crystalline/amorphous regions in case of semi-crystalline polymers. Due to the homogeneous distribution, MOF particles are also present in the vicinity of the pores. The cumulative effect of self-orientation/self-polarization of PVDF dipoles and the presence of MOF particles in the inner surface of the pores (as charge carriers) creates the charge separation between upper and lower part of the pore, which is further stabilised by the self-induction effect of the induced self-oriented electroactive β− and γ−phases. Each charge separated micro-void is termed as giant micro-sized dipole and the porous dielectric material is termed as hetero-charged ferroelectret. When the MEH is subjected to an axial compressive stress, the micro-cavities are squeezed and the distance between the upper and inner surface of the voids get contracted. As a result, the giant micro-dipoles along with the self-polarized interfacial nano-scale dipoles of β− and γ−crystals are deformed. Thus, an enhanced piezoelectric potential difference is created between the top and bottom electrodes. In addition, the vertical compressive stress on MEH creates a potential in the hybrid material, which further accelerates the chain orientation in all-trans manner via stress induced polarization [6]. As an outcome, the free electrons are forced to flow through the external circuit to the MEH to balance the generated potential change on the MEH, which enables the generation of positive peak of output voltage (V_{oc}) as well as output current (I_{sc}). When the applied vertical stress is released, a reverse mechanism is occurred. The MEH recovered its original state and the accumulated electrons go back through the external circuit. As an

outcome, V_{oc} shows a transient peak in opposite direction with comparatively lower amplitude than the positive peak due to the damping effect occurring when the device regaining its original structure after removal of stress. Besides that, I_{sc} shows a negative peak with lower discrepancy in amplitude compared to the voltage peak [36].

3.3.9 Theoretical Analysis of Energy Harvesting
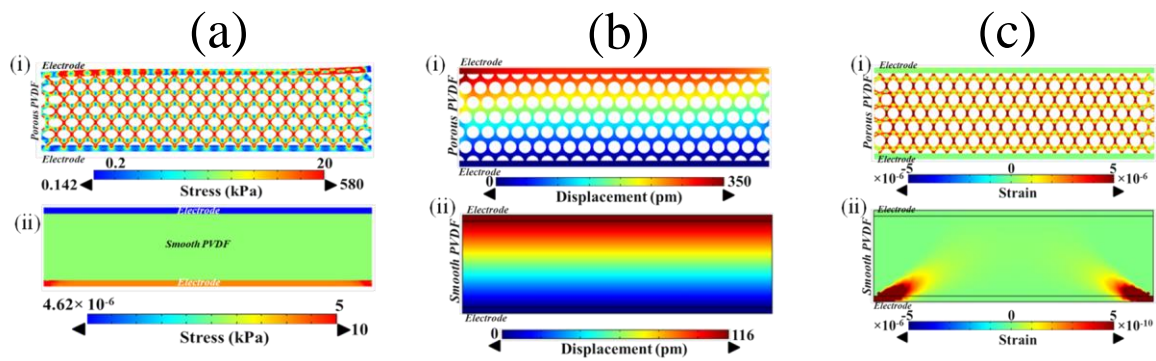
Figure 3.16 Finite element method (FEM) based simulation on (a) generated stress, (b) displacement and (c) generated strain of the PVDF@MOF composite ferroelectret and Neat PVDF film under stressed condition of 10 kPa.

To understand the role of porosity in ferroelectret structure in comparison to the Neat PVDF smooth film, a finite element method (FEM) based analysis, where it is found that the confinement and amplification of applied stress, strain and thus displacement is much superior due to void structure (Figure 3.16). In order to understand the enhanced energy harvesting performance of the PVDF@MOF ferroelectret in comparison to smooth Neat PVDF film, FEM based simulation has been performed under 10 kPa of pressure. In this simulation, experimentally obtained engineered porous structure of 2 μm diameter and 0.4 μm of inter-pore distance were considered. Interesting fact is that applied stress is confined and enhanced within the inter-pore region as shown in Figure 3.16(a(i)). In contrast, no such confinement and enhancement was observed in case of smooth PVDF film Figure 3.16(a(ii)).

For example, in smooth Neat PVDF film the applied stress of 10 kPa is quickly dissipated from upper electrode to lower electrode, but for porous PVDF film, the stress is enhanced to 580 kPa due to confinement within inter-pore region. As a result, porous PVDF@MOF composite ferroelectret experiences higher displacement of 350 pm (Figure 3.16(b(i))) in comparison to smooth PVDF film (~ 116 pm) (Figure 3.16(b(ii))). Furthermore, due to stress confinement and enhancement, a substantial improvement in strain confinement within inter-pore region followed by enhancement of 5×10^{-6} has been observed for porous PVDF film (Figure 3.16(c(i))) which is higher than that of smooth PVDF film (~5×10^{-10}) (Figure 3.16(c(ii))). As a matter of fact, generated stress and strain are uniformly distributed within porous PVDF composite film which is not observed in case of smooth PVDF film. Rather, stress and strain are quickly transmitted to the lower electrode region and concentrated in the interface region of lower electrode and lower portion of PVDF film which is not helpful for overall deformation and electricity generating performance of the PVDF film. Therefore, it is very evident that energy harvesting performance of the device is largely modulated by engineered porous structure obtained by 3-D MOF material.

3.3.10 Mechano-sensitivity Test

To evaluate the applicability of the MEH as a sensitive pressure sensor, some experiments were carried out on porous ferroelectret MEH. Firstly, different sized leaves of different weights (ranging from 12 mg to 479 mg) were dropped upon the MEH from a particular height (3 cm). Significantly, the MEH can detect as low as 0.8 Pa corresponding to the leaf of 12 mg. Figure 3.17(a) and 3.17(b) show that the generated output voltage approaches linearity with respect to the increased external impact and MEH exhibits a mechano-sensitivity of 8.6 V/kPa in a pressure region up to 35 Pa. The mechano-sensitivity (S) can be estimated by calculating the change of voltage (ΔV) on the basis of applied pressure change (ΔP), as $S = \frac{\Delta V}{\Delta P}$. To estimate the mechano-sensitivity of the MEH in a wide pressure range,
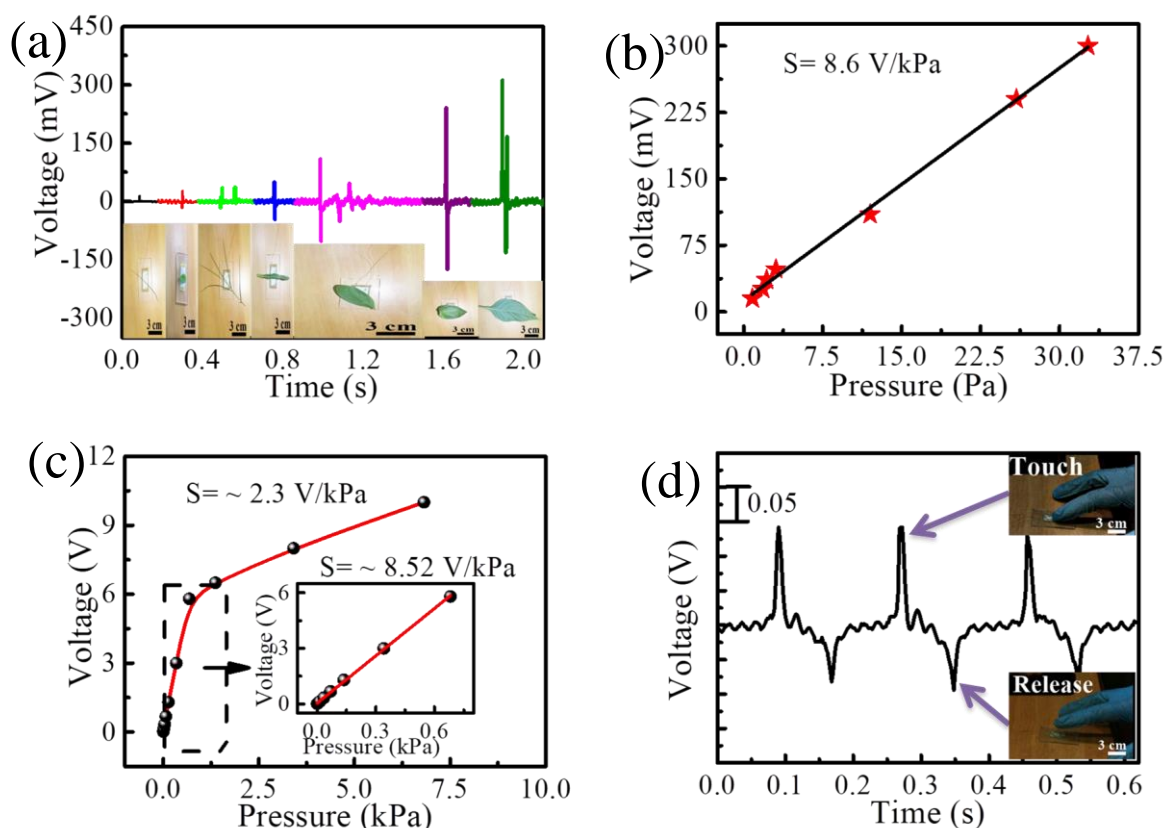
Figure 3.17 (a) The output voltage responses during different types of leaves falling from same height on the upper surface of the MEH. (b) The output voltage shows linear behaviour with respect to the applied stress exerted by different leaves. (c) The generated output voltage as a function of pressure when different weights from an analytical weight box (ranging from 10 mg to 100 g) dropping on the upper surface of the MEH from a particular distance 3 cm. The inset shows the linear variation of voltage up to 1 kPa pressure. (d) The ultra-touch (by finger) response obtained from the MEH.

another experiment was performed, where different weights (ranging from 10 mg to 100 g from an analytical weight box) were dropped upon the MEH from a fixed distance of 3 cm. The MEH produced distinct voltage signals corresponding to different weights (Figure 6c). As seen in the inset of Figure 3.17(c), the MEH exhibited a high mechano-sensitivity of 8.52 V/kPa in a low pressure region up to 1 kPa. In addition, the voltage-pressure relationship

maintains linearity in this pressure region. The mechano-sensitivity significantly reduces to 2.3 V/kPa in the higher pressure region (>1 kPa). It is possibly due to the theoretical limits of effective strain in piezoelectric materials in the high-pressure region [74]. Moreover, our device managed to detect as low as 0.75 Pa pressure in this experiment. These two experiments indicate its very low pressure detection limit (<1 Pa) as well as its wide range of pressure sensing. The mechano-sensitivity of our MEH/sensor is relatively high compared to some previous works on piezoelectric and ferroelectret materials [74-78]. In addition, our device shows remarkable response towards ultra-touch by finger on the top of the MEH (Figure 3.17(d)). A comparison is presented in Table 3.4, indicating the advantage of PVDF@MOF composite ferroelectret with respect to the reported PVDF and its co-polymer based ferroelectret as energy harvester and pressure sensor.

Owing to its high mechano-sensitivity, MEH can be used as a wearable pressure sensor. Most of the human activities are considered in this pressure regime. Especially skin related movements, swallowing, coughing, speech signal, arterial pulse involve subtle to moderate pressure change.

Table 3.4. Comparison of overall performance of PVDF@MOF based MEH with reported PVDF and its co-polymer based ferroelectrets.

	Nano Lett. **2011**, 11, 5142	*Adv. Energy Mater.* **2014**, 4, 1301624	*Mater. Chem. Phys.* **2017**, 186, 327	*J.Mater. Chem. A* **2017**, 5, 189	*Phys. Chem. Chem. Phys.* **2015**, 17, 7275	**Our work**
Preparation method	ZnO nanowires template assisted method	ZnO nanoparticle etched sponge like PVDF	Solution casting with ZnO NP etching, active material P(VDF-	Solution casting with polyelectrolyte nafion solution	Solution casting with hygroscopic Mg salt	Solution casting, 3D MOF assisted PVDF

118

		HFP)				
Poling	Electric field of 60V/μm applied for 1 h	Electric field of 60V/μm applied for 1 h in an oil bath	Self-poled	Self-poled	Self-poled	Self-poled
Output voltage	2.6 V	11 V	9V	7.4 V	~8 V	12 V
Input stimuli	sonic wave, 100dB, 100 Hz	Not given	0.36 MPa	60 N	Not given	10 kPa
Power	0.17 mW/cm^3	0.16 mW/cm^3	1.21 mW/cm^2	14.6 V/cm^2	58.8 nW,	32 μW/cm^2
d_{33} (pC/N)	32.5	Not given	15.2	Not given	Not given	143
Pressure sensitivity	Not given	Not given	1 μV/Pa.	Not given	Not given	8.52 V/kPa
Application	Sonic wave driven piezoelectric nanogenerator	Integratable nanogenerator system (driven by surface oscillation)	self-powered wireless sensor for detecting the subtle pressure and some weak human activities	self-powered piezoelectric energy harvester	Piezoelectric energy harvester with LED and capacitor charging	Healthcare monitoring with wireless data transmission, operation of consumer electronics

3.4 Applications

3.4.1 Self-Powered Physiological Signal Monitoring

To monitor the high mechano-sensitivity of MEH towards subtle motions near the human skin, the device is attached to the throat of an adult male using an adhesive tape. As shown in Figure 3.18a and 3.18c, the MEH is able to recognise speech signal. During the pronunciation of three alphabetic characters of "M", "O" and "F", the device was exposed to the volunteer's voice vibration. As a result, MEH can sense the delicate pressure change induced by the complex muscle movement around the throat during phonation. Noticeably, three distinct
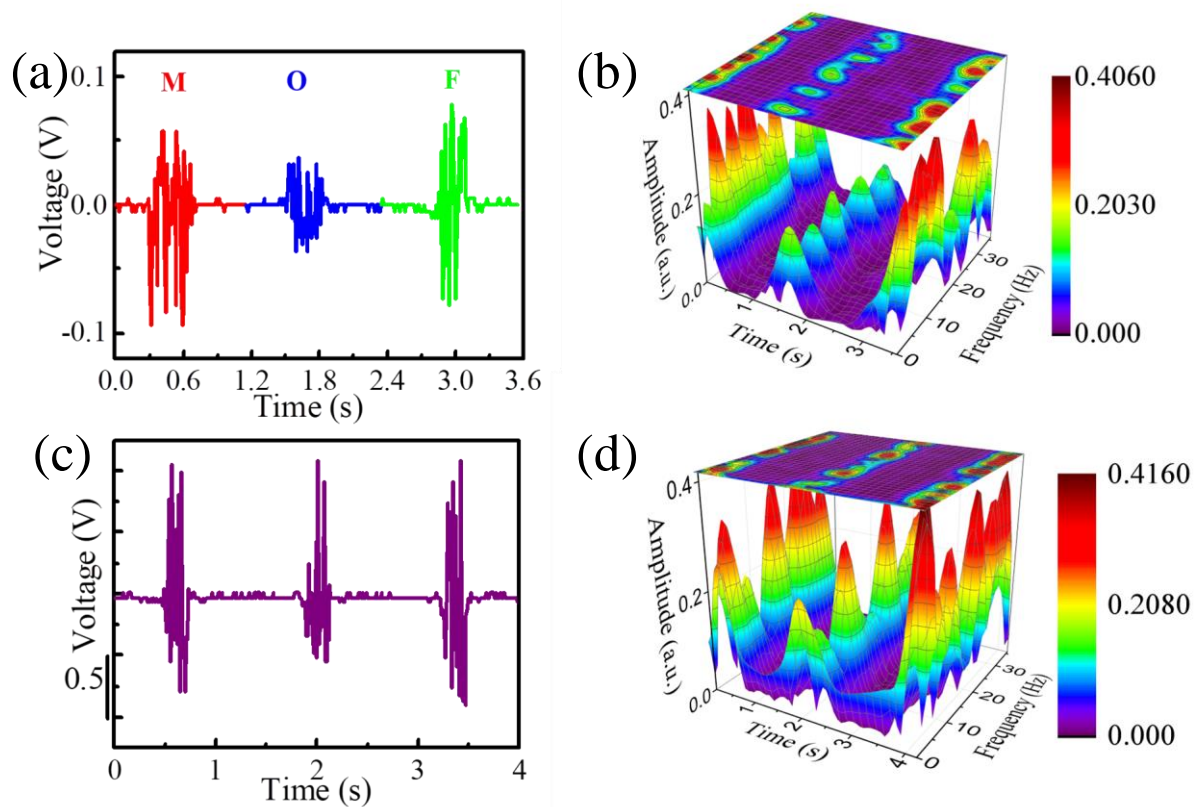
Figure 3.18 Application of MEH in different human physiological signal monitoring during (a) pronunciation of different alphabets "M", "O", "F" along with (b) STFT processed 3D spectrogram and (c) speaking of word "MOF" repeatedly with its (d) STFT processed 3D spectrogram.

output patterns associated with the three letters have been appeared, as shown in Figure 3.18(a). The short time Fourier transform (STFT) processed spectrogram is depicted in Figure 3.18(b) in order to reveal the corresponding frequency distribution of the pronounced three letters. In addition, the volunteer was asked to pronounce a word "MOF" repeatedly and the MEH shows excellent repeatability by generating characteristic waveform of the pronounced word (Figure 3.18(c)). The STFT processed 3D spectrogram (Figure 3.18(d)) also reveals four or five distinct phases during pronunciation of the word. Thus, MEH might have the potential to be applied as a mechano-acoustic sensor in speech rehabilitation training,
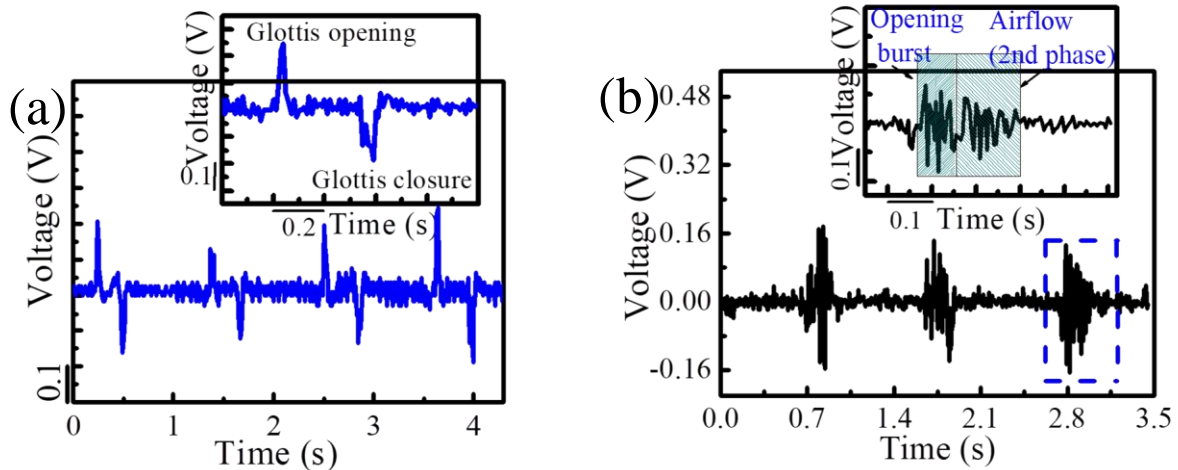
Figure 3.19 (a) Response curve during continuous swallowing (enlarged view of one single waveform) and (b) coughing signal with magnified view of one single coughing action in the upper inset.

national security sector and even healthy or unhealthy situation recognition. In addition, the MEH enables to monitor the gulping (swallowing) related movements and the corresponding reproducible waveforms are presented in Figure 3.19(a). Actually, the swallowing gesture follows the mechanism of upward and downward motions of thyroid cartilage associated with the Laryngeal prominence (the Adam's apple). When the MEH was attached to the tester's throat, glottis opening and closure behaviour were precisely identified through identical voltage generation, as shown in the upper inset of Figure 3.19(a). Therefore, the device can be used in clinical assessment of swallowing disorders such as dysphagia, odynophagia and early detection of sudden infant death syndrome (SIDS) in sleeping infants. Furthermore, the MEH can non-invasively sense the thoracic pressure developed due to the vocal cord vibration during repeated coughing actions, as presented in Figure 3.19(b). The magnified view of one single coughing action (upper inset of Figure 3.19(b)) shows that the device can also distinguish different phases of cough such as, initial opening burst, secondly a blaring air flow followed by a final glottis closure [79, 80]. In addition, the waveform and the frequency band of a bronchitis patient must be different, which might be examined by our MEH based

sensor. Thus, it can be used as a vibro-tactile sensor in the clinical diagnosis of chronic obstructive pulmonary diseases such as, asthma, bronchitis etc.

3.4.2 Wrist Pulse Monitoring and Wireless Application
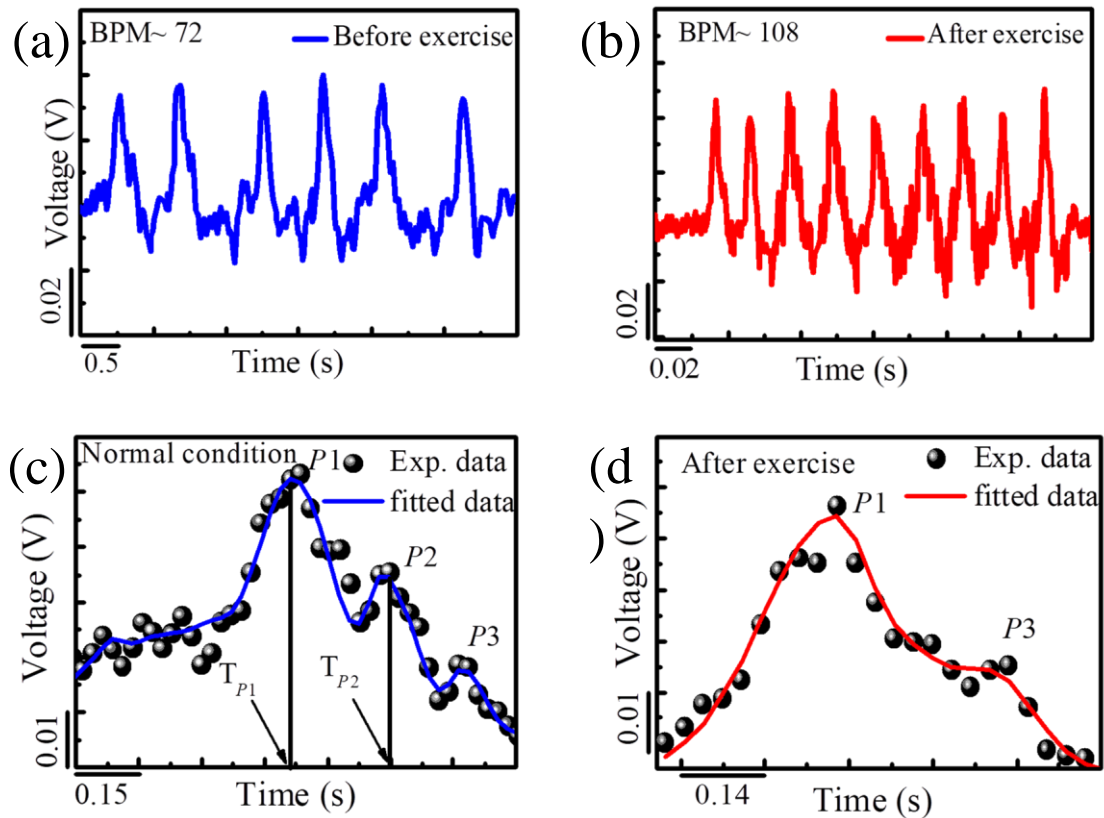
Figure 3.20 The voltage outputs during real-time wrist pulse monitoring in (a) normal condition and (b) after exercise condition. The enlarged view of one single pulse waveform during (c) normal condition and (d) after exercise.

Owing to its high sensitivity towards subtle pressure changes, the MEH was attached to the wrist of a male adult to capture real time arterial wrist pulse induced by heart beats at the wrist. Since, wrist pulse is among the vital physiological markers, which is useful in determining heart rate and arterial blood pressure as well as different cardiovascular diseases through constant monitoring, so the detection of such vital signal in non-invasive mode is always beneficial for health care sector. As shown in Figure 3.20(b), the intensity and

122

frequency of the wrist pulse increased significantly after exercise (100 beats/minute (BPM)) compared to the normal condition (78 beats/minute [BPM]) (Figure 3.20(a)). It is due to the increased rate of heart pumping to maintain the oxygen supply delivered to muscles during the exercise. It is noteworthy to mention that the MEH can detect and differentiate the arterial wrist pulse between the normal and exercise situation with excellent repeatability. The magnified waveform of one single peak (before exercise) clearly exhibits three distinct characteristic peaks such as, early systolic pressure peak ($P1$), late systolic pressure peak ($P2$) and early diastolic pressure peak ($P3$) respectively, as shown in Figure 3.20(c), whereas, only 2 peaks ($P1$ and $P3$) are obtained after exercise (Figure 3.20(d)). These three peaks are very essential to derive some commonly used health monitoring parameters namely the radial augmentation index, $AI_r = {P2}/{P1}$, the time delay between $P1$ and $P2$, $\Delta T = T_{P2} - T_{P1}$ and the diastolic augmentation index, $DAI = {P3}/{P1}$ [74]. In addition, these parameters and peaks provide important physiological information such as arterial stiffness, coronary artery disease, left ventricular load, vascular aging, myocardial infraction. The calculated values of these parameters are $AI_r = 0.55$, $\Delta T = 0.24$s at normal condition, which are characteristic values for a healthy person. Thus, our device might be useful in clinical diagnosis of health issues related to heart and hypertension through continuous monitoring of pulse, pulse frequency and associated pulse waveforms [74].

In addition, a wireless circuit system was built to transmit the wrist pulse waveform to a smart phone using an Arduino microcontroller unit (MCU) prototyping platform (Arduino UNO R3 ATMEGA 328P) to meet the increased demand for real-time personalized remote health monitoring. A block diagram of the total feature is given in Figure 3.21(a). As shown in Figure 3.21(b), the wireless signal transferring unit consists of power converter, a data conversion control module, a signal acquisition-amplification module, and wireless data transmission system (bluetooth module) for wireless data transmission. The bluetooth module
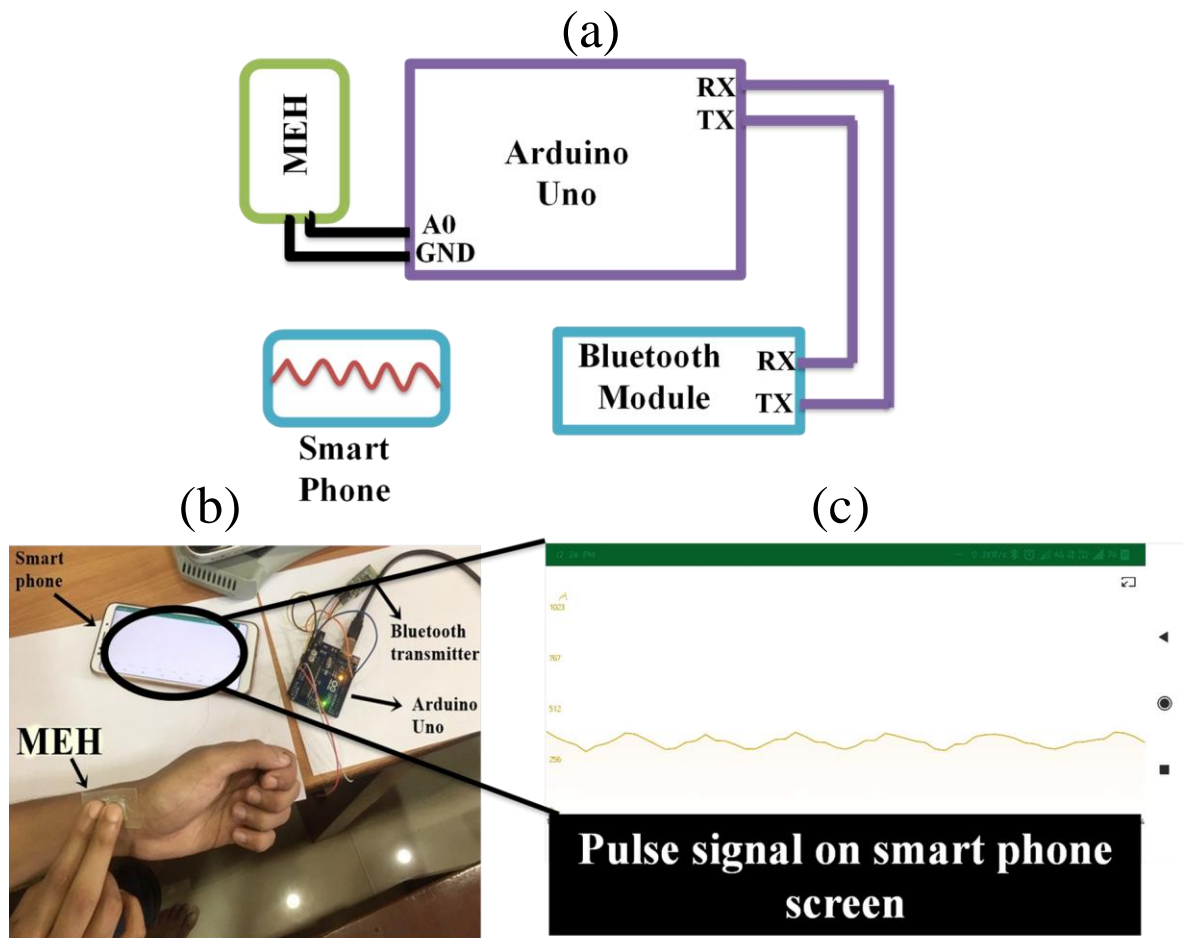
Figure 3.21 (a) Block diagram of the Bluetooth module attached MEH for wireless wrist pulse monitoring. (b) Photograph of wireless pulse detecting and transferring from MEH to a smart phone. (c) A magnified view of the smart phone screen is illustrating the wrist pulse signal.

was connected with the MEH. The signal acquisition and communication model receives the wrist pulse signal through our device when it is subjected to subtle pressure change. Then, it is amplified and the enlarged analogue signals are converted to digital signals by data conversion control module and the Bluetooth module transfers the data to the android phone. As an outcome, the wrist pulse signal can be displayed on the screen of the smart phone as depicted in Figure 3.21(c).

These results clearly indicated its wide potential application towards personalized non-invasive physiological signal monitoring.

3.5 Conclusion

In summary, we followed a simple facile pathway for synthesizing a cadmium metal centred 3D porous MOF ([CdI$_2$-INH=CMe$_2$]) where isoniazid moieties serve as organic struts. On account of its highly porous structure, a MOF derived porous ferroelectret PVDF film (PVDF@MOF) with its mechanical energy harvesting application is demonstrated because of the high yield of electroactive phase formation. The MEH shows superior piezoelectric output performance (open circuit voltage of 12V and maximum output power of 32 μW/cm^2) where traditional electrical poling step is completely avoided. On the other hand, the effect of stress-strain confinement in the porous structure on the mechano-electrical performance of the MEH was further investigated by FEM simulation method. In addition, MEH exhibits ultra-high mechano-sensitivity (8.52 V/kPa) as well as very low pressure detection limit of <1Pa. The high mechano-sensitivity of MEH was further used to detect different physiological activities and vital signals attached to desired body parts. Most importantly, using its capability to detect wrist pulse, a wireless wrist pulse detection and transmission module was established for remote health monitoring. Owing to its multidimensional pressure sensing ability, the MEH proves itself to be a promising candidate for auto-powered electronics, real time wearable medical devices and artificial intelligence.

3.6 References

1. Kim, D. H.; Lu, N.; Ma, R.; Kim, Y. S.; Kim, R. H.; Wang, S.;Wu, J.; Won, S. M.; Tao, H.; Islam, A.; Rogers John, A. Epidermal Electronics. *Science* **2011**, *333*, 838−843.

2. Chen, X.; Tian, H.; Li, X.; Shao, J.; Ding, Y.; An, N.; Zhou, Y. A High Performance P(VDF-TrFE) Nanogenerator with Self-Connected and Vertically Integrated Fibers by Patterned EHD Pulling. *Nanoscale* **2015**, *7*, 11536−11544.

3. Bowen, C. R.; Kim, H. A; Weaver, P. M.; Dunn, S. Piezoelectric and Ferroelectric Materials and Structures for Energy Harvesting Applications. *Energy Environ. Sci.* **2014**, *7*, 25−44.

4. Hu, Y.; Wang, Z. L. Recent Progress in Piezoelectric Nanogenerators as a Sustainable Power Source in Self-Powered Systems and Active Sensors. *Nano Energy* **2015**, *14*, 3−14.

5. Zhou, Y.; He, J.; Wang, H.; Qi, K.; Nan, N.; You, X.; Shao, W.; Wang, L.; Ding, B.; Cui, S. Highly Sensitive, Self-Powered and Wearable Electronic Skin Based on Pressure-Sensitive Nanofiber Woven Fabric Sensor. *Sci. Rep.* **2017**, *7*, 12949−12957.

6. Roy, K.; Ghosh, S. K.; Sultana, A.; Garain, S.; Xie, M.; Bowen, C. R.; Henkel, K.; Schmeiber, D.; Mandal. D. A Self-Powered Wearable Pressure Sensor and Pyroelectric Breathing Sensor Based on GO Interfaced PVDF Nanofibers. *ACS Appl. Nano Mater.* **2019**, *2*, 2013−2025.

7. Zhang Y., Jeong, C. K.; Wang, J.; Sun, H.; Li, F.; Zhang, G.; Chen, L-Q, Zhang, S.; Chen, W.; Wang, Q. Flexible Energy Harvesting Polymer Composites based on Biofibril-Templated 3-Dimensional Interconnected Piezoceramics. *Nano Energy*, **2018**, *50*, 35–42.

8. Won, S. S.; Kawahara, M.; Glinsek, S.; Lee, J.; Kim, Y.; Jeong, C. K.; Kingon, Angus I.; Kim, S-H. Flexible Vibrational Energy Harvesting Devices Using Strain-Engineered Perovskite Piezoelectric Thin Films. *Nano Energy*, **2019**, *55*, 182–192.

9. Wang, F-X.; Zhang, S-H.; Wang, L-J.; Zhang, Y-L.; Lin, J.; Zhang, X-H.; Chen, T.; Lai, Y-K.; Pan, G-B.; Sun, L-N. An Ultrahighly Sensitive and Repeatable Flexible

Pressure Sensor Based on PVDF/PU/MWCNT Hierarchical Framework-Structured Aerogels for Monitoring Human Activities. *J. Mater. Chem. C*, **2018**, *6*, 12575-12583.

10. Hamaguchi, K.; Ma, Y.; Takada. M.; Nishijima, T.; Shimura, T. Telecommunication Systems in Smart Cities. *Hitachi Rev.* **2012**, *61*, 152−158.

11. Guo, W.; Tan, C.; Shi, K.; Li, J.; Wang, X-X.; Sun, B.; Huang, X.; Long, Y-Z.; Jiang, P. Wireless Piezoelectric Devices Based on Electrospun PVDF/BaTiO$_3$ NW Nanocomposite Fibers for Human Motion Monitoring. *Nanoscale* **2018**, *10*, 17751−17760.

12. Cheng, L.; Yuan, M.; Gu. L.; Wang, Z.; Qin, Y.; Jing, T.; Wang, Z. L. Wireless, Power-Free and Implantable Nanosystem for Resistance-Based Biodetection. *Nano Energy* **2015**, *15*, 598−606.

13. Pruvost, M.; Smit, W. J.; Monteux, C.; Poulin, P.; Colin, A. Polymeric Foams for Flexible and Highly Sensitive Low-Pressure Capacitive Sensors. *Njp Flexible Electronics* **2019**, *3*, 1−7.

14. Luna, A.; Pruvost M.; Yuan, J.; Zakri, C.; Neri, W.; Monteux, C.; Poulin, P.; Colin, A. Giant Electrostrictive Response and Piezoresistivity of Emulsion Templated Nanocomposites. *Langmuir* **2017**, *33*, 4528−4536.

15. Xing, F.; Jie, Y.; Cao, X.; Li, T.; Wang, N. Natural Triboelectric Nanogenerator Based on Soles for Harvesting Low-Frequency Walking Energy. *Nano Energy* **2017**, *42*, 138−142.

16. Wang, Z. L.; Song, J. Piezoelectric Nanogenerators Based on Zinc Oxide Nanowire Arrays. *Science* **2006**, *312*, 242−246.

17. Alam, M. M.; Ghosh, S. K.; Sultana, A.; Mandal, D. Lead-Free $ZnSnO_3$/MWCNTs-Based Self-Poled Flexible Hybrid Nanogenerator for Piezoelectric Power Generation. *Nanotechnology* **2015**, *26*, 165403−165408.

18. Chen, X.; Xu, S.; Yao, N.; Shi, Y. 1.6 V Nanogenerator for Mechanical Energy Harvesting Using PZT Nanofibers. *Nano Lett.* **2010**, *10*, 2133–2137.

19. Park, K.; Xu, S.; Liu, Y.; Hwang, G.-T.; Kang, S.-J. L.; Wang, Z. L.; Lee, K. J. Piezoelectric $BaTiO_3$ Thin Film Nanogenerator on Plastic Substrates. *Nano Lett.* **2010**, *10*, 4939–4943.

20. Martins, P.; Lopes, A. C.; Mendeza, S. L. Electroactive Phases of Poly(vinylidene fluoride): Determination, Processing and Applications. *Prog. Polym. Sci.* **2014**, *39*, 683−706.

21. Lovinger, A. J. Ferroelectric Polymers. *Science* **1983**, *220*, 1115−1121.

22. Ramasundaram, S.; Yoon, S.; Kim, J. K.; Park, C. Preferential Formation of Electroactive Crystalline Phases in Poly(vinylidene fluoride)/Organically Modified Silicate Nanocomposites. *J. Polym Sci Part B: Polym. Phys.* **2008**, *46*, 2173–2187.

23. Mandal, D.; Henkel, K.; Schmeißer, D. The Electroactive β-Phase Formation in Poly(vinylidene fluoride) by Gold Nanoparticles Doping. *Materials Letters.* **2012**, *73*, 123−125.

24. Maji, S.; Sarkar, P. K.; Aggarwal, L.; Ghosh, S. K.; Mandal, D.; Sheet, G.; Acharya, S. Self-Oriented β-Crystalline Phase in the Polyvinylidene Fluoride Ferroelectric and Piezo-Sensitive Ultrathin Langmuir–Schaefer film. *Phys. Chem. Chem. Phys.* **2015**, *17*, 8159−8165.

25. Lee, J. E.; Guo, Y.; Lee, R. E.; Leung, S. N. Fabrication of Electroactive Poly(vinylidene fluoride) through Non-Isothermal Crystallization and Supercritical CO_2 Processing. *RSC Adv.* **2017**, *7*, 48712–48722.

26. Ribeiro, C.; Costa, C. M.; Correia, D. M.; Nunes-Pereira, J.; Oliveira, J.; Martins, P.; Goncalves, R.; Cardoso, V. F.; Lanceros-Mendez, S. Electroactive Poly(vinylidene fluoride)-Based Structures for Advanced Applications. *Nature Protocols* **2018**, *13*, 681–704.

27. Cai, X.; Lei, T.; Sun, D.; Lin, L. A Critical Analysis of the α, β and γ phases in Poly(vinylidene fluoride) Using FTIR. *RSC Adv.* **2017**, *7*, 15382–15389.

28. Sokhanvar, S; Dargahi,J; Najarian, S; Arbatani,S. Piezoelectric Polymers: PVDF Fundamentals, in Tactile Sensing and Displays. Hoboken, NJ, USA: Wiley, 2012.

29. Park, M.; Choi, Y.-Y.; Kim, J.; Hong, J.; Song, H. W.; Sung, T.-H.; No, K. The Piezoresponse Force Microscopy Investigation of Self-Polarization Alignment in Poly(vinylidene fluoride-co-trifluoroethylene) Ultrathin Films. *Soft Mater.* **2012**, *8*, 1064−1069.

30. Andrew, J. S.; Clarke, D. R. Enhanced Ferroelectric Phase Content of Polyvinylidene Difluoride Fibers. *Langmuir* **2008**, *24*, 670−672.

31. Mandal, D.; Kim, K. J.; Lee, J. S. Simple Synthesis of Palladium Nanoparticles, β-Phase Formation, and the Control of Chain and Dipole Orientations in Palladium-Doped Poly(vinylidene fluoride) Thin Films. *Langmuir* **2012**, *28*, 10310−10317.

32. Yadav, S. K.; Mahapatra, S. S.; Cho, J. W.; Park, W. C.; Lee, J. Y. Enhanced Mechanical and Dielectric Properties of Poly(vinylidene fluoride)/Polyurethane/Multi-walled Carbon Nanotube Nanocomposites. *Fibers and Polymers* **2009**, *10*,756−760.

33. Biswas, A.; Henkel, K.; Schmeißer, D.; Mandal, D. Comparison of the Thermal Stability of the α, β and γ Phases in Poly(vinylidene Fluoride) Based on In-Situ Thermal Fourier Transform Infrared Spectroscopy. *Phase Transitions* **2017**, *90*, 1205−1213.

34. Correia, D. M.; Barbosa, C.; Costa, C. M.; Reis, P. M.; Esperanca, J. M. S. S.; Bermudez, V. D.; Lanceros-Méndez, S. Ionic Liquid Cation Size-Dependent Electromechanical Response of Ionic Liquid/Poly(vinylidene Fluoride)-Based Soft Actuators. *J. Phys. Chem. C* **2019**, *123*, 12744−12752.

35. Li, H.; Dai, H.; Zhang, Y.; Tong, W.; Gao, H.; An, Q. Surface-Enhanced Raman Spectra Promoted by a Finger Press in an All-Solid-State Flexible Energy Conversion and Storage Film. *Angew. Chem.* **2017**, *129*, 2693–2698.

36. Ghosh, S. K.; Sinha, T. K.; Mahanty, B.; Mandal, D. Self-poled Efficient Flexible "Ferroelectretic" Nanogenerator: A New Class of Piezoelectric Energy Harvester. *Energy Technol.* **2015**, *3*, 1190–1197.

37. Mahanty, B.; Ghosh, S. K.; Garain, S.; Mandal, D. An Effective Flexible Wireless Energy Harvester/Sensor Based on Porous Electret Piezoelectric Polymer. *Materials Chemistry and Physics.* **2017**, *186*, 327−332.

38. Que, R.; Shao, M.; Wang, S.; Ma, D. D. D.; Lee, S.-T. Silicon Nanowires with Permanent Electrostatic Charges for Nanogenerators. *Nano Lett.* **2011**, *11*, 4870–4873.

39. Wang, C.; Cai, L.; Feng, Y.; Chen, L.; Yan, W.; Liu, Q.; Yao, T.; Hu, F.; Pan, Z.; Sun, Z.; Wei, S.; An Electrostatic Nanogenerator Based on ZnO/ZnS Core/Shell Electrets with Stabilized Quasi-Permanent Charge. *Appl. Phys. Lett.* **2014**, *104*, 243112-1−243112-4.

40. Zhang, Y.; Bowen, C. R. Ghosh, S. K.; Mandal, D.; Khanbareh, H.; Arafa, M.; Wan, C. Ferroelectret Materials and Devices for Energy Harvesting Application. *Nano Energy* **2019**, *57*, 118−140.

41. Ghosh, S. K.; Biswas, A.; Sen, S.; Das, C.; Henkel, K.; Schmeisserc, D.; Mandal, D. Yb^{3+} Assisted Self-Polarized PVDF Based Ferroelectretic Nanogenerator: A Facile

Strategy of Highly Efficient Mechanical Energy Harvester Fabrication. *Nano Energy* **2016**, *30*, 621−629.

42. Li, W.; Torres, D.; Diaz, R.; Wang, Z.; Wu, C.; Wang, C.; Wang, Z. L.; Sepulveda, N. Nanogenerator-based Dual-Functional and Self-Powered Thin Patch Loudspeaker or Microphone for Flexible Electronics. *Nat. Commun.* **2017**, *8*, 15310.

43. Cao, Y.; Figueroa, J.; Li, W.; Chen, Z.; Wang, Z. L. Sepulveda, N. Understanding the Dynamic Response in Ferroelectret Nanogenerators to Enable Self-Powered Tactile Systems and Human-Controlled Micro-Robots. *Nano Energy* **2019**, *63*, 103852–103859.

44. Cha, S. N.; Kim, S. M.; Kim, H.; Ku, J.; Sohn, J. I.; Park, Y. J.; Song, B. G.; Jung, M. H.; Lee, E. K.; Choi, B. L.; Park, J. J.; Wang, Z. L.; Kim, J. M.; Kim, K. Porous PVDF As Effective Sonic Wave Driven Nanogenerators. *Nano Lett.* **2011**, *11*, 5142–5147.

45. Mao, Y.; Zhao, P.; McConhy, G.; Yang, H.; Tong, Y.; Wang, X. Sponge-Like Piezoelectric Polymer Films for Scalable and Integratable Nanogenerators and Self-Powered Electronic Systems. *Adv. Energy Mater.* **2014**, *4*, 1301624 (1–7).

46. Jana, S.; Jana, R.; Sil, S.; Dutta, B.; Sato, H. Roy, P. P.; Dutta, A.; Akitsu, T.; Sinha, C. Influence of Axial Linkers on Polymerization in Paddle-Wheel Cu(II) Coordination Polymers for the Application of Optoelectronics Devices. *Cryst. Growth Des.* **2019**, *19*, 6283−6290.

47. Naskar, K.; Dey, A.; Dutta, B.; Ahmed, F.; Sen, C.; Hedayatullah Mir, M.; Roy, P. P.; Sinha, C. Intercatenated Coordination Polymers (ICPs) of Carboxylato Bridged Zn(II) Isoniazid and Their Electrical Conductivity. *Cryst. Growth Des.* **2017**, *17*, 3267−3276.

48. Naskar, K.; Dey, A.; Maity, S.; Bhunia, M. K.; Roy, P. P.; Sinha, C. Novel Porous Polycatenated Iodo-Cadmium Coordination Polymer for Iodine Sorption and Electrical Conductivity Measurement. *Cryst. Growth Des.* **2019**, *19*, 2206−2218.

49. Liu, Y.; Lin, S.; Liu, Y.; Sarkar, A. K.; Bediako, J. K.; Kim, H. Y.; Yun, Y.-S. Super-Stable, Highly Efficient, and Recyclable Fibrous Metal–Organic Framework Membranes for Precious Metal Recovery from Strong Acidic Solutions. *Small* **2019**, *15*, 1805242-1−1805242-9.

50. Botas, J. A.; Calleja, G.; Sánchez-Sánchez, M; Orcajo, M. G. Cobalt Doping of the MOF-5 Framework and Its Effect on Gas-Adsorption Properties. *Langmuir*, **2010**, *26*, 5300–5303.

51. Guo, Q.; Ren, L.; Kumar, P.; Cybulskis, V. J.; Mkhoyan, K. A.; Davis, M. E., Tsapatsis, M. A Chromium Hydroxide/MIL-101 (Cr) MOF Composite Catalyst and Its Use for the Selective Isomerization of Glucose to Fructose. *Angew. Chem.* **2018**, *130*, 5020–5024.

52. Hang, T.; Zhang, W.; Ye, H.-Y.; Xiong, R.-G. Metal–Organic Complex Ferroelectrics. *Chem. Soc. Rev.* **2011**, *40*, 3577–3598.

53. Dwyer, D. B.; Dugan, N.; Hoffman, N.; Cooke, D. J.; Hall, M. G.; Tovar, T. M.; Bernier, W. E.; Decoste, J.; Pomerantz, N. L.; Jones, W. E. Chemical Protective Textiles of UiO-66-Integrated PVDF Composite Fibers with Rapid Heterogeneous Decontamination of Toxic Organophosphates. *ACS Appl. Mater. Interfaces* **2018**, *10*, 34585–34591.

54. Lu, A. X.; McEntee, M.; Browe, M. A.; Hall, M. G.; Decoste, J. B.; Peterson, G. W. MOFabric: Electrospun Nanofiber Mats from PVDF/UiO-66-NH$_2$ for Chemical Protection and Decontamination. *ACS Appl. Mater. Interfaces* **2017**, *9*, 13632–13636.

55. Kim, J. O.; Kim, J. Y.; Lee, J. C.; Park, S.; Moon, H. R.; Kim, D. P. Versatile Processing of Metal-Organic Framework-Fluoropolymer Composite Inks with Chemical Resistance and Sensor Applications. *ACS Appl. Mater. Interfaces* **2019**, *11*, 4385–4392.

56. Hu, L.; Zhang, Y.; Lu, W.; Lu, Y.; Hu, H. Easily Recyclable Photocatalyst Bi_2WO_6/MOF/PVDF Composite Film for Efficient Degradation of Aqueous Refractory Organic Pollutants under Visible-Light Irradiation. *J. Mater. Sci.* **2019**, *54*, 6238–6257.

57. Liu, Y.; Lin, S.; Liu, Y.; Sarkar, A. K.; Bediako, J. K.; Kim, H. Y.; Yun, Y.-S. Super-Stable, Highly Efficient, and Recyclable Fibrous Metal-Organic Framework Membranes for Precious Metal Recovery from Strong Acidic Solutions. *Small* **2019**, *15*, 1805242.

58. Zhang, X.; Zhang, Q.; Yue, D.; Zhang, J.; Wang, J.; Li, B.; Yang, Y.; Cui, Y.; Qian, G. Flexible Metal-Organic Framework-Based Mixed-Matrix Membranes: A New Platform for H_2S Sensors. *Small* **2018**, *14*, 1801563.

59. Zhao, X. H.; Ma, S. N.; Long, H.; Yuan, H.; Tang, C. Y.; Cheng, P. K.; Tsang, Y. H. Multifunctional Sensor Based on Porous Carbon Derived from Metal-Organic Frameworks for Real Time Health Monitoring. *ACS Appl. Mater. Interfaces* **2018**, *10*, 3986–3993.

60. Liu, X.; Su, G.; Guo, Q.; Lu, C.; Zhou, T.; Zhou, C.; Zhang, X. Hierarchically Structured Self-Healing Sensors with Tunable Positive/Negative Piezoresistivity. *Adv. Funct. Mater.* **2018**, *28*, 1706658.

61. Lopes, A. C.; Costa, C. M.; Tavares, C. J.; Neves, I. C.; Lanceros-Mendez, S. Nucleation of the Electroactive γ Phase and Enhancement of the Optical

Transparency in Low Filler Content Poly(vinylidene)/Clay Nanocomposites. *J. Phys. Chem. C* **2011**, *115*, 18076–18082.

62. Lizundia, E.; Reizabal, A.; Costa, C. M.; Maceiras, A.; Lanceros-Mendez, S. Electroactive -Phase, Enhanced Thermal and Mechanical Properties and High Ionic Conductivity Response of Poly (Vinylidene Fluoride)/Cellulose Nanocrystal Hybrid Nanocomposites. *Materials* **2020**, *13*, 743 (1–16).

63. Abdullah, I. Y.; Yahaya, M.; Jumali, M. H. H.; Shanshool, H. M. Effect of Annealing Process on the Phase Formation in Poly(Vinylidene Fluoride) Thin Films. In *AIP Conference Proceedings* **2014**, *1614*, 147–151.

64. Tashiro, K.; Kobayashi, M.; Tadokoro, H. Vibrational Spectra and Disorder-Order Transition of Poly(Vinylidene Fluoride) Form III. *Macromolecules* **1981**, *14*, 1757–1764.

65. Satapathy, S.; Pawar, S.; Gupta, P. K.; Varma, B. R. Effect of Annealing on Phase Transition in Poly(Vinylidene Fluoride) Films Prepared Using Polar Solvent. *Bull. Mater. Sci.* **2011**, *34*, 727-733.

66. Kobayashi, M.; Tashiro, K.; Tadokoro, H. Molecular Vibrations of Three Crystal Forms of Poly(Vinylidene Fluoride). *Macromolecules* **1975**, *8*, 158–170.

67. Soin, N.; Boyer, D.; Prashanthi, K.; Sharma, S.; Narasimulu, A. A.; Luo, J.; Shah, T. H.; Siores, E.; Thundat, T. Exclusive Self-Aligned β-Phase PVDF Films with Abnormal Piezoelectric Coefficient Prepared via Phase Inversion. *Chem. Commun.* **2015**, *51*, 8257–8260.

68. Bystrov, V. S.; Bystrova, N. K.; Paramonova, E. V.; Vizdrik, G.; Sapronova, A. V.; Kuehn, M.; Kliem, H.; Kholkin, A. L. First principle calculations of molecular polarization switching in P(VDF–TrFE) ferroelectric thin Langmuir–Blodgett films. *J. Phys.: Condens. Matter* **2007**, *19*, 456210.

69. Gaur, A.; Tiwary, S.; Kumar, C.; Maity, P. A Bio-based Piezoelectric Nanogenerator for Mechanical Energy Harvesting using Nanohybrid of Poly(vinylidene fluoride). *Nanoscale Adv.* **2019**, *1*, 3200–3211.

70. Wang, Z. L. Towards Self-Powered Nanosystems: From Nanogenerators to Nanopiezotronics. *Adv. Funct. Mater.* **2008**, *18*, 3553–3567.

71. Sirohi, J.; Chopra, I. Fundamental Understanding of Piezoelectric Strain Sensors. *J. Intell. Mater. Syst. Struct.* **2000**, 11, 246–257.

72. Maity, K.; Garain, S.; Henkel, K.; Schmeiβer, D.; Mandal, D. Natural Sugar-Assisted, Chemically Reinforced, Highly Durable Piezoorganic Nanogenerator with Superior Power Density for Self-Powered Wearable Electronics. *ACS Appl. Mater. Interfaces.* **2018**, *10*, 44018−44032.

73. Kepler, R. G.; Anderson, R. A. Piezoelectricity and Pyroelectricity in Polyvinylidene Fluoride. *J. Appl. Phys.* **1978**, *49*, 4490–4494.

74. Park, D. Y.; Joe, D. J.; Kim, D. H.; Park, H.; Han, J. H.; Jeong, C. K.; Park, H.; Park, J. G.; Joung, B.; Lee, K. J. Self-Powered Real-Time Arterial Pulse Monitoring Using Ultrathin Epidermal Piezoelectric Sensors. *Adv. Mater.* **2017**, *29*, 1702308-1−1702308-9.

75. Persano, L.; Dagdeviren, C.; Su, Y.; Zhang, Y.; Girardo, S.; Pisignano, D.; Huang, Y.; Rogers, J. A. High Performance Piezoelectric Devices Based on Aligned Arrays of Nanofibers of Poly(vinylidene fluoride-co-trifluoroethylene). *Nat. Commun.* **2013**, *4*, 1633-1–1633-10.

76. Graz, I.; Kaltenbrunner, M.; Keplinger, C.; Schwödiauer, R.; Bauer, S.; Lacour, S. P.; Wagner, S. Flexible Ferroelectret Field-Effect Transistor for Large-Area Sensor Skins and Microphones. *Appl. Phys. Lett.* **2006**, *89*, 073501-1–073501-3.

77. Sharma, T.; Je, S.-S.; Gill, B.; Zhang, J. X.; Patterning Piezoelectric Thin Film PVDF–Tr-FE Based Pressure Sensor for Catheter Application. *Sens. Actuators A.* **2012**, *177*, 87–92.

78. Zhang, X.; Zhang, X.; Sessler, G. M.; Gong, X. Quasi-Static and Dynamic Piezoelectric Responses of Layered Polytetrafluoroethylene Ferroelectrets. *J. Phys. D: Appl. Phys.* **2014**, *47*, 015501−015507.

79. Piirila, P.; Sovijarvi, A. R. A. Objective Assessment of Cough. *Eur. Respir. J.* **1995**, *8*, 1949−1956.

80. Thorpe, C. W.; Toop, L. J.; Dawson, K. P. Towards a Quantitative Description of Asthmatic Cough Sounds. *Eur. Respir. J.* **1992**, *5*, 685−692.

Chapter 4

All Organic-Inorganic Pyroelectric Energy Harvester

4.1 Introduction

With the rapid development of portable electronics, smart sensors and wearable medical devices, it is hard to meet the increasing energy demand. As an outcome, the utilization of green and renewable energy sources which include solar, thermal, wind, mechanical vibrations gradually increases [1-3]. Exploration of these ubiquitously abundant energy sources is the long-term solution for low power nanoscale electronics and sensors. In this context, piezoelectric and pyroelectric nanogenerators (NGs) are of potential interest because of their self-powered nature. However, concept of self-powered energy harvesters was proposed long back in 2006 by Wang et al [4]. Among them, piezoelectric material utilizes mechanical vibration induced strain to develop electricity whereas pyroelectric effect solely relies on the change in dipole orientation due to periodic thermal fluctuation [5-7].

Till date, different materials have been widely studied to fabricate pyroelectric nanogenerators (PyNGs) such as ZnO, CdS, CdSe, $KNbO_3$ nanowires, PVDF and its co-polymers by adapting different synthetic procedure and methodologies [6-12]. Though there still exist adequate challenges regarding the output performance, flexibility, sensitivity and wearability of the devices associated with different sensory applications. Therefore, selection of pyroelectric material and electrode substance is of great concern to develop a highly efficient PyNG which can simultaneously scavenge thermal energy as well as extend its application as a wearable sensor.

Among the aforementioned pyroelectric materials, PVDF and its co-polymers are highly desirable due to its promising intrinsic flexibility, low cost, light weight and biocompatibility[6-7]. Currently, electrospinning is an intensively explored technique which provides micro to nano-sized fibers with predominant ferroelectric β-phase [13]. The highly extensional flow of the polymer solution promotes the all-trans (TTTT) conformation among

the all five chain conformations ($\alpha, \beta, \gamma, \delta$ and ϵ phases) [13, 14]. However, random alignment of fibers along with non-uniformly in fiber diameter distribution restricts the performance and sensitivity of the objective device. As a matter of concern, confinement of nanofillers in PVDF matrix can intriguingly strengthen and optimize their properties by improving fiber diameter, mechanical ferroelectric and electrical properties [15, 16]. Recently, incorporation of inorganic fillers (magnetic nanoparticles, semiconducting fillers, ceramic fillers), conductive nanofillers (CNTs, Mxene, graphene) with PVDF matrix has been an attractive approach to enhance the intrinsic properties [17-22]. Graphene based nanofillers gathered intensive focus because of providing high mechanical, electrical, thermal properties and large surface area [23]. Some recent research works reveal the usage of modified graphene based fillers to promote more $\beta-$phase in PVDF [24]. However, there still remains a significant challenge regarding perfect choice of electrode material to construct an environment friendly superior PyNGs for wearable health monitoring. Traditionally, metal/metal coated electrodes have been used as top and bottom electrode [25, 26]. However, it suffers from poor adhesion with nanofiber mat, brittleness and robustness. As a result, interfacial shear stress destabilizes the whole system which further affects the electrical conductivity of the device, rendering its applicability in wearable devices. Concomitant to these facts conductive polymer electrodes would be an appropriate choice due to their innate flexibility, good connectivity and satisfactory conductivity. Among the organic electrodes, PEDOT:PSS is frequently used as an alternative electrode. PEDOT:PSS has gathered immense attention due to its commercial availability, high stretchability, bicompatability, tunable conductivity and stability.

In this approach, we have successfully coated PEDOT:PSS on functionalized graphene modified PVDF nanofiber mat owing to fabricate a highly efficient pyroelectric nanogenerator, which can be further used as a self-powered temperature sensor and wearable

breathing sensor for human respiration monitoring. Respiration rate is significantly a critical parameter because alteration of respiration rate signifies many symptoms related to respiratory disorder [27]. Presently, wearable devices have been developed for in-home monitoring of respiration rate which would provide a respiratory health profile for the patients with known medical issues. Till date, several respiratory sensors based on piezo- and triboelectric mechanism has been established [28-30]. However, PyNG concerning breathing rate monitoring has been rarely explored [5, 6, 12]. In this context, our all organic-inorganic pyroelectric nanogenerator (A-PyNG) will provide an exciting platform to monitor human breathing rate from periodic inhale-exhale process, extending viable applications in biomedical diagnosis and informatics as well as waste heat energy harvesting.

4.2 Experimental Section

4.2.1 Synthesis of GO

Graphene oxide was produced by oxidizing graphite powder using the modified Hummers' method [33]. In brief, 6 g of graphite powder was thoroughly mixed with 3 g of $NaNO_3$ in the 100 mL of cold concentrated sulphuric acid. The solution was then stirred well in an ice bath that was maintained below 5 ^{o}C. A mass of 15 g of $KMnO_4$ was then gradually added to the resulting solution while being continuously stirred. After removal from the cooling bath, stirring of the mixture was continued at room temperature. Afterwards, 200 mL of water was added to the solution and the temperature was increased to 98 ^{o}C while being continuously stirred. Then, 500 mL of de-ionized water and 30 mL of 30% H_2O_2 were added until effervescence has ceased and the colour of the solution changed to light brown and was left overnight. The brown precipitate was then separated from the supernatant and then washed repeatedly with 5% (V/V) HCl. Finally the material was centrifuged with deionized (DI)

water followed by drying in a vacuum oven. Then, 100 mg of the as-prepared GO was collected and dissolved in EG for further synthesis.

Figure 4.1 (a) Solvothermal synthesis scheme of CdS-rGO nanocomposite from GO. (b and c) Schematic illustration of C-PVDF nanofiber mat preparation to A-PyNG fabrication.

4.2.2 Solvothermal Preparation of CdS-rGO Nanocomposite

The synthesis of CdS-rGO nanocomposite was typically initiated by making a homogeneous dispersion of graphene oxide (GO) in ethylene glycol (EG). Afterwards, stoichiometric amount of cadmium acetate dihydrate [Cd(CH$_3$COO)$_2$. 2H$_2$O] and thiourea [SC(NH$_2$)$_2$] were added in the GO dispersion followed by continuous stirring for half an hour. The resulting solution was hydrothermally treated in a Teflon-lined autoclave at 180 °C for several hours as described through the schematic presented in Figure 4.1(a). Then, the precipitate was collected, thoroughly washed by ethanol and DI water after cooling down the entire system.

Ultimately, the product was dried at 60 ˚C to obtain greenish coloured CdS-rGO nanocomposite for further characterization and experiments.

4.2.3 Synthesis of Pure CdS Nanoparticles

In order to compare, yellowish pure CdS nanoparticles without graphene sheet were prepared under similar experimental conditions as that for CdS-rGO nanocomposite.

4.2.4 Preparation of Nanofibers

Firstly, a spinning solution of pure PVDF was prepared by dissolving PVDF pellets in a mixed solvent of 6:4 volume ratio of N,N-dimethylformamide (DMF)/acetone at a polymer/solvent concentration of 12 % w/v under continuous stirring at 60 ˚C for 3 h until a clear homogeneous solution was obtained. Later, as-prepared CdS-rGO nanocomposite (1 wt% (w/v)) was added into the pure PVDF solution and kept for gentle stirring at 60 ˚C prior to complete dissolution. It was ultra-sonicated before electrospinning. Neat PVDF solution was also taken in countfor comparison purpose. The electrospinnig process was conducted by filling the resulting solution in a 10 mL hypertonic syringe (Dispovan) tipped with a stainless steel needle (22 G). The positive electric field/bias voltage (9 kV) was applied between tip to Al foil wrapped grounded collector plate (at a distance of 10 cm) with a constant flow rate of 0.4 mL/h. Same parameters were maintained during the electrospinning of neat PVDF solution for executing controlled experiments. In addition, collected neat PVDF (N-PVDF) and CdS-rGO embedded composite (C-PVDF) nanofibers were further dried at 60 ˚C for 4 h to remove all the residual solvents to attain stable nanofibers for additional experiments and device fabrication.

4.2.5 Preparation of PEDOT:PSS Electrode and PyNG Fabrication

The organic electrode was prepared by gently mixing 0.1 N HCl with a PEDOT:PSS suspension in a weight ratio of 3:4, following our previous work [5]. After that, Xylitol

pellets (1:4 w/w ratio with PEDOT) were added to the solution under vigorous stirring. The mixture was allowed to heat in a sealed water bath for several hours to achieve the gel formation. The as-synthesized PEDOT:PSS gel was repeatedly rinsed with DI water to eliminate the extra residue. Subsequently, the gel was pasted over previously cut C-PVDF nanofiber mat (in desired size) to construct the PEDOT:PSS film (effective electrode area: 20 mm × 10 mm) electrode under heat treatment at 80 ˚C. As a result, polymer over polymer architecture based all organic-inorganic pyroelectric nanogenerator (A-PyNG) was fabricated. In contrast, an A-PyNG made of N-PVDF was also assembled for performance comparison. A systematic scheme is illustrated in Figure 4.1(b and c), which include nanofiber preparation to device fabrication.

4.2.6 Characterization Methods

The X-ray diffraction patterns and crystalline phases of the as-synthesized CdS-rGO and composite nanofibers were recorded by X-ray diffractometer (Bruker, D8 Advance) equipped with a Cu Kα (λ = 0.154 nm) with an X-ray source under an operating voltage and current of 40 kV and 40 mA, respectively. The associated vibrational bands and respective crystalline phases of the nanofibers were further characterized by Fourier Transform Infrared Spectroscopy (FT-IR, TENSOR II, Bruker). Morphological analysis was further conducted by FE-SEM (INSPECT F50) operating at an acceleration voltage of 20 kV and high resolution transmission electron microscope HRTEM (JEOL-JEM 2100) operating at 200 kV. X-ray photoelectron spectroscopy (XPS) was carried out by a thermo-electron system equipped with a Al-Kα excitation source and a PHOIBOS 150 MCD (Specs GmbH, Germany) analyzer. To examine the pyroelectric nature under alternating external temperature oscillations, an IR lamp (Phillips PAR38 175 W) with a constant heat flux density of 340 mW/cm^2 was employed and periodical switching of "ON" and "OFF" state

was accompanied by a frequency generator. The heat flux was calibrated by a thermal power sensor (THORlabs Germany, peak wavelength of 700 nm). A heat sink was used for cooling the device after irradiation. The test devices were irradiated from a distance of 10 cm from the IR-lamp source. The temperature was calculated using a K-type thermocouple attached to the electrode surface. The V_{oc} and I_{sc} were measured with a Keithley 6517B electrometer (input resistance > 200 TΩ and noise < 1 fA). The temperature fluctuation during breathing was also evaluated by the K-type thermocouple.

4.3 Results and Discussion

4.3.1 Crystallographic and Structural Analysis of CdS-rGO

The crystalline phases of the as-prepared pure CdS NP and CdS-rGO nanocomposite along with their structure were determined using XRD. It is evident from the pattern (as illustrated in Figure 4.2) that both of the samples possess exactly same diffraction peaks. The peaks at 26.5^o, 43.9^o, and 52.1^o are indexed to (111), (220), and 311) crystal planes respectively corresponding to cubic CdS phase [31]. Interestingly, the main peak due to GO at $2\theta = 11.1^o$ is totally disappeared in CdS/rGO nanocomposite [6]. Thus, it can be assumed that the oxygen functional groups of GO were sufficiently reduced during the solvothermal processing of CdS/rGO nanocomposite. Additionally, no separate peak for rGO at $2\theta = 26^o$ is noticed in the XRD pattern of CdS/rGO [32]. It implies that the rGO peak at 26° might be overlapped or shielded by the diffraction peak of cubic CdS at 26.5^o. Therefore, rGO has no remarkable effect on the crystal planes of the composite. Moreover, rGO addition slightly increases the average crystallite size of CdS NP as calculated using Scherrer equation.

$$D = \frac{K\lambda}{\beta cos\theta}$$

where, *K* is a constant (0.89), λ is the wavelength (0.1541 nm) of the Cu-Kα X-ray radiation, β is the full-width (in radian) at half maxima (FWHM) of the diffraction peak and θ is the Bragg's angle.
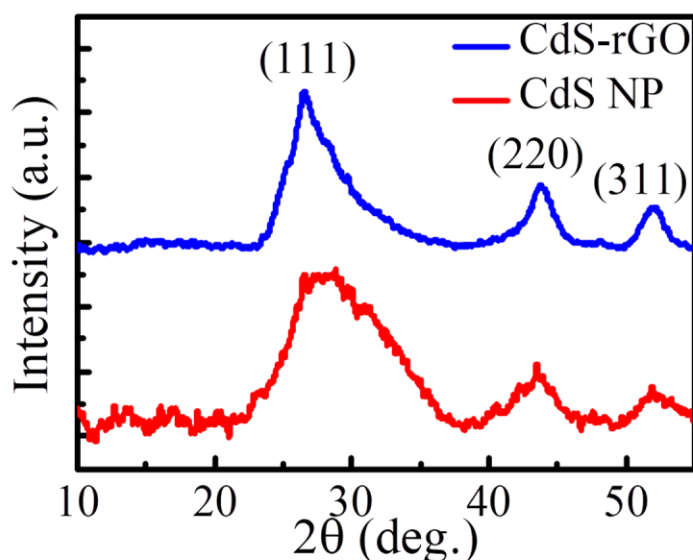
Figure 4.2 XRD pattern of as-synthesized pure CdS NPs and CdS-rGO nanocomposite.

The calculated crystallite size of blank CdS and CdS-rGO nanocomposite are 4 nm and 4.6 nm respectively. Therefore, it indicates that rGO sheets specifically assist CdS NPs to nucleate as well as improve the crystallinity by providing a large surface area.

4.3.2 Morphology Study of CdS-rGO:

Figure 4.3(a and b) distinctly reveal that almost spherical shaped CdS NPs are grafted on the surface of rGO sheet. The average diameter of the coated NPs has been measured to be about 220 nm as shown in Figure 4.3(b). In contrast, as-synthesized pure CdS NPs have well-defined spherical shape with average diameter of 250-260 nm as shown in Figure 4.3(c). Consequently, it can be deduced that introduction of rGO in the nanocomposite formation marginally reduced the size of NPs. However, comparatively small sized CdS NPs are

145
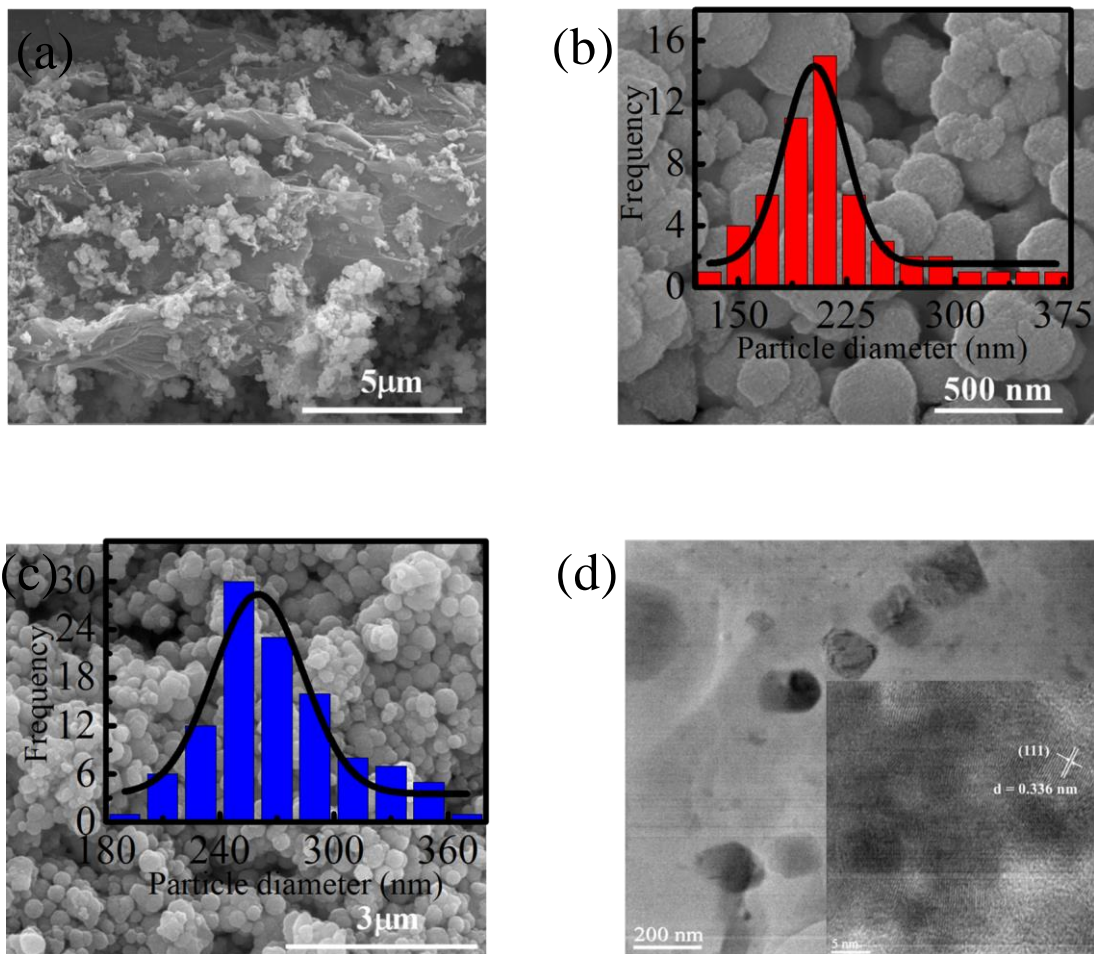
Figure 4.3 (a) FE-SEM image of CdS-rGO along with (b) the enlarged view (inset: particle diameter distribution). (c) FE-SEM micrograph of CdS nanoparticles with particle diameter distribution in the inset. (d) HR-TEM image of CdS-rGO with magnified view in lower inset.

unevenly and randomly distributed over the 2D surface of rGO. Additionally, solvothermal process gives rise to folds and wrinkles on the layered structure of rGO. The HR-TEM image (follow Figure 4.3(d)) of CdS-rGO supports the above findings from FE-SEM image. Furthermore, the close contact between CdS and rGO can be identified from HR-TEM image (Figure 4.3(d)), indicating the interaction of CdS NPs with rGO through electrostatic interaction or charge transfer mechanism [31]. Lattice fringes with 0.336 nm of inter-planner distance was observed from the magnified HR-TEM image as illustrated in the inset of Figure

146

4.3(d) [32]. This is in accordance with the d-spacing of (111) plane of cubic CdS. Above results point out the successful preparation of CdS-rGO nanocomposites, which were accordingly used in nanofibers and device fabrication.

4.3.3 UV-Vis Absorption and PL Spectra of CdS-rGO

The optical behaviour of the synthesized nanomaterials was studied using UV-Vis absorption spectroscopy, presented in Figure 4.4(a). In both cases for CdS NPs and CdS-rGO nanocomposite, absorbance in visible region can be found [33]. For CdS NPs, a slight neck formation can be observed before the sharp peak near 500 nm. It is reflected from Figure 4.4(a) that absorbance in visible region is adequately increased in case of CdS-rGO compared to pure CdS. These results reasonably indicate strong coupling between CdS and rGO in the nanocomposite along with its effective solar energy utilization.
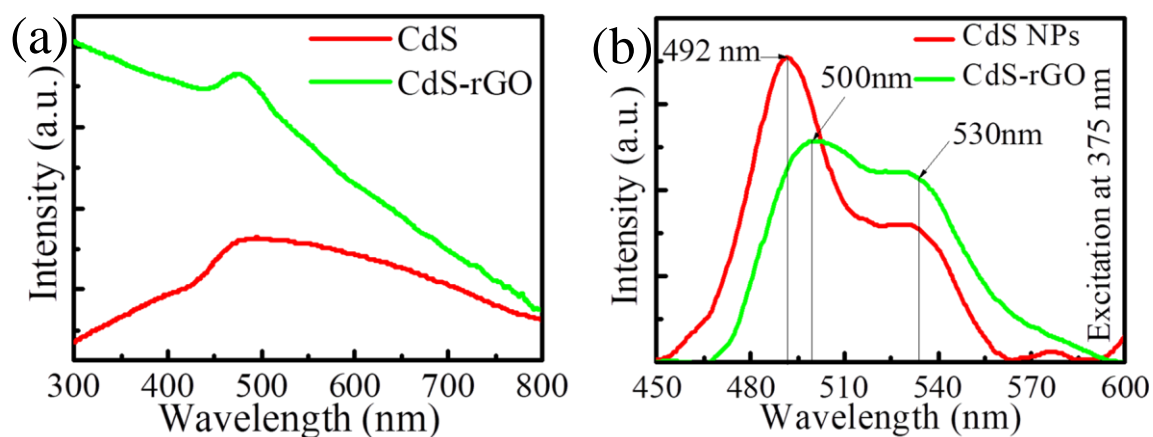
Figure 4.4 (a) UV-Vis absorption and (b) PL spectra of as-synthesized CdS-rGO.

In addition, PL spectra of both samples (Figure 4.4(b)) show two consecutive emission peaks at around 500 nm and 530 nm. The obtained PL intensity decreased for CdS-rGO nanocomposite in comparison with pure CdS nanoparticles. This quenching phenomenon presumably associated with effective electron transfer from CdS to rGO (acting as good

147

electron acceptor), which is further described through an interaction model illustrated in Figure 4.5 [34]. The energetically favourable band alignment of CdS and rGO facilitates the photo-excited electron transport and leading to charge separation in the composite. Above results point out the successful preparation of CdS-rGO nanocomposites, which were accordingly used in nanofibers and device fabrication.
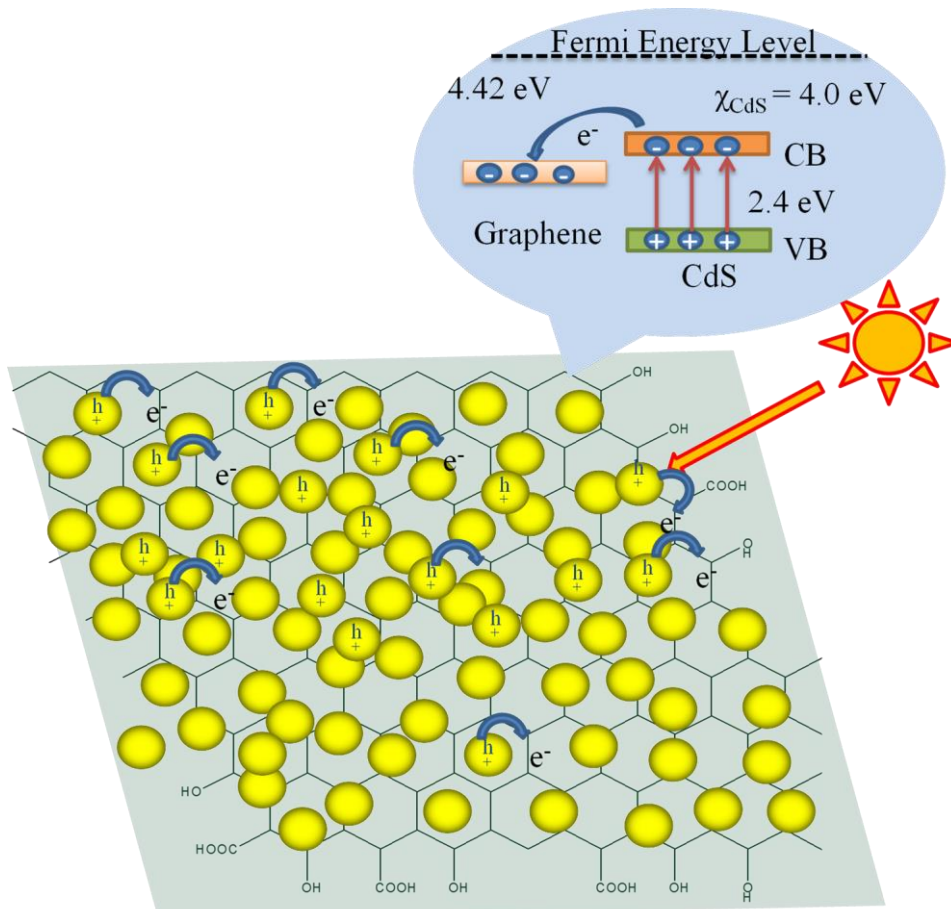
Figure 4.5 Schematic illustration showing the charge transfer phenomena under visible light radiation.

4.3.4 Morphology of the Nanofibers

Figure 4.6(a) reflects the bead-free morphology of the as-spun C-PVDF nanofibers. Fiber mat typically consists of randomly oriented nanofibers with a high degree of porosity and average fiber diameter of 95±10 nm, as shown in corresponding histogram profile (inset of Figure
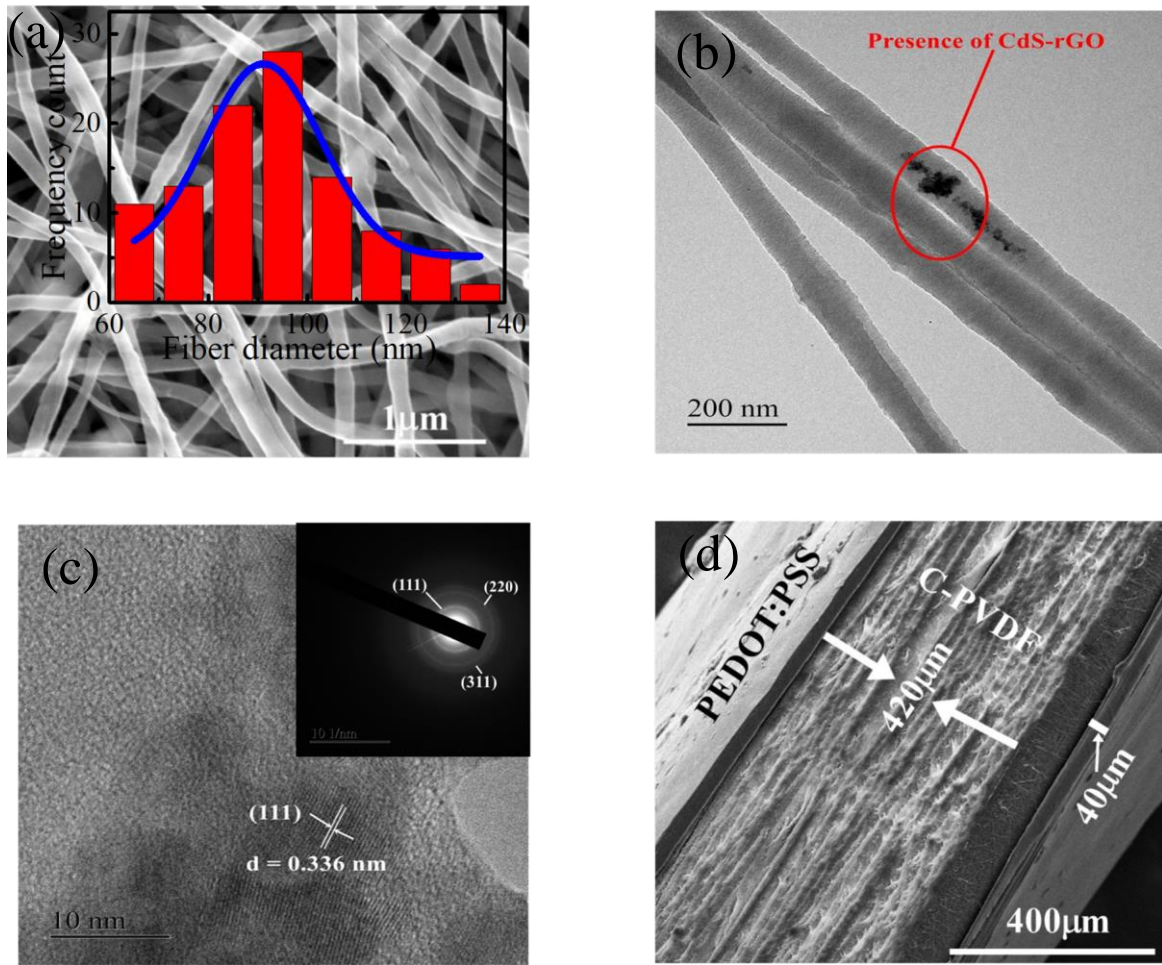
Figure 4.6 (a) FE-SEM image (inset showing fiber diameter distribution) and (b) HR-TEM image of C-PVDF. (c) Magnified view of HR-TEM image with corresponding SAED pattern. (d) Cross-sectional FE-SEM image of A-PyNG illustrating the good connectivity of PEDOT:PSS electrode with C-PVDF mat.

4.6(a)). Moreover, wrinkle-free smooth surface was obtained during the electrospinning of C-PVDF. It is evident from the HR-TEM image that CdS-rGO nanocomposites are well embedded in the nanofibers as marked in Figure 4.6(b). The selected area electron diffraction (SAED) pattern (upper inset of Figure 4.6(c)) reveals that there exist three distinct inside diffraction rings associated with (111), (220) and (311) crystal planes of cubic CdS nanoparticle, indicating its polycrystalline nature [31]. Additionally, lattice fringes associated

149

with the d-spacing of (111) plane of cubic CdS NPs have been detected in the magnified view of HR-TEM image (shown in the inset of Figure 4.6(c)). It should be emphasized that incorporation of CdS-rGO predominantly reduced the fiber diameter. It is because of charge density increment of the nanocomposite solution (PVDF/CdS-rGO). Thus, electrified jet of the composite solution will experience more Coulombic force/elongation compared to that of pure PVDF electrospinning solution. The shrink in fiber diameter might influence the crystallinity and overall performance of the system. To gain the insight about all organic device (electrode/active layer/electrode) architecture, a cross-sectional FE-SEM image was obtained (illustrated in Figure 4.6(d)), which confirms the compact attachment of PEDOT:PSS layer with the active layer of C-PVDF nanofiber mat. Apparently the nanofiber mat thickness is 420 μm and that of the adjacent PEDOT:PSS electrode is 40 μm as mentioned in Figure 3c.

4.3.5 Identification and Quantification of Crystallographic Phases

In order to identify different crystallographic phases of the nanofibers, their crystallinity and the effect of CdS-rGO addition combination of XRD and FT-IR have been performed consecutively. The curve-deconvoluted XRD profile (Figure 4.7(a)) of N-PVDF shows the reflection peaks at $2\theta = 18.6°$ and $26.5°$, characteristic of the non-polar α–phase [5, 6]. Eventually, the major characteristic peak at $2\theta = 20.6°$ is basically an overlapped reflection of (110/200) plane of β–phase and (110) of γ–phase. These indicate the coexistence of non-polar (α) and polar phases (β and γ) in N-PVDF. Whereas, the dual nature peak of β and γ get intensified for C-PVDF nanofibers and α–phase peak intensity totally diminished evidently, for C-PVDF fibers as marked in Figure 4.7(b). FT-IR spectra are also consistent with the results obtained from XRD. The characteristic vibrational bands corresponding to different elctroactive and non-polar phases are summarized in Figure 4.7(c). In particular, β
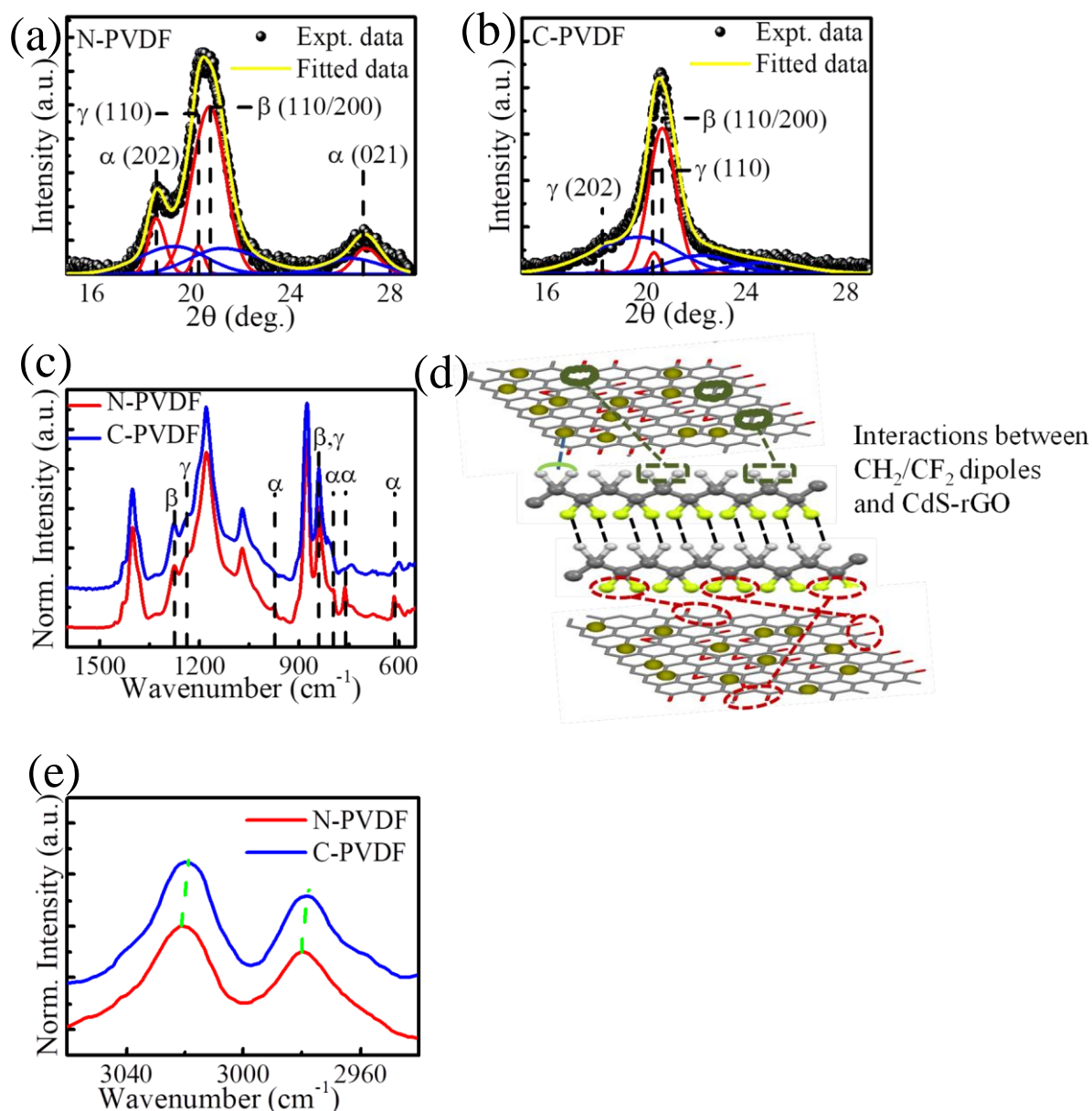
Figure 4.7 (a, b) XRD pattern and (c) FT-IR spectra (in the range of 1600-600 cm^{-1}) of N-PVDF and C-PVDF. (d) Scheme presents various interaction between CdS-rGO and PVDF dipoles. (e) FT-IR spectra (in the range of 3060-2940 cm^{-1}) of N-PVDF and C-PVDF.

and γ phases both superimposed at wavenumber (ν) = 841 cm^{-1} [6]. Moreover, the 841 cm^{-1} band was assigned to calculate total electroactive phase content along with the relative amount of each electroactive phase. The total electroactive phase content (F_{EA}) along with

relative amount of electroactive phases (β & γ) (Table 4.1) i.e., *F(β)* and *F(γ)* can be evaluated using these following equations.

$$F_{EA} = \frac{A_{841}}{\left(\frac{K_{841}}{K_{764}}\right)A_{764} + A_{EA}} \times 100\%$$

$$F(\beta) = F_{EA} \times \left(\frac{A_\beta}{A_\beta + A_\gamma}\right)$$

$$F(\gamma) = F_{EA} \times \left(\frac{A_\gamma}{A_\beta + A_\gamma}\right)$$

where, A_{841} and A_{764} signify the absorbance intensities at 841 cm^{-1} and 764 cm^{-1}, respectively, and K_{841} (7.7×10^4 cm^2 mol^{-1}) and K_{764} (6.1×10^4 cm^2 mol^{-1}) are the absorption coefficients at respective wavenumbers. A_β and A_γ are the intensities (area) calculated under the deconvoluted curves of the 841 cm^{-1} peak.

Table 4.1 Electroactive phase content and crystallinity.

Sample	*%F$_{EA}$*	*%F$_\beta$*	*%F$_\gamma$*	*%χ$_C$*
N-PVDF	78	56	22	52
C-PVDF	98	84	14	64

However, β and γ phases can be distinguished by their characteristic peaks at 1276 and 1234 cm^{-1} respectively. For both the cases (N-PVDF and C-PVDF), γ–phase appeared as a weak band at 1234 cm^{-1}, whereas, an intense peak exclusively emerged at 1276 cm^{-1} for β–phase. The absorption bands at ν = 975, 796, 764, 613 cm^{-1} corresponding to non-polar α–phase are detected in N-PVDF [6]. In contrast, these bands are totally disappeared in C-PVDF. Thus, C-PVDF nanofibers predominantly consist of β–phase. Additionally, electroactive phase content (*F$_{EA}$*) of 98% has been achieved for C-PVDF due to the amplification of 841 cm^{-1} band, sufficiently greater than that of N-PVDF. Indeed, complete reduction of α–phase and

considerable enhancement of β–phase ensure the remarkable effect of CdS-rGO nanocomposite in C-PVDF.

It can be deduced that concurrent poling and stretching during electrospinning process give rise to electroactive β–phase. However, it could not diminish all the α–phases. It indicates the existence of specific interaction between CdS-rGO and dipoles of PVDF, which is responsible for the preferential ordering of PVDF macromolecular chain in all-trans manner and successful reduction of α–phases in C-PVDF. Intriguingly, CdS nanoparticles are coupled to rGO surface through charge transfer (electron-hole transport) or electrostatic interaction. Besides, rGO is a very good migrator and acceptor of electrons, which indicates the electron rich property of rGO. As a matter of fact, a strong affinity towards electropositive CH_2 dipoles of PVDF has been created via C-H⁴⁴⁴⁴π interaction. In addition, presence of terminal hydroxyl groups (−OH) of rGO indicates a possible intermolecular H-bonding (O−H⁴⁴⁴⁴F) with the CF_2 dipoles of PVDF chain. Moreover, CdS is polar covalent due to significant electronegativity difference (0.9) between Cd and S. As a result, inhomogeneity in electron density gives rise to dipoles in CdS covalent bond. Therefore, a strong dipole-dipole interaction might be present between CdS and $−CH_2/−CF_2$ dipoles of PVDF. A schematic is presented in Figure 4.7(d) showing possible interactions.

It is evident that specific bands of CH_2 symmetric $[\nu_s(CH_2)]$ and CH_2 asymmetric $[\nu_{as}(CH_2)]$ stretching shifted towards lower frequency region for C-PVDF as shown in Figure 4.7(e), which elucidates the above mentioned interactions. Thus, it can be summarized that synergistic effect of different interactions between CdS-rGO nanocomposite and PVDF dipoles tends to transform non-electroactive α–phase into polar β–phase by overcoming the energy barrier, successively nucleating enhanced electroactive phase.

In addition, the overall crystallinity of the C-PVDF nanofiber is significantly improved due to interaction provided by CdS-rGO dopant. The overall degree of crystallinity (χ_C) (Table 4.1) was calculated using the following equation.

$$\chi_C = \frac{\sum A_{CR}}{\sum A_{cr} + \sum A_{amr}} \times 100\%$$

where, ΣA_{cr} and ΣA_{amr} represent the summation of the total integral areas of crystalline diffraction peaks and amorphous halo, respectively. It might influence the pyroelectric response of all organic-inorganic pyroelectric nanogenerator (A-PyNG).

4.3.6 Temperature Dependent FT-IR Spectroscopy
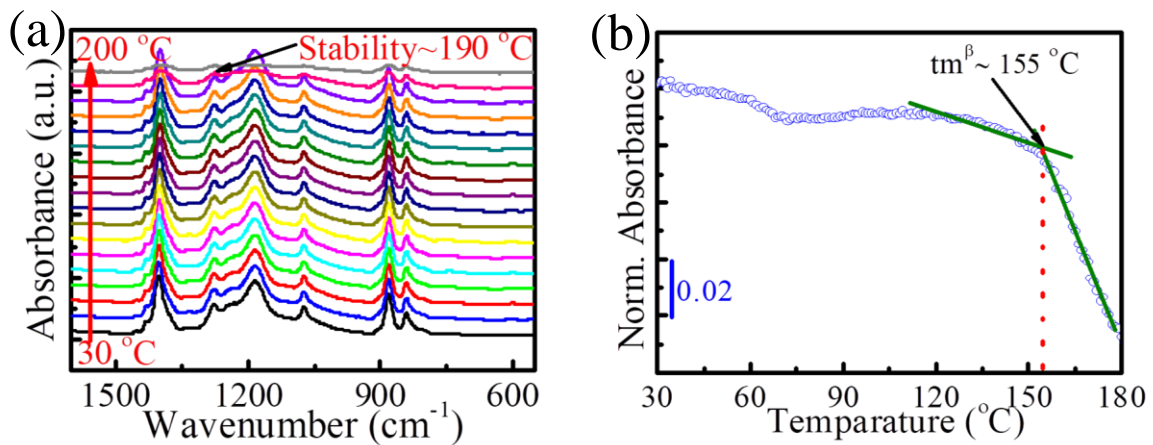
Figure 4.8 (a) Temperature dependent FT-IR spectra of C-PVDF in 10 ˚C interval. (b) The change in absorbance of β-phase w.r.t temperature variation (from 30 ˚C to 200 ˚C).

To evaluate the thermal stability of ferroelectric β-phase in C-PVDF nanofibers, thermal behaviour of the vibrational band at 1276 cm^{-1} representing the crystalline β-phase, was determined by performing in situ temperature dependent FT-IR spectroscopy (depicted in Figure 4.8(a, b)). According to Figure 4.8(b), the melting temperature of the β-phase is 155 ^{o}C, which is accredited to the starting temperature of ferroelectric to paraelectric phase transition [17]. Nevertheless the absorption band still exists up to 190 ^{o}C as marked in Figure

4.8(a). Therefore, the device can be implemented to a wide range of temperature ($30\,^{\circ}$C to $190\,^{\circ}$C). It can be noticed from Figure 4.8(a) that the crystalline β-phase at 1276 cm^{-1} does not relax back to α-phase due to any thermal motion. Thus, addition of CdS-rGO provides some plausible interactions which lead to a thermodynamically stable β-phase by restricting the motion of –CH$_2$/–CF$_2$ dipoles in PVDF chain.

4.3.7 X-ray Photoelectron Spectroscopy of Nanofibers

The compositional changes or conformational ordering of PVDF chains in C-PVDF due to the addition of CdS-rGO were further corroborated by X-ray photoelectron spectroscopy (XPS) as shown in Figure 4.9(a and b). Binding energies of each line were rectified in terms of F1s core level spectrum. The following discrepancies are evaluated during analysis.

1. The high resolution C1s core level spectrum of N-PVDF (as shown in Figure 4.9(a)) exhibits two peaks at binding energy levels of -289.5 and -294 eV, which are associated with two main carbon species i.e., CH$_2$ and CF$_2$ respectively. In contrast, a distinct chemical shift in lower binding energy level has been witnessed for C-PVDF nanofibers, where CH$_2$ and CF$_2$ peaks can be spotted at -288.9 and -293.5 eV respectively. Apart from the noticeable chemical shift, a substantial reduction in peak intensity for CF$_2$ species can be noticed if the CH$_2$ peak is normalized, as indicated by Δh in Figure 4c. As a consequence, it leads to a significant decrease in CF$_2$ peak area (ΔA_{CF2}) of 28% and slight enhancement of 4.6% CH$_2$ peak area ((ΔA_{CH2}) in case of C-PVDF nanofibers compared to that of N-PVDF nanofibers.

2. Moreover, slight broadening of another peak positioned at -688.1 eV can be identified in C-PVDF nanofibers from high resolution F1s core level spectrum (Figure 4.9(b)). The asymmetry occurred in lower binding energy side.
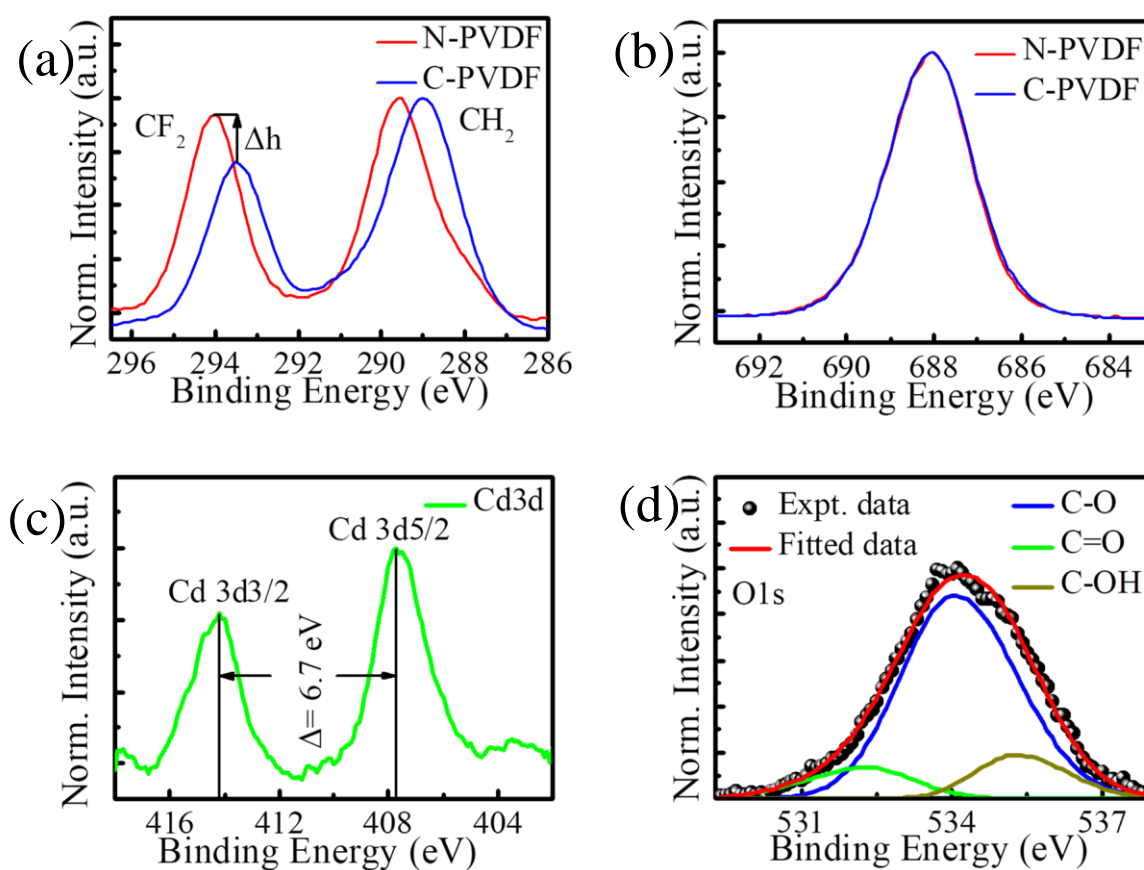
Figure 4.9 High resolution core level XPS spectra of (a) C1s and (b) F1s spectra of N-PVDF and C-PVDF. High resolution XPS spectra of (c) Cd 3d and (d) O 1s corresponding to C-PVDF.

The above experimental findings clearly conclude that there must be some considerable change in electronic environment of PVDF chain due to the interfacial interaction of CH_2 and CF_2 dipoles with partially reduced different functional groups of rGO and CdS nanoparticles attached to the rGO sheets. Additionally, Figure 4.9(c) shows core level doublet peaks of Cd 3d, appeared due to spin-orbit coupling at 414.2 eV and 407.7 eV corresponding to the $Cd_{d3/2}$ and $Cd_{d5/2}$ with a peak separation of 6.7 eV. It is noteworthy to mention that located peaks of Cd 3d are slightly shifted to the higher binding energy level in the composite as compared to the reported standard values of CdS nanoparticle. The red shift in binding energy might be

attributed to different nanoparticle size, their dispersion and interaction of CdS nanoparticles to the supporting substrate rGO sheet through electron-hole transfer [35, 36]. Moreover, curve de-convolution of high resolution O1s peak confirms the presence of C=O (oxygen double bonded to aromatic carbon), C-O (oxygen single bonded to carbon) and C-OH (phenolic oxygen/hydroxyl group attached to carbon) as assigned through different segments in Figure 4.9(d) [37]. This result indicates the presence of rGO in C-PVDF with lower carbonyl/carboxyl group content. Therefore, the oxygen functional groups of rGO sheet in association with CdS nanoparticle took part in the interfacial interaction with PVDF dipoles to obtain increased electroactive phase.

4.3.8 Pyroelectric Energy Harvesting Response
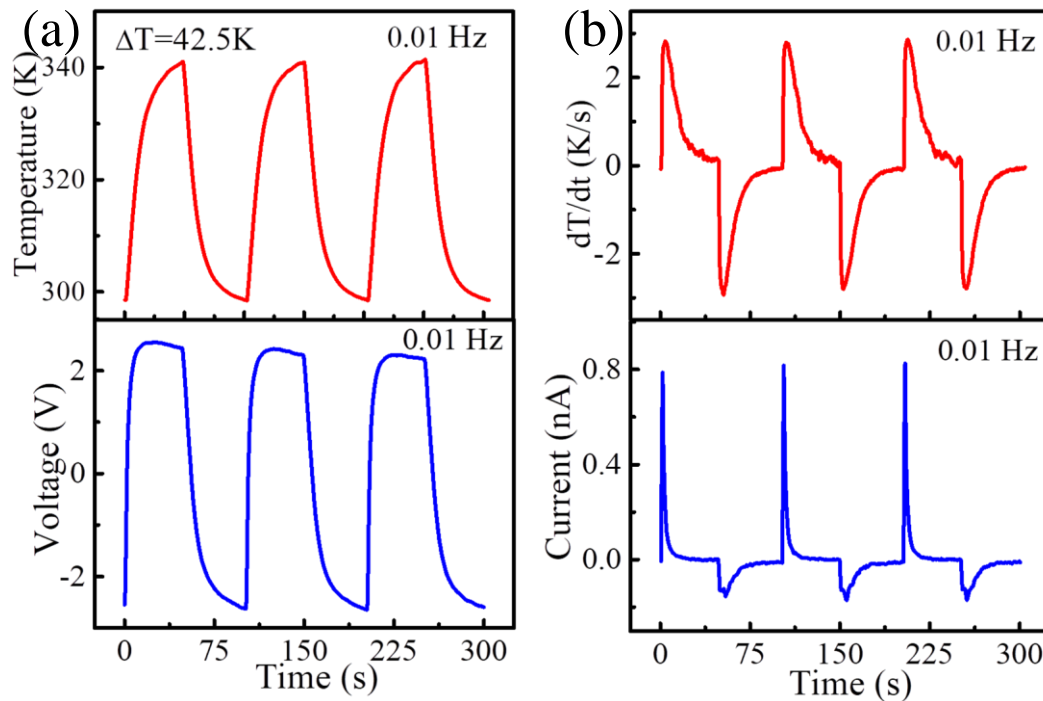
Figure 4.10 (a) Cyclic temperature variation (ΔT) with measured pyroelectric output voltages and (b) time dependent rate of change in temperature (dT/dt) with corresponding recorded pyroelectric current output under the exposure of IR-irradiation under 0.01 Hz switching frequency.

The pyroelectric performance of the all organic-inorganic pyroelectric nanogenerator (A-PyNG) was extensively studied in terms of open-circuit voltage/short-circuit current under different IR assisted heating and cooling cycle utilizing C-PVDF as an active layer and PEDOT:PSS film as organic electrode material. The ambient temperature was maintained nearly 293 K during the experiments. Figure 4.10 shows a real time cyclic temperature change (ΔT= 42.5 K) with corresponding rate of change in temperature (dT/dt= 3 K/s) and positive output voltage/current pulse (2.55 V/0.8 nA) under the switching frequency of 0.01 Hz IR irradiation. Therefore, the system can act in a large temperature difference. The dipoles of the C-PVDF start to oscillate by absorbing thermal energy (dT/dt > 0) while switching on the IR source. It leads to reduction in polarization density at the electrode surface. As an outcome, a positive pyroelectric output is obtained due to the generation of potential difference between top and bottom electrode.
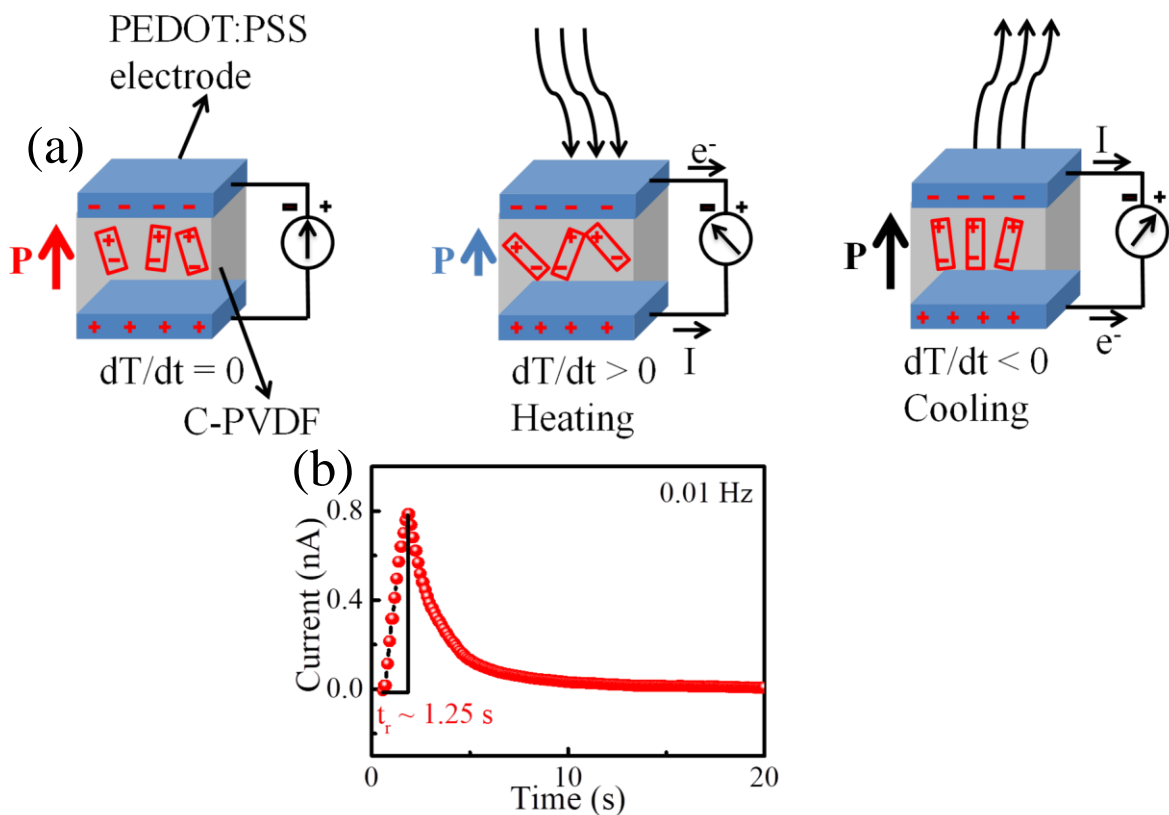
Figure 4.11 (a) Pyroelectric mechanism of A-PyNG and (b) single current peak under 0.01 Hz IR-irradiation frequency.

Subsequently, turning off the temperature source (dT/dt < 0) brings back the dipoles in previously ordered manner, which causes increase in surface polarization followed by negative output. A schematic is provided in Figure 4.11(a) describing the aforementioned mechanism. The current signal approaches the maximum value within a very short range of time (response time, t_r ~ 1.25 s under 0.01 Hz cyclic temperature change) followed by an exponential decay as illustrated in enlarged positive current peak in Figure 4.11(b).
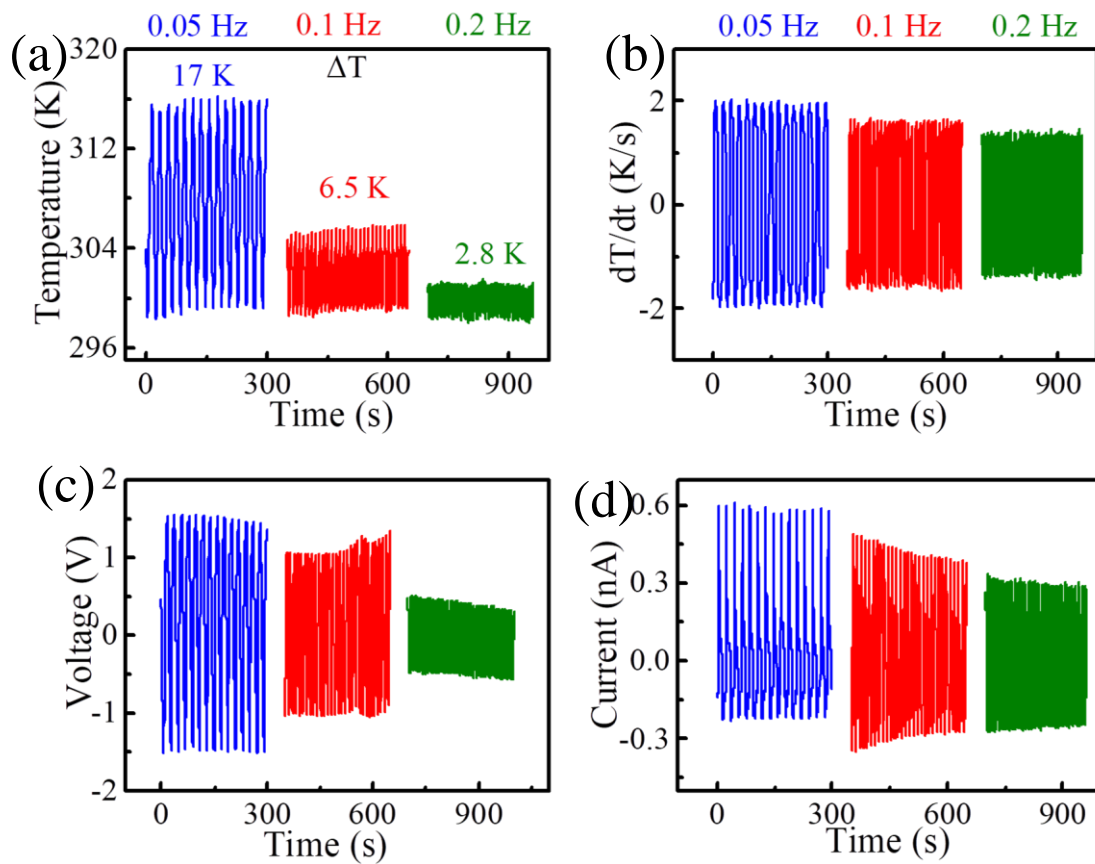
Figure 4.12 (a) Cyclic temperature variation (ΔT), (b) time dependent rate of change in temperature (dT/dt), (c) measured pyroelectric output voltages and (d) recorded pyroelectric current output under the exposure of IR-irradiation under 0.05 Hz, 0.1 Hz and 0.2 Hz switching frequency.

The response time is comparable to other pyroelectric and thermoelectric sensors [38]. In addition, continuous pyroelectric responses of A-PyNG under different magnitude of

temperature fluctuation with varying frequency are respectively depicted in Figure 4.12(a to d). A cyclic temperature change of $\Delta T = 42.5$ K to 2.8 K resulted in a decrease in pyroelectric voltage and current of $V_{oc} \sim 2.55$ V to 0.5 V and $I_{sc} \sim 0.8$ nA to 0.33 nA respectively. Thus, irradiation frequency increment (0.01 Hz to 0.2 Hz) considerably influenced the pyroelectric output. It is due to the reduction in irradiation time with increasing switching frequency which leads to lower amount of heat to reach the A-PyNG surface, thereby less polarization change. It can be observed from Figure 4.13(a and b) that pyroelectric output voltage and current waveforms linearly changed with ΔT and dT/dt respectively, which is reconcilable with the following theoretical relationships $I_{sc} = pA\,{dT}/{dt}$ and $V_{oc} = \frac{p}{\varepsilon}t\Delta T$ [7], where I_{sc}, V_{oc}, p, A, t, ΔT, dT/dt denote pyroelectric current, voltage, pyroelectric co-efficient, effective electrode area, thickness along polarization direction, change in temperature and rate of change in temperature respectively. It is noteworthy to mention that A-PyNG is capable of detecting and converting very low temperature change ($\Delta T = 2.8$ K) to output signal. Moreover, pyroelectric co-efficient (*p*) of C-PVDF was assessed to be $p \sim -63$ $\mu C/(m^2 K)$ according to Lang-Steckel method, $I_{sc} = hw\,{dT}/{dt}$ where *h* and *w* precisely symbolize thickness and width of nanofibers respectively. Therefore, the exhibited pyroelectric output and pyroelectric co-efficient of A-PyNG is sufficiently higher in comparison to N-PVDF made (organic/metal/synthetic electrode based) PyNG [5, 6]. The superior performance of A-PyNG can be attributed to the following aspects:

1. Firstly, electrode material PEDOT:PSS polymer film exhibits excellent photon energy absorption ability, photo-thermal heat localization capacity and outstanding electrical conductivity [5], additionally its relatively greater adhesion property to hydrophobic C-PVDF nanofiber surface as illustrated in Figure 4.6(d).

2. Oxygen functional groups of rGO intensively absorb mid-IR radiation. Additionally, the radiation absorbance of rGO is quite high. The absorbed IR actively increases the temperature of rGO as well as C-PVDF nanofiber mat by exciting the C-C bond by producing phonons.

3. rGO basically consists of several microsized monolayers of graphene intercalated covalently through different oxygen functional groups such as C=O, C-O, C-OH as evident from XPS result presented in Figure 4.9. Consequently, it yields oxygen defects/mass defects leading significant structural change (hybridisation sp^2 to sp^3) and subsequent band deformation. Moreover, the defects might overlay to enhance the effective size. Therefore, the alteration in local vibrational characteristics stimulates the acoustic mismatch causing enhanced phonon scattering. Thus a significant reduction in thermal conductivity is observed in rGO compared to single-layered graphene. Furthermore, incorporation of oxygen functional groups break the reflection symmetry of graphene, might be affecting the thermal conductivity.

4. In addition, the polymer matrix might aggregate between the graphitic layers preventing the thermal dissipation.

5. Besides, enhanced ferroelectric β-phase content and improved crystallinity of C-PVDF have extensive effect on the improved performance of A-PyNG.

These factors synergistically coupled to promote improved pyroelectric performance in A-PyNG. Furthermore, the pyroelectric output power of the A-PyNG was evaluated by recording instantaneous output voltage across varying load resistances (R_L) ranging from 0.25 GΩ to 1 TΩ under IR radiation frequency of 0.01 Hz with dT/dt of 2.93 K/s (output voltage as a function of load resistance shown in Figure 4.13(c). The maximum output power ($P = \frac{V^2}{R_L}$) is calculated to be 183 pW (as shown in Figure 4.13(d)). The overall pyroelectric
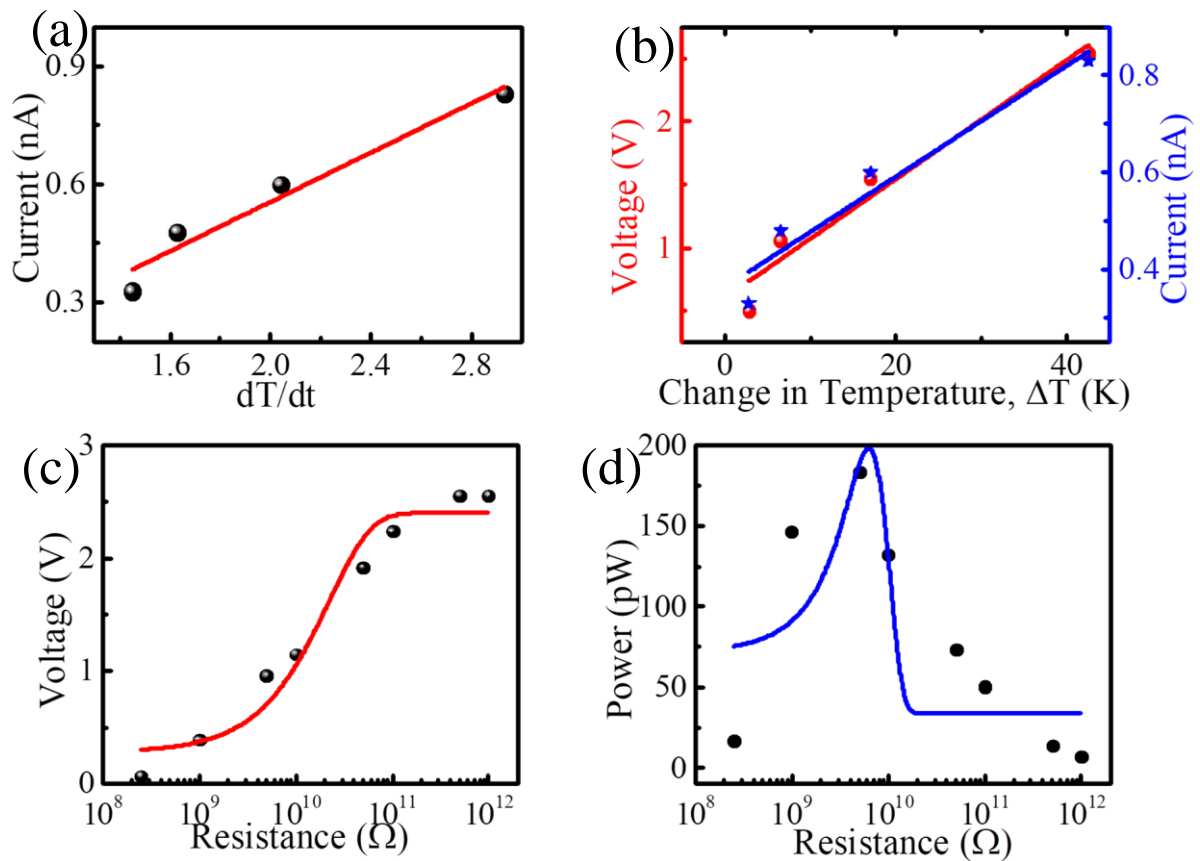
Figure 4.13 (a) Pyroelectric current variation vs dT/dt, (b) pyroelectric current and voltage variation w.r.t change in temperature (ΔT). (c) Pyroelectric voltage and (d) power output variation with varying load resistance.

performance of A-PyNG is comparable/higher than many previously reported pyroelectric devices, as reported in Table 4.2. The above results precisely indicate the utilization of A-PyNG in temperature sensing (from low to moderate temperature change) and self-powered wearable biomedical application.

Table 4.2 Comparison of the pyroelectric output power of A-PyNG with reported NGs.

Active Material	Electrode Material	Pyroelectric Co-efficient	Output Voltage/Current	References
PVDF nanofiber	Polyester fabric	4 nCm^{-2}K^{-1}	70 mV/20 pA	*ACS Appl. Nano Mater.* 2019, 2, 2013–2025
PVDF/GO nanofiber	Polyester fabric	**27** nCm^{-2}K^{-1}	100 mV/45 pA	*ACS Appl. Nano Mater.* 2019, 2, 2013–2025
PVDF nanofiber	Cu foil tape	Not given	Not given/20000 pA	*J. Mater. Chem. A* 2018, 6, 3500–3509
PVDF/MWCNT nanofiber	Polyester fabric (Ni-Cu plated)	60 nCm^{-2}K^{-1}	250 mV/71 pA	*Mater. Adv.* 2021, 2, 4370-4379
PVDF/CH$_3$NH$_3$PbI$_3$ nanofiber	Conductive fabric	0.044 nCm^{-2}K^{-1}	41.78 mV/18.2 pA	*ACS Appl. Mater. Interfaces* 2019, 11, 27279−27287
PVDF/PANI nanofiber	PEDOT:PSS	42 μCm^{-2}K^{-1}		*ACS Appl. Electron. Mater.* 2021, 1, 248−259
PVDF film	Cu foil	27 μCm^{-2}K^{-1}	192 V/12 μA	*J. Mater. Chem. A* 2014, 2, 11940 – 11947
PVDF film	Platinum	27.2 μCm^{-2}K^{-1}	150 V/0.12 μAcm^{-2}	*Nano Energy* 2016, 22, 19-26
Hoof tandon	Not given	4 nCm^{-2}K^{-1}	Not given	*Nature* 1966, 212, 704−705
Fluorapatite/gelatin	Not given	50 nCm^{-2}K^{-1}	Not given	*Biomacromolecules* 2015, 16, 2814−2822
KNbO3-PDMS composite	Ag and ITO films	800 nCm^{-2}K^{-1}	2 mV/ 20 pA	*Adv. Mater.* 2012, 24, 5357−5362
PVDF/CdS-rGO nanofiber	PEDOT:PSS	63 μCm^{-2}K^{-1}	2.55 V/0.8 nA	*This work*

4.4 Application: Self-Powered Pyroelectric Breathing Sensor Application

To explore the potential of converting different time dependent temperature oscillation into electricity, a practical application of A-PyNG has been demonstrated. Initially, A-PyNG was constructed in desired shape. Afterwards, it was mounted on a particular position of N-95
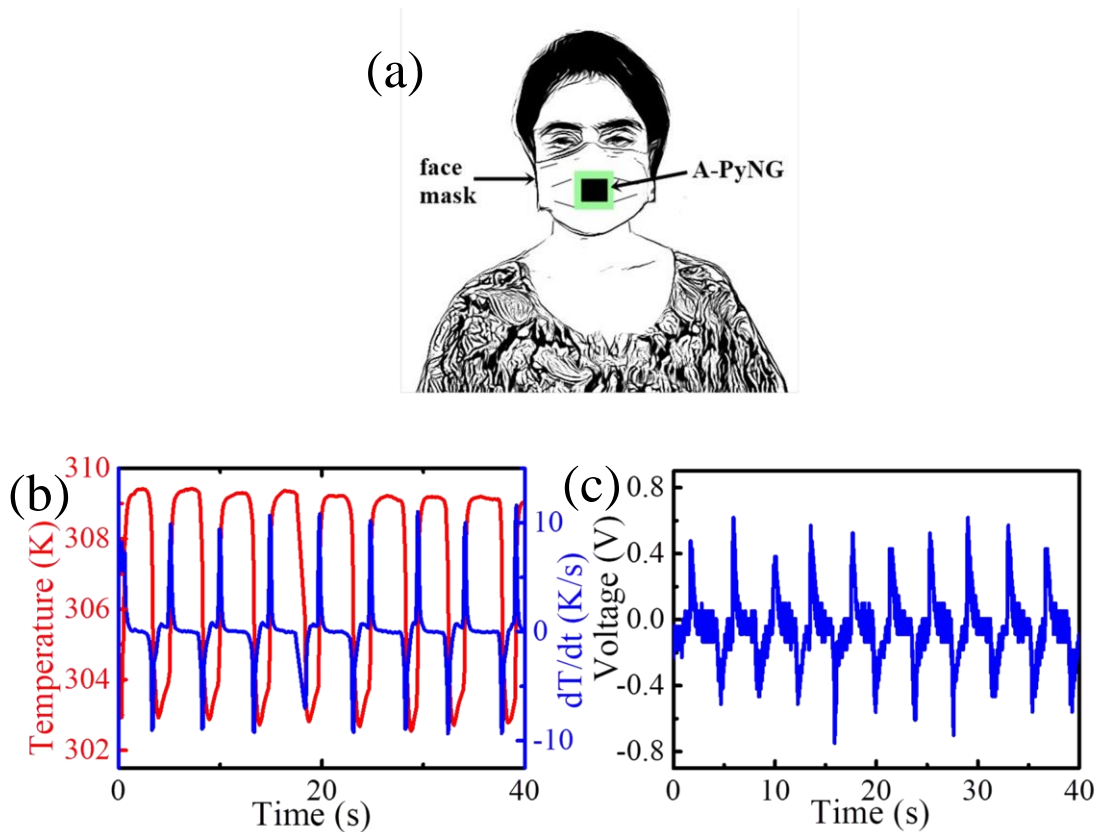
Figure 4.14 (a) Schematic of A-PyNG attached to a face mask for building pyroelectric face mask. (b and c) Variation of temperature gradient and pyroelectric voltage output under dynamic inhale-exhale process (application of breathing/respiratory sensor) respectively.

breathing mask in such a way so that most of the air flow could accumulate over the A-PyNG during dynamic inhale-exhale process. The entire arrangement was worn on a healthy volunteer's face as face mask to carry out the experiment. Additionally, the experiment was conducted at ambient temperature ~ 293 K. Accordingly the inhaled air temperature was 293 K and the exhaled air temperature from lungs should be same as normal body temperature ~310 K. Therefore, temperature difference concerning inhaled and exhaled air throughout the continuous breathing process will create a time dependent temperature gradient around mouth resulting in pyroelectric effect. To determine the absolute temperature of the system and the relative change in temperature, a thermal sensor was attached on the surface of A-PyNG. As

illustrated in Figure 4.14(a), recorded minimum and maximum temperature of A-PyNG was nearly 303 K and 309.6 K respectively. Therefore, the normal respiration process produced a temperature variation of 6.6 K with a fast rate of change in temperature of 10 K/s underneath the mask (shown in Figure 4.14(b)). As a consequence, the open-circuit voltage reached up to 0.6 V in this experimental condition as shown in Figure 4.14(c). The mechanism of dipolar orientation/polarization change during this dynamic procedure is similar as the pyroelectric effect due to periodic heating and convective cooling. The process of cooling during respiration was accompanied by inhaling the comparatively cooler atmospheric air. Therefore, above findings validated the feasibility of A-PyNG as an efficient breathing sensor.

Respiration rate is a vital sign for different pulmonary disorders such as sleep apnea, asthma, emphysema, bronchitis, chronic obstructive pulmonary disease etc. Moreover, R_{res} is associated with in-out air flow and lung volume. Therefore, alteration in respiration rate is an early sign of serious pulmonary dysfunction. From the depicted results, respiration rate (R_{res}) of the subject can also be monitored using the following equation, $R_{res} = \frac{1}{t_m - t_{m-1}} \times 60 \ (bpm)$ [39]. The calculated respiration rate for the volunteer is 14 breaths per minute (bpm), which is the normal respiration rate (12-16 cycles per minute) for an adult at rest condition. Thus, A-PyNG is capable of self-powered monitoring of real time respiration rate as well as pulmonary health especially for aged persons and patients suffering from respiratory illness.

4.5 Conclusion

In summary, we have demonstrated the successful development of an all organic-inorganic pyroelectric energy harvester based on graphene functionalized nanocomposite (CdS-rGO) induced PVDF nanofiber and PEDOT:PSS conducting polymer. It is evident that the device

achieved an enhanced pyroelectric output of 2.55 V/0.8 nA with an instantaneous output power of 183 pW under 0.01 Hz thermal oscillation. The customization of PEDOT:PSS organic electrode and incorporation of CdS-rGO nanocomposite indeed influence the enhanced thermal energy harvesting efficiency of A-PyNG. In addition, high sensitivity of the device towards different temperature gradients (moderate to low temperature change, 42.5 K to 2.8 K) suggests its potential of being a self-powered temperature sensor. Most importantly, A-PyNG is capable of scavenging thermal energy from the temperature fluctuation created by dynamic inhale-exhale process. Additionally, its ability to record human respiration rate enable the device to act as a wearable breathing sensor. Therefore, this research provides a route to fabricate efficient pyroelectric energy harvester by polymer on polymer stacking, which may be appropriate for different applications such as temperature imaging, waste heat energy utilization and self-powered medical diagnosis.

4.6 References

1. Zheng, L.; Cheng, G.; Chen, J.; Lin, L.; Wang, J.; Liu, Y. S.; Li, H. X.; Wang, Z. L. A Hybridized Power Panel to Simultaneously Generate Electricity from Sunlight, Raindrops, and Wind around the Clock. *Adv. Energy Mater.* **2015**, *5*, 1501152.

2. Ma, M. Y.; Liao, Q. L.; Zhang, G.; Zhang, Z.; Liang, Q. J.; Zhang, Y. Self-Recovering Triboelectric Nanogenerator as Active Multifunctional Sensors. *Adv. Funct. Mater.* **2015**, *25*, 6489−6494.

3. Xie, M.; Zabek, D.; Bowen, C.; Abdelmageed, M.; Arafa, M. Wind-driven Pyroelectric Energy Harvesting Device. *Smart Mater. Struct.* **2016**, *25*, 125023.

4. Wang, L. Z.; Song, J. Piezoelectric Nanogenerators Based on Zinc Oxide Nanowire Arrays. *Science,* **2006**, *312*, 242−246.

5. Ghosh, K. S.; Sinha, K. T.; Xie, M.; Bowen, R. C.; Garain, S.; Mahanty, B.; Roy, K.; Henkel, K.; Schmeißer, D.; Kim, K. J.; Mandal, D. Temperature−Pressure Hybrid

Sensing All-Organic Stretchable Energy Harvester. *ACS Appl. Electron. Mater.* **2021**, *3*, 1, 248–259.

6. Roy, K.; Ghosh, K. S.; Sultana, A.; Garain, S.; Xie, M.; Bowen, R. C.; Henkel, K.; Schmeiβer, D.; Mandal, D. A Self-Powered Wearable Pressure Sensor and Pyroelectric Breathing Sensor Based on GO Interfaced PVDF Nanofibers. *ACS Appl. Nano Mater.* **2019**, *2*, 4, 2013–2025.

7. Zabek, D.; Seunarine, K.; Spacie, C.; Bowen, C. Graphene Ink Laminate Structures on Poly(vinylidene difluoride) (PVDF) for Pyroelectric Thermal Energy Harvesting and Waste Heat Recovery. *ACS Appl. Mater. Interfaces* **2017**, *9*, 9161−9167.

8. Yang, Y.; Guo, W.; Pradel, C. K.; Zhu, G.; Zhou, Y.; Zhang, Y.; Hu, Y.; Lin, L.; Wang, L. Z. Pyroelectric Nanogenerators for Harvesting Thermoelectric Energy. *Nano Lett*. **2012**, *12*, 2833−2838

9. Gan, W. C.; Majid, W. H. Abd. Effect of TiO_2 on Enhanced Pyroelectric Activity of PVDF Composite. *Smart Mater. Struct.* **2014**, *23*, 045026 (1-9).

10. Berlincourt, D.; Jaffe, H.; Shiozawa, R. L. Electroelastic Properties of the Sulfides, Selenides, and Tellurides of Zinc and Cadmium. *Phys. Rev.*, **1963**, *129*, 1009−17.

11. Yang, Y.; Jung, H. J.; Yun, K. B.; Zhang, F.; Pradel, C. K.; Guo, W.; Wang, L. Z. Flexible Pyroelectric Nanogenerators Using a Composite Structure of Lead-Free KNbO(3) Nanowires. *Adv. Mater.*, **2012**, *24*, 5357−5362.

12. Xue, H.; Yang, Q.; Wang, D.; Luo, W.; Wang, W.; Lin, M.; Liang, D.; Luo, Q. A Wearable Pyroelectric Nanogenerator and Self-Powered Breathing Sensor. *Nano Energy*, **2017**, *38*, 147–154.

13. Huang, S.; Yee, A. W.; Tjiu, C. W.; Liu, Y.; Kotak, M.; Boey, F. C. Y.; Ma, J.; Liu, T.; Lu, X. Electrospinning of Polyvinylidene Difluoride with Carbon Nanotubes:

Synergistic Effects of Extensional Force and Interfacial Interaction on Crystalline Structures. *Langmuir* **2008**, *24,* 13621-13626.

14. Ribeiro, C.; Costa, M. C.; Correia, M. D.; Pereira, N-. J.; Oliveira, J.; Martins, P.; Gonçalves, R.; Cardoso, F. V.; Méndez, L-. S. Electroactive Poly(vinylidene fluoride)-Based Structures for Advanced Applications. *Nature Protocols* **2018**, *13*, 681–704.

15. Levitt, A. S.; Alhabeb, M.; Hatter, C. B.; Sarycheva, A.; Dion, G.; Gogotsi, Y. Electrospun MXene/Carbon Nanofibers as Supercapacitor Electrodes. *J. Mater. Chem. A* **2019**, *7*, 269–277.

16. Chen, S.; Han, D.; Hou, H. High Strength Electrospun Fibers. *Polym. Adv. Technol.* **2011**, *22* (3), 295–303.

17. Ghosh, S. K.; Mandal, D. Synergistically Enhanced Piezoelectric Output in Highly Aligned 1D Polymer Nanofibers Integrated All-fiber Nanogenerator for Wearable Nano-Tactile Sensor. *Nano Energy* **2018**, *53*, 245−257.

18. Mandal, D.; Kim, K. J.; Lee, J. S. Simple Synthesis of Palladium Nanoparticles, β-Phase Formation, and the Control of Chain and Dipole Orientations in Palladium-Doped Poly(vinylidene fluoride) Thin Films. *Langmuir* **2012**, *28*, 10310−10317.

19. Liao, Y.; Zhang, C.; Zhang, Y.; Strong, V.; Tang, J.; Li, X. G.; Kalantar-Zadeh, K.; Hoek, E. M. V.; Wang, K. L.; Kaner, R. B. Carbon Nanotube/Polyaniline Composite Nanofibers: Facile Synthesis and Chemosensors. *Nano Lett.* **2011**, *11* (3), 954–959.

20. Zhang, S.; Ni, W.; Kou, X.; Yeung, M. H.; Sun, L.; Wang, J.; Yan, C. Formation of Gold and Silver Nanoparticle Arrays and Thin Shells on Mesostructured Silica Nanofibers. *Adv. Funct. Mater.* **2007**, *17* (16), 3258–3266.

21. Ren, H.; Zheng, L.; Wang, G.; Gao, X.; Tan, Z.; Shan, J.; Cui, L.; Li, K.; Jian, M.; Zhu, L. Transfer-Medium-Free Nanofiber-Reinforced Graphene Film and

Applications in Wearable Transparent Pressure Sensors. *ACS Nano* **2019**, *13* (5), 5541–5548.

22. Shao, W.; Tebyetekerwa, M.; Marriam, I.; Li, W.; Wu, Y.; Peng, S.; Ramakrishna, S.; Yang, S.; Zhu, M. Polyester@MXene Nanofibers-Based Yarn Electrodes. *J. Power Sources* **2018**, *396*, 683–690.

23. Jaleh, B.; Jabbari, A. Evaluation of Reduced Graphene Oxide/ZnO Effect on Properties of PVDF Nanocomposite Films. *Appl. Surf. Sci.* **2014**, *320*, 339−347.

24. Garain, S.; Jana, S.; Sinha, K. T.; Mandal, D. Design of In Situ Poled Ce^{3+}-Doped Electrospun PVDF/Graphene Composite Nanofibers for Fabrication of Nanopressure Sensor and Ultrasensitive Acoustic Nanogenerator. *ACS Appl. Mater. Interfaces* **2016**, *8*, 4532−4540.

25. Cha, S.; Kim, M. S.; Kim, H.; Ku, J.; Sohn, I. J.; Park, J. Y.; Song, G. B.; Jung, H. M.; Lee, K. E.; Choi, L. B. Porous PVDF as Effective Sonic Wave Driven Nanogenerators. *Nano Lett.* **2011**, *11*, 5142.

26. Fang, J.; Wang, X.; Lin, T. Electrical Power Generator from Randomly Oriented Electrospun Poly(vinylidene fluoride) Nanofibre Membranes. *J. Mater. Chem.* **2011**, *21*, 11088−11091.

27. Khan, Y.; Ostfeld, E. A.; Lochner, M. C.; Pierre, A.; Arias, C. A.; Monitoring of Vital Signs with Flexible and Wearable Medical Devices. *Adv. Mater.* **2016**, *28*, 4373–4395.

28. Rajala, S.; Lekkala, J. Film-Type Sensor Materials PVDF and EMFi in Measurement of Cardiorespiratory Signals: A review. *IEEE Sensors J.* **2012** , *12* , 439.

29. Chiu, Y-.Y.; Lin, Y-. W.; H.-Y. Wang, Y-. H.; Huang, B-. S.; Wu, H-. M. Development of a Piezoelectric Polyvinylidene Fluoride (PVDF) Polymer-Based

Sensor Patch for Simultaneous Heartbeat and Respiration Monitoring. *Sens. Actuators, A* **2013**, *189*, 328−334.

30. Yi , F.; Lin, L.; Niu, S.; Yang, K. P.; Wang, Z.; Chen, J.; Zhou, Y.; Zi, Y.; Wang, J.; Liao, Q.; Zhang, Y.; Wang, L. Z. Stretchable-Rubber-Based Triboelectric Nanogenerator and Its Application as Self-Powered Body Motion Sensors. *Adv. Funct. Mater.* **2015**, *25*, 3688.

31. Li, Q.; Guo, B.; Yu, J.; Ran, J.; Zhang, B.; Yan, H.; Gong, R. J. Highly Efficient Visible-Light-Driven Photocatalytic Hydrogen Production of CdS-Cluster-Decorated Graphene Nanosheets. *J. Am. Chem. Soc.* **2011**, *133*, 10878–10884.

32. Zhang, N.; Yang, Q-. M.; Tang, R-. Z.; Xu, J-.Y. CdS–Graphene Nanocomposites as Visible Light Photocatalyst for Redox Reactions in Water: A Green Route for Selective Transformation and Environmental Remediation. *Journal of Catalysis* **2013**, *303*, 60–69.

33. Wua, J.; Baia, S.; Shena, X.; Jiang, L. Preparation and Characterization of Graphene/CdS Nanocomposites. *Appl. Surf. Sci.* **2010**, *257*, 747–751.

34. Kaveri, S.; Thirugnanam, L.; Dutta, M.; Ramasamy, J.; Fukata, N. Thiourea Assisted One-Pot Easy Synthesis of CdS/rGO Composite by the Wet Chemical Method: Structural, Optical, and Photocatalytic Properties. *Ceram. Int.* **2013**, *39*, 9207–9214.

35. Lee, Y. K.; Kim, M.; Hahn, J.; Suh, S. J.; Lee, I.; Kim, K.; Han, W. S. Assembly of Metal Nanoparticle-Carbon Nanotube Composite Materials at the Liquid/Liquid Interface. *Langmuir* **2006**, *22,* 1817−1821.

36. Li, J.; Tang, S.; Lu, L.; Zeng, C. H. Preparation of Nanocomposites of Metals, Metal Oxides, and Carbon Nanotubes via Self-Assembly. *J. Am. Chem. Soc*. **2007**, *129*, 9401–9409.

37. Gupta, B.; Kumar, N.; Panda, K.; Kanan, V.; Joshi, S.; Fisher, V-. I. Role of Oxygen Functional Groups in Reduced Graphene Oxide for Lubrication. *Sci Rep* **2017**, *7*, 45030.

38. Sultana, A.; Ghosh, K. S.; Alam, M.; Sadhukhan, P.; Roy, K.; Xie, M.; Bowen, R. C.; Sarkar, S.; Das, S.; Middya, R. T.; Mandal, D. Methylammonium Lead Iodide Incorporated Poly(vinylidene fluoride) Nanofibers for Flexible Piezoelectric-Pyroelectric Nanogenerator. *ACS Appl. Mater. Interfaces* **2019**, *11*, 27279–27287.

39. Chen, S.; Wu, N.; Ma, L.; Lin, S.; Yuan, F.; Xu, Z.; Li, W.; Wang, B.; Zhou, J.; Non-Contact Heartbeat and Respiration Monitoring Based on Hollow-Microstructure Self-Powered Pressure Sensor. *ACS Appl. Mater. Interfaces* **2018**, *10*, 3660−3667.

Chapter 5

Graphene Oxide Assisted PVDF Nanofiber Based Piezo- and Pyroelectric Nanogenerator

5.1 Introduction

Recent progress in wearable pressure sensors and electronic skins (E-skins) that are able to mimic human skin and organs by transducing external stimuli such as strain, pressure, temperature and humidity, have led to research interest [1-4] in new materials for sensing during physiological activities, health care monitoring and medical diagnosis [5-10]. A number of research groups have demonstrated flexible and sensitive pressure sensors based on gold nanowires [11], metal nanoparticles [12, 13], carbon based materials such as carbon nanotubes [14, 15], graphene [16] and polymers incorporated with a range of sensing materials that exploit a variety of sensing mechanisms which include piezoresistive, piezoelectric, piezocapacitive and triboelectric effects. Among these mechanisms, sensors based on piezoelectric and triboelectric materials, often termed *nanogenerators* (NGs), are promising for self-powered sensing applications [17]. However, triboelectric sensors are based on capacitors with an air-gap which may be sensitive to undesired side-effects such as static electricity, stray capacitances and temperature variations. In contrast, piezoelectricity is driven by the material polarisation due to the separation of electrical charges where the resulting polarisation is changed as a result of an external mechanical stimulus. To date, several NGs have been developed using a range of inorganic piezoelectric materials such as lead zirconate titanate (PZT), $BaTiO_3$, $ZnSnO_3$, CdS, ZnO and GaN which have exhibited promising vibrational energy harvesting performance [18-22]. However, the high cost, high stiffness, high density, complex processing route, brittleness and toxic components during processing restrain their utilization in wearable electronics and health-care monitoring. However, organic ferroelectric polymers such as, poly(vinylidene fluoride) (PVDF) (chemical formula: $(CH_2–CF_2)_n$) and its copolymers are advantageous in terms of flexibility, low density, large-area and low cost processing and environmental-friendly (lead-free) fabrication which has led to interest in these materials towards NG engineering and sensor

173

implementation. The piezoelectric and ferroelectric behaviour of semi-crystalline PVDF is attributed to the polar phases such as $\beta-$ (TTTT conformation) and $\gamma-$ phase (T$_3$GT$_3$G′ conformation), whereas the $\alpha-$ phase (TGTG′ conformation) is non-polar [23-28].

Therefore, efforts have been made to achieve effective $\beta-$ phase nucleation in a PVDF matrix; this includes the use of uniaxial or biaxial mechanical stretching at elevated temperature, electrical poling and spin coating. In this regard, the electrospinning process is a relatively simple technique for $\beta-$ phase transformation, whereby large stretching forces are applied on electrified solution jets for producing in-situ poled nanofibers that can be several centimetres in length and have a micro/nano-size diameter [26, 29, 30]. More recently, graphene as a highly conductive, rigid and thin 2D- material, has gathered significant attention as a promising material in the field of multi-functional wearable electronics and biomedical engineering due to its biocompatibility and excellent energy storage potential [31, 32]. The incorporation of nanofillers, which include 2D- materials such as transition metal dichalcogenides (TMDCs), graphene and graphene nanocomposites, for example, Ce^{3+}/graphene and CdS/rGO nanocomposites can increase the polar content of the PVDF nanofibers and have been employed for energy harvesting applications [26, 29, 30]. Despite their noticeable energy harvesting performance, Ce^{3+}/graphene and CdS/rGO nanocomposites doped PVDF nanofibers have yet to be used as a wearable pressure sensor and pyroelectric breathing sensor. For example, a Ce^{3+}/graphene based device was used as an acoustic sensor and wind energy harvester [26]. In other work, a CdS/rGO based device was demonstrated as a mechanical energy harvester with a relatively low output voltage [30]. A current challenge in the use of graphene in biomedical applications stems from its costly manufacturing process and lack of batch production efficiency. To overcome these disadvantages, graphene oxide (GO), a graphene derivative, can be used with a similar functionality and is capable of being used in mass production.

In this chapter, a facile and low cost approach to fabricate highly flexible, sensitive and self-powered wearable pressure and temperature sensor is presented for the creation of epidermal devices based on GO encapsulated PVDF nanofibers. The graphene oxide was synthesized using a solution based chemical treatment approach. The graphene based piezo- and pyro-electric nanogenerator (GPPNG) is shown to exhibit a high sensitivity to both static and dynamic tactile stimuli with a high pressure sensitivity of up to 4.3 V/kPa and can also detect a pressure as low as 10 Pa. The low range detection limit makes it favourable as a wearable pressure sensor. In addition, it is demonstrated that there is potential to generate an output power density up to ~6.2 mW/m^2 and ~1.2 nW/m^2 under mechanical and thermal fluctuations respectively. We further demonstrate that the GPPNG sensor can accurately detect and discriminate different skin related stresses induced by finger bending and stretching, wrist bending, vocal vibrations (speech signals) and other human body motions. Finally, the PVDF/GO based device can be utilized as a pyroelectric breathing sensor. These wide ranging properties extend the potential application of GPPNG towards energy harvesting, low power electronics and biomedical fields which include personal health monitoring, acute heart and breathe disease diagnosis, human-computer interaction as well as portable electronic devices.

5.2 Experimental Section

5.2.1 Synthesis of GO

Graphene oxide was produced by oxidizing graphite powder using the modified Hummers' method [33]. Figure 5.1(a) shows the synthesis and molecular structure of GO. In brief, 6 g of graphite powder was thoroughly mixed with 3 g of $NaNO_3$ in the 100 mL of cold concentrated sulphuric acid. The solution was then stirred well in an ice bath that was maintained below 5 ^{o}C. A mass of 15 g of $KMnO_4$ was then gradually added to the resulting
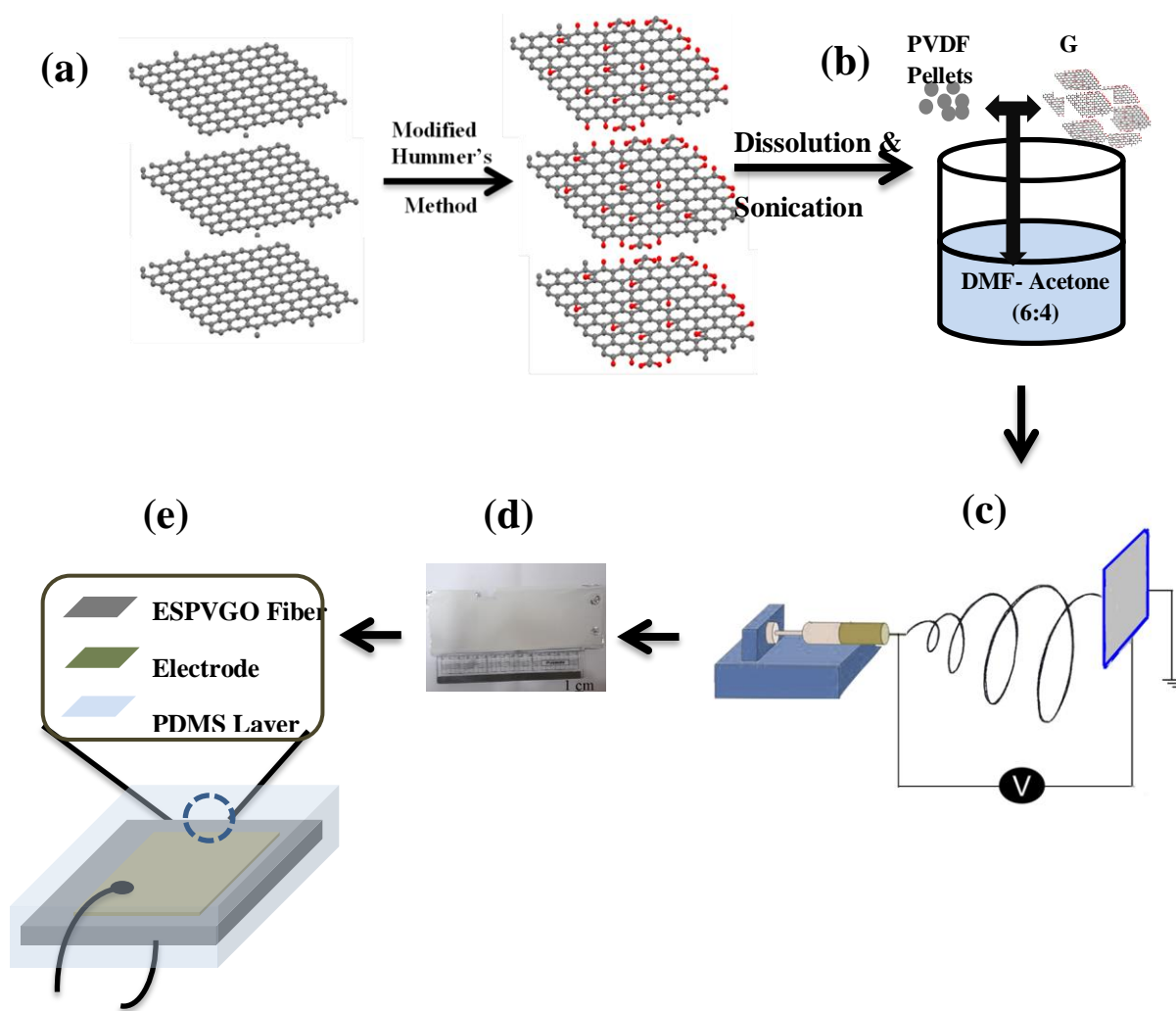
Figure 5.1 Schematic route for the fabrication of GPPNG. (a) Preparation and molecular structure of graphene oxide using the modified Hummer's method. (b) Preparation of spinning solution. (c) Experimental setup for preparation of pure PVDF and PVDF/GO nanofibers. (d) Image of large piece PVDF/1 wt.% GO fiber prepared via electrospinning (7×18 cm^2). (e) A sketch of the nanogenerator stack.

solution while being continuously stirred. After removal from the cooling bath, stirring of the mixture was continued at room temperature. Afterwards, 200 mL of water was added to the solution and the temperature was increased to 98 $^{\circ}$C while being continuously stirred. Then, 500 mL of de-ionized water and 30 mL of 30% H$_2$O$_2$ were added until effervescence has ceased and the colour of the solution changed to light brown and was left overnight. The

brown precipitate was then separated from the supernatant and then washed repeatedly with 5% (V/V) HCl. Finally the material was centrifuged with deionized (DI) water followed by drying in a vacuum oven. Then, 100 mg of the as-prepared GO was collected and dissolved in EG for further synthesis and analysis.

5.2.2 Preparation of PVDF/GO Nanofibers

To prepare the spinning solutions, firstly, 12 wt% PVDF was dissolved in a mixed solvent of DMF and acetone (6:4) and it was stirred for 3 hours at 60 ^{o}C. Successively, GO powder with different weight ratios (0.25, 0.5 and 1 (w/v)%) was immersed into the PVDF solution while being vigorously stirred for 8 hours at 60 ^{o}C as elaborated in Figure 5.1(b). In order to achieve a homogeneous dispersion of GO, the resulting solution was sonicated in an ultrasonic bath for half an hour. A reference PVDF solution without GO was also prepared and electrospun under the same condition to execute control experiments.

The electrospinning solution was filled into a 10 mL hypertonic syringe with a diameter of 0.8 mm to initiate the eletrospinning process. All nanofibers were prepared under a high bias voltage of 12.5 kV using a commercial electrospinning instrument. A schematic in Figure 5.1(c) demonstrates the typical electrospinning set-up. The solution was forced by a syringe pump and injected into the needle at a flow rate of 1.2 mL/hour. The nanofibers were deposited on a Al-foil wrapped collector plate, as shown in Figure 5.1(c), where the collector was positioned at a 12 cm distance to the needle tip. Finally the four sets of nanofibers were dried at 60 ^{o}C for 8 hours to ensure that all of the solvents are released and to obtain stable nanofibers for further characterisation and nanogenerator device fabrication. Nanofibers, with and without GO are indexed as PVDF/1 wt.% GO, PVDF/0.5 wt.% GO, PVDF/0.25 wt.% GO and pure PVDF for decreasing wt.% content of GO (1, 0.5, 0.25 and 0 wt.%) in PVDF respectively.

5.2.3 Fabrication of NGs

A schematic describing the complete fabrication procedure of the NG is shown in Figure 5.1 (a-e). The flexible, low-cost, light weight hybrid nanogenerators were fabricated using a copper (Cu)–nickel (Ni) plated fine knit polyester fabric (Coatex Industries, India) as the electrode material. Firstly, a (~25 mm x 50 mm) area of nanofiber was cut from the electrospun fiber (Figure 5.1(d)). Then, the top and bottom electrodes were prepared using a polyester fabric with an active contact area of ~18 mm x 44 mm. Finally, the electrode/ nanofiber/ electrode configuration was enclosed between two layers of PDMS (thickness ~0.8 mm, prepared in a mixture with a curing agent (ratio 10:1) which was cured in an oven at 60 °C for 1 hour) to form the desired NG, as shown in Figure 5.1(e). Nanogenerators comprising PVDF/1 wt.% GO (1 wt.% GO) and pure PVDF (0 wt.% GO) are termed GPPNG and NPPNG respectively. Figure 5.2(a-c) shows intrinsic flexibility of the assembled GPPNG.
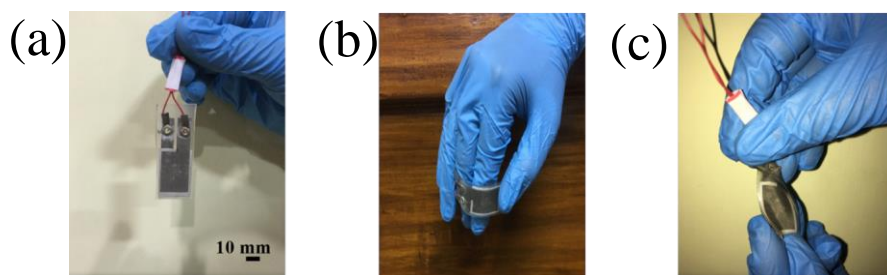
Figure 5.2 (a-c) Images of the fabricated flexible GPPNG sensor and its bending and twisting ability respectively.

5.2.4 Characterization Methods

The X-ray diffraction patterns and crystalline phases of the as-prepared GO and composite nanofibers were recorded by X-ray diffractometer (Bruker, D8 Advance) with a Cu Kα (λ = 0.154 nm) with an X-ray source at an operating voltage and current of 40 kV and 40 mA, respectively. The characteristic vibrational bands and crystalline phases of the nanofibers were further characterized by Fourier Transform Infrared Spectroscopy (FT-IR, TENSOR II,

Bruker). Morphological analysis of GO and nanofibers were carried out by FE-SEM (INSPECT F50) operating at an acceleration voltage of 20 kV and high resolution transmission electron microscope HRTEM (JEOL-JEM 2100) operating at 200 kV. The Raman spectra of the exfoliated GO were measured using a Micro-Raman spectrometer (Lab RAM HR, Jobin Yvon). The piezoelectric open circuit voltage was recorded using a National Instrument (NI) Data acquisition (DAQ) device (NI, USB 6000) using a sampling rate of 1000 samples per second, interfaced with a computer with a standalone program created using LabVIEW software. X-ray photoelectron spectroscopy (XPS) was performed by a thermo-electron system equipped with a Al-Kα excitation source and a semi spherical electron analyser made by Leybold-Heraeus. The d_{33} values of the samples were measured by d_{33}-meter (Piezoest, PM300) in HI/d_{33} mode (capacitance, C measurement of the material is inactive) under an applied force of 0.4 N and a frequency of 110 Hz. The instrument was calibrated with a piezometer reference sample with a d_{33} value of 349 pC/N.
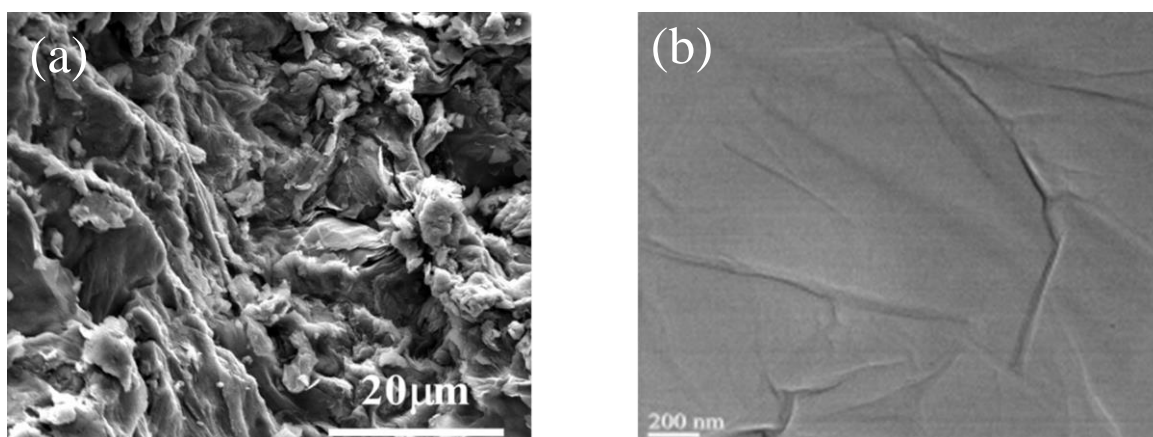
Figure 5.3 (a) FE-SEM image of as-synthesized few layered GO with (b) HR-TEM image.

5.3 Results and Discussion

5.3.1 Morphology Study of GO

From the FE-SEM micrographs, shown in Figure 5.3(a), it can be seen that the prepared GO consists of randomly aggregated, crumpled, thin and wrinkled sheet-like structures. These closely associated layered sheets form a disordered solid, which is due to the formation of sp^3 carbon from the planar sp^2 carbon during the oxidation and heating process [36]. In addition, the HR-TEM image in Figure 5.3(b) reveals the thin, transparent and wrinkled structure of GO due to sheet folding; this is also confirmed by the FE-SEM images [34, 35].

5.3.2 XRD Pattern of GO

Figure 5.4(a) represents the XRD pattern of GO synthesized by modified Hummer's method. It is well established that the main graphitic peak at $2\theta = 26.7^{\circ}$ (corresponding to interlayer spacing of ~ 0.34 nm) disappears when it is oxidised and a sharp diffraction peak is observed at $2\theta = 11.1^{\circ}$ with an interlayer spacing of 0.75 nm. During the advancement of oxidation process, oxygen functional groups are attached in between the layers, which increase the interlayer spacing of graphite.

5.3.3 Raman Spectra of GO

As shown in the Raman spectrum in Figure 5.4(b), the graphite powder shows a prominent G band located at 1576 cm^{-1} and two weaker peaks featured at 1360 and 2700 cm^{-1}, corresponding to D and 2D bands respectively [1]. In case of GO (Figure 5.4(c)), the G band is broadened and up-shifted to 1594 cm^{-1} and the D band becomes intensified. The G band appeared due to the first order scattering of the E_{2g} mode. In addition, the D and 2D bands correspond to the second order double resonant process between the non-equivalent K points in the Brillouin zone of Graphene [2]. The D-peak intensity is a measure for degree of
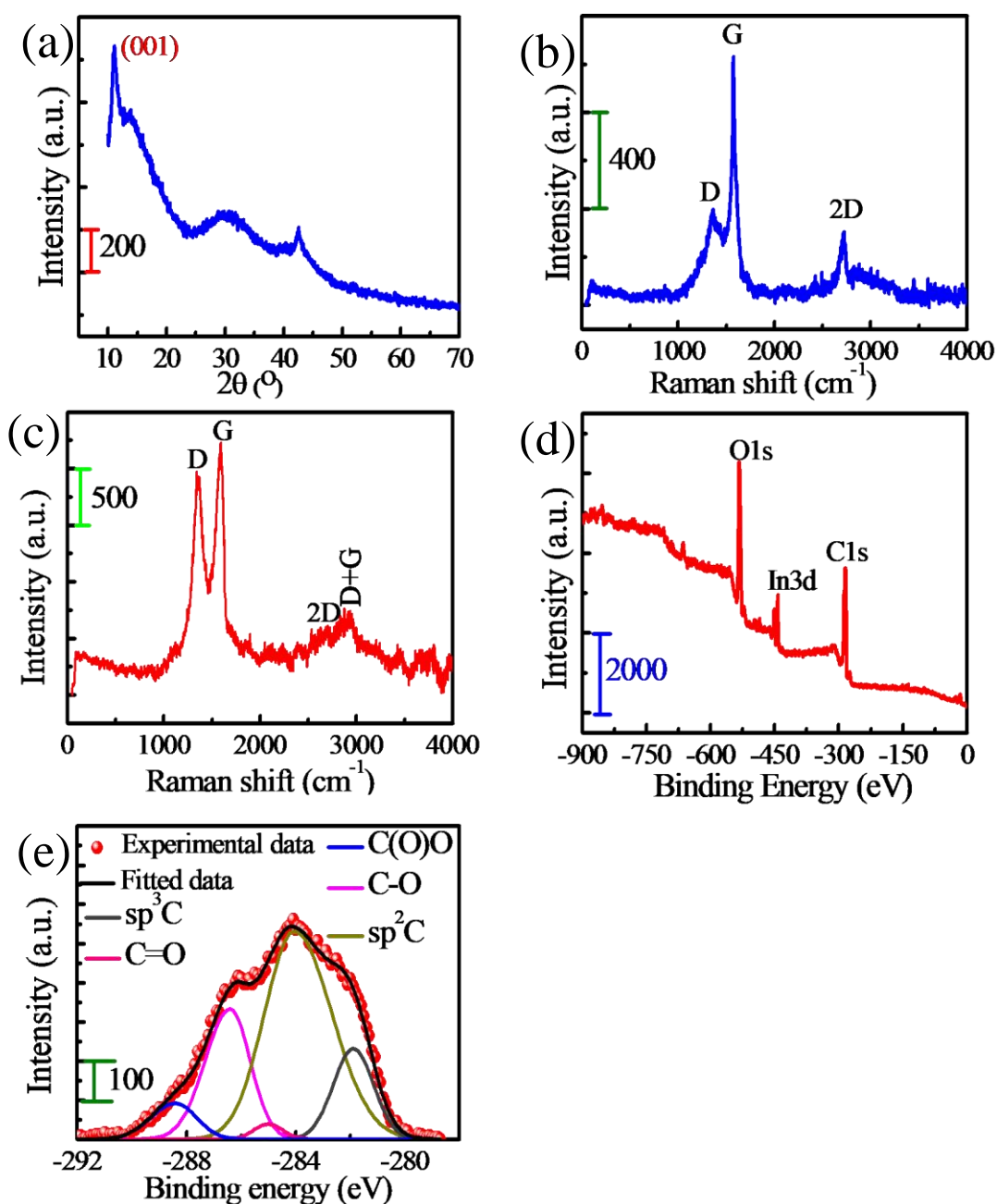
Figure 5.4 (a) XRD pattern of GO. Raman spectra of (b) graphite powder and (c) graphene oxide (GO). (d) XPS survey spectra of GO (XPS was measured by pasting the GO powder on indium wire. So, In3d peak has appeared). (e) High resolution deconvoluted C1s XPS spectra of GO.

disorder. The 2D peak is attributed to double resonance transitions resulting in the production of two phonons in opposite momentum [1]. This weak and broad peak appearing in GO is

another sign of disorder. During the extensive oxidation process, structural defects are induced due to the attachment of oxygen functional groups to the basal plane of graphene. This is the reason behind the reduction in size of the in-plane sp^2-domains, promotion of intensified D band and the blue shift of G band in GO. Another defect activated peak is featured at 2970 cm^{-1}, named as D+G band.

5.3.4 XPS of GO

To investigate the formation of GO and to confirm the presence of oxygen functionalities, XPS was carried out on the as-synthesized GO. The XPS survey spectra of GO (Figure 5.4(d)) shows peaks associated with C1s and O1s, which appeared at 285 and 533 eV respectively. The high resolution spectral analysis of the C1s characteristic peak, shown in Figure 5.4(e), indicates the presence of five different peaks at 283.7, 285, 286.2, 287.7, 288 eV, which correspond to the sp^2C, sp^3C, –C–O, –C=O and –COO– groups, respectively [47].

5.3.5 Morphology of PVDF/GO Nanofibers

The surface morphology of the PVDF/1 wt.% GO nanofibers is presented in Figure 5.5(a). The surface of the as-prepared composite nanofiber is rougher than that of the PVDF electrospun fibers (Figure 5.5(b)) due to the incorporation of the GO nanofiller. The TEM image, shown in Figure 5.5(c) indicates that the PVDF/1 wt.% GO nanofibers consist of randomly oriented fibers without any agglomeration, which is in accordance with the FE-SEM image in Figure 5.5(a). GO was homogeneously dispersed in the PVDF matrix because of its carbon based structure and presence of oxygen linked functional groups and no agglomeration was observed on the surface of the PVDF/GO fibers. Furthermore, the prepared fibers are formed with a stable morphology and no cracks were detected so that the fibers did not become brittle. The PVDF/1 wt.% GO nanofibers have a relatively smaller diameter (~125 nm) compared to the pure PVDF fiber (~270 nm) prepared under the same conditions as presented in the inset of Figure 5.5(a) and Figure 5.5(b). The incorporation of
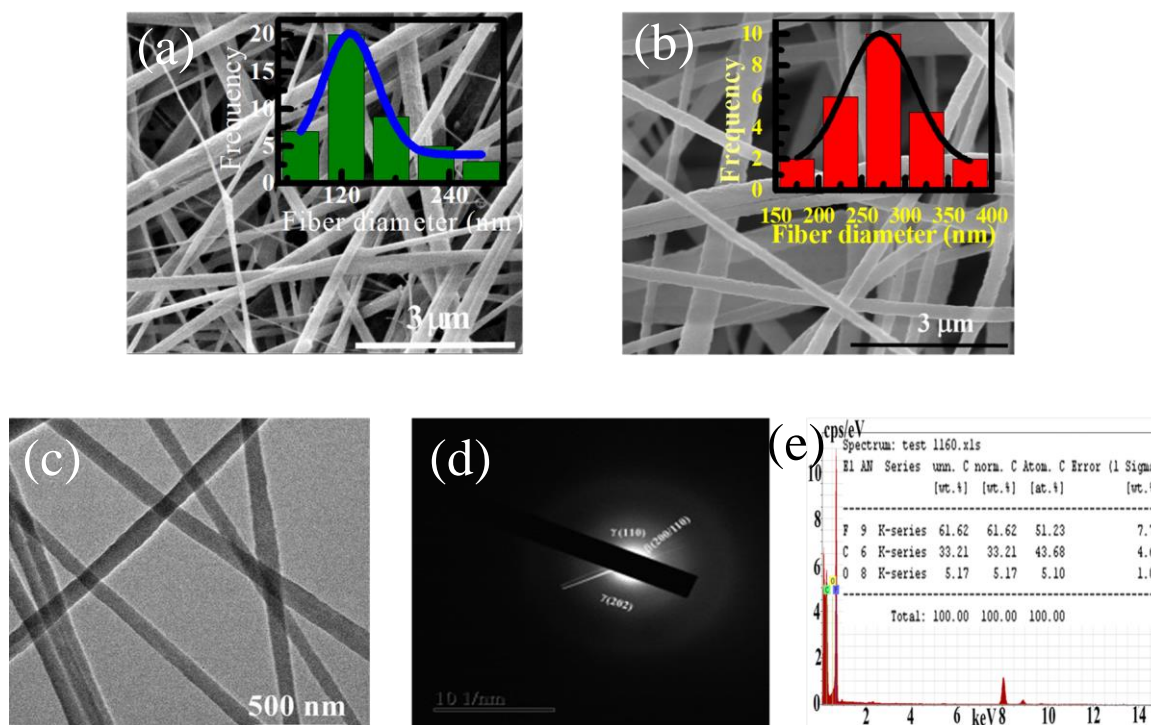
Figure 5.5 FE-SEM micrographs of (a) PVDF/1 wt.% GO and (b) pure PVDF fibers with corresponding fiber diameter distribution are shown in the inset. (c) TEM image of PVDF/1 wt.% GO including the (d) SAED pattern. (d) EDX spectra of PVDF/1 wt % GO. The elemental atomic percentages of carbon, oxygen and fluorine are shown in the inset.

GO considerably reduces the average fiber diameter and this is a result of the cumulative charge density of the dispersed GO sheets due to the application of a high voltage to the solution and the fiber jet during electro-spinning. This also facilitates the electrostatic repulsion and Coulombic force on the Taylor cone which leads to a relatively reduced fiber diameter of the PVDF/GO nanocomposites [29, 37]. The crystallinity, mechanical properties and overall energy harvesting performance are also improved due to a decrease in fiber diameter for the PVDF/1 wt.% GO composites [26, 38]. It is also evident from the TEM image in Figure 5.5(c) that the GO is well dispersed in the fiber matrix since GO contains several functional groups. Thus, it is expected that the embedded GO in the fiber matrix can

influence the electrical conductivity, piezoelectric properties and pressure-temperature sensitivity. The selected area electron diffraction (SAED) pattern of the doped fiber, as shown in the Figure 5.5(d), revealed the presence of electroactive β– and γ– phases. From electron dispersive X-ray spectroscopy (EDX) (Figure 5.5(e)), the presence of carbon, fluorine, oxygen in PVDF/1 wt.% GO can be observed which indicates the presence of oxygen functional groups in the fiber matrix.

5.3.6 Crystallographic Phase Identification and Quantification

The FT-IR spectra of electrospun pure PVDF nanofibers and PVDF/1 wt.% GO composite fibers are shown in Figure 5.6(a). For the pure PVDF nanofibers, the characteristic vibrational peaks are observed at $\bar{v}$ = 613, 764, 796 and 975 cm^{-1}, which correspond to the nonpolar α– phase. The appearance of two additional intense peaks at 1275 and 1233 cm^{-1} confirm the nucleation of the polar β– phase (TTTT) and the semi-polar γ– phase (TTTG), respectively [23-26].

For the PVDF/GO nanofiber based on PVDF/1 wt.% GO, all α– peaks are diminished and signals corresponding to the electroactive β– and γ– phases have appeared. A systematic study of other fibers with other GO contents (PVDF/0.25 wt.% GO, PVDF/0.5 wt.% GO) revealed that the intensity of electro-active β– and γ– phases gradually increases with an increasing GO concentration (Figure 5.6(b and c)). In order to undertake a qualitative analysis of the α–, β– and γ– phases, the absorbance intensities are normalized to the 1072 cm^{-1} peak as it is linearly dependent on fiber thickness, regardless of crystalline modification [28]. Generally, the vibrational bands of the β– and γ– phases of the PVDF coincide since both contain the same TTT in the chain conformation and gives rise to common vibrational peaks, such as at 841 cm^{-1} [26, 28, 39, 40]. The peak at 841 cm^{-1} for the PVDF/1 wt.% GO nanofibers is more intense than pure PVDF, which indicates the specific electrostatic interaction between the π-electron cloud and the oxygen containing functional groups
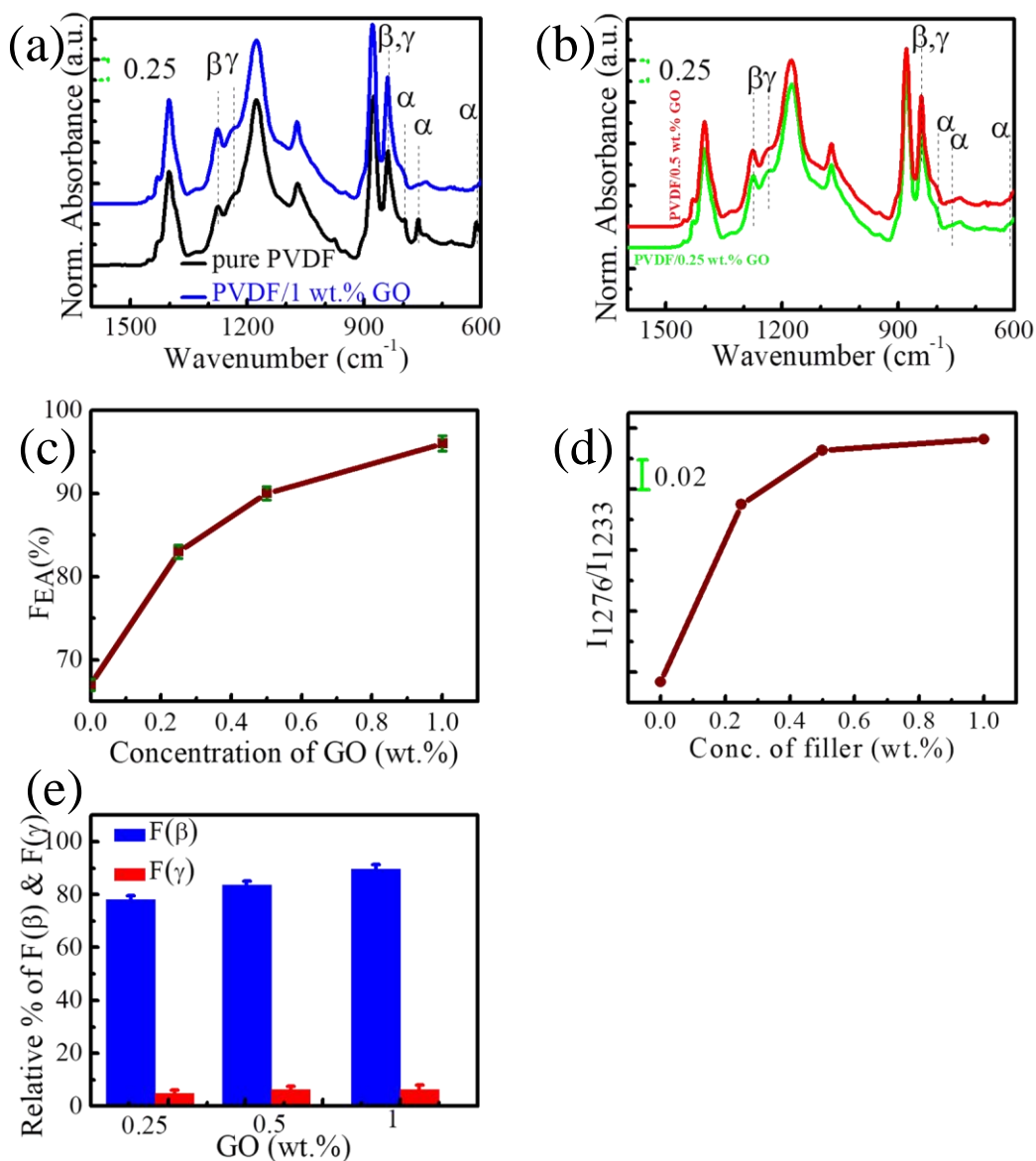
Figure 5.6 FT-IR spectra of (a) pure PVDF, PVDF/1 wt.% GO fibers (b) PVDF/0.25 wt % GO and PVDF/0.5 wt % GO fibers in the wavenumber range of 1600-600 cm^{-1}. (c) Relative percentage of F_{EA} as a function of the GO concentration. (d) Variation of the FT-IR absorption intensity ratio of β and γ phases (I_{1276}/I_{1233}) of pure PVDF and PVDF/GO fibers with respect to the concentration of GO. (e) The bar diagram represents the relative percentage of $F(β)$ and $F(γ)$ for PVDF/GO fibers.

(carbonyl and carboxylic groups) in GO and the $-CH_2/-CF_2$ dipoles of PVDF [41, 42]. It can be clearly observed from the absorption band intensity ratio I_{1276}/I_{1233} (Figure 5.6(d)) that the γ–crystalline growth is almost negligible with respect to the β–phase when the GO concentration is increased gradually (Figure 5.6(e)). Thus, it can be concluded that the PVDF/1 wt.% GO nanofibers consist of the largest proportion of ferroelectric β–phase.

In addition, it is worth noting that a strong absorption band appears at 841 cm^{-1}, which is a common characteristic of both β– and γ–phases. Thus, the absorption intensity of 841 cm^{-1} band is used to quantify the relative proportion of the electroactive phase (F_{EA}), as a result of both β– and γ–phases [43, 44].

The total electroactive phase content (F_{EA}) and relative proportion of electroactive phases (β & γ) i.e., $F(\beta)$ and $F(\gamma)$ can be calculated using these following equations.

$$F_{EA} = \frac{A_{841}}{\left(\frac{K_{841}}{K_{764}}\right)A_{764}+A_{EA}} \times 100\%$$

$$F(\beta) = F_{EA} \times \left(\frac{A_\beta}{A_\beta+A_\gamma}\right)$$

$$F(\gamma) = F_{EA} \times \left(\frac{A_\gamma}{A_\beta+A_\gamma}\right)$$

where, A_{841} and A_{764} signify the absorbance intensities at 841 cm^{-1} and 764 cm^{-1}, respectively, and K_{841} (7.7×10^4 cm^2 mol^{-1}) and K_{764} (6.1×10^4 cm^2 mol^{-1}) are the absorption coefficients at respective wavenumbers. A_β and A_γ are the intensities (area) under the deconvoluted curves of the 841 cm^{-1} main peak that are described as β and γ.

A F_{EA} of 96% is achieved for the PVDF/1 wt.% GO fiber as shown in Figure 5.6(c). Furthermore, the absorbance peak at 764 cm^{-1} (non-polar α–phase) which appears as a result of CF_2 bending and the skeletal bending vibrational mode, is completely diminished in the FT-IR spectra of the ESPVGO1.0 fiber (Figure 5.6(a)). The 841 cm^{-1} has been deconvoluted to calculate the relative fraction of electroactive β– and γ– phases and is shown in Figure

5.7(a). Frequency shifts of the CH_2 symmetric and CH_2 asymmetric vibrational FT-IR modes in the frequency region of 3060-2940 cm^{-1} for PVDF/1 wt.% GO compared to pure PVDF (Figure 5.7(b)) indicates an interaction between PVDF and GO. A noticeable shift of these bands towards a lower frequency can be observed, which points toward the presence of an interfacial interaction between the superficial charge existing on the GO sheet and $-CH_2/-CF_2$ dipoles of PVDF in the nanocomposite system [24, 44].

Figure 5.7 (a) The deconvolution of the FT-IR spectra (920–780 cm^{-1}) for GO doped PVDF fibers with different GO concentrations (1, 0.5, 0.25 wt.% from top to bottom). (b) FT-IR spectra of pure PVDF and PVDF/1 wt % GO fibers in the wavenumber range of 3060–2940 cm^{-1}.

Figure 5.8 Curve deconvolution of the XRD pattern in the 2θ range of 15-25° for (a) pure PVDF, PVDF/1 wt.% GO and (b) PVDF/0.5 wt % GO (top) and PVDF/0.25 wt % GO (bottom). The degree of crystallinity of β, γ and α− phases is also provided.

To evaluate the crystallinity of the nanofibers from the XRD pattern of the related polarized phases, a curve deconvolution technique was performed [26, 29, 44]. From the curve deconvoluted XRD pattern, as shown in Figure 5.8(a), the data of pure PVDF nanofibers show a diffraction peak at 18.2° (202), which is characteristic of α− crystalline phase and this is in accordance with the FT-IR spectra presented in Figure 5.6(a). Furthermore, two additional crystalline phases can be observed at 20.3° (110) and 20.8° (110/200) [23, 26], which are attributed to electroactive γ− and β− phases, respectively. The reason behind the electroactive phase formation in the pure PVDF nanofibers is that the molecular chains of PVDF are uniaxially stretched by the high electrical forces during the electrospinning process, which forces the –CH$_2$/ –CF$_2$ dipoles for in-situ orientation [37, 45]. Furthermore, characteristic non-polar α− phase peaks at 17.6° (100), 18.2° (202) and 19.9° (110) are

diminished in the PVDF/GO nanofibers of PVDF/1 wt.% GO. The intense diffraction peaks at 20.5° emphasizes the dual signature of both the $\beta-$ and $\gamma-$ phases [23, 39]. Curve deconvolution assigns the sharp peak at 20.5° as the predominant $\beta-$ phase with the co-existence of lower content of $\gamma-$ phase at 20.3° and at 18.5°. The total degree of crystallinity (χ_C) and the crystallinity of the individual phases are calculated using curve deconvolution methodology using the following equations.

$$\chi_C = \frac{\sum A_{CR}}{\sum A_{cr} + \sum A_{amr}} \times 100\%$$

$$\chi_{C\beta} = \chi_C \times \frac{\sum A_\beta}{\sum A_\beta + \sum A_\gamma}$$

$$\chi_{C\gamma} = \chi_C \times \frac{\sum A_\gamma}{\sum A_\beta + \sum A_\gamma}$$

where, ΣA_{cr} and ΣA_{amr} represent the summation of the total integral areas of crystalline diffraction peaks and amorphous halo, respectively. Furthermore, ΣA_β and ΣA_γ are the total integral intensities (area) under crystalline $\beta-$ and $\gamma-$ phases, respectively.

The deconvoluted XRD patterns of PVDF/0.5 wt.% GO (0.5 wt.% GO) and PVDF/0.25 wt.% GO (0.25 wt.% GO) are also shown in Figure 5.8(b). The highest degree of crystallinity was obtained for the PVDF/1 wt.% GO fiber, which is almost 68% whereas the pure PVDF is 53% and the degree of crystallinity gradually increases with the incorporation of GO. In particular, the incorporation of GO improves $\beta-$ phase crystallinity significantly [41, 46]. This is due to complete adsorption of the PVDF chain on the large surface provided by GO and this adsorption leads to the complete conversion of TGTG′ chains into TTTT chains. The heterogeneous nucleation of $\beta-$ and $\gamma-$ phase of the PVDF chain on the GO surface increases the crystallinity and the crystallization temperature. The average crystallite size of the $\beta-$

(D_β) and $\gamma-(D_\gamma)$ phases are calculated using Debye-Scherrer equation, as shown below and these values are tabulated in Table 5.1:

$$D = \frac{K\lambda}{\beta cos\theta}$$

where, K is a constant (0.89), λ is the wavelength (0.1541 nm) of the Cu-Kα X-ray radiation, β is the full-width (in radian) at half maxima (FWHM) of the intense diffraction peak and θ is the diffraction angle.

Table 5.1 The degree of crystallinity and size of β- and γ- crystallites for different composite fibers.

Sample	χ_C (%)	β-crystallite size (D_β) (nm)	γ-crystallite size (D_γ) (nm)
Pure PVDF	53	5	14
PVDF/0.25 wt % GO	57	6	17
PVDF/0.5 wt % GO	63	8	16
PVDF/1 wt % GO	68	7	16

5.3.7 XPS Study of Nanofibers

To understand the compositional changes related to conformational ordering of the PVDF chain due to the incorporation of GO in the PVDF nanofiber, XPS was performed over pure PVDF and the PVDF/1 wt.% GO nanofibers. In the high resolution C1s core level spectrum of pure PVDF, which is shown in Figure 5.9(a), two main peaks are present with binding energies of 287.1 eV and 291.7 eV, which indicate two main carbon species, CH_2 and CF_2 respectively. A chemical shift toward lower binding energies can be detected for the CH_2 and CF_2 peaks in PVDF/1 wt.% GO, with binding energies of 286.3 eV and 290.7 eV. Furthermore, a substantial decrease in intensity of the CF_2 peak and an increase of the peak
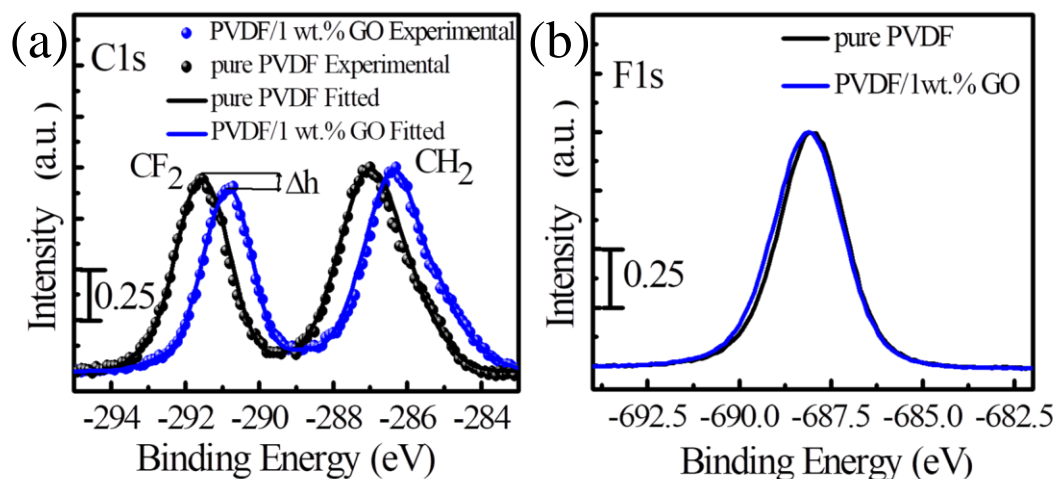
Figure 5.9 High resolution XPS spectra of pure PVDF and PVDF/1 wt.% GO in the (a) C1s and (b) F1s core level regions.

area of the CH$_2$ species for the PVDF/1 wt.% GO nanofibers are also observed in comparison to the pure PVDF. These two observations suggest that there is significant distinction in the electronic environment of the –CH$_2$ and –CF$_2$ dipoles in the PVDF chain of the PVDF/1 wt.% GO nanofibers. In addition, the high resolution F1s core level spectrum, as shown in Figure 5.9(b), reveal that PVDF/1 wt.% GO exhibits a minor asymmetry at the higher binding energy level compared to pure PVDF, which is positioned at 688.1 eV. These results indicate an interaction between the –CH$_2$/–CF$_2$ dipoles of PVDF and oxygen functional groups present in GO.

5.3.8 Mechanism of Phase Conversion

Therefore it is evident from the above mentioned data that β– and γ– phase nucleation has occurred in the PVDF/GO composite nanofibers because of an interaction between the negatively charged GO nanosheet and the dipoles of the PVDF fiber [41]. The conversion of the non-polar α– phase to the electroactive β– and γ– phase is a result of the electrostatic interaction and/or the intermolecular hydrogen bonding between the oxygen containing

functional groups and $-CH_2/-CF_2$ dipoles of the PVDF [41, 48, 49], which leads to improved ferroelectric performance for piezoelectric based sensing and energy harvesting applications [50, 51]. To understand the interaction present between the PVDF chain and GO sheet, a hypothetical model is constructed based on the results, which is described in the schematic in Figure 5.10.
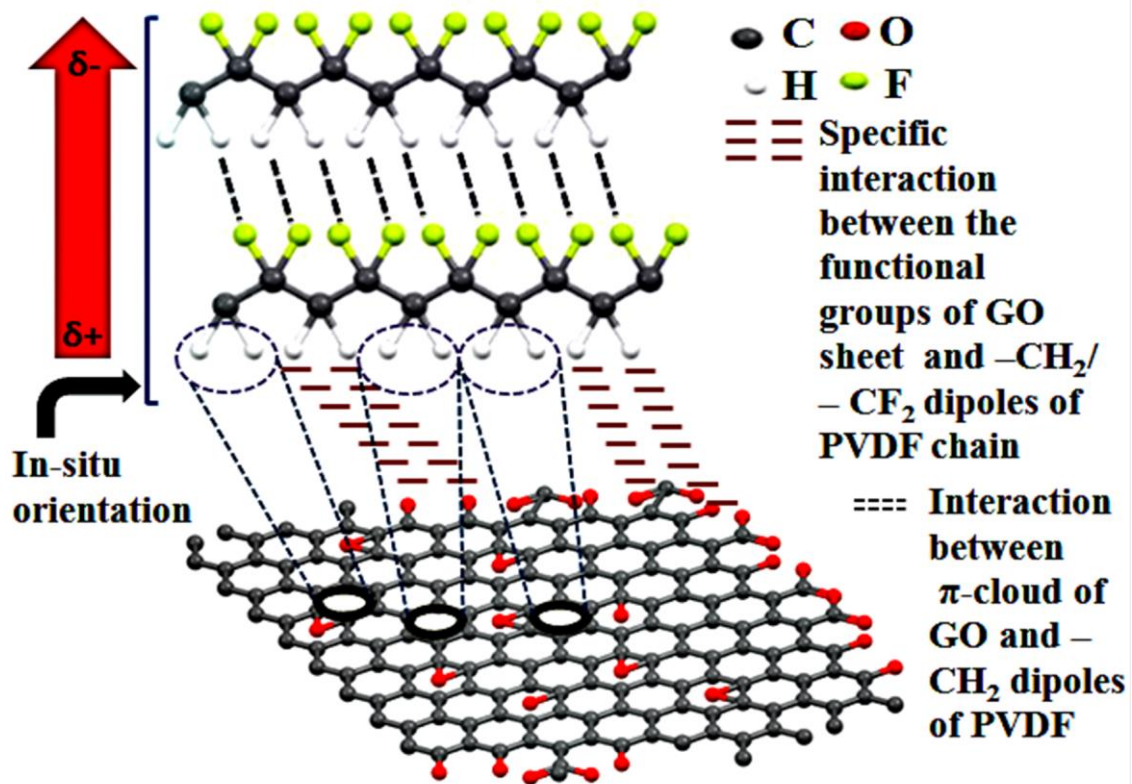
Figure 5.10 Schematic of a hypothetical model for electroactive phase nucleation and interactions present in PVDF/1 wt.% GO nanofibers.

5.3.9 Piezoelectric Energy Harvesting Performance

The piezoelectric performance with respect to the open circuit output voltage was recorded using a repetitive motion applied by a finger on the surface of the NGs at a frequency of ~ 4 Hz. The process was performed using a bare finger covered by a polyethylene glove under the repeating compressive force of 7 N and associated applied stress amplitude of 8.8 kPa, respectively. An open circuit voltage of ~7 V was measured for the PVDF/1 wt.% GO based
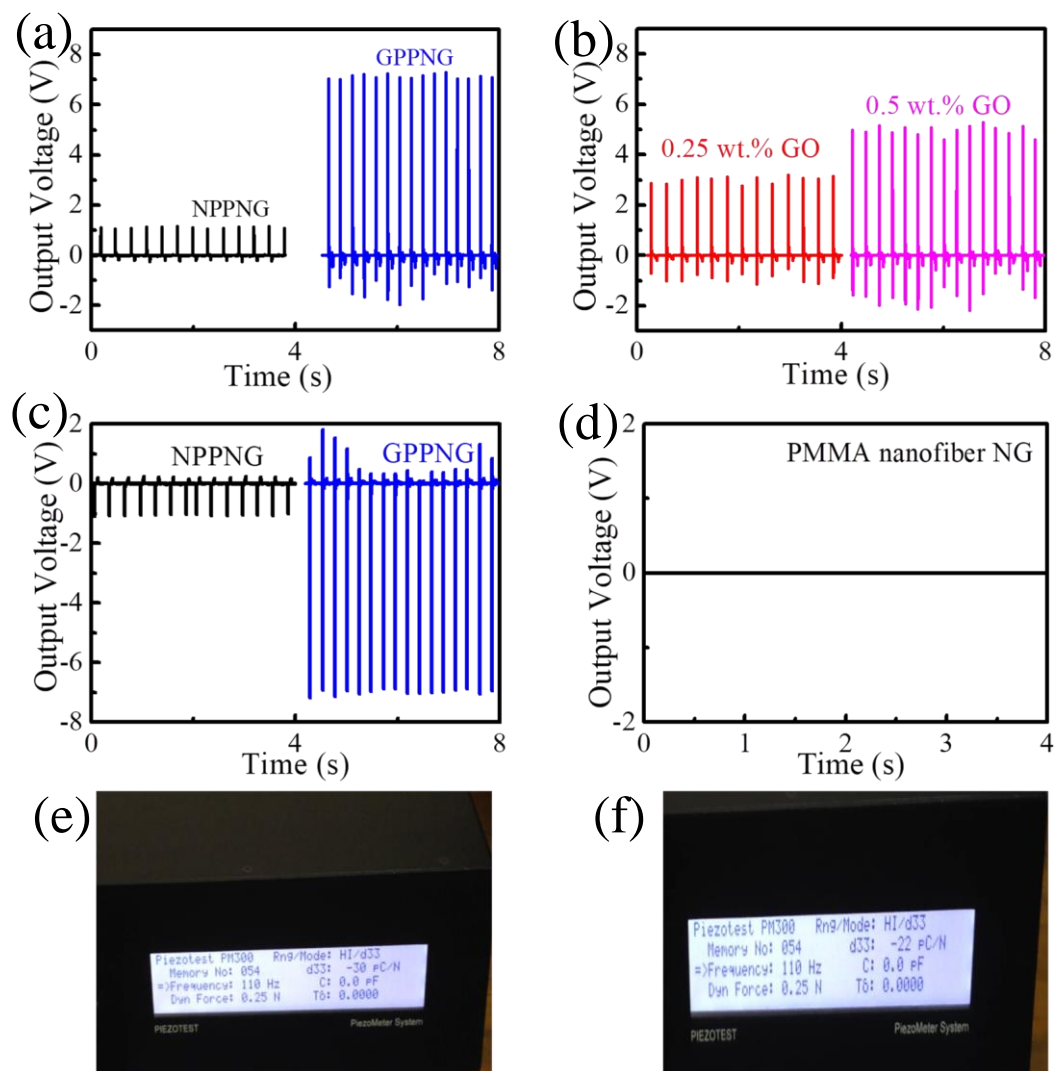
Figure 5.11 Open-circuit output voltages from (a) pure PVDF (NPPNG), PVDF/1 wt.% GO (GPPNG) nanogenerator devices (b) the NGs made of PVDF/0.25 wt % GO and PVDF/0.5 wt % GO in forward connection during repetitive impact by a human finger at ~4 Hz and (c) NPPNG, GPPNG in reverse connection. (d) PMMA nanofiber based nanogenerator during repetitive finger human finger impact motion under the frequency of ~4 Hz. Piezoelectric charge coefficient (d_{33}) values for (e) PVDF/1 wt.% GO and (f) pure PVDF nanofibers.

device (GPPNG), whereas, ~1 V was generated for the pure PVDF based device (NPPNG), which is shown in Figure 5.11(a). The recorded output voltages from other NGs are shown in

Figure 5.11(b). The output voltage with a reverse electrode connection was also measured (Figure 5.11(c)), which clearly indicated that an output of similar amplitude, but with reversed polarity, was observed. This indicates that the potential difference is a result of the change in dipole moment of the system under stress; i.e. it is a stress induced polarization change due to the piezoelectric effect [52]. As a control, we have tested a nanogenerator in the same configuration but with only poly(methyl methacrylate) (PMMA) nanofibers and did not observe any out voltage response. Therefore, it can be concluded that the response is piezoelectric (Figure 5.11(d)). When the GPPNG is subjected to a vertical mechanical stress, the piezoelectric β-crystal structures of the nanofibers are deformed and thus a potential difference is developed between the two electrodes. As an outcome, the external free electrons are forced to the GPPNG, leading to a strong enhancement in piezoelectric response by converting the distorted structure into its stable form. When the external strain is released from the GPPNG surface, the potential difference between the two electrodes diminishes and the accumulated free electrons gradually move back through the external circuit, generating an electric current in the reverse direction [53]. As shown in Figure 5.11(a and b), the open circuit voltage gradually increased with an increase of the GO content in the PVDF mat. The maximum recorded output voltage is 7 V at a 1 wt.% filler loading which is approximately seven times higher than that exhibited by the NG containing pure PVDF nanofibers. This enhancement is associated with the increased longitudinal piezoelectric charge coefficient, $d_{33} \sim -30$ pC/N (Figure 5.11(e)) in comparison to the pure PVDF nanofiber (~ -22 pC/N) (Figure 5.11(f)). A comparison is presented in Table 5.2.

Table 5.2 Comparison of the piezoelectric coefficient of PVDF/1 wt % GO with the reported materials.

Sr. No.	Active Materials	Piezoelectric Co-efficient (d_{33})	References
1.	$BaTiO_3$ -Wood cellulose fiber	4.8 ± 0.4 pC N^{-1}	*ACS Appl. Mater. Interfaces* **2014**, 6, 7547–7553
2.	Diphenylalanine peptide	17.9 pm V^{-1}	*Nat. Commun.* **2016**, 7, 13566–13571.
3.	M13 bacteriophage (phage)	7.8 pm V^{-1}	*Nat. Nanotechnol.* **2012**, 7, 351–356
4.	P(VDF-HFP) films	24 pC N^{-1}	*Polym. Eng. Sci.* **2007**, 47, 1630–1633
5.	Solution grown ZnO nanorods on Ag films	4.41 pm∕V	*J. Appl. Phys.* **2007**, 101, 014316–014321
6.	ZnO	12.4 pC N^{-1}	*Appl. Phys. Lett.* **1998**, 73, 3851–3853
7.	P(VDF-TrFE) copolymer film	18 pC N^{-1}	*J. Polym. Sci. B: Polym. Phys.* **2014**, 52, 496–506
8.	PVDF film	24 pC N^{-1}	*J. Polym. Sci. B: Polym. Phys.* **2004**, 42, 3487–3495
9.	$CoFe_2O_4$−SDS/PVDF	23 pC N^{-1}	*J. Phys. Chem. C* **2012**, 116, 15790–15794
10.	Silver nanowires (Ag NWs) doped PVDF fibers	29.8 pC N^{-1}	*Fourth Int. Conf. on Smart Mater. and Nanotech. in Eng.***2013**, 879314, DOI: 10.1117/12.2026758.
11.	PVDF/GO nanofibers	30 pC N^{-1}	This work

The reason behind the increased output performance is due to the electrostatic interaction between the negatively charged GO nano-sheet embedded in PVDF nanofibers with the –CH_2/–CF_2 dipoles present in PVDF. This interaction not only incorporates the nucleation but also stabilises the electroactive *β*- phase (surface charge induced polarisation) in the PVDF nanofiber mat [54]. Therefore, the high quality crystal structure and the existence of

delocalised π- electrons and oxygen functional groups present in the layered structure of the GO improve the piezoelectric performance of the hybrid system. Thus, the PVDF/GO system (GPPNG) can be used as a real time power source in various self-powered portable electronic devices. Further experiments and applications are now carried out and discussed using the GPPNG due to its better piezoelectric performance.
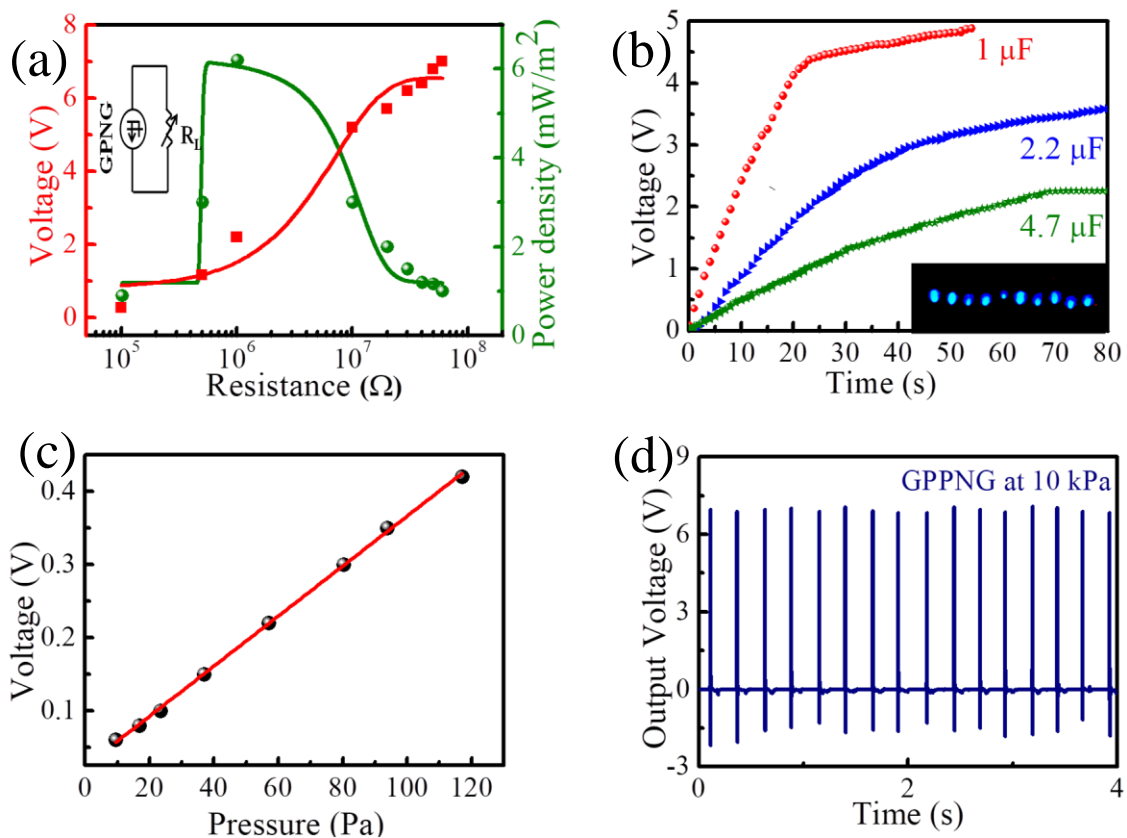
Figure 5.12 (a) Output voltage (circuit diagram shown as inset) and output power density of the GPPNG as a function of different load resistances. (b) Capacitor charging performance of different capacitors (1, 2.2, 4.7 µF) as function of time during repeated finger impact on the GPPNG (10 illuminating blue LEDs as shown in the inset). (c) Open-circuit output voltage of the GPPNG under different applied pressure. (d) Open-circuit output voltage of GPPNG at 10 kPa pressure and under the frequency of ~4 Hz.

To evaluate the instantaneous electrical power output performance, the GPPNG was directly connected to electrical loads at different resistances (R_L) ranging from 100 kΩ to 60 MΩ (while applying force of 7 N at a frequency of ~4 Hz). The measured output voltage as a function of external load resistances is shown in Figure 5.12(a). The output voltage gradually increases with increasing load resistance, since the discharge of the devices is reduced and approaches the open circuit voltage of 7 V at a high load resistance; i.e. on approaching an infinitely high resistance. The variation of power density (P) with respect to R_L in Figure 5.12(a) was quantified using the following equation, $P = \frac{1}{A}\frac{V^2}{R_L}$, where V is the voltage drop across R_L and A is effective electrode area. The maximum instantaneous output power density of ~6.2 mW/m^2 was achieved at a R_L of 1 MΩ. It has been observed that, the output power density of our GPPNG is found to be superior with respect to current state of the art nanogenerators as given in Table 5.3.

In addition to output voltage performance, to demonstrate the energy storage ability and the application of piezoelectric energy conversion performance, three capacitors (i.e., 1, 2.2, 4.7 μF) were individually connected to the GPPNG through a full wave bridge rectifying circuit and charged by repeated human finger taping (Figure 5.12(b)). It was observed that, the PVDF/GO based device (GPPNG) efficiently charged up the capacitors when subjected to an episodic pressure of 8.8 kPa. The charging voltage across the capacitors reached a steady state (4.9, 3.6 and 2.3 V) following an exponential path within a short time scale of 54, 80 and 80 seconds for the 1, 2.2 and 4.7 μF capacitors, respectively. The energy stored (E_{stored}) within the capacitors reached maximum in case of 2.2 μF and reached up to 14.25 μJ. Here, E_{stored} can be calculated as $E_{stored} = \frac{CV^2}{2}$, where, C is the capacitance of the capacitor and V is the voltage across the capacitor. The output power is also sufficient to illuminate more than 10 blue LEDs in series by repeated human finger impact of similar load, as shown in the inset

of Figure 5.12(b). Thus, the GPPNG can be used as a power generator or small scale energy scavenger to drive self-powered electronic devices.

Table 5.3 Comparison of the output performances of the GPPNG with the reported NGs.

Sr. No.	Materials	Output Voltage	Power/Power Density	References
1.	P(VDF-TrFE) nanowires	4.8 V	Not given	*J. Mater. Chem. C* **2015**, 3, 11806–11814
2.	ZnO	9V (peak to peak)	$0.02\ \mu W/cm^2$	*ACS Appl. Mater. Interfaces*, 2019, 11, 6078–6088
3.	P(VDF-TrFE)/BaTiO$_3$ film	0.6 V	$0.28\ \mu W$	*Composites Part B* **2015**, 72, 130–136
4.	Direct-write PVDF nanofibers	30 mV	Not given	*Nano Lett.* **2010**, 10, 726–731
5.	Aligned BaTiO$_3$ films	6.5 V	$0.021\ \mu W$	*J. Mater. Chem. A* **2015**, 3, 9965–9971
6.	Aligned P(VDF-TrFE) nanofibers	1.5 V	Not given	*Nat. Commun.* **2013**, 4, 1633–1642
7.	PVDF/ZnO nanocomposite	1.81 V	$0.21\ \mu W.cm^{-2}$	*Polym. Adv. Technol.* **2018**, 29, 143–150
8.	PVDF/NaNbO$_3$/RGO nanocomposite	2.16 V	Not given	*Compos. Sci. Technol.* **2017**, 149, 127–133
9.	PVDF–graphene nanocomposites	1.3 V(peak to peak)	36 nW	*Smart Mater. Struct.* **2013**, 22, 085017–085026
10.	PZT nanofiber	1.63 V	$0.03\ \mu W$	*Nano Lett.* 2010, 10, 2133–2137
11.	PVDF/GO nanofiber	7 V	$6.2\ mW/m^2$	This work

5.3.10 Mechano-sensitivity Test

Furthermore, to investigate the low range pressure (σ_a) sensing performance of the GPPNG composed of PVDF/1 wt.% GO nanofibers, light-weight substances of different masses were dropped on the upper surface of the GPPNG from a height of 3 cm. The GPPNG could detect

an external pressure as low as ~10 Pa and generated an output response of 0.06 V. The generated output voltage changes almost linearly with respect to the increased implied pressure in the low pressure regime as seen in Figure 5.12(c). The calculated mechanical impact sensitivity (S) can be expressed as $S = \frac{\Delta V}{\Delta \sigma_a}$, where ΔV and $\Delta \sigma_a$ are termed as differences of V and σ_a respectively and the sensitivity of the GPPNG in the low pressure region (S= 4.3 V/kPa) is higher than several previously reported piezoelectric pressure sensors. A detailed comparison table of piezoelectric pressure sensitivity is provided in Table 5.4.

Table 5.4 Summary of the reported piezoelectric pressure sensors and their performances.

Sr. No.	Materials	Sensitivity	Reference
1.	Laterally aligned PZT aingle-crystal nanowires	0.14 V/kPa	*ACS Appl. Mater. Interfaces* **2017**, 9, 24696–24703
2.	P(VDF-TrFE) nano-tube	0.05 V/kPa	*Adv. Energy Mater.* **2014**, 4, 1400723–1400730
3.	P(VDF-TrFE) thin film	0.75 mV/kPa	*Sens. Actuators A* **2012**, 177, 87–92
4.	Cellular PP/α-Si:H	0.1 V/kPa	*Appl. Phys. Lett.* **2006**, 89, 073501–073503
5.	PTFE/porous PTFE	1.5 V/kPa	*J. Phys. D: Appl. Phys.* **2014**, 47, 015501–015510
6.	Cellular fluorocarbon	1.54 V/kPa	*Nano Energy* **2017**, 32, 42–49
7.	Aligned P(VDF-TrFE)/MWCNT composites	540 mV/N (device dimension 1.5 cm × 1.5 cm)	*Nanomaterials* **2018**, 8, 1021-1032
8.	Piezoelectric fiber array vertically integrated P(VDF-TrFE)	269.4 mV/N (device dimension 10 mm × 10 mm)	*Nanoscale* **2015**, 7, 11536–11544
9.	Carbonized electrospun polyacrylonitrile/barium titanate (PAN-C/BTO) nanofiber film	1.44 V/N (device dimension 1.5 cm × 1.5 cm)	*ACS Appl. Mater. Interfaces* **2018**, 10, 15855−15863
10.	Electrospun PVDF/BaTiO$_3$ nanowire (NW) nanocomposite fibers	0.017 V/kPa	*Nanoscale* **2018**, 10, 17751-17760

11.	Eletrospun PVDF fabric	42 mV/N (device dimension 19.7 mm^2)	*Smart Mater. Struct.* **2011**, 20, 045009-045015
12.	P(VDF-TrFE) film	0.01 V/N (device dimension 2.25 mm^2)	*J. Microelectromech. Syst.* **2008**, 17, 334–341
13.	PVDF-MWCNT-OMMT	0.011 V/N (device dimension 4 cm× 4 cm)	*Org. Electron.* **2017**, 50, 121–129
14.	P(VDF-TrFE)/CMOS transistor	0.050 V/N (device dimension 1.5 cm× 1.5 cm)	*IEEE Sensors J.* **2011**, 11, 3216–3226
15.	PVDF/GO nanofibers	4.3 V/kPa	This work

In the large pressure range, the sensitivity of the GPPNG gradually decreases. The output voltage of 7 V is obtained at a pressure of 8.8 kPa, which is the maximum output performance during periodic impact by a human finger. The output performance was also measured at 10 kPa and the recorded output voltage is almost 7 V (Figure 5.12(d)). Therefore, the output signal becomes saturated in higher pressure range. This is possibly due to the theoretical limits of effective strain in piezoelectric materials in the high pressure region [55]. Hence, the GPPNG has the capability to be used as a self-powered E-skin for biomedical applications such as sensing static tactile stimuli, vocal cord vibrations during coughing, swallowing movements of human throat and speech signal recognition due to its sensitive pressure sensing capability.

5.3.11 Pyroelectric Energy Harvesting Performance

To evaluate the pyroelectric short circuit peak current and open circuit peak voltage, the GPPNG was placed under an IR radiation test set-up and a controlled temperature oscillation was applied to the device under periodic illumination of IR light and convective cooling. The GPPNG can readily harvest thermal energy due to the pyroelectric properties of the PVDF/1 wt.% GO nanofibers [52]. When a periodic thermal fluctuation is applied to the PVDF/GO based device (GPPNG), there is a clear enhancement of output performance with respect to the device made from pure PVDF nanofiber (NPPNG). When the temperature increases from
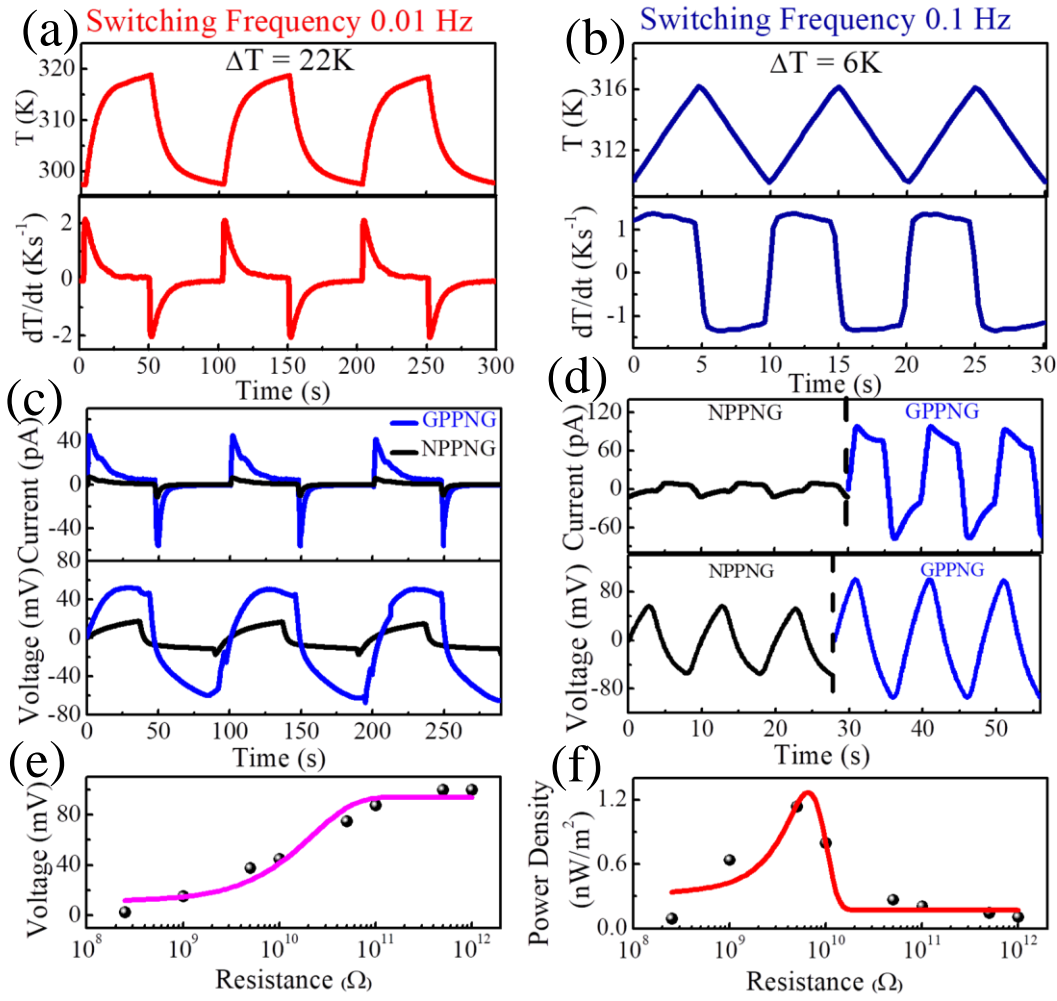
Figure 5.13 Time dependent cyclic temperature change (upper panels) and rate of change of temperature (*dT/dt*, lower panels) in the switching frequency of (a) 0.01 Hz and (b) 0.1 Hz. (c and d) Pyroelectric short circuit current (upper panels) and open circuit voltage (lower panels) measurement of the GPPNG under same switching frequency. (e) Output voltage and (f) power density as a function of external resistance varying from 250 MΩ to 1 TΩ when the GPPNG was driven by periodic thermal cycling (at 0.1 Hz).

room temperature to 318 K (*ΔT* = 22K and *dT/dt* = 2.12 K s^{-1}) (Figure 5.13(a)) the GPPNG shows an output peak current of 45 pA at a lamp switching frequency of 0.01 Hz, which is nearly seven times higher than that of NPPNG, as shown in Figure 5.13(c). When the

switching frequency changes from 0.01 Hz to 0.1 Hz, ($\Delta T = 6K$ and $dT/dt = 1.3$ K s^{-1}) (Figure 5.13(b)) the increase in peak output current is around 10 times higher than that of NPPNG (Figure 5.13(d)). When exposed to temperature changes, it can be observed that the short circuit current (I_{sc}) shows a positive peak if the material is heated ($dT/dt > 0$) and a negative peak during the convective cooling process ($dT/dt < 0$). This is due to the decrease in the level of spontaneous polarization during heating process, forcing the surface charges to flow between the two polar surfaces. When the device is subsequently cooled, current flows in the reverse direction due to the attractive force of the free charges to the polar surfaces [56-58]. In Figure 5.13(c and d), the GPPNG generates approximately 60 mV and 100 mV at a switching frequency of 0.01 Hz and 0.1 Hz respectively. Thus, it can be concluded that incorporation of the GO sufficiently increased the pyroelectric performance of the GPPNG. This improved performance can be described in terms of the following two factors:

1) The existence of a variety of oxygen-oriented functional groups within GO enhances the absorption in the mid-IR region. The absorbed IR is converted into heat, which increases the temperature of GO by exciting the C-C bond, yielding phonons. Due to this effect, a decrease in resistance is caused by the incident IR, which triggers a temperature-sensitive conductance change [59].

2) The thermal conductivity of GO can be ascribed by the increase in the interlayer coupling, which is provided by the covalent interactions of the oxygen atoms.

The pyroelectric coefficient of the GPPNG is described in terms of the following equations. Under short circuit conditions, $I_{sc} = P^*A \, dT/dt$ and in open circuit condition, $V_{oc} = \frac{P^*}{\varepsilon} \, t \, \Delta T$ [56, 60], where I_{sc} is the short circuit pyroelectric current, V_{oc} is the open circuit pyroelectric voltage, A is the electrode area, dT/dt is the rate of change in temperature, ΔT is the change of temperature, ε is the relative permittivity of the material, t is the thickness across the polarization direction and P^* is the pyroelectric coefficient respectively. Appling

our experimental data, the projected pyroelectric coefficient of the PVDF/1 wt.% GO is 27 $nCm^{-2}K^{-1}$, which is almost six times higher than the pure PVDF fiber (4 $nCm^{-2}K^{-1}$). The maximum generated output power density (Figures 5.13(e and f)) was found to be ~1.2 nW/m^2, which is assessed using the relation $P = \frac{1}{A}\frac{V_{oc}^2}{R_L}$, when periodic thermal energy was applied to the GPPNG at a switching frequency of 0.1 Hz. Thus, our device can be used as a promising waste heat energy harvester in addition to its piezoelectric energy harvesting and biomedical implementation.

5.4 Applications

5.4.1 Wearable Piezoelectric Pressure Sensor

In order to demonstrate the GPPNG as a self-powered wearable pressure sensor, it was attached to various human body parts for monitoring physiological signals. The GPPNG was employed on the wrist to evaluate the sensing features of the wearable nanogenerator for mechanical stimuli such as stretching and bending and the sensing performance and generated voltage was measured, as depicted in Figure 5.14(a). During a quick downward wrist bending motion, a sudden static tensile strain was exerted on the sensor, resulting in an overall increase of the voltage and it was retrieved by straightening the wrist to its original configuration. The response of the bending/relaxation motion of the wrist is a combined result of the stretching, bending effect of the skin (skin deformation) and the pressure is imparted by joint motion during repeated wrist bending. Additionally, flexing and extension of the elbow can be clearly distinguished by fixing the strain sensor on the joint area of the elbow using adhesive tape, as shown in Figure 5.14(b). Therefore, it can be concluded that the GPPNG strain sensor exhibits distinct output signals of different patterns related to numerous stimuli of synovial joints such as the wrist and elbow. Our device comprising of electrospun PVDF/ 1 wt.% GO nanofibers may be valuable in epidermal electronic systems fabrication and in medical applications such as monitoring patient and athlete motion.
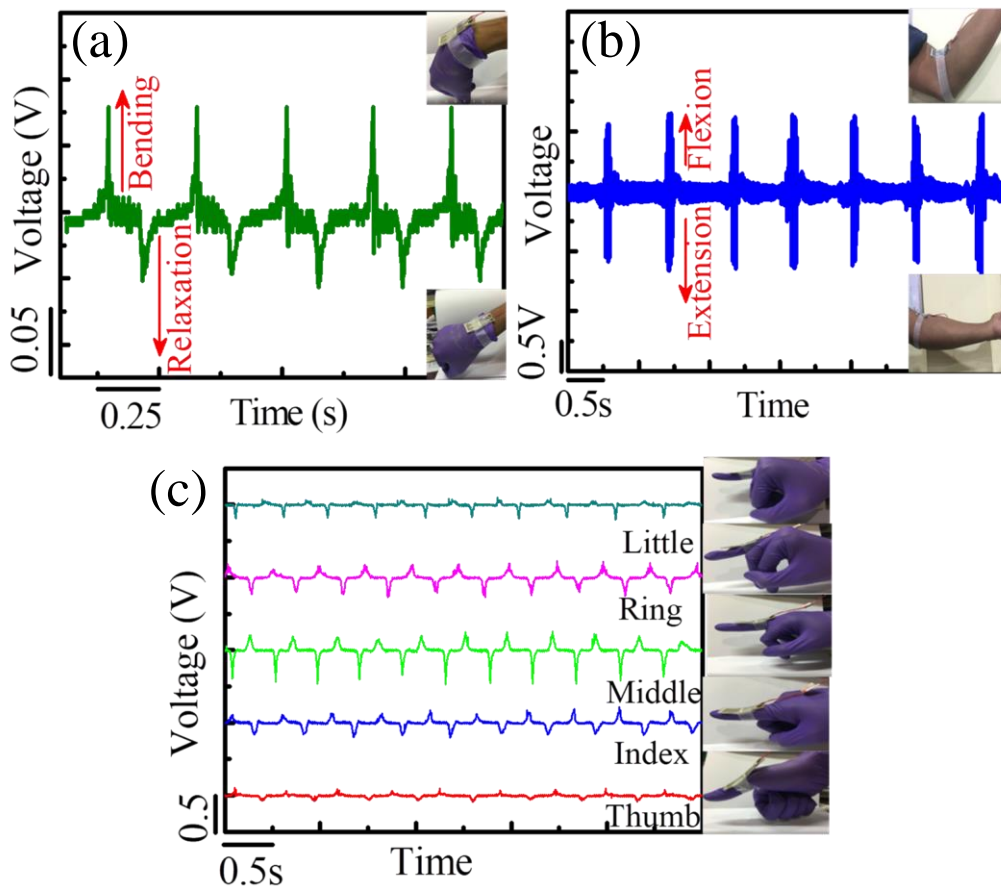
Figure 5.14 (a) Photograph of wrist joint bending, stretching when GPPNG sensor is attached on the top surface of the wrist and corresponding piezo-response with respect to output voltage signal is illustrated. Monitoring the (b) elbow joint (c) finger bending and stretching motion by detecting relative changes in output voltage signal as a function of time.

Furthermore, to demonstrate the potential of the GPPNG as a human motion detector, the GPPNG sensor was mounted on the top surface of individual fingers of a right hand and the corresponding sensing performance was monitored. As shown in Figure 5.14(c), the sensor can readily detect and discriminate between bending and stretching motion of each finger such as the thumb, index, middle, ring and little finger. The sensor exhibits different patterns of output signals by measuring voltage changes associated with variations in the bending. In

addition, these five independent strain sensors can be assembled into a wearable glove (data glove) to utilize it in remote patient monitoring system using wireless communication module to transmit the information of a sick patient to the cell phone of a doctor [61]. Such a data glove may be useful in the field of fine motion control in robotics such as drone, radio controlled car and to examine human body configuration [61-63]. More importantly, this wearable skin interactive strain sensor does not limit any human motion due to its high flexibility and light-weight nature.

Moreover, to allow the graphene based sensors to be worn near the skin for a real world application, the whole system was sandwiched using two layers of PDMS (Figure 5.1(e)). However, it should be emphasized that graphene oxide exhibits itself no cytotoxic reactions on human skin [64, 65] and graphene based materials are also appropriate for neural prosthetic devices, which are based on carbon [66], which indicate the potential biocompatibility of our GPPNG.

The GPPNG sensor can also be utilized to detect and monitor phonation (speech). When the sensor was fixed to the subject's throat, it was able to precisely monitor the pressure difference created by the muscle movement during speaking. As shown in Figure 5.15(a), it shows sensitivity towards specific phonation recognition. During the pronunciation of different alphabetic characters such as "A", "B", "C", "D" and "E", the stress originated from vocal vibrations due to the complex muscle movement all over the throat was transferred to the sensor. Thus, the sensor exhibits distinguishable output signal waveforms for each alphabetic character. It can be concluded from the short time Fourier transform (STFT) processed spectrograms for all five characters that maximum amplitude of all characters is approximately inside the frequency range of 250-300 Hz and in the higher frequency range of ~450 Hz and is in accordance with the fast Fourier transform (FFT) profile of each alphabetic character (Figure 5.15(b-f)). These results show that the self-powered wearable pressure
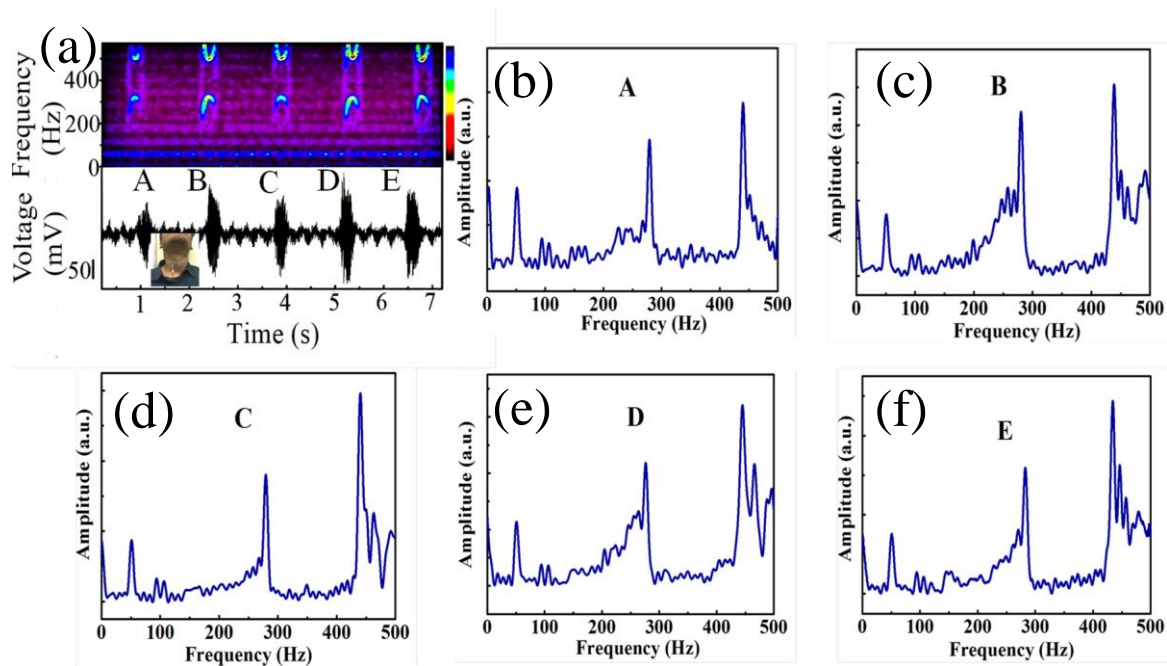
Figure 5.15 (a) Photograph of the GPPNG attached to the throat of a male participant during speaking of "A", "B", "C", "D", "E". Recorded output voltage response curves during pronunciation of these letters with FFT signal in the upper part are also shown. (b-f) FFT processed frequency spectrum profile during pronunciation of the letters "A", "B", "C", "D" and "E" as indicated in the diagrams when GPPNG is attached to a human throat.

sensor has potential application as a sound detecting skin and in speech rehabilitation training [67-69]. In addition, our device shows reproducible sensing property and repeatability towards thoracic pressure developed due to vibration of the tissue around vocal cord during repeated coughing action. The GPPNG sensor can successfully detect the two or three distinct phases of cough (Figure 5.16(a)), consisting initial opening burst, the blaring airflow (second phase) and possibly a final glottal closure [70, 71] as shown in the inset of Figure 5.16(a). The STFT processed signal of one single cough waveform (Figure 5.16(b)) validates its generation due to vibration of the vocal cord (200-450 Hz). Therefore, the GPPNG can be used to monitor the airway flow mechanics during coughing and for successive analysis and

206
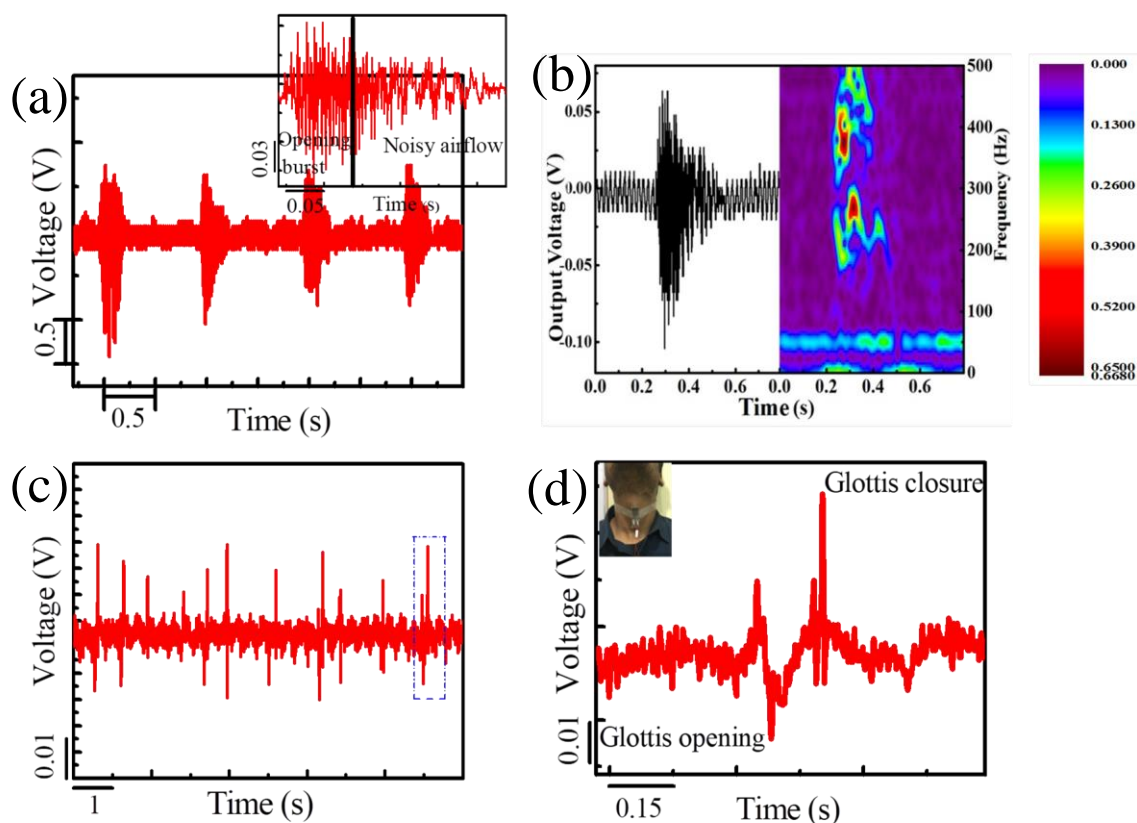
Figure 5.16 (a) Relative changes in the output voltage signal as a function of time when monitoring a coughing action (enlarged view is depicted in the inset). (b) The STFT processed spectrogram of one single cough signal. (c) Responsive curves of a swallowing exercise. (d) Magnified view of one swallowing signal marked in part.

diagnosis of coughing related to asthma and other bronchopulmonary respiratory diseases [70, 72, 73]. Furthermore, the complex gulping (swallowing) behaviour was also recorded reliably and repeatedly via the pressure sensor when attached to a human throat (Figures 5.16(c and d)). The relative change in voltage indicates the opening and closing event of the glottis associated with the muscle movement of the throat during agglutination behaviour. Such devices can be useful in sensor operated rehabilitation game for patients undergoing dysphagia and odynophagia (painful swallowing) [74]. All results indicate that the as-

prepared GPPNG sensor showed high sensitivity, repeatability and stability towards subtle pressure changes near human skin, stretching, bending and other physiological signals, indicating its wide futuristic application in personal health assessment and clinical diagnosis.

5.4.2 Pyroelectric Breathing Sensor
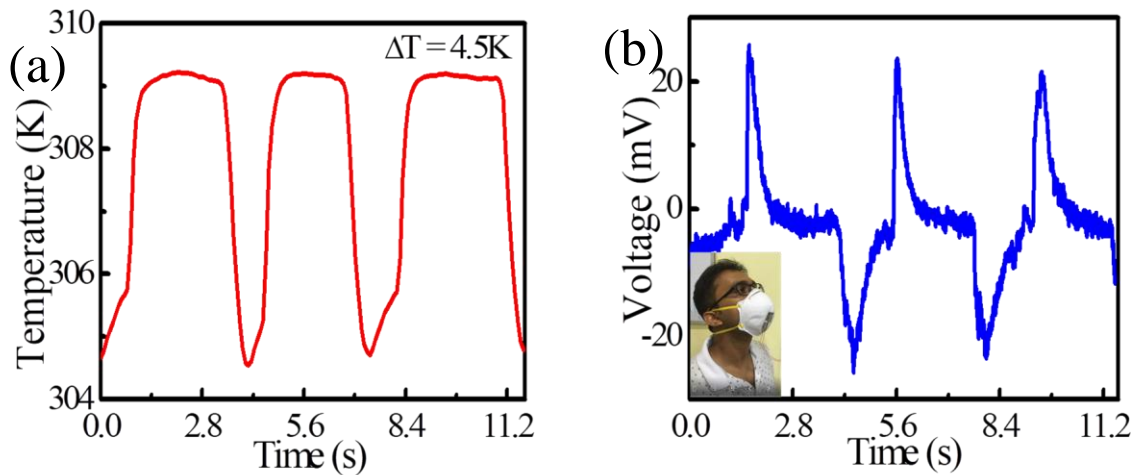
Figure 5.17 (a) The temperature fluctuation and (b) recorded open circuit voltage of the GPPNG (photo of the GPPNG attached to a N95 breathing mask is shown in the inset) driven by human respiratory at room temperature.

In addition to the piezoelectric sensing applications reported above, the GPPNG can be used as a self-powered breathing sensor as well as temperature sensor for human health monitoring and diagnosis. To demonstrate its use, the GPPNG was mounted on a N95 mask at the location where most of the airflow during respiration process is condensed (inset of Figure 5.17(b)). The whole system was worn on the human face and a temperature sensor was attached to the GPPNG during the experiment to record the real-time temperature fluctuations during breathing. The continuous breathing process led to periodic temperature differences around the mouth and the recorded temperature fluctuation during this respiratory process is almost 5K, as shown in Figure 5.17(a). Figure 5.17(b) clearly indicates the open circuit

voltage of the GPPNG, which is generated due to pyroelectric effect under the given experimental condition. The temperature of the airflow during respiration is similar to body temperature. Therefore, it is possible to harvest waste heat energy from respiration [75] by wearing the above mentioned system on the face in low temperature regions and in the winter season. Moreover, the breathing rate and breathing pattern are the vital signs of human health in detecting medical problems as they provide the information about how the cardiorespiratory system is working. The normal respiration rate for an adult at rest is 14 to 18 breaths per minute. Unusual respiration rates such as bradypnea (abnormally slow rate), tachypnea (abnormally rapid rate) are the alarming signs of various hidden diseases and psychological stress. In addition, unusual breathing patterns are also associated with different health conditions. For an example, Cheyne-Stokes breathing is an accurate sign of left ventricular dysfunction, especially for older patients (~80 years). From the featured results it is clear that the GPPNG is able to provide the information (rate and pattern) regarding human respiration. Moreover, its lightweight and high sensitivity make it a high-potential candidate for breathing sensor for real time health monitoring of aged persons and patients.

5.5 Conclusion

In conclusion, we have presented a novel wearable pressure sensor based on biocompatible graphene oxide doped PVDF nanofibers, which exhibited superior piezoelectric and pyroelectric sensing performance compared to pure PVDF nanofibers. The preparation of the PVDF/GO nanofibers via electrospinning and the complete fabrication strategy of the pressure and temperature sensor device are relatively simple with the combined advantages of a cost-effective fabrication process and potential for large-scale production and flexibility. We have demonstrated that the PVDF/GO nanofiber based sensor exhibits a high pressure sensitivity of 4.3 V/kPa, with a low detection limit up to 10 Pa. The sensor exhibits outstanding response for detecting a variety of human physiological signals such as joint

movements, coughing signals, swallowing and monitoring throat muscle movement in real time during repeated speaking of different alphabetic characters, confirming its potential for voice recognition. Moreover, the PVDF/GO nanofiber based device exhibits superior pyroelectric performance compared to pure PVDF with a maximum output power density of ~1.2 nW/m^2. Furthermore, it can sense periodic temperature fluctuation during continuous breathing process and the potential temperature sensing ability makes it promising as a breathing sensor. The fabricated system has promising applications in wearable smart skin for medical diagnostics, human health monitoring and power sources for wearable electronics and E-skin applications.

5.6 References

1. Wang, Y.; Yang, R.; Shi, Z.; Zhang, L.; Shi, D.; Wang, E.; Zhang, G. Super-Elastic Graphene Ripples for Flexible Strain Sensors. *ACS Nano* **2011**, 5, 3645−3650.

2. Takei, K.; Takahashi, T.; Ho, J. C.; Ko, H.; Gillies, A. G.; Leu, P. W.; Fearing, R. S.; Javey, A. Nanowire Active-Matrix Circuitry for Low-Voltage Macroscale Artificial Skin. *Nat. Mater.* **2010**, 9, 821−826.

3. Ghosh, S. K.; Mandal, D. Bio-assembled Piezoelectric Prawn Shell made Self-Powered Wearable Sensor for Non-invasive Physiological Signal Monitoring. *Appl. Phys. Lett.* **2017**, 110, 123701−123705.

4. Tao, L-Q.; Zhang, K-N.; Tian, H.; Liu, Y.; Wang, D-Y.; Chen, Y-Q.; Yang, Y.; Ren, T-L. Graphene-Paper Pressure Sensor for Detecting Human Motions. *ACS Nano* **2017**, 11, 8790−8795.

5. Chen, X.; Shao, J.; An, N.; Li, X.; Tian, H.; Xu, C.; Ding, Y. Self-Powered Flexible Pressure Sensors with Vertically Well-Aligned Piezoelectric Nanowire Arrays for Monitoring Vital Signs. *J. Mater. Chem. C* **2015**, 3, 11806–11814.

6. Zheng, L.; Shuai, C.; Wang, L.; Jiang, K.; Shen, G. An Ultra-Sensitive and Rapid Response Speed Graphene Pressure Sensors for Electronic Skin and Health Monitoring. *Nano Energy*, **2016**, 23, 7–14.

7. Zhou, Y.; He, J.; Wang, H.; Qi, K.; Nan, N.; You, X.; Shao, W.; Wang, L.; Ding, B.; Cui, S. Highly Sensitive, Self-Powered and Wearable Electronic Skin Based on Pressure-Sensitive Nanofiber Woven Fabric Sensor. *Scientific Reports*, **2017**, 7, 12949−12957.

8. Kim, D.H.; Lu, N.; Ma, R.; Kim, Y.S.; Kim, R.H.; Wang, S.; Wu, J.; Won, S. M.; Tao, H.; Islam, A; Rogers, John A. Epidermal Electronics. *Science* **2011**, 333, 838–843.

9. Lee, K.Y.; Gupta, M. K.; Kim, S.W. Transparent Flexible Stretchable Piezoelectric and Triboelectric Nanogenerators for Powering Portable Electronics. *Nano Energy* **2015**, 14, 139–160.

10. Schwartz, G.; Tee, B. C. K.; Mei, J.; Appleton, A. L.; Kim, D. H.; Wang, H.; Bao, Z. Flexible Polymer Transistors with High Pressure Sensitivity for Application in Electronic Skin and Health Monitoring. *Nat. Commun.* **2013**, 4, 1859–1867.

11. Gong, S.; Schwalb W.; Wang, Y.; Chen, Y.; Tang, Y.; Si, J.; Shirinzadeh, B.; Cheng, W. A Wearable and Highly Sensitive Pressure Sensor with Ultrathin Gold Nanowires. *Nat. Commun.* **2013**, 5, 3132−3139.

12. Segev-Bar, M.; Landman, A.; Nir-Shapira, M.; Shuster, G.; Haick, H. Tunable Touch Sensor and Combined Sensing Platform: Toward Nanoparticle-Based Electronic Skin. *ACS Appl. Mater. Interfaces* **2013**, 5, 5531−5541.

13. Maheshwari, V.; Saraf, R. F. High-Resolution Thin-Film Device to Sense Texture by Touch. *Science* **2006**, 312, 1501−1504.

14. Jiang, M. J.; Dang, Z. M.; Xu, H. P. Giant Dielectric Constant and Resistance-Pressure Sensitivity in Carbon Nanotubes/Rubber Nanocomposites with Low Percolation Threshold. *Appl. Phys. Lett*. **2007**, 90, 042914−042916.

15. Dang, Z.-M.; Jiang, M.-J.; Xie, D.; Yao, S.-H.; Zhang, L.-Q.; Bai, J. Supersensitive Linear Piezoresistive Property in Carbon Nanotubes∕Silicone Rubber Nanocomposites. *J. Appl. Phys.* **2008**, 104, 024114−024119.

16. Chen, L.; Chen, G. H.; Lu, L. Piezoresistive Behavior Study on Finger-Sensing Silicone Rubber/Graphite Nanosheet Nanocomposites. *Adv. Funct. Mater.* **2007**, 17, 898−904.

17. Fan, F. R.; Tang, W.; Wang, Z. L. Flexible Nanogenerators for Energy Harvesting and Self-Powered Electronics. *Adv. Mater.* **2016**, 28, 4283–4305.

18. Lang, S. B.; Das-Gupta, D. K. *Pyroelectricity: Fundamentals and Applications. Handbook of Advanced Electronic and Photonic Materials and Devices* **2000**, 4, 22−50.

19. Lin, Y-F.; Song, J.; Ding, Y.; Lu, S-Y.; Wang, Z. L. Piezoelectric Nanogenerator Using CdS Nanowires. *Appl. Phys. Lett.* **2008**, 92, 022105−022107.

20. Kang, H. B.; Chang, J.; Koh, K.; Lin, L.; Cho, Y. S. High Quality Mn-Doped (Na,K)NbO$_3$ Nanofibers for Flexible Piezoelectric Nanogenerators. *ACS Appl. Mater. Interfaces* **2014**, 6, 10576−10582.

21. Park, K. I.; Xu, S.; Liu, Y.; Hwang, G. T.; Kang, S. J. L.; Wang, Z. L.; Lee, K. J. Piezoelectric BaTiO$_3$ Thin Film Nanogenerator on Plastic Substrates. *Nano Lett.* **2010**, 10, 4939−4943.

22. Wang, Z. L.; Song, J. Piezoelectric Nanogenerators Based on Zinc Oxide Nanowire Arrays. *Science* **2006**, 312, 242−246.

23. Ghosh, S. K.; Alam, M. M.; Mandal, D. The *In Situ* Formation of Platinum Nanoparticles and Their Catalytic Role in Electroactive Phase Formation in Poly(vinylidene fluoride): A Simple Preparation of Multifunctional Poly(vinylidene fluoride) Films Doped with Platinum Nanoparticles. *RSC Adv.* **2014**, 4, 41886−41894.

24. Mandal, D.; Kim, K. J.; Lee, J. S. Simple Synthesis of Palladium Nanoparticles, β-Phase Formation, and the Control of Chain and Dipole Orientations in Palladium-Doped Poly(vinylidene fluoride) Thin Films. *Langmuir* **2012**, 28, 10310−10317.

25. Jana, S.; Garain, S.; Sen, S.; Mandal, D. The Influence of Hydrogen Bonding on Dielectric Constant and Piezoelectric Energy Harvesting Performance of Hydrated Metal Salt Mediated PVDF Films. *Phys. Chem. Chem. Phys.* **2015**, 17, 17429−17436.

26. Garain S.; Jana, S.; Sinha, T. K.; Mandal, D. Design of In Situ Poled Ce^{3+}-Doped Electrospun PVDF/Graphene Composite Nanofibers for Fabrication of Nanopressure Sensor and Ultrasensitive Acoustic Nanogenerator. *ACS Appl. Mater. Interfaces* **2016**, 8, 4532−4540.

27. Lovinger, A. J. Ferroelectric Polymers. *Science* **1983**, 220, 1115−1121.

28. Martins, P.; Lopez, A. C.; Mendeza, S. L. Electroactive Phases of Poly(vinylidene fluoride): Determination, Processing and Applications. *Prog. Polym. Sci.*, **2014**, 39, 683−706.

29. Maity, K.; Mahanty, B.; Sinha, T. K.; Garain, S.; Biswas, A.; Ghosh, S. K.; Manna, S.; Ray, S. K.; Manadal, D. Two-Dimensional Piezoelectric MoS_2-Modulated Nanogenerator and Nanosensor Made of Poly(vinlydine Fluoride) Nanofiber Webs for Self-Powered Electronics and Robotics. *Energy Technol.* **2016**, 4, 1−11.

30. Roy, K., Mandal, D. CdS Decorated rGO Containing PVDF Electrospun Fiber Based Piezoelectric Nanogenerator for Mechanical Energy Harvesting Application. *AIP Conference Proceedings* 1942, 2018, 050125−050128.

31. Yadav, S. K.; Cho, J. W. Functionalized Graphene Nanoplatelets for Enhanced Mechanical and Thermal Properties of Polyurethane Nanocomposites. *Appl. Surf. Sci.* **2013**, 266, 360−367.

32. Tong, W.; Zhang, Y.; Yu, L.; Luan, X.; An, Q.; Zhang, Q.; Lv, F.; Chu, P. K.; Shen, B.; Zhang, Z. Novel Method for the Fabrication of Flexible Film with Oriented Arrays of Graphene in Poly(vinylidene fluoride-*co*-hexafluoropropylene) with Low Dielectric Loss. *J. Phys. Chem. C* **2014**, 118, 10567−10573.

33. Hummers, W. S.; Offeman, R. E. Preparation of Graphitic Oxide. *J. Am. Chem. Soc.* **1958**, 80, 1339−1339.

34. Zhang H.; Feng, P. X. Fabrication and Characterization of Few-Layer Graphene. *Carbon* **2010**, 48, 359–364.

35. Ortolani, L.; Cadelano, E.; Veronese, G. P.; Colombo, L.; Morandi, V. Folded Graphene Membranes: Mapping Curvature at the Nanoscale. *Nano Letters* **2012**, 12, 5207–5212.

36. Xian, H.; Peng, T.; Sun, H.; Wang, J. The Effect of Thermal Exfoliation Temperature on the Structure and Supercapacitive Performance of Graphene Nanosheets. *Nano-Micro Lett*. **2015**, 7, 17–26.

37. Mandal D.; Henkel, K.; Schmeißer, D. Improved Performance of a Polymer Nanogenerator Based on Silver Nanoparticles Doped Electrospun P(VDF–HFP) Nanofibers. *Phys. Chem. Chem. Phys.* **2014**, 16, 10403−10407.

38. Zeng, W.; Tao, X. M.; Chen, S.; Shang, S.; Chan, H. L. W.; Choy, S. H. Highly Durable All-Fiber Nanogenerator for Mechanical Energy Harvesting. *Energy Environ. Sci.* **2013**, 6, 2631−2638.

39. Ince-Gunduz, B. S.; Alpern, R.; Amare, D.; Crawford, J.; Dolan, B.; Jones, S.; Kobylarz, R.; Reveley, M.; Cebe, P. Impact of Nanosilicates on Poly(vinylidene

fluoride) Crystal Polymorphism: Part 1. Melt-Crystallization at High Supercooling. *Polymer* **2010**, 51, 1485−1493.

40. Sharma, M.; Madras, G.; Bose, S. Contrasting Effects of Graphene Oxide and Poly(ethylenimine) on the Polymorphism in Poly(vinylidene fluoride). *Cryst. Growth Des.* **2015**, 15, 3345−3355.

41. Liu, X.; Ma, J.; Wu, X.; Lin, L.; Wang, X. Polymeric Nanofibers with Ultrahigh Piezoelectricity via Self-Orientation of Nanocrystals. *ACS Nano* **2017**, 11, 1901−1910.

42. Karan, S. K.; Mandal, D.; Khatua, B. B. Self-Powered Flexible Fe-Doped RGO/PVDF Nanocomposite: An Excellent Material for a Piezoelectric Energy Harvester. *Nanoscale* **2015**, 7, 10655−10666.

43. Adhikary, P.; Garain, S.; Mandal, D. The Co-Operative Performance of a Hydrated Salt Assisted Sponge Like P(VDF-HFP) Piezoelectric Generator: An Effective Piezoelectric Based Energy Harvester. *Phys. Chem. Chem. Phys.* **2015**, 17, 7275−7281.

44. Garain, S.; Sinha, T. K.; Adhikary, P.; Henkel, K.; Sen, S.; Ram, S.; Sinha, C.; Schmeiβer, D.; Mandal, D. Self-Poled Transparent and Flexible UV Light-Emitting Cerium Complex−PVDF Composite: A High-Performance Nanogenerator. *ACS Appl. Mater. Interfaces* **2015**, 7, 1298−1307.

45. Mandal, D.; Yoon, S; Kim, K. J. Origin of Piezoelectricity in An Electrospun Poly(vinylidene fluoride-trifluoroethylene) Nanofiber Web-Based Nanogenerator and Nano-Pressure Sensor. *Macromol. Rapid Commun*. **2011**, 32, 831−837.

46. Huang, L.; Lu, C.; Wang, F.; Wang, L. Preparation of PVDF/Graphene Ferroelectric Composite Films by *In Situ* Reduction with Hydrobromic Acids and their Properties. *RSC Adv.* **2014**, 4, 45220−45229.

47. Fan, Z. J.; Kai, W.; Yan, J.; Wei, T.; Zhi, L. J.; Feng, J.; Ren, Y. M.; Song, L.-P.; Wei, F. Facile Synthesis of Graphene Nanosheets via Fe Reduction of Exfoliated Graphite Oxide. *ACS. Nano* **2011**, 5, 191−198.

48. Lopes, A. C.; Costa, C. M.; Tavares, C. J.; Neves, I. C.; Lanceros-Mendez, S. Nucleation of the Electroactive γ Phase and Enhancement of the Optical Transparency in Low Filler Content Poly(vinylidene)/Clay Nanocomposites. *Phys. Chem. C* **2011**, 115, 18076−18082.

49. Lopes, A. C.; Carbineiro, S. A. C.; Pereira, M. F. R.; Botelho, G.; Lanceros-Mendez, S. Nanoparticle Size and Concentration Dependence of the Electroactive Phase Content and Electrical and Optical Properties of Ag/Poly(vinylidene fluoride) Composites. *ChemPhysChem* **2013**, 14, 1926−1933.

50. Bowen, C. R.; Kim, H. A.; Weaver, P. M.; Dunn, S. Piezoelectric and Ferroelectric Materials and Structures for Energy Harvesting Applications. *Energy Environ. Sci.* **2014**, 7, 25–44.

51. Lingam, D.; Parikh, A. R.; Huang, J.; Jain A.; Minary- Jolandan, M. Nano/Microscale Pyroelectric Energy Harvesting: Challenges and Opportunities. *Int. J. Smart Nano Mater.* **2013**, 4, 229–245.

52. Lee, K. Y.; Kim, D.; Lee, J. H.; Kim, T. Y.; Gupta, M. K.; Kim, S. W. Unidirectional High-Power Generation via Stress-Induced Dipole Alignment from ZnSnO$_3$ Nanocubes/Polymer Hybrid Piezoelectric Nanogenerator. *Adv. Funct. Mater.* **2013**, 24, 37–43.

53. Lee, J. H.; Yoon, H. J.; Kim, T. Y.; Gupta, M. K.; Lee, J. H.; Seung, W.; Ryu, H.; Kim, S. W. Micropatterned P(VDF-TrFE) Film-Based Piezoelectric Nanogenerators for Highly Sensitive Self-Powered Pressure Sensors. *Adv. Funct. Mater.* **2015**, 25, 3203−3209.

54. Mao, Y.; Zhao, P.; McConohy, G.; Yang, H.; Tong, Y.; Wang, X. Sponge-Like Piezoelectric Polymer Films for Scalable and Integratable Nanogenerators and Self-Powered Electronic Systems. *Adv. Energy Mater.* **2014**, 4, 1301624–1301630.

55. Park, D. Y.; Joe, D. J.; Kim, D. H.; Park, H.; Han, J. H.; Jeong, C. K.; Park, H.; Park, J. G.; Joung, B.; Lee, K. J. Self-Powered Real-Time Arterial Pulse Monitoring Using Ultrathin Epidermal Piezoelectric Sensors. *Adv. Mater.* **2017**, 29, 1702308−1702316.

56. Lee, J-H.; Ryu, H.; Kim, T-Y.; Kwak, S-S.; Yoon, H-J.; Kim, T-H.; Seung, W.; Kim, S. W. Thermally Induced Strain-Coupled Highly Stretchable and Sensitive Pyroelectric Nanogenerators. *Adv. Energy Mater.* **2015**, 5, 1500704–1500709.

57. Xie, M.; Zabek, D.; Bowen, C.; Abdelmageed, M.; Arafa, M. Wind-driven Pyroelectric Energy Harvesting Device. *Smart Mater. Struct.* **2016**, 25, 125023–125030.

58. Zabek, D.; Taylor, J.; Boulbar, E L.; Bowen, C. R. Micropatterning of Flexible and Free Standing Polyvinylidene Difluoride (PVDF) Films for Enhanced Pyroelectric Energy Transformation. *Adv. Energy Mater.* **2015**, 5, 1401891–1401896.

59. Bae, J. J.; Yoon, J H.; Jeong, S.; Moon, B H.; Han, J T.; Jeong, H. J.; Lee, G-W.; Whang, H R.; Lee, Y H.; Jeong, S Y.; Lim, S. C. Sensitive Photo-Thermal Response of Graphene Oxide for Mid-Infrared Detection. *Nanoscale* **2015**, 7, 15695–15700.

60. Zabek, D.; Seunarine, K.; Spacie, C.; Bowen, C. Graphene Ink Laminate Structures on Poly(vinylidene difluoride) (PVDF) for Pyroelectric Thermal Energy Harvesting and Waste Heat Recovery. *ACS Appl. Mater. Interfaces* **2017**, 9, 9161−9167.

61. Ghosh, S. K.; Adhikary, P.; Jana, S., Biswas, A.; Sencadas, V.; Dutta Gupta, S.; Tudu, B.; Mandal, D. Electrospun Gelatin Nanofiber Based Self-Powered Bio-*e*-skin for Health Care Monitoring. *Nano Energy* **2017**, 36, 166–175.

62. Tee, B. C.; Wang, C.; Allen, R.; Bao, Z. An Electrically and Mechanically Self-Healing Composite with Pressure- and Flexion-Sensitive Properties for Electronic Skin Applications. *Nat. Nanotechnol.* **2012**, 7, 825−832.

63. Deng, W.; Yang, T.; Jin, L.; Yan, C.; Huang, H.; Chu, X.; Wang, Z.; Xiong, D.; Tian, G.; Gao, Y.; Zhang, H.; Yang, W. Cowpea-Structured PVDF/ZnO Nanofibers Based Flexible Self-Powered Piezoelectric Bending Motion Sensor Towards Remote Control of Gestures. *Nano Energy* **2019**, 55, 516–525.

64. Pelin, M.; Fusco, L.; Leon, V.; Martin, C.; Criado, A.; Sosa, S.; Vazquez, E.; Tubaro, A.; Prato, M. Differential Cytotoxic Effects of Graphene and Graphene Oxide on Skin Keratinocytes. *Scientific Reports* **2017**, 7, 40572−40583.

65. Conroy, J.; Verma, N. K.; Smith, R. J.; Rezvani, E.; Duesberg, G. S.; Coleman, J. N.; Volkov, Y. Biocompatibility of Pristine Graphene Monolayers, Nanosheets and Thin Films. **2014**, arXiv:1406.2497 [q-bio.CB] or arXiv:1406.2497v1 [q-bio.CB].

66. Fabbro, A.; Scaini, D.; Leon, V.; Vazquez, E.; Cellot, G.; Privitera, G.; Lombardi, L.; Torrisi, F.; Tomarchio, F.; Bonaccorso, F.; Bosi, S.; Ferrari, A. C.; Ballerini, L.; Prato, M. Graphene-Based Interfaces Do Not Alter Target Nerve Cells. *ACS Nano* **2016**, 10, 615–623.

67. Sultana, A.; Ghosh, S. K.; Sancadas, V.; Zheng, T.; Higgins, M. J.; Middya, T. R.; Mandal, D. Human Skin Interactive Self-Powered Wearable Piezoelectric Bio-e-skin by Electrospun Poly-L-lactic Acid Nanofibers for Non-invasive Physiological Signal Monitoring. *J. Mater. Chem. B* **2017**, 5, 7352–7359.

68. Ghosh, S. K.; Mandal, D. Sustainable Energy Generation from Piezoelectric Biomaterial for Non-invasive Physiological Signal Monitoring. *ACS Sustainable Chem. Eng.* **2017**, 5, 8836–8843.

69. Chen, X.; Parida, K.; Wang, J.; Xiong, J.; Lin, M-F.; Shao, J.; Lee, P. S. A Stretchable and Transparent Nanocomposite Nanogenerator for Self-Powered Physiological Monitoring. *ACS Appl. Mater. Interfaces* **2017**, 9, 42200–42209.

70. Pirilia, P.; Sovijarvi, A. R. A. Objective Assessment of Cough. *Eur Respir J* **1995**, 8, 1949–1956.

71. Thorpe, C. W.; Toop, L. J.; Dawson, K. P. Towards a Quantitative Description of Asthmatic Cough Sounds. *Eur Respir J* **1992**, 5, 685−692.

72. Thorpe, W.; Kurver, M.; King, G.; Salome, C. In *Acoustic Analysis of Cough.*, **The Seventh Australian and New Zealand Intelligent Information Systems Conference,** IEEE, Perth, Western Australia, 18-21 November, **2001**, 391−394.

73. Chen, X.; Li, X.; Shao, J.; An, N.; Tian, H.; Wang, C.; Han, T.; Wang, L.; Lu, B. High-Performance Piezoelectric Nanogenerators with Imprinted P(VDF-TrFE)/BaTiO$_3$ Nanocomposite Micropillars for Self-Powered Flexible Sensors. *Small* **2017**, 13, 1604245–1604256.

74. Nicholls, B.; Ang, C. S.; Efstratiou, C, Lee, Y; Yeo, W-H. In *Swallowing Detection for Game Control: Using Skin-Like Electronics to Support People with Dysphagia.*, 2017 IEEE International Conference on Pervasive Computing and Communications Workshops (PerCom Workshops) IEEE, Kona, HI, USA, 13-17 March, **2017**, **DOI:** 10.1109/PERCOMW.2017.7917598.

75. Xue, H.; Yang, Q.; Wang, D.; Luo, W.; Wang, W.; Lin, M.; Liang, D.; Luo, Q. A Wearable Pyroelectric Nanogenerator and Self-Powered Breathing Sensor. *Nano Energy* **2017**, 38, 147–154.

Chapter 6

Conclusion and Future Outlook

6.1 General Conclusion

This thesis unveils different strategies adapted for successful fabrication of efficient piezo- and pyroelectric nanogenerators (NGs) towards versatile self-powered applications. In particular, the main objective is to harvest mechanical and thermal energy from environment to pave a way towards battery free alternative energy source. It includes synthesis of materials, characterizations, fabrications, optimizations, theoretical analysis and applications involving self-powered flexible electronics to wearable health monitoring. This thesis has been accomplished by compiling the following works.

In the first approach, a 2D MOF incorporated composite PVDF nanofiber was successfully prepared using electrospinning technique. It has been realised that the non-piezoelectric MOF helped to improve the piezoelectric component of the PVDF nanofiber. Furthermore, a highly sensitive PNG was made comprising the composite fiber, which shows different self-powered applications such as human motion sensing and acoustoelectric conversion. The detailed characterization, fabrication strategy and piezoelectric performance were exclusively elaborated in chapter 2.

In the second phase of work, a new class of piezoelectric energy harvester termed as ferroelectret nanogenerator was fabricated. The polymer ferroelectret film was prepared by solvent casting method via incorporation of a 3D MOF in PVDF matrix. Owing to its high mechano-sensitivity, the ferroelectret film was further mounted on wrist to detect and monitor wrist pulse wirelessly.

Furthermore, an all organic-inorganic approach was adapted to harvest pyroelectric energy. It is indeed a simple and facile strategy where we employed an organic electrode on CdS-rGO embedded composite PVDF nanofiber mat (C-PVDF) for better connectivity and durability. The all organic-inorganic pyroelectric nanogenerator (A-PyNG) shows excellent pyroelectric

output. Moreover, it was mounted on an N-95 mask for monitoring inhale and exhale process. This application demonstrates its potential to be used as a breathing sensor in biomedical sector.

In the final phase of work, a highly efficient strategy to prepare a hybrid energy harvester (piezo- and pyroelectric energy) was innovatively presented. GO modulated PVDF nanofiber mat was eventually used for energy harvesting. The hybrid energy harvester was suitable for non-invasive monitoring of vital signs. On the other hand, it can be used for powering up consumer electronics. As a proof of evidence, it can drive several light emitting diodes (LEDs). Moreover, it shows outstanding energy storage ability for different commercially available capacitors (capacitances of 1, 2.2, 4.7 μF).

We are pretty sure that our research findings and sensory applications will pave the way for next generation self-powered portable electronics to wearable and non-invasive biomedical sensors.

6.2 Future Prospect

A couple of promising applications of piezo- and pyroelectric nanogenerators have been demonstrated in this thesis. However, I believe that there exist more attractive materials or interesting applications waiting for being explored. It has opened various new possibilities as discussed below:

Hybrid NGs are also a matter of study for scientists. Pyroelectric materials integrated to solar energy harvesting can open up a more extensive array of novel applications, for example all in one energy conversion as well as storage device.

Recently, triboelectric nanogenerator (TENG) is also an outstanding technology for mechanical to electrical energy conversion. Moreover, it currently dominates the field of NGs

due to high output power generation. If PNGs and TENGs could be combined by taking advantages of both of their own merits, it is possible that future researchers would come up with innovative NG array with high efficiency, device design, small size and wide range of applications.

Enormous developments have been made to construct NGs for in vitro conditions. However, it is still a great challenge to establish NGs in vivo environments to enable its application particularly as everyday engrafted bio-devices. The NGs should be non-hazardous, which could harvest the biomechanical energy within the human body for example, blood flow, heart beats, blinking and muscle contracting etc.

Another great prospect of this research is to develop self-charging power cells by the integrating both energy harvesting and storage system in a single portable device. In modern electronics it is highly essential to design a compact and wearable electronic device which could not only harvest electrical energy from the abundant mechanical sources but also synchronously store the energy for further applications.

We have already demonstrated that assimilation of different MOFs can generate highly efficient piezoelectric and polymer ferroelectret NGs. However, piezoelectricity of MOFs is rarely explored. Therefore, developing new class of MOFs with high piezoelectric co-efficient can pave the way for self-powered electronics with miniaturization and multi-functionalization.

Additionally, δ-phase of PVDF is not yet explored in terms of nanogenerator applications. However, it has similar potential to be applied in different sensory application. Thus, there relies a broader opportunity to apply δ -PVDF in charging portable electronics to helath care monitoring.